

Magnetoresistance and ion bombardment induced  
magnetic patterning

Dissertation Universität Bielefeld

Volker Höink

January 22, 2008

## **Erklärung**

Hiermit erkläre ich, dass ich die vorliegende Arbeit selbstständig verfasst und keine anderen als die angegebenen Hilfsmittel verwendet habe.

Bielefeld, 22. Januar 2008

Gutachter:

Prof. Dr. Günter Reiss

Prof. Dr. Dario Anselmetti

Datum des Einreichens der Arbeit: 23. Januar 2008

# Publications

## Peer review journals

- J. Schmalhorst, M. Sacher, V. Höink, G. Reiss, D. Engel, and A. Ehresmann, *X-ray absorption and magnetic circular dichroism studies of ion bombarded ferromagnet-antiferromagnet bilayers*, Physical Review B **70** (2004) 184403
- D. Engel, A. Ehresmann, J. Schmalhorst, M. Sacher, V. Höink, and G. Reiss, *Initialization of unidirectional anisotropy in a ferromagnetantiferromagnet bilayer by keV-He ion bombardment*, Journal of Magnetism and Magnetic Materials **293** (2005) 849853
- V. Höink, M. D. Sacher, J. Schmalhorst, and G. Reiss, D. Engel, D. Junk, and A. Ehresmann, *Postannealing of magnetic tunnel junctions with ion-bombardment modified exchange bias*, Applied Physics Letters **86** (2005) 152102
- J. McCord, R. Schäfer, K. Theis-Bröhl, H. Zabel, J. Schmalhorst, V. Höink, H. Brückl, T. Weiss, D. Engel, and A. Ehresmann, *Domain propagation in He-ion-bombarded magnetic wires with opposite exchange bias*, Journal of Applied Physics **97** (2005) 10K102
- A. Ehresmann, D. Engel, T. Weis, A. Schindler, D. Junk, J. Schmalhorst, V. Höink, M. D. Sacher, and G. Reiss, *Fundamentals for magnetic patterning by ion bombardment of exchange bias layer systems*, Physica Status Solidi (b) **243**, No. 1 (2006) 2936
- Katharina Theis-Bröhl, Max Wolff, Andreas Westphalen, and Hartmut Zabel, Jeffrey McCord, Volker Höink, Jan Schmalhorst, and Günther Reiss, Tanja Weis, Dieter Engel, and Arno Ehresmann, Ulrich Rücker, and Boris P. Toperverg, *Exchange-bias instability in a bilayer with an ion-beam imprinted stripe pattern of ferromagnetic/antiferromagnetic interfaces*, Physical Review B **73** (2006) 174408
- V. Höink, M. D. Sacher, J. Schmalhorst, G. Reiss, D. Engel, T. Weis, and A. Ehresmann, *Thermal stability of magnetic nanostructures in ion-bombardment-*

*modified exchange-bias systems*, Physical Review B **73** (2006) 224428

- V. Höink, M. D. Sacher, J. Schmalhorst, G. Reiss, D. Engel, T. Weis, and A. Ehresmann, *Switchable resonant x-ray Bragg scattering on a magnetic grating patterned by ion bombardment*, Journal of Applied Physics **100** (2006) 063903  
This article has been selected for the October 9, 2006 issue of Virtual Journal of Nanoscale Science & Technology (Volume 14, Issue 15).
- J. Schmalhorst, M. D. Sacher, V. Höink, G. Reiss, A. Hütten, D. Engel, and A. Ehresmann, *Magnetic and chemical properties of Co<sub>2</sub>MnSi thin films compared to the Co<sub>2</sub>MnSi/Al-O interface*, Journal of Applied Physics **100** (2006) 113903  
This article has been selected for the December 18, 2006 issue of Virtual Journal of Nanoscale Science & Technology (Volume 14, Issue 25).
- K. Theis-Bröhl, B.P. Toperverg, A. Westphalen, H. Zabel, J. McCord, V. Höink, J. Schmalhorst, G. Reiss, T. Weis, D. Engel, A. Ehresmann, and U. Rücker, *Polarized neutron reflectometry study on a magnetic film with an ion beam imprinted stripe pattern*, Superlattices and Microstructures **41** (2007) 104
- I. Ennen, V. Höink, A. Weddemann, A. Hütten, J. Schmalhorst, G. Reiss, C. Waltenberg, P. Jutzi, T. Weis, D. Engel, and A. Ehresmann, *Manipulation of magnetic nanoparticles by the strayfield of magnetically patterned ferromagnetic layers*, Journal of Applied Physics **102** (2007) 013910
- V. Höink, D. Meyners, J. Schmalhorst, G. Reiss, D. Junk, D. Engel and A. Ehresmann, *Reconfigurable magnetic logic for all basic logic functions produced by ion bombardment induced magnetic patterning*, Applied Physics Letters **91** (2007) 162505,  
This article has been selected for the October 29, 2007 issue of Virtual Journal of Nanoscale Science & Technology (Volume 16, Issue 18).
- V. Höink, J. Schmalhorst, G. Reiss, T. Weis, D. Lengemann, D. Engel, and A. Ehresmann, *Influence of ion bombardment induced patterning of exchange bias in pinned artificial ferrimagnets on the interlayer exchange coupling*, submitted
- V. Höink, X. Kou, J. Schmalhorst, G. Reiss, T. Weis, D. Lengemann, and A. Ehresmann, *Ion bombardment induced magnetic patterning of reference electrodes in magnetic tunnel junctions with MgO barrier*, in preparation

## Patent

One patent application has been submitted to the DPMA (Deutsches Patent und Markenamt) on July 21, 2007.

## Other publications

- J. Schmalhorst, M. Sacher, S. Kämmerer, V. Höink, A. Hütten, G. Reiss, D. Engel, and A. Ehresmann, *Implementation of Co<sub>2</sub>MnSi electrodes in magnetic tunnel junctions: magnetic and chemical bulk properties compared to the interface*, BESSY annual report 2004, p. 364 (www.bessy.de)
- Marc D. Sacher, Volker Höink, Jan Schmalhorst, and Günter Reiss, *Surface sensitive X-ray magnetic circular dichroism (XMCD) measurements of Al<sub>2</sub>O<sub>3</sub> capped magnetite (Fe<sub>3</sub>O<sub>4</sub>) for implementation in a magnetic tunnel junction*, BESSY annual report 2005, p. 218 (www.bessy.de)
- V. Höink, M. D. Sacher, J. Schmalhorst, G. Reiss D. Engel, T. Weis, and A. Ehresmann, *Resonant x-ray Bragg scattering on a magnetic grating patterned by ion bombardment in a magnetic field*, BESSY annual report 2005, p.303 (www.bessy.de)
- K. Theis-Bröhl, M. Wolff, H. Zabel, B.P. Toperverg, J. McCord, V. Höink, J. Schmalhorst, G. Reiss, T. Weis, D. Engel, and A. Ehresmann, *Magnetic order in exchange bias patterns in a continuous film*, Institut Laue-Langevin annual report 2006 (www.ill.eu)

## Conferences

- V. Höink, J. Schmalhorst, G. Reiss, D. Engel, D. Junk and A. Ehresmann, *Ladungstransport in mit He-Ionen bestrahlten Tunnelelementen*, talk at DPG-Spring meeting 2004, Regensburg
- V. Höink, M.D. Sacher, J. Schmalhorst, G. Reiss, D. Engel, T. Weis and A. Ehresmann, *Thermal stability of magnetic nanostructures in ion-bombardment-modified exchange bias systems*, poster at DPG-Spring meeting 2005, Berlin
- V. Höink, M.D. Sacher, K. Rott, J. Schmalhorst, G. Reiss, D. Engel, T. Weis, and A. Ehresmann, *Thermal stability of three dimensional structured exchange bias systems with ion bombardment induced magnetic patterning*, poster at DPG-Spring meeting 2006, Dresden
- V. Höink, X. Kou, J. Schmalhorst, G. Reiss, T. Weis, D. Engel, and A. Ehresmann, *Magnetic patterning of exchange biased CoFeB electrodes by ion bombardment in magnetic tunnel junctions with MgO barrier*, poster at Third Joint European Magnetic Symposia 2006, San Sebastian
- V. Höink, J. Schmalhorst, G. Reiss, T. Weis, D. Engel, and A. Ehresmann, *Influence of ion bombardment induced patterning of exchange bias in pinned artificial ferrimagnets on the interlayer exchange coupling*, poster at DPG-Spring meeting 2007, Regensburg
- V. Höink, X. Kou, J. Schmalhorst, G. Reiss, T. Weis, D. Lengemann, and A. Ehresmann, *Ion bombardment induced magnetic patterning of reference electrodes in magnetic tunnel junctions with MgO barrier*, submitted for DPG-Spring meeting 2008, Berlin

- V. Höink, D. Meyners, J. Schmalhorst, G. Reiss, D. Junk, D. Engel and A. Ehresmann, *Reconfigurable magnetic logic for all basic logic functions produced by ion bombardment induced magnetic patterning*, submitted for DPG-Spring meeting 2008, Berlin

# Contents

<b>1</b>	<b>Introduction</b>	<b>10</b>
<b>2</b>	<b>Theoretical and experimental basics</b>	<b>13</b>
2.1	Exchange Bias . . . . .	13
2.2	Ion bombardment induced magnetic patterning . . . . .	19
2.2.1	Manipulation of exchange bias by ion bombardment . . . . .	19
2.2.2	Local manipulation by ion bombardment . . . . .	22
2.3	Tunnel magnetoresistance . . . . .	23
2.3.1	Giant magnetoresistance . . . . .	25
2.4	Interlayer exchange coupling . . . . .	26
2.5	Néel coupling . . . . .	29
2.6	Measurement methods and experimental setups . . . . .	30
2.6.1	Sputter deposition . . . . .	30
2.6.2	Topographic patterning . . . . .	31
2.6.3	Magnetic patterning . . . . .	31
2.6.4	Magnetoresistance measurements . . . . .	34
2.6.5	IETS . . . . .	35
2.6.6	MOKE . . . . .	36
2.6.7	AGM . . . . .	37
2.6.8	PEEM . . . . .	37
2.6.9	MFM . . . . .	39
2.6.10	SEM . . . . .	40
2.6.11	Ion bombardment . . . . .	41
2.7	Simulation programs . . . . .	41
2.7.1	SRIM . . . . .	41
2.7.2	Downhill simplex minimization in multidimensions . . . . .	43
<b>3</b>	<b>Applicability of IBMP</b>	<b>45</b>
3.1	X-ray scattering on a magnetic grating . . . . .	46
3.1.1	Introduction . . . . .	46
3.1.2	Experiment . . . . .	46
3.1.3	Results and Discussion . . . . .	47
3.1.4	Summary . . . . .	52
3.2	Thermal stability of magnetic patterns . . . . .	54
3.2.1	Experiment . . . . .	54
3.2.2	AGM investigations . . . . .	54
3.2.3	PEEM: only magnetic pattern . . . . .	61

3.2.4	PEEM: crossed gratings . . . . .	68
3.2.5	PEEM: elliptic & triangular . . . . .	72
3.2.6	Summary . . . . .	76
3.3	IB and pinned artificial ferrimagnet . . . . .	77
3.3.1	Introduction . . . . .	77
3.3.2	Experiment . . . . .	78
3.3.3	Results and discussion . . . . .	78
3.3.4	Summary . . . . .	107
3.4	IBMP of MTJs with alumina barrier . . . . .	108
3.4.1	IB of standard MTJs . . . . .	108
3.4.2	IB of inverted MTJs . . . . .	110
3.5	Postannealing of ion bombarded $\text{Al}_2\text{O}_3$ based MTJs . . . . .	113
3.5.1	Postannealing of standard $\text{Al}_2\text{O}_3$ based MTJs . . . . .	113
3.5.2	Postannealing of inverted $\text{Al}_2\text{O}_3$ based MTJs . . . . .	116
3.5.3	Summary . . . . .	122
3.6	IBMP of single MTJs . . . . .	123
3.6.1	Experiment . . . . .	123
3.6.2	Results . . . . .	123
3.7	IBMP and standard MgO based MTJs . . . . .	125
3.7.1	Effect of IB on standard MgO based MTJs . . . . .	125
3.7.2	Postannealing of standard MgO based MTJs . . . . .	144
3.7.3	Summary . . . . .	151
3.8	IBMP and inverted MgO based MTJs . . . . .	154
3.8.1	Layer stack optimization for IBMP . . . . .	154
3.8.2	Optimization of IB parameters for inverted stacks . . . . .	160
3.8.3	IB and inverted MgO-MTJs: experiment . . . . .	173
3.8.4	Summary . . . . .	186
<b>4</b>	<b>Applications</b>	<b>188</b>
4.1	Magnetically patterned sensor . . . . .	189
4.2	Nanoparticle manipulation by strayfields . . . . .	193
4.2.1	Introduction . . . . .	193
4.2.2	Experiment . . . . .	193
4.2.3	Results and Discussion . . . . .	194
4.2.4	Summary . . . . .	200
4.3	Reconfigurable Magnetic Logic . . . . .	201
4.3.1	Theoretical proposal . . . . .	201
4.3.2	Experimental proof of principle . . . . .	208
<b>5</b>	<b>Summary</b>	<b>213</b>
<b>6</b>	<b>Acknowledgments</b>	<b>216</b>
<b>A</b>	<b>Layer stacks</b>	<b>218</b>
<b>B</b>	<b>Thermal stability — elliptic structures</b>	<b>221</b>
<b>C</b>	<b>Ru-AFi — calculated magnetization reversal</b>	<b>224</b>



<i>CONTENTS</i>	9
<b>D Ru-AFi — calculation with <math>K_i</math></b>	<b>228</b>
<b>E Cu-AFi — measurement and calculation</b>	<b>230</b>

# Chapter 1

## Introduction

Many innovations have been made in the field of magnetoresistance during the last years, and several new applications have been proposed or are already on the market.

One example are hard disks, where magnetoresistive read heads [1, 2, 3] allow higher information storage densities because small magnetic strayfields can be detected with a high spacial resolution. Recently, the introduction of the tunnel magnetoresistance (TMR) in read heads in combination with perpendicular recording allowed a steep increase of the storage density [4, 5].

Furthermore, two other applications have been reported in the field of information technology. While the magnetic random access memory (MRAM) [6, 7, 8], which combines, e.g., the advantage of DRAM to be fast with the advantage of a hard disk to keep the data without power consumption, is commercially available since 2006 [9, 10], the reconfigurable magnetic logic [11, 12, 13, 14, 15] is still in the state of development.

Apart from the information technology, the good scalability and high sensitivity to external magnetic fields makes the use of magnetoresistive elements advantageous for all kinds of magnetic field sensors. This type of sensors can be used in as different fields as, e.g., in a car for the monitoring of the rotation of wheels for an electronic stability program or the engine speed [16, 17], for the detection of the magnetic strayfield of magnetic nanoparticles in biotechnological applications, as, e.g., in lab-on-a-chip structures [2, 18, 19], for the detection of the distribution of current density in integrated circuits for failure analysis [20], or for the protection against counterfeiting by the detection of magnetic ink on bank notes [21, 22, 23] and checks [24, 22].

The Nobel price for physics which was awarded 2007 to Peter Grünberg and Albert Fert for the discovery of the giant magnetoresistance (GMR) demonstrates the actuality of this field.

The main feature of all magnetoresistive effects is the dependence of the resistance on the magnetization of one or more ferromagnetic (FM) layers. In the case of GMR and TMR, which are the magnetoresistive effects with the largest significance for the development of future applications, the key property is the relative orientation of the magnetization of thin ferromagnetic layers which are separated by a non magnetic interlayer. In samples which show the tunnel magnetoresistive effect,

this interlayer is an isolator. The majority of samples investigated in this work was of this kind. One element consisting of these layers is usually denoted as magnetic tunnel junction (MTJ). The big advantage of MTJs compared to systems showing the giant magnetoresistance is that the maximum change of the resistance, also denoted as TMR or GMR amplitude, is much larger. Recently, a TMR amplitude of 500% at room temperature and 1010% at low temperature has been reported [25]. Furthermore, the MTJs show a good scalability.

For all applications mentioned above, it is useful when the magnetization of one FM layer can be manipulated by an external magnetic field while the other one is fixed. If this is fulfilled, the resistance of the MTJ reflects the orientation of the magnetization of the free FM layer.

The most frequently used concept to keep the magnetization of one FM layer fixed is to place an antiferromagnetic layer directly below or on top of this layer. This results under certain conditions in a unidirectional anisotropy, also denoted as *exchange bias*, which “pins” the direction of the FM layer. The direction of this pinning can be defined homogeneously on a whole sample by mechanisms as field cooling or the deposition in a magnetic field.

A promising method to define this direction locally is the bombardment with light ions in the presence of a magnetic field. Here, the direction of the unidirectional anisotropy can be defined by the magnetic field selectively on the area which is bombarded by ions. This enables a magnetic patterning without creating topographic structures. It has been shown that with this method the unidirectional anisotropy can be defined for several combinations of antiferromagnetic and ferromagnetic materials [26, 27, 28, 29].

One example for the application of this technique in combination with the GMR effect is a magnetic angle sensor which can be produced more easily by ion bombardment [30]. More applications of magnetically patterned FM layers are under development.

In this thesis the combination of the magnetic patterning of the unidirectional anisotropy and the tunnel magnetoresistance effect is investigated.

That it is in principle possible to use the magnetic patterning by ion bombardment to magnetically structure the pinned layer in MTJs with alumina barrier has been shown in my diploma thesis. Furthermore, it has been shown that the side effects which have been observed after this treatment can be at least reduced by an additional heating step.

Starting from this point, the applicability of ion bombardment induced magnetic patterning (IBMP) in general and the combination of IBMP and MTJs in particular is investigated and new applications are developed.

After a short introduction to the necessary experimental and theoretical basics, the potential of the IBMP is demonstrated in chapter 3.1 by the presentation of a magnetic grating for soft x-rays which can be switched on and off by an external magnetic field.

The thermal stability of magnetic structures defined by IBMP are investigated in chapter 3.2 to make sure that an application in a potentially hot environment as, e.g., in a car is not prevented by ion bombardment induced effects.

The applicability of the combination of IBMP with artificial ferrimagnets, which are frequently used in MTJs to tune the magnetic moment of the electrodes, is described in chapter 3.3. Artificial ferrimagnets consist of two FM layers separated by a non-magnetic metal layer and are essential for a successful shrinking of MTJs.

The investigations regarding the IBMP of the pinned reference electrode of MTJs with alumina barrier carried out during my diploma thesis are extended in the chapters 3.4 and 3.5. In particular, the parameters of the additional heating step have been modified to improve the result from a reduction of the side effects to a removal of the side effects of ion bombardment.

Because experiments with MTJs with MgO barrier, which show a significantly higher TMR amplitude of up to 500% at room temperature [25] compared to up to 70% for MTJs with alumina barrier [31], have been published during the work for this thesis, also MTJs with this new barrier material have been investigated (chapter 3.7). As these MTJs turned out to be much more sensible to the side effects of ion bombardment than MTJs with alumina barrier, adjustments to the MTJ stack as well as the ion bombardment parameters are suggested in chapter 3.8. Furthermore, experiments implementing several of these suggestions have been carried out.

An application of a magnetic patterning of systems showing GMR is suggested in chapter 4.1. Here, the strayfield of the magnetically patterned system is used to attract magnetic nanoparticles to a sensor where they can be detected. The test whether magnetic nanoparticles can be caught by the strayfield of magnetically patterned FM layers can be found in chapter 4.2.

The application of the magnetic patterning of the pinned reference layer in MTJs for a new type of a reconfigurable magnetic logic is suggested in chapter 4.3. Apart from the description of the idea of this magnetic logic, which can represent all basic logic functions with only two MTJs, one can also find a proof of principle.

## Chapter 2

# Theoretical and experimental basics

In the investigated systems, consisting of thin layers with thicknesses in the range of a few nanometers, interesting effects can be found which are not present in the bulk material. These effects have to be understood to get the optimum configuration of the system for the desired application. In the following chapter some of these effects will be introduced and some theoretical as well as experimental basics will be described which are essential for the understanding of the experimental results. At the end of each topic, references are given where the reader can find a more detailed information than it can be given here.

### 2.1 Exchange Bias

The notation *exchange bias* (EB) describes a coupling between one ferromagnetic (FM) layer and one antiferromagnetic (AF) layer resulting in a unidirectional anisotropy. It has been described for the first time by Meiklejohn and Bean [32, 33] in 1956 for Co nanoparticles with an oxide shell.<sup>1</sup>

When the anisotropy direction is distributed homogeneously on the probed part of the sample and the magnetization reversal process is investigated in the direction parallel/antiparallel to the direction of the anisotropy (easy axis), this effect results in a shift of the hysteresis loop of the FM layer [Fig. 2.1 (a)].<sup>2</sup> The shift of the hysteresis loop ( $H_{EB}$ ) due to this unidirectional anisotropy will be denoted as exchange bias field or simply as exchange bias.<sup>3</sup>

The magnetization reversal process of the same sample measured perpendicular to the unidirectional anisotropy is shown in Fig. 2.1 (b). This direction is usual denoted as hard axis.

---

<sup>1</sup>In this work only exchange bias at thin layers will be used. A recent review about EB in combination with ferromagnetic nanoparticles can be found in [34, 35].

<sup>2</sup>The details of the stack and field cooling for this and many other samples used in this work can be found in appendix A.

<sup>3</sup>Oersted (Oe) is used as unit for the magnetic field  $H$  in this thesis ( $1 \text{ Oe} = 1000/4\pi \text{ A/m} \approx 79.58 \text{ A/m}$ ).

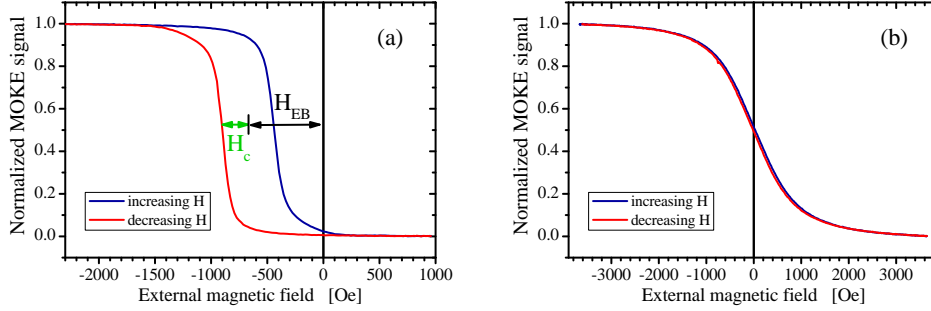


Figure 2.1: Hysteresis loop of pinned CoFe layer (stack  $CoFe_{TS}^{PEEM3nm}$ ) measured by MOKE (a) parallel / antiparallel to the unidirectional anisotropy (easy axis) and (b) perpendicular to the unidirectional anisotropy (hard axis).

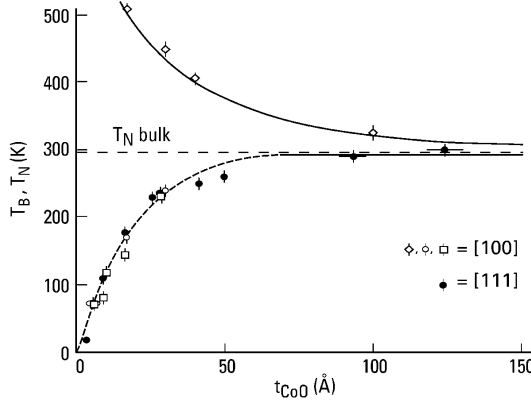


Figure 2.2: Néel temperature ( $\diamond$ ) and blocking temperatures ( $\bullet$ ,  $\circ$ , and  $\square$ ) depending on the AF layer thickness for a  $Fe_3O_4$  (100 Å)/CoO ( $x$  Å) system. (from [36])

To set the direction of the anisotropy, e.g., homogeneously on a sample, the exchange bias direction has to be initialized. The most frequently used methods to do this are the deposition of the layers in the presence of a magnetic field (field growth) and the heating of the sample in an external magnetic field ( $H_{FC}$ ) above the temperature at which the EB vanishes (blocking temperature) and cooling it down in the field. The last method is called field cooling.

The blocking temperature  $T_B$  is especially for thin layers not identical with the Néel temperature  $T_N$  of the antiferromagnet above which the spins in the AF layer do no longer show a spontaneous order. An example of the dependence of  $T_B$  and  $T_N$  on the AF thickness is shown in Fig. 2.2. While the Néel temperature is increasing with decreasing CoO thickness, the blocking temperature decreases significantly.

In general, the origin of the exchange bias is considered to be related to the exchange coupling between the ferromagnetic and antiferromagnetic layer as it was already proposed in the first publications on this effect by *Meiklejohn and Bean* [32, 33]. As several theories have been proposed to explain the microscopic details of this coupling, in the following lines the basic idea of some of them will be summarized.

The first approach [38] is a very simple one. It is assumed that the AF spins at

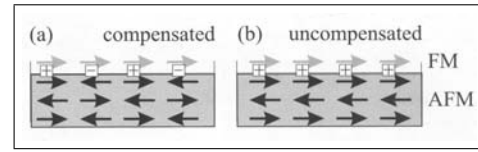
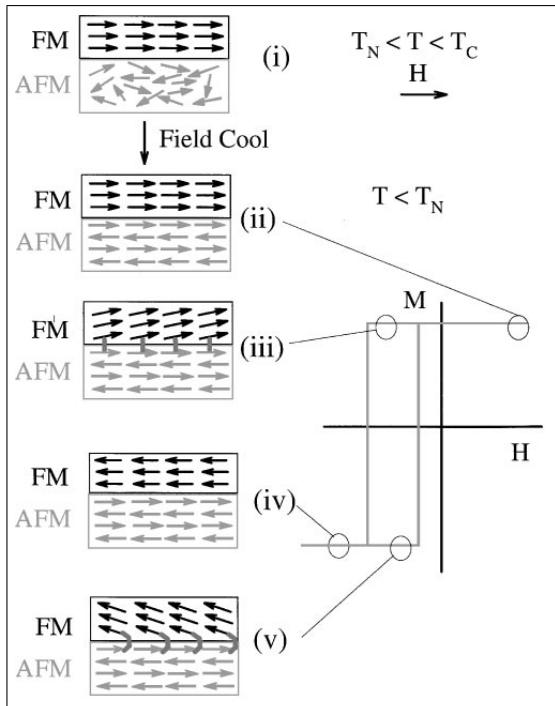


Figure 2.3: Sketch of spins at the interface between AF layer (bottom) and FM layer (top) for (a) a compensated and (b) an uncompensated interface. + and - symbolize energetically favorable and unfavorable configuration of adjacent spins, respectively. (from [37])

Figure 2.4: Simple model for exchange bias interaction. (from [38])

the interface are not compensated (compare Fig. 2.3). In Fig. 2.4 the field cooling process is shown for a perfectly uncompensated interface.

When the sample is heated to a temperature above the Néel temperature of the AF layer but below the Curie temperature of the FM layer, the spins in the FM layer can be aligned parallel to an external magnetic field [Fig. 2.4 (i)]. The spins in the AF layer are not ordered at this temperature.

When the sample is cooled below the Néel temperature in the presence of the magnetic field, the spins at the interface of the AF layer are influenced by the adjacent spins of the FM layer via the exchange coupling. In Fig. 2.4 a ferromagnetic coupling of these spins is assumed. The order of the other spins in the AF layer is determined by the interface spins [Fig. 2.4 (ii)].

When a magnetization reversal process starts with an external magnetic field parallel to the magnetic field during field cooling, the orientation of the FM layer magnetization is not altered [Fig. 2.4 (ii)]. If the direction of the magnetic field is inverted and the strength of the magnetic field increases, a torque acts on the spins of the FM layer to follow the external magnetic field. If the anisotropy of the AF layer is large enough to keep the spins in the AF layer fixed<sup>4</sup> a torque acts on the FM spins due to the exchange coupling at the interface which counteracts the torque due to the external magnetic field. Therefore, a higher external magnetic field is necessary to turn the FM layer magnetization until at large negative magnetic fields in Fig. 2.4 the magnetization is saturated [Fig. 2.4 (iv)]. When the external magnetic field is decreased again, the same effect is responsible for an earlier switching of the FM layer magnetization [Fig. 2.4 (v)].

<sup>4</sup>If the AF anisotropy is smaller than the coupling between the AF and the FM layer, the rotation of the FM spins can drag the AF spins and an enhancement of the coercivity instead of a shift of the hysteresis loop occurs.

This intuitive approach is not sufficient to give a quantitative description of the exchange bias coupling. With the equation

$$H_{EB} = -\frac{J_{EB}}{\mu_0 M_{FM} t_{FM}} \quad (2.1)$$

( $J_{EB}$ : interfacial exchange energy per unit area,  $M_{FM}$ : saturation magnetization of ferromagnetic layer,  $t_{FM}$ : thickness of FM layer, [39]) resulting from this model, one gets values for the shift of the hysteresis loop which are significantly larger than the experimentally observed ones [39].

Furthermore, this model does not contain the effect of several parameters which have been found to be important in the experiments as, e.g., the interface roughness or the AF spin structure [35].

*Néel* supposed a model where a domain wall or a partial domain wall parallel to the interface can occur [35, 39]. This would reduce the coupling strength to the values observed experimentally.

Furthermore, other authors proposed models where domain walls parallel to the interface play an important role. *Mauri et al.* [40], e.g., introduced a concept of domain walls in the AF layer parallel to the interface which limits the exchange bias coupling as a reaction on the too large values obtained with the model of Meiklejohn and Bean.

These models did not include explicitly the roughness of the interface which is always present in real samples. In the random field model proposed by *Malozemoff* [41, 42, 43], a randomness of the exchange interaction at the interface due to, e.g., interface roughness or alloying at the interface results in the formation of permanent domains in the AF layer with domain walls perpendicular to the interface. With this method a good agreement between the predicted and the experimentally observed exchange bias field for, e.g., CoO/Co has been obtained [39].

Another model which uses a varying spin pattern in the AF layer has been proposed by *Fulcomer and Charap* [44] for polycrystalline samples. Here, the grains in the AF layer are treated independently. The FM layer is assumed to have one homogeneous magnetization direction. When the free energy of one grain is calculated with this model, one gets one local and one global minimum (Fig. 2.5). The energy barrier between these minimums depends, e.g., on the volume of the grain. Therefore, different grain sizes result in different barrier heights and a different amount of energy is necessary to get from the local to the global minimum and vice versa. This energy can be provided, e.g., by the temperature during the field cooling or the energy locally added by ion bombardment.

Very small grains might be jumping back and forth between both minimums all the time due to the thermal energy. They do not contribute to the exchange bias coupling or the coercivity. Samples where the anisotropy is just large enough not to be influenced by the thermal energy at room temperature can be dragged by the exchange coupling between the FM and the AF interface spins when the magnetization direction of the FM layer changes. These grains contribute to an enlarged coercivity but not to the exchange coupling. Larger grains with a large anisotropy are not



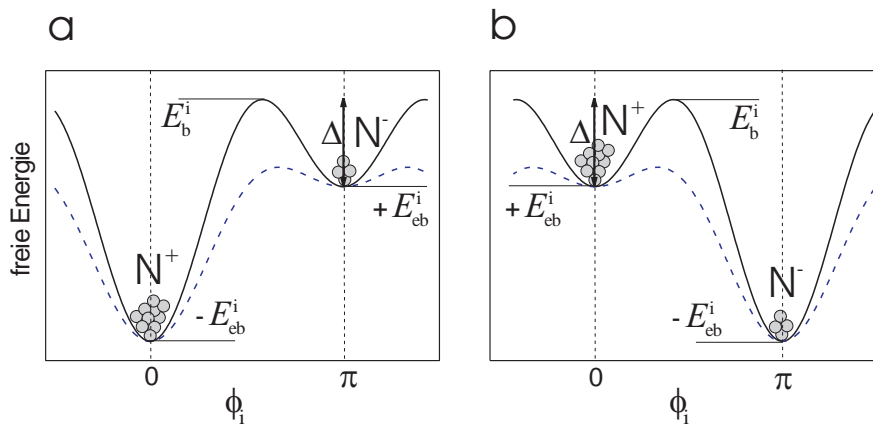


Figure 2.5: Free energy of grain  $i$  in the AF layer in dependence of the angle  $\phi_i$  between the magnetic moment of the AF grain at the AF/FM interface and the easy axis of the FM layer under the assumption that both layers have a uniaxial anisotropy with parallel anisotropy axes. The solid black line is valid for a large grain while the dashed blue line is valid for a smaller grain with the same area in contact to the FM layer but only half of the volume of the larger grain.  $E_{eb}^i$  and  $E_b^i$  denote the exchange energy of grain  $i$  at the interface and the barrier height of the larger grain, respectively.  $\Delta$  represents the energy barrier which has to be overcome by a larger grain to change from the local to the global minimum.  $N^+/N^-$  grains contribute positively/negatively to the EB coupling. (b) represents the energy versus angle distribution for an orientation of the FM layer magnetization which is antiparallel to the one present in (a). (from [45] based on [44])

altered by the thermal energy at room temperature or the exchange coupling at the interface. These grains contribute to the exchange bias via the exchange coupling at the AF/FM interface.

When additional energy is added to the system by, e.g., annealing or ion bombardment, grains which have been stable before can change to the global minimum and the exchange bias is enlarged after the sample is cooled down to RT.

*Stiles and McMichael* also proposed a model for polycrystalline AF/FM bilayers [46]. They assumed independent antiferromagnetic grains whose antiferromagnetic order is influenced by the ferromagnetic magnetization during the field cooling. The strength of the exchange bias is determined in this model by a combination of the strength of the average direct coupling at the interface and the energy of (partial) domain-walls which wind up during the reversal of the ferromagnetic magnetization if the coupling at the interface is strong enough.

In the *domain state model* [47, 48, 49, 37] the formation of an irreversible pattern of domains in the bulk of the AF layer perpendicular to the AF/FM interface is the main source of uncompensated spins at the interface. These are responsible for the exchange bias coupling. Defects make the generation of the domain walls energetically more favorable. Therefore, up to a certain amount of defects, an increase of the number of defects in the bulk of the AF layer should increase the strength of the EB coupling. This has been observed experimentally in epitaxially grown Co/CoO layers [47].

In this work the manipulation of the EB direction in polycrystalline layers with a grain size in the range of a few 10 nm is investigated. For this type of samples the model by Fulcomer and Charap has been extended by *Ehresmann et al.* to explain the influence of the ion bombardment on the exchange bias [50, 45, 29]. The main ideas are that the ion bombardment (IB) can turn the grains according to the external field during IB by local hyperthermal heating and that the defects generated by the IB can change the effective size of the grains and, therefore, change the barrier height (also compare chapter 2.2). This argumentation will be used occasionally in the following chapters.

Due to the large number of investigations published about this topic,<sup>5</sup> this chapter can only give a rough overview over the basic ideas of the exchange bias theories. For a more detailed information, the reader is referred to the cited articles and the numerous reviews as, e.g., [38, 51, 52, 53, 35, 39, 54].

In this work frequently an annealing temperature of 275°C is used for the field cooling. This temperature is due to an optimization of the annealing with respect to the tunnel magnetoresistance amplitude of magnetic tunnel junctions (see chapter 2.3) with a alumina barrier described in Ref. [55]. As one can see in Fig. 2.6 this does not necessarily result in the largest possible exchange bias coupling.

---

<sup>5</sup>The review paper [35], e.g., has a reference list with 793 items.

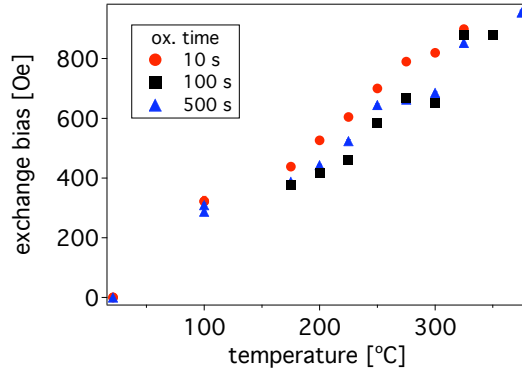


Figure 2.6: Dependence of the exchange bias of the CoFe reference layer of magnetic tunnel junctions with alumina barrier on the annealing temperature for different oxidation times of the barrier. (from [55])

## 2.2 Ion bombardment induced magnetic patterning

### 2.2.1 Manipulation of exchange bias coupling by ion bombardment in a magnetic field

The EB can not only be manipulated by, e.g., field cooling or field growth, but also by ion bombardment in a magnetic field. Several examples for a manipulation of the EB magnitude (e.g., [56, 57, 58]) and direction (e.g., [26, 59]) by IB have been published during the last years. It was found that arbitrary directions of the EB can be obtained by IB in dependence of the direction of the magnetic field during the bombardment [60].

Of high importance for the manipulation of the EB by ion bombardment is the antiferromagnet/ferromagnet (AF/FM) material combination. While an enlargement and rotation of the EB is possible, e.g., for the bombardment of FeMn/NiFe (Fig. 2.7 (a), [30, 61, 59]), or NiO/NiFe (Fig. 2.7 (c), [62]) with He ions, only a reduction of the EB has been observed for the bombardment of PtMn/NiFe with He ions (Fig. 2.7 (b), [30, 61]). This has been explained by the fact that only the chemically ordered phase of PtMn is antiferromagnetic while the disordered phase is paramagnetic [61].

On the other hand for the bombardment of PtMn/CoFe samples with 40 keV C ions and a capping layer which prevents the majority of the C ions from penetrating the CoFe/PtMn interface, a rotation of the EB direction has been found in a CoFe/PtMn system (Fig. 2.7 (d), [63]). This shows that not only the antiferromagnetic material is important but the whole system of AF/FM/capping layer in combination with the type of ions and the ion energy has to be considered to predict the effect of ion bombardment in a magnetic field on the EB (compare chapter 3.8.2).

Other experiments with the bombardment of pinned FM layers with C ions showed that, e.g., the EB direction in a CoFe/IrMn system can be inverted by bombardment with C ions [63]. In this case the same EB field as before IB has been obtained after the IB induced change of the EB direction.

Another example for experiments regarding the ion bombardment with different types of ions is, e.g., the bombardment of CoFe/IrMn bilayers with 30 keV Ga ions in a focused ion beam setup [64]. Here, the EB direction has been turned and a shift of the hysteresis loop of up to about half of the value before IB has been obtained.

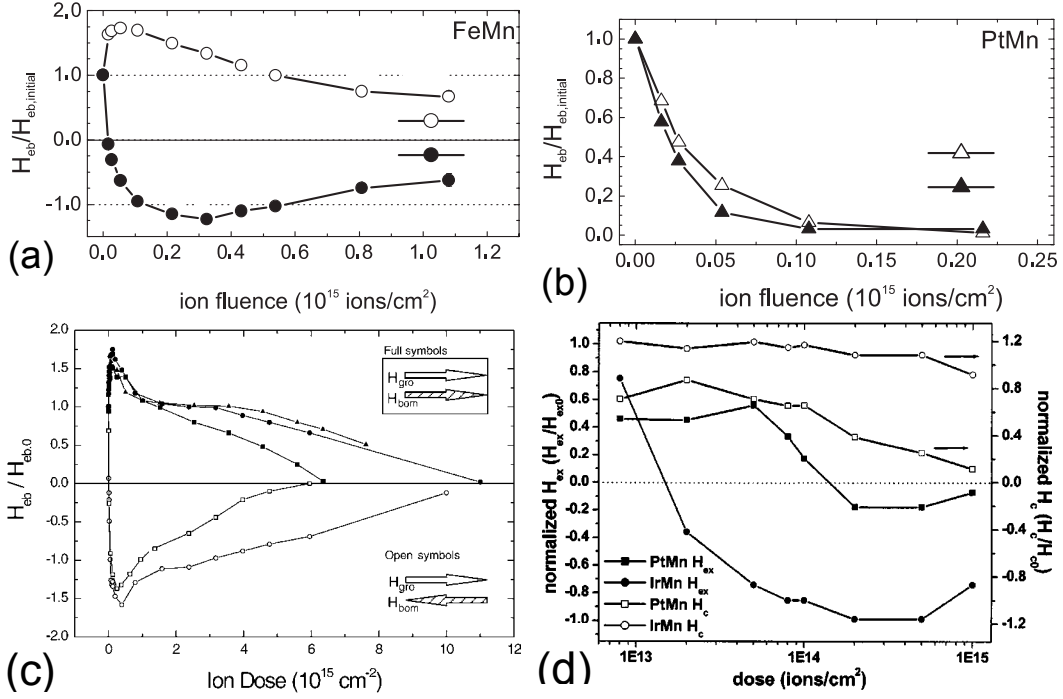


Figure 2.7: Exchange bias field  $H_{EB}$  for various ion doses normalized on the value before IB. (a) FeMn/NiFe bombarded with 10 keV He ions with the magnetic field during ion bombardment  $H_{IB} \uparrow\uparrow$  (open circles) and  $\uparrow\downarrow$  (solid circles) to  $H_{FC}$  (full stack (all thicknesses in nm): Cu 15/NiFe 5/FeMn 10 /Cr 2), (b) PtMn/NiFe bombarded with 10 keV He ions with  $H_{IB} \uparrow\uparrow$  (open triangles) and  $\uparrow\downarrow$  (solid triangles) to  $H_{FC}$  (full stack: Cu 15/NiFe 5/PtMn 10 /Cr 2), (c) NiO/NiFe bombarded with He ions of the energy 5 keV (squares), 10 keV (circles) and 20 keV (triangles) for  $H_{IB} \uparrow\uparrow$  (full symbols) and  $\uparrow\downarrow$  (open symbols) (full stack: NiO 50/NiFe 5/ Ta 2), (d) PtMn/CoFe (solid squares) and IrMn/CoFe (solid circles) bombarded with 40 keV C ions in a magnetic field  $\uparrow\downarrow$  to  $H_{FC}$  (open symbols show the coercive field) (full stack: NiFeCr 5/CoFe 10/PtMn20 (or IrMn 7)/NiFeCr 5/Ta 50) ((a) and (b) from [30], (c) from [62], (d) from [63])

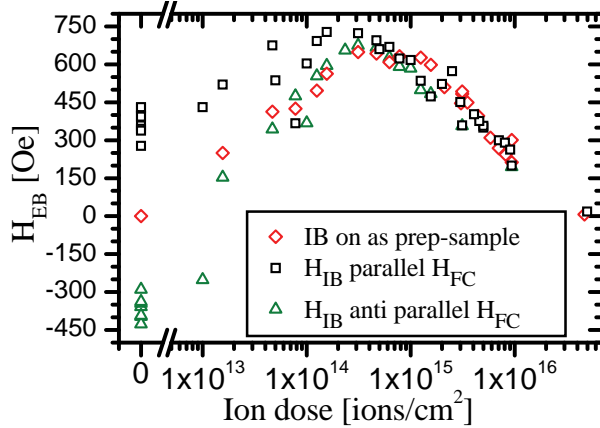


Figure 2.8: Shift of hysteresis loop of pinned FM layer due to EB ( $H_{EB}$ ) extracted from MOKE measurements on sample *hMTJ* (IrMn/CoFe) for several ion doses and ( $\diamond$ ) IB without FC ( $\square$ )  $H_{IB}$  parallel  $H_{FC}$  and ( $\triangle$ )  $H_{IB}$  antiparallel  $H_{FC}$ . The sign of the values of  $H_{EB}$  for the antiparallel case has been reversed to reach a better comparability of the maximum EB. (Ion energy  $E_{IB}=10$  keV)

Experimental results can be found for several other AF/FM combinations like, e.g., CrMnPt/NiFe [45] or NiMn/NiFe [65]. For the antiferromagnetic material IrMn used in this work, examples for a manipulation of the direction and the size of the EB coupling can be found in the literature [60, 66, 45, 67, 68] and will be shown in this thesis. Fig. 2.8 shows as an example the ion dose dependence of a sample with a CoFe/IrMn bilayer for the bombardment with 10 keV He ions.

The characteristic ion dose dependence of the exchange bias (compare Fig. 2.8) can be explained by a superposition of at least two effects. One effect is the enlargement of the EB in the direction of the external magnetic field during IB by, e.g., local hyperthermal heating (compare extended model of hyperthermal heating in chapter 2.1, [50]) or the generation of defects and an increasing number of domain walls in the AF<sup>6</sup> [26, 57] (compare domain state model in chapter 2.1, [37]). The other effect is decreasing the EB coupling by an ion bombardment induced intermixing at the AF/FM interface reducing the exchange coupling between the AF and the FM layer [56, 26, 45, 69].

The enlargement of the EB after ion bombardment in a magnetic field compared to the same sample after field cooling seems to be not only due to the higher energy deposited during hyperthermal heating, but is also related to structural changes in the sample. This can be seen in experiments [26] where the EB direction of a field cooled FeNi/FeMn layer system first is rotated by 180° by IB and then is rotated back by field cooling. In these experiments the maximum EB field observed after this procedure was larger than the EB before the IB [26]. This can be explained by the additional defects<sup>7</sup> remaining in the AF layer after the additional field cooling [26] and/or a change of the effective volume of the AF grains [50, 45]. But apart from the changes in the bulk of the AF layer also the presence of the FM

<sup>6</sup>Mougin *et al.* assume in [26] that the magnitude of the EB is linearly proportional to the number of displaced atoms in the AF layer.

<sup>7</sup>Milteny *et al.* found an enlargement of the EB in epitaxially grown Co/CoO layers of up to a factor of three when they diluted the volume part of the AF layer away from the interface by nonmagnetic defects [47].

layer during the ion bombardment is necessary as it has been shown by Poppe *et al.* [69].

Another possibility of a magnetic patterning induced by ion bombardment is the manipulation of the interlayer exchange coupling in artificial ferrimagnets (compare chapter 2.4 and 3.3).

Furthermore IB can be used to influence magnetic properties like the coercivity, curie temperature or the anisotropy [70, 71, 72, 73]. But as this work is focused on the manipulation of the EB coupling the reader is referred to the literature for more information about this aspect of IB induced manipulations.

### 2.2.2 Local manipulation of exchange bias resulting in a magnetic pattern

When only a part of the sample is modified by the ions, a magnetic pattern can be obtained. This can be achieved, e.g., by using a focused ion beam (FIB) [71, 58, 73, 68] or by bombarding the sample through a resist mask [59, 30, 74, 71] which stops the ions on parts of the sample. Furthermore, it has been reported that the use of a non-contact stencil mask (a membrane with drilled holes) is possible, as well [75]. The advantage of masks compared with FIB is the possibility of bombarding larger areas at one time. In contrast to this, when using FIB, one has to scan over the bombarded area with the small ion beam what is much more time consuming for larger samples.

Very small structures in the range down to 20 nm can be prepared [28]. Limiting factors are, e.g., the minimum size of the structures in a resist mask or the diameter of the ion beam in a focused ion beam. Furthermore, scattering of ions in the sample can widen the ion beam significantly. Several parameters influence the width of the modified volume in the sample. SRIM<sup>8</sup> simulations of 10 keV He ions hitting on a solid gold block on exactly the same point result, e.g., in a lateral projected ion range<sup>9</sup> of about 22 nm while for the same simulations for 30 keV He ions one gets 48 nm. Aside from the ion energy the target material (40 nm lateral projected ion range for 10 keV He ions on an aluminum block) the type of ions (2.4 nm lateral projected ion range for 10 keV Ga ions on a gold block) has a large influence on the scattering of the ions. Furthermore, single ions can reach points in a larger distance from the point where they hit the surface as one can see in the projection of the ion and recoil trajectories in Fig. 2.9.

In this work resist masks have been used to define the bombarded area. Several types of lithography have been used to produce this masks (for details see chapter 2.6.3).

More details about the manipulation of the exchange bias by ion bombardment in

---

<sup>8</sup>SRIM is a program for Monte Carlo simulations obtainable at [www.srim.org](http://www.srim.org). (for details see chapter 2.7.1)

<sup>9</sup>The *lateral projected ion range* is defined as the average of the absolute values of the projected lateral displacements from the axis of the ion beam [76].

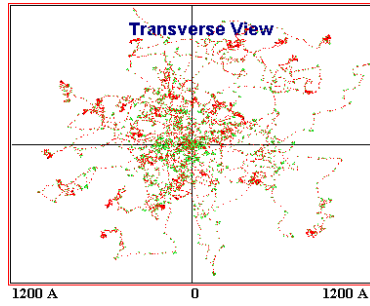


Figure 2.9: SRIM simulation: Projection of trajectories of 10 keV He ions (red) in a gold block observed from above the block. The trajectories of recoiling Au atoms are marked in green.

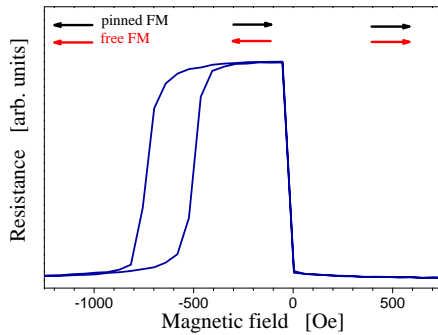


Figure 2.10: Resistance in dependence of the external magnetic field measured at a magnetic tunnel junction with stack  $MTJ_{AlOx}^{std}$  (for details see chapter A). The arrows symbolize the direction of the magnetization of the two ferromagnetic layers.

a magnetic field and ion bombardment induced magnetic patterning can be found, e.g., in [45, 28, 29, 77, 78, 79].

## 2.3 Tunnel magnetoresistance

For applications as, e.g., magnetic sensors [2, 18, 19, 80], read heads for hard discs [1, 2, 3], magnetic random access memory [6, 7, 8, 9, 10] or a reconfigurable magnetic logic [11, 12, 13, 14, 15] elements are needed which change their resistance in dependence of an external magnetic field.

The magnetoresistive effects which are already frequently used in these fields today and have the largest significance for future applications are the giant magnetoresistance (GMR) and the tunnel magnetoresistance (TMR). On the following pages some basics of the GMR and the TMR will be briefly described as this effect has been used in this work.

When two metals are divided by a sufficiently thin insulator,<sup>10</sup> some electrons can tunnel through this barrier. This quantum mechanical effect is known for a long time [81]. In 1971 Tedrow and Meservy found that the tunneling current between thin superconducting aluminum films and ferromagnetic nickel films is spin dependent [82].

When ferromagnetic layers are used on both sides of the isolator, the tunnel current through the insulator can depend on the relative orientation of the magnetizations of the two FM layers (Fig. 2.10). The arrows in Fig. 2.10 symbolize the direction

<sup>10</sup>In this thesis only  $Al_2O_3$  and MgO barriers have been used.

of the magnetization of the two ferromagnetic layers. For antiparallel orientated magnetizations usually a higher resistance is found.

The tunnel magnetoresistance amplitude is defined as

$$TMR \equiv \frac{R_{max} - R_{min}}{R_{min}}. \quad (2.2)$$

$R_{max}$  ( $R_{min}$ ) denotes the maximum (minimum) resistance.

Although this effect has for low temperatures been reported for the first time by Juliere in 1975 [83], the first large TMR amplitudes at room temperature (above 10%) have been reported independently by Moodera [84] and Miyazaki [85] in 1995.<sup>11</sup> Today, TMR amplitudes at room temperature up to 70% [31] for magnetic tunnel junctions (MTJs) with  $\text{Al}_2\text{O}_3$  barrier and 500% (1010% at 5 K) for MTJs with MgO barrier [25] have been found.

The basic idea of the dependence of the resistance on the relative orientation of the ferromagnetic (FM) layer magnetizations is connected to the assumption that one can treat the tunneling of electrons with two different spin directions independently. When the direction of the spin during the tunneling is conserved, spin up (down) electrons from one electrode can tunnel only into spin up (down) states in the other electrode. As the tunnel conductance is proportional to the spin dependent density of states in both electrodes, different densities of states for spin up and spin down result in different tunnel probabilities in dependence of the spin direction. In magnetic materials the spin splitting at the Fermi level results in an unequal number of spin up and spin down states. As an extreme example, half-metallic FM electrodes have to be mentioned which have only for one spin direction (called majority spin direction) electron states at the Fermi level. If both electrodes consist of this (idealized) material and their magnetization directions are aligned parallel, the majority electrons can tunnel into the majority states at the other side of the barrier and a high tunnel current can be observed. When both magnetizations are aligned antiparallel, the product of the initial and final densities of states is zero for both spin directions and the tunnel current is zero.

An important requirement for a highly spin polarized tunnel current and a high TMR amplitude are a high spin polarization at the barrier/electrode interface. But a high spin polarization of the electrodes alone does not necessarily result in a high magnetoresistance effect. Other effects as, e.g., spinflip scattering at magnetic defects in the barrier, or additional not spin polarized currents across the barrier due to, e.g., hopping over chains of defects in the barrier or pinholes can reduce the polarization of the current through the barrier significantly.

More details about this effects will be described in chapter 3.4 to 3.8.1.

Various possibilities to obtain an antiparallel alignment of the magnetizations of the two FM layers adjacent to the barrier as, e.g., the application of FM layers with different coercivities have been described in the literature. In this thesis, the exchange bias coupling is used to shift the hysteresis loop of one FM layer (to *pin*

---

<sup>11</sup>More details about the historic development of the tunnel magnetoresistance can be found, e.g., in [6].



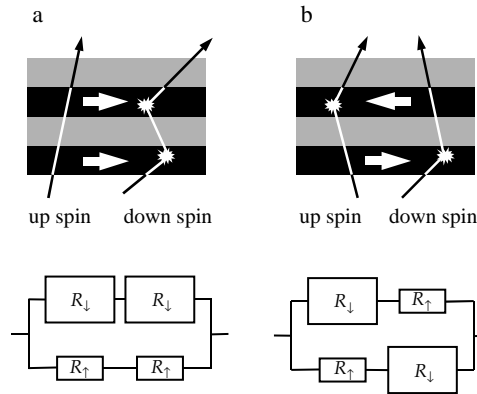


Figure 2.11: Electron transport in a ferromagnet/not magnet multilayer for (a) parallel (b) antiparallel alignment of adjacent FM layer magnetizations. *upper part*: The arrows symbolize electron trajectories of electrons with spin up (spin parallel to magnetization pointing to the right) and spin down (spin parallel to magnetization pointing to the left). Black layers are ferromagnetic, gray layers are not magnetic. *lower part*: resistor model [97, 98] corresponding to the magnetic configuration in the upper part. (from [96])

the magnetization of this layer) and, therefore, obtain the high resistance plateau with an antiparallel alignment of the FM magnetizations (compare Fig. 2.10 and chapter 2.1).

A detailed description of tunnel magnetoresistance can be found, e.g., in [86, 55, 87, 88, 89, 90, 91].

### 2.3.1 Giant magnetoresistance

The term *giant magnetoresistance* (GMR) describes a dependence of the resistance of ferromagnetic (FM) layer / non magnetic (NM) layer / FM layer structures on the relative orientation of the magnetization direction of the FM layers. The effect has been reported for the first time by G. Binash *et al.* [92] from the group of P. Grünberg and Baibich *et al.* [93] from the group of A. Fert.

A qualitative explanation of the GMR effect can be given with the simple Mott two-current model [94, 95, 96]. It contains two main assumptions: As the spin does not switch its direction during most of the scattering events, the conductivity due to spin up and spin down electrons can be treated as two independent currents and the scattering probability of electrons in magnetic metals depends strongly on their spin orientation. When one assumes that the scattering probability is larger for electrons with a spin antiparallel to the magnetization of the FM layer compared to electrons with a spin parallel to the magnetization, the resistance for a parallel and an antiparallel alignment of two FM layers can be described. In the parallel case [Fig. 2.11 (a)] electrons with a spin up (parallel to the magnetization pointing to the right) have a low scattering probability in both layers as their spin is aligned parallel to the magnetization in both layers. In contrast to this, the scattering probability

of spin down electrons (spin parallel to magnetization of FM layer pointing to the left) is high in both layers.

In the simple resistor model<sup>12</sup> shown in the lower part of Fig. 2.11, the independent spin up and spin down channels can be considered as parallel wired resistors. Each channel consists of a serial wiring of the resistance corresponding to the scattering probability at each layer. The low (high) scattering probability of the spin up (spin down) electrons in both layers results in a low (high) resistance for both layers.

In the case of an antiparallel alignment each type of electrons has a large scattering probability (high resistance) in one layer and a low one in the other layer. Therefore, the total resistance is larger in the case of an antiparallel alignment of the magnetizations of the two FM layers.

This result of the simple model fits to the experimental observations.

A detailed description of giant magnetoresistance with more sophisticated models and several examples of applications can be found, e.g., in [99, 96, 90, 100, 101, 102].

## 2.4 Interlayer exchange coupling

The interlayer exchange coupling (IEC) influences the relative orientation of the magnetization direction of ferromagnetic layers separated by a nonmagnetic spacer. It is frequently applied, e.g., in magnetic tunnel junctions to modify the stray field of ferromagnetic electrodes. Here, the trilayer is usually denoted as artificial ferromagnet (AFi).

It was first observed by Grünberg *et al.* for Fe/Cr/Fe layers in 1986 [103]. In 1990 Parkin *et al.* [104] found oscillations of the interlayer exchange coupling in Co/Ru, Co/Cr and Fe/Cr multilayers, as a function of spacer thickness.

An impressive way to show the alternating ferromagnetic and antiferromagnetic type of the coupling for a Fe/Cr/Fe sample has been presented by Unguris *et al.* in Ref. [105] (Fig. 2.12). The domain pattern of two ferromagnetic layers separated by a Cr wedge [see sketch in Fig. 2.12 (a)] has been investigated by scanning electron microscopy with polarization analysis. Black and white color in Fig. 2.12 (b) represent an opposite orientation of the magnetization. The horizontal division results from two domains with opposite magnetization orientation in the lower Fe layer (substrate). The alternating black and white contrast with increasing interlayer thickness shows the alternating ferromagnetic and antiferromagnetic coupling in dependence of the Cr thickness.

To describe the IEC quantitatively the coupling parameters can be determined. The areal energy density connected to the interlayer exchange coupling of two ferromagnetic layers with an angle  $\Delta\phi$  between their magnetizations can be described by [99]:

$$E_{IEC} = -J_L \frac{\mathbf{M}_1 \cdot \mathbf{M}_2}{|\mathbf{M}_1| \cdot |\mathbf{M}_2|} - J_Q \left( \frac{\mathbf{M}_1 \cdot \mathbf{M}_2}{|\mathbf{M}_1| \cdot |\mathbf{M}_2|} \right)^2 \quad (2.3)$$

$$= -J_L \cos(\Delta\phi) - J_Q [\cos(\Delta\phi)]^2 \quad (2.4)$$

<sup>12</sup>This model is helpful for the imagination of the problem but it does not give a quantitative description of the GMR [96].

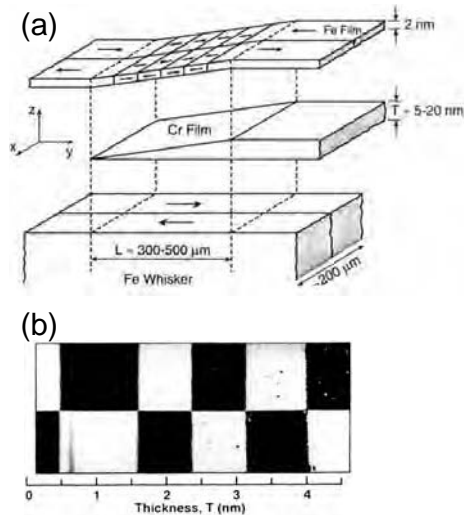


Figure 2.12: (a) Sketch of the sample investigated by Unguris *et al.*: Cr wedge on Fe(100) single crystal whisker substrate with Fe overlayer. The arrows show the direction of the magnetization of the Fe. (b) Domain pattern of Fe film obtained by scanning electron microscopy with polarization analysis. (from [105])

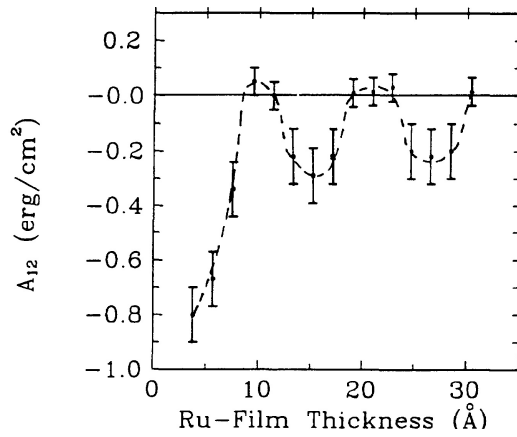


Figure 2.13: Interlayer exchange coupling constant (here denoted as  $A_{12}$ ) in Co/Ru multilayers in dependence of Ru thickness. ( $1 \text{ erg/cm}^2 = 1 \text{ mJ/m}^2$ ) For detailed definition of  $A_{12}$  see [106, 107, 108]. (from [108])

Here  $M_i$  is the magnetization of layer  $i$  and  $J_L$  and  $J_Q$  are the bilinear and bi-quadratic coupling constants. Depending on the size and sign of the two constants different kinds of coupling occur. For a small  $J_Q$  and a larger positive  $J_L$  a ferromagnetic coupling can be observed while a small  $J_Q$  in combination with a larger negative  $J_L$  results in an antiferromagnetic coupling. When a negative  $J_Q$  is the dominating term, a  $90^\circ$  type of interlayer exchange coupling can be found.

An example of an experimentally determined oscillating coupling constant in Co/Ru multilayers in dependence of the Ru interlayer thickness is shown in Fig. 2.13. The coupling constants have been determined by Fassbender *et al.* by Brillouin light scattering [108].

In some systems as, e.g., Fe/Au(110), superimposed oscillations with different frequencies have been found [99]. The frequencies of this oscillations can be connected to extremal distances called calipers ( $Q_i$ ) in the Fermi surface of the interlayer material by  $\lambda = 2\pi/Q_i$  [99]. An example of these calipers for the Fermi surface of Au can be seen in Fig. 2.14. The theoretically predicted oscillation periods are in good agreement with the experimental results [109].

This kind of observations for several systems (see, e.g., [110] for further examples) leads to an explanation of the bilinear IEC effect which is based on the spin de-

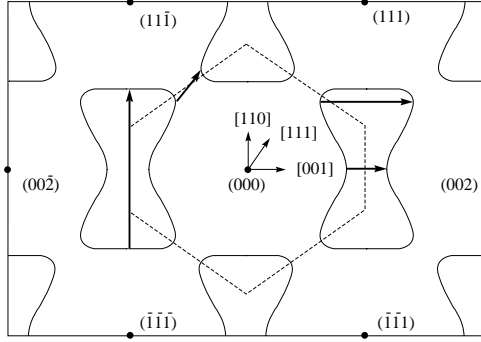


Figure 2.14: Cross section of Fermi surface of Cu along the  $(1\bar{1}0)$  plane passing through the origin. The solid arrows in the  $(001)$ ,  $(111)$  and  $(110)$  orientation indicate the Vectors  $\mathbf{Q}_i$ . (from [109])

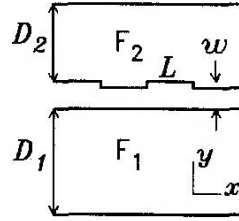


Figure 2.15: AFi with FM layers with thickness  $D_1$  and  $D_2$  and interlayer thickness  $w$ . The upper FM layer has one monolayer high terraces of length  $L$  while the lower interlayer/FM layer interface is smooth. (from [111])

pendent reflection of electron waves at the interfaces between the interlayer and the FM layers [99, 110]. The interference of the reflected electron waves results in spin dependent quantum well states. These quantum well states have a different energy for different relative orientations of the FM layer magnetizations because of the spin dependence of the reflection. The periodic nature of the coupling for varying interlayer thickness is due to a change of the energy of the quantum well states with changing interlayer thickness. When the states pass through the Fermi energy they fill or empty and, therefore, the energy of the system changes.

But the IEC does not only depend on the thickness of the interlayer, but also oscillations depending on the thickness of the FM layer and even of a nonmagnetic capping layer have been found [99, 109]. This is explained by the influence of reflection at the interface of the FM layer and the capping layer and the interface of the capping layer to the vacuum on the quantum well states [109, 110].

Therefore, a modification of the band structure of the interlayer and the reflection probabilities at the surfaces of the interlayer, e.g., by IB will result in a modification of the IEC.

The considerations above were dealing with the bilinear interlayer exchange coupling. For the microscopic origin of the biquadratic interlayer exchange coupling term different mechanisms, e.g., based on fluctuations of the interlayer thickness and loose spins of magnetic atoms in the interlayer have been proposed [111, 112, 110]. As in some systems the bilinear IEC oscillates with a periodicity of two monolayers, in this kind of systems one monolayer high terraces (Fig. 2.15) result in adjacent areas with opposite (ferromagnetic vs. antiferromagnetic) coupling. When the size of this terraces is smaller than the Néel wall width, it is not possible to compensate this alternating coupling with a corresponding domain pattern. In this case, the total energy due to the bilinear interlayer coupling and the exchange coupling inside

the FM layer is minimized when the FM layers have a  $90^\circ$  orientation and one can observe an effective orthogonal coupling. [111, 112] In this theory an increasing  $J_Q$  is predicted for an increasing area of mono-layer-high terraces of the FM layer at the interface to the interlayer. Experimental results with a good agreement to the predictions of this theory have been published, e.g., for a Fe/Cu/Fe system in Ref. [113].

Furthermore, a theory based on magnetic dipole coupling due to not correlated roughness at the interlayer/FM layer interface has been proposed [112]. Like the bilinear IEC in the first approach for varying interlayer thickness due to terraces, the dipole coupling is assumed to vary laterally due to the roughness. Again, the  $90^\circ$  coupling would represent the lowest total energy of (magnetostatic) coupling between the FM layers and exchange stiffness inside the FM layer. An experimental test of this theory has been reported in Ref. [114] for samples with a Fe/Au/Fe stack. The difference between the biquadratic interlayer exchange coupling of samples with a large and with a low roughness at the interfaces has been compared with predictions resulting from this model. A good agreement has been found.

A third approach which was developed to explain the strong temperature dependence of the biquadratic IEC in some samples is based on the influence of loose spins of magnetic impurities in the interlayer. These paramagnetic spins are only indirectly coupled to the FM layers via a mediation by the interlayer electrons. This theory predicts an increase of the biquadratic IEC for an increasing number of magnetic impurities [111, 112]. A corresponding dependence of the biquadratic coupling on the amount of Fe placed in the middle of the interlayer of an Fe/Ag/Fe system has been reported in Ref. [115].

Furthermore, it is possible that a combination of an antiferromagnetic bilinear IEC and a FM coupling via ferromagnetic pinholes results in a  $90^\circ$  coupling [110].

For samples with an antiferromagnetic interlayer a theory called *torsion model* has been suggested [110]. As no such materials have been used here, this model will not be considered in this work.

As the IB can cause a change of the band structure and the reflectivity at the interfaces by, e.g., intermixing, creation of point defects and interstitials or local heating effects, it can be expected that the strength of the bilinear IEC and/or the wavelength of the IEC oscillation are modified by the ion bombardment. Furthermore it can be expected that the roughness of the interlayer/FM layer interface will be modified and that magnetic impurities in the interlayer are generated. Therefore, an influence of IB on the biquadratic IEC is very likely as well. The combination of IB and IEC will be discussed in detail in chapter 3.3.

For more details about the interlayer exchange coupling see, e.g., [116, 109, 99, 110, 117]. The descriptions in this chapter are mainly based on the first four references.

## 2.5 Néel coupling

The Néel coupling is often as well referred to as magnetostatic coupling or orange peel coupling. It results in a parallel orientation of the magnetization of two ferro-

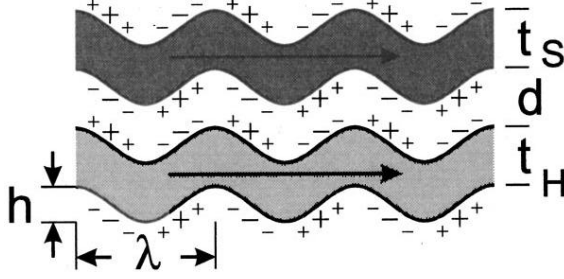


Figure 2.16: Sketch of tunnel barrier between two ferromagnetic layers with strong correlated roughness.  $t_S$ : thickness of magnetically soft FM layer,  $t_H$ : thickness of hard FM layer,  $d$ : thickness of nonmagnetic interlayer (barrier),  $\lambda$ : wavelength of roughness,  $+/-$  symbolize magnetic dipoles (from [118])

magnetic layers separated by a nonmagnetic layer. It is often observed in magnetic tunnel junctions (see chapter 2.3), where it results in a shift of the hysteresis loop of the free ferromagnetic layer.

Figure 2.16 shows a sketch of the two FM layers separated by a nonmagnetic interlayer (e.g., the barrier of a MTJ). Due to the roughness of the FM/interlayer interfaces magnetic dipoles symbolized by  $+/-$  in Fig. 2.16 can be found. When the roughness of both surfaces of the interlayer is correlated, the interaction due to the magnetic strayfields of the magnetic dipoles at the interfaces of the interlayer can be described by the following equation [119, 120].

$$J_{\text{Néel}} = \frac{\pi^2 h^2}{\sqrt{2}\lambda} \mu_0 M_{\text{sat}}^1 M_{\text{sat}}^2 \exp(-2\pi\sqrt{2}d/\lambda) \quad (2.5)$$

Here  $\lambda$  is the wavelength of the correlated roughness and  $M_{\text{sat}}^1$  and  $M_{\text{sat}}^2$  are the saturation magnetizations of the two FM layers. A parallel alignment of the magnetization of both FM layers is energetically favorable due to the strayfields of the magnetic dipoles. An extension of this model including the interaction of the dipoles at the surfaces of the FM layers not connected to the interlayer can be found in Ref. [120].

## 2.6 Measurement methods and experimental setups

### 2.6.1 Sputter deposition

All samples have been deposited by dc or rf magnetron sputter deposition on silicon wafers or glass substrates. Most of the work has been carried out with a commercial sputter tool Leybold CLAB 600. Single samples or layers have been deposited with a Leybold CLAB560 and a home made sputter deposition system.

The basic principle of sputter deposition is to extract ions from a plasma and accelerate them to a target. Only Ar ions have been used for this work. When the Ar ions hit the target, atoms are knocked out of the target and some of them hit the sample which is mounted above the target.

Permanent magnets can be mounted in the sputter chamber (CLAB600) or on the sample holder (CLAB600 and CLAB560) to initialize the exchange bias coupling by field growth.

The elemental concentrations which are stated for alloyed materials (except  $\text{Al}_2\text{O}_3$ ) in this work are the concentrations of the sputter targets. When nothing else is

stated, the following compositions have been used:  $\text{Ir}_{17}\text{Mn}_{83}$ ,  $\text{Co}_{70}\text{Fe}_{30}$ <sup>13</sup>,  $\text{Ni}_{80}\text{Fe}_{20}$  (Py), and  $\text{Co}_{40}\text{Fe}_{40}\text{B}_{20}$ . Due to different sputter rates of different elements, the real concentration of the elements in the alloys on the sample might be slightly different. For the sake of readability, in this thesis the alloys mentioned above will mostly be denoted only by the material combination (e.g., IrMn instead of  $\text{Ir}_{17}\text{Mn}_{83}$ ).

More details about the sputter deposition and the used tools can be found, e.g., in [121, 15, 122, 18, 123, 66, 124].

### 2.6.2 Topographic patterning

To measure the tunnel magnetoresistance in the present layered samples, it is necessary to prepare small structures (compare chapter 2.6.4).

To obtain these structures, a resist capping on squared areas of the sample with an area in the range of  $5\mu\text{m} \times 5\mu\text{m}$  to  $300\mu\text{m} \times 300\mu\text{m}$ , each, has been prepared by electron beam lithography in a LEO 1530 electron microscope with the Raith ELPHY software and negative resist AR-N 7500/18,<sup>14</sup> with laser lithography in a Heidelberg Instruments DWL 66 tool, or with UV lithography with home made masks<sup>15</sup> in a Lot Oriel tool. For laser and UV lithography mainly the positive resist AR-P-535/AR-P-5350 has been used.

Usually, first the sample is spin coated with the resist. Then, the sample is heated to remove the solvent, some parts of the resist are exposed to light/electrons, and finally the resist is developed to remove the positive (negative) resist on the exposed (not exposed) areas.

On the areas which are not protected by the remaining resist, the upper layers of the sample are removed by Ar ion beam etching in a Roth&Rau UniLab or a home made ion beam etching tool until only the lower conduction line remains.

After the resist has been removed small “towers” which are denoted as magnetic tunnel junctions (MTJ) are left.

More details about the used tools and the patterning methods can, e.g., be found in [55, 15, 123, 66, 125].

### 2.6.3 Ion bombardment induced magnetic patterning

In this work resist masks have been used to define the bombarded area for the ion bombardment induced magnetic patterning (compare chapter 2.2). Several types of lithography have been used to produce this masks.

---

<sup>13</sup>Single samples have been deposited with  $\text{Co}_{50}\text{Fe}_{50}$ . These are explicitly denoted as  $\text{Co}_{50}\text{Fe}_{50}$  in the text.

<sup>14</sup>The positive resist AR-610.03 (PMMA) which is partly used in extra thick layers to protect the sample against He ions can not be used for Ar etching.

<sup>15</sup>These masks have been prepared with laser lithography, sputter deposition of an approximately 50 nm thick metal (e.g., Ta) layer and lift off techniques.

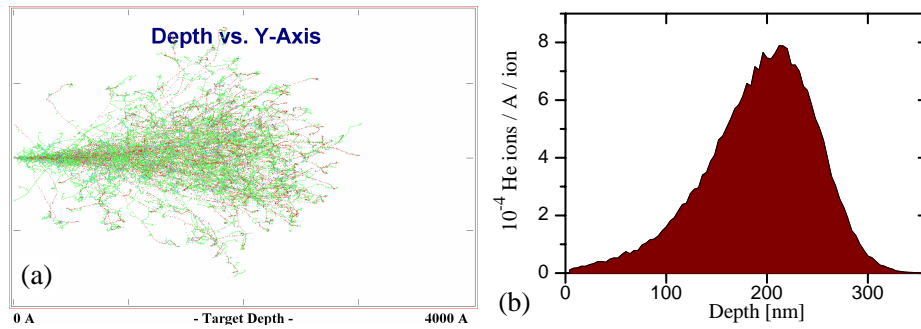


Figure 2.17: Range of 10 keV He ions in PMMA calculated with SRIM: (a) ion trajectories (moving ions: red, stopped ions: black; trajectories of recoiling atoms from PMMA: H=green, C=blue, O=purple) and (b) distribution of He ion stopped at a certain depth per Å depth and impinging ion. The parameters for PMMA (Polymethyle Methacrylate) included in the SRIM compound directory have been used.

For electron beam lithography the positive resist AR-P 610.03 (PMMA) and the negative resist AR-N 7500/18 have been used. When deposited by spinning for 30 s with 2000 (4000) spins per minute, for AR-P 610.03 a thickness of 130 nm (80 nm) can be expected [126].

SRIM simulations of 10 keV He ions hitting on PMMA resist have shown that most of the ions are stopped in a depth of about 300 nm<sup>16</sup> (Fig. 2.17). Therefore, it is necessary to use more than one layer of this resist to protect the sample against the ions. Usually four layers of PMMA with a total thickness of about 500 nm have been produced by spin coating the sample four times with a spinning speed of 2000 rotations/min and a spinning duration of 30 s. Between the spinning steps the sample has been heated for 5 min to about 150°C. After the last spinning step it has been heated for 15 min. The experimental observations confirm that this resist layers are sufficient to block the 10 keV He ions.

For the negative resist AR-N 7500/18 a resist layer thickness of 450 nm to 500 nm after spinning for 30 s at 4000 rotations/min can be expected [126].

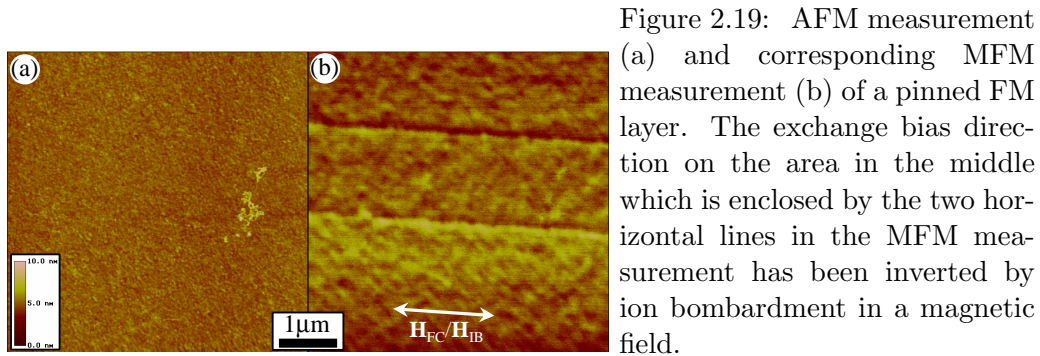
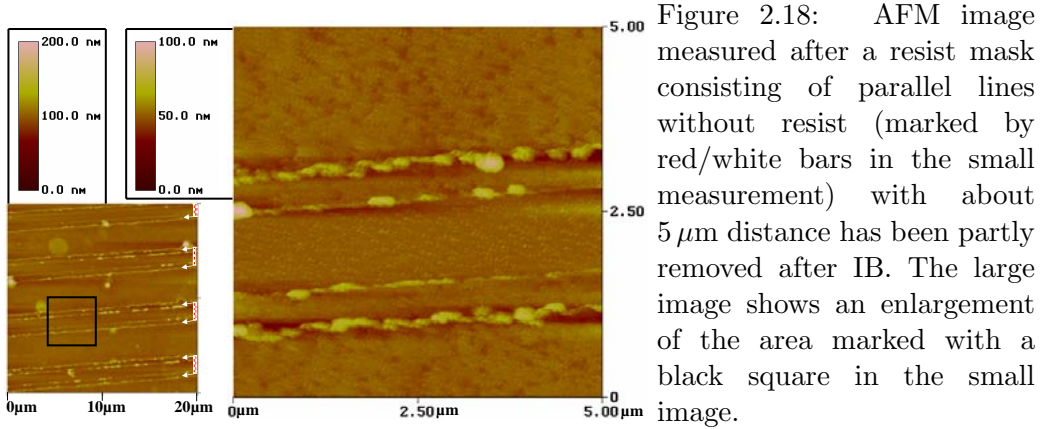
For UV lithography and laser lithography the resist AR-P 5350 from Allresist GmbH has been used. For this resist a thickness of about 1000 nm (800 nm) can be expected when it is deposited by spin coating with 30 s spinning at 4000 rotations/min (6000 rotations/min) [126].

Therefore, it can be expected that single resist layers of AR-N 7500/18 and AR-P 5350 are sufficient to block He ions in the investigated energy range.

During experiments which make use of the possibility to manipulate the magnetic properties of, e.g., pinned FM layers without a significant change of the topographic structure the removing of the resist should be carried out with care. This step has been found to be challenging for some bombarded samples. This effect seems to occur especially when a longer period of time (several months) passes between the coating of the sample with resist and the removing of the resist.

<sup>16</sup>Similar calculations for He ions with an energy of 20 keV result in a penetrated PMMA thickness of about 500 nm. In this work 10 keV ions have been used in combination with PMMA.





One example for such a sample can be seen in the atomic force microscopy (AFM) measurement in Figure 2.18. The parallel lines which were structured by electron beam lithography with four layers of PMMA are still clearly visible although the sample has been removed in the remover AR-300-70 for about 7 hours. This is far more than the usually required time. The reason for the fact that at each side of each line two up to about 150 nm high resist lines have developed is not clear. It might be connected to the shape of the resist at the edges of the bombarded area. Usually the resist does not build a perfect step at the edges of exposed areas but one observes an over- or undercut. This kind of double layers have been observed on one other sample as well.

But nevertheless it has been shown in most of the cases that it is possible to remove the resist without significant residues. One example of a similar sample with a bombarded grating is shown in Fig. 2.19. In this case, the bombarded lines can be found only in the MFM image where the magnetic stray field of the Néel walls at the sides of the bombarded line result in a MFM signal. In the AFM measurement on the left side no hint for the existence of the magnetically structured EB can be found.

Special attention has been paid to this topic whenever it was important for the experiment (compare, e.g., chapter 4.2).

### 2.6.4 Magnetoresistance measurements

The electric properties of the TMR samples have been determined by two point measurements perpendicular to the plane.

Therefore, magnetic tunnel junctions with a size of  $5\mu\text{m} \times 5\mu\text{m}$  to  $300\mu\text{m} \times 300\mu\text{m}$  have been prepared in the way described above.

Most of the MTJs have been contacted carefully with a thin gold needle from the top. The contact to the lower conduction line has been obtained by pressing a thicker gold needle hard on the sample outside the MTJ and scratching to destroy the barrier.

Samples which have been measured at low temperatures have been contacted by Au-wire bonding.

To determine the resistance in dependence of the external magnetic field, a constant bias voltage is applied while the external magnetic field is varied. If nothing else is stated, a bias voltage of 10 mV has been used.

Measurements where both FM layers change the direction of their magnetization as shown in Fig. 2.10 are usually denoted as *major loops*, while measurements with small magnetic fields where only the not pinned FM layer changes its magnetization direction significantly are called *minor loops*.

The width of a minor loop measured in the direction of the easy axis can be changed by applying an additional magnetic field perpendicular to the easy axis. This effect can be characterized by measuring minor loops with several values of the perpendicular magnetic field and plotting the switching fields in a graph. These graphs are called *switching field asteroids*. Several examples of switching field asteroids can be found in chapter 4.3.

When the minimum area resistance product  $R_A^{\text{min}}$  is stated, the resistance in saturation has been multiplied with the area of the magnetic tunnel junction. The area resistance product  $R_A$  is the product of the junction area  $A$  and the average resistance for parallel and antiparallel aligned magnetization directions ( $R_A = A \times (R^{\uparrow\uparrow} + R^{\uparrow\downarrow})/2$ ).  $R_A^{\text{min}}$  and  $R_A$  are independent of the junction area as long as the resistance of the MTJ is significantly higher than the resistance of the experimental setup, including the contact resistance between gold needle and sample surface, which is usually in the range of  $1\ \Omega$ - $3\ \Omega$ .

Low temperature measurements have been carried out in an Oxford Instruments closed cycle helium cryostat, which provides temperatures down to about 12 K, if nothing else is stated.

Other types of measurements which have been carried out with these experimental setups are current voltage measurements with various constant magnetic fields and inelastic electron tunneling spectroscopy which is described in more detail in the next chapter.

More details about these setups can be found, e.g., in [55, 15, 121, 123, 66, 125].

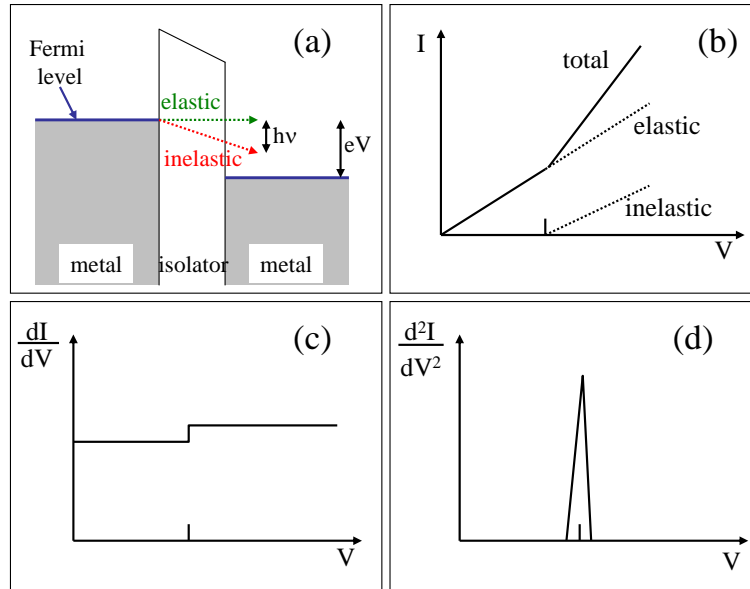


Figure 2.20: (a) Sketch of metal/isolator/metal trilayer (energy versus thickness). Blue lines represent the Fermi level. The gray areas represent filled electron states in the metal layers. The Fermi levels of the metals are shifted with respect to each other due to an applied voltage  $V$ . (b) Current versus voltage graph for a tunnel element with only elastic tunneling up to a certain voltage indicated by a small vertical line and an onset of inelastic tunneling at this voltage. (c)  $dI/dV$  versus voltage measurement resulting from (b), (d)  $d^2I/dV^2$  versus voltage measurement resulting from (b). These graphs are based on a figure in Ref. [127].

### 2.6.5 Inelastic electron tunnel spectroscopy

When a voltage is applied to a metal/isolator/metal trilayer, electrons can tunnel from electron states in one electrode to free states in the other electrode [Fig. 2.20 (a)].<sup>17</sup> When the electrons do not lose energy during this process it is called elastic tunneling. When the electrons lose energy, e.g., due to the creation of phonons (vibrational excitations, frequency  $\nu$ ), this effect is called inelastic tunneling. An inelastic process can only happen when the electron has enough energy to, e.g., create a phonon. Therefore, for each type of inelastic tunneling processes there is a minimum energy below which this process can not be found.

When this energy is reached, e.g., by increasing the applied bias voltage, the conductance is increased [Fig. 2.20 (b)].

The change of the gradient of the current versus voltage graph due to the onset of this inelastic tunneling process results in a step in the  $dI/dV$  versus voltage curve [Fig. 2.20 (c)].

The usual way of plotting inelastic electron tunnel spectroscopy (IETS) measurements is a  $d^2I/dV^2$  versus voltage graph [Fig. 2.20 (d)]. In this kind of graph the step in the  $dI/dV$  versus voltage curve resulting from the onset of the inelastic tunneling process is represented by a peak.

<sup>17</sup>This explanation of the principle of inelastic electron tunnel spectroscopy is based on Ref. [127].

In this work a quantity proportional to  $d^2I/dV^2$  will be frequently called *IETS signal*.

To measure IETS spectra of magnetic tunnel junctions, a low temperature is necessary because the thermal energy at room temperature corresponds to about 25 mV. This thermal smearing would mask many of the peaks observed at MTJs. Therefore, the measurements have been carried out in an Oxford Cryodrive 1.5 closed cycle He cryostat at about 12.5 K or in a pumped liquid He bath cryostat at about 2 K.

To obtain a  $dI/dV$  versus voltage curve, a two point measurement has been carried out where a dc bias voltage with overlaid ac voltage has been applied by an electronic measurement setup called measurement box in the following.<sup>18</sup> The defined voltage is kept fixed by the measurement box. Therefore, variations of the resistance will have no influence on the voltage. The resulting current is detected and amplified by the measurement box. The measured current is used as an input for a Stanford SR830DSP lock-in amplifier. The lock-in amplifier has also been used as a source of the overlaid ac voltage. Ac voltages in the range of 0.5 mV to 2 mV have been used. The output of the lock-in amplifier is proportional to the variation of the current due to the ac voltage. Therefore, this signal is proportional to  $dI/dV$ . The IETS signal proportional to  $d^2I/dV^2$  has been obtained by differentiating this signal. For all measurements shown in the same graph in this work, the signal has been adjusted to compensate for different amplifications used at the measurement box and the lock-in amplifier and similar measurement details. Therefore, measurements shown in the same graph are comparable. This is not always the case for measurements shown in different figures. Here, the absolute values of the IETS signal might vary although the shape of the measurement is not affected by this factor.

The goal of IETS measurements carried out at MTJs is to learn more about the processes which have an influence on the electron transport through the barrier and, therefore, are responsible for the height of the resistance and the tunnel magnetoresistance and many other properties like, e.g., the bias voltage dependence of the TMR amplitude.

More information about inelastic electron tunnel spectroscopy can be found in Ref. [127, 128, 129]. A more detailed description of the experimental setup can be found in [130, 125].

### 2.6.6 Magneto optical Kerr effect

The magneto optical Kerr effect (MOKE) is used to investigate qualitatively the change of the magnetization under the influence of an external magnetic field.

The light emitted by a laser diode ( $\lambda = 675$  nm) is linearly polarized by a filter before it hits the sample. The reflected light passes an additional polarization filter (analyzer) and the light which passes this filter is detected. Because the polariza-

---

<sup>18</sup>This electronic setup is the same as used for measuring, e.g., the major loops and current voltage curves.

tion of the reflected light depends on the orientation of the magnetization of the sample, also the amount of the light which reaches the detector depends on the sample magnetization direction. Therefore, a change in the orientation of the sample magnetization results in a change of the signal. This method is used to analyze the magnetization reversal process induced by a varying external magnetic field.

In metals the characteristic attenuation length determining the probing depth is of the order of  $\lambda = 10\text{-}20\text{ nm}$  at visible frequencies as they are used here ( $I/I_0 = \exp(-t/\lambda)$ ,  $I_0$  initial intensity,  $I$  intensity after optical path  $t$  in medium, [131]).

More details about this measurement method and the used experimental setup can, e.g., be found in [131, 132, 133, 134, 135, 136].

### 2.6.7 Alternating gradient magnetometer

The alternating gradient magnetometer (AGM) is used to investigate quantitatively the change of the magnetic moment under the influence of an external magnetic field.

For the measurements shown within this thesis, an Princeton Measurements Corporation MicroMag AGM has been used. This tool allows measurements at room temperature as well as at elevated temperatures when the sample is placed in a heated He flow.

The sample is mounted on a thin rod in between a large pair of coils which can apply an external magnetic field of up to 14 kOe. One or two additional pairs of small coils are located close to the sample. With these coils a small alternating gradient field is applied. The response of the sample to this alternating gradient field is detected in dependence of the external magnetic field by a piezo crystal at the end of the thin rod. From this signal the magnetic moment of the sample can be determined. After a calibration of the tool the absolute magnetic moment of the sample can be determined.

To obtain the magnetization from the measured magnetic moment of the sample, the volume of the FM layer is needed. Therefore, the area of the samples has been determined by taking a photo of the sample and analyzing this photo with the program AnalySIS.<sup>19</sup> This enables in combination with the layer thickness determined from the used sputter times to calculate the volume of the FM layer.

More details about this measurement method and the used experimental setup can, e.g., be found in [137, 133, 138]

### 2.6.8 X-ray photoemission electron microscopy

In a photoemission electron microscope (PEEM) the sample is irradiated by x-rays. When the energy of the photons is larger than the work function of the sample, electrons are emitted. An electron-optical imaging system consisting of several electron-

---

<sup>19</sup>The image processing with AnalySIS has been carried out by Inga Ennen.

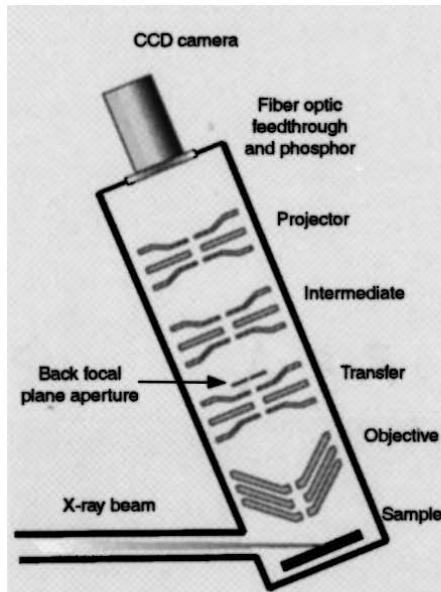


Figure 2.21: Sketch of the *PEEM 2* photoemission electron microscope at beamline 7.3.1.1 at the Advanced Light Source, Berkeley, CA. (from [139])

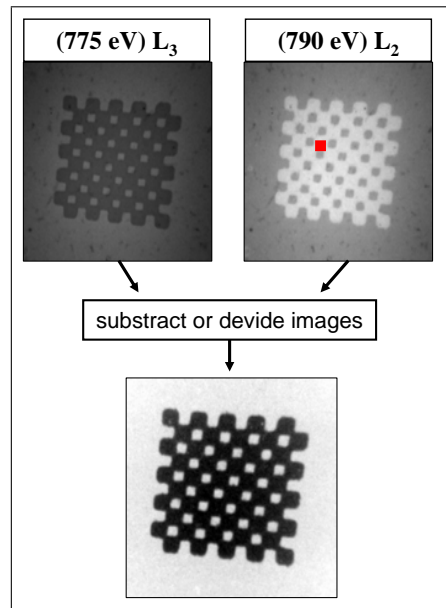


Figure 2.22: PEEM measurements at the Co  $L_3$  edge and at the Co  $L_2$  edge and the difference of both measurements showing the magnetic contrast. The PEEM signal at the area indicated by the red square for several photon energies can be found in Fig. 2.23.

optical lenses (compare Fig. 2.21) can transfer an image of the emitted electrons onto a detector. With this method modern PEEM instruments reach resolutions which approach 10 nm [139].

To obtain an elemental contrast, the energy of the photons can be tuned. When the energy hits the absorption edges of the investigated material (also called *white lines*), more photons are absorbed and the number of emitted secondary electrons is strongly enhanced (Fig. 2.23).

Furthermore, a magnetic contrast can be obtained since the absorption of left and right handed circularly polarized x-rays depends on the relative orientation of the polarization of the photons and the magnetic moment of the sample. When a polarized photon excites an electron, the angular momentum of the photon can be transferred to the electron. Due to the spin dependent band structure in ferromagnetic materials, the probability of the excitation depends on the relative orientation of the magnetic moment of the excited electron and, therefore, the polarization of the photon and the magnetization of the FM layer. This effect is called x-ray magnetic circular dichroism (XMCD) [140, 141, 142, 121, 143, 144, 145].

The XMCD effect has, for a given photon polarization, an opposite sign at the  $L_2$  and  $L_3$  edges because at this photon energies the excited electrons originate from the

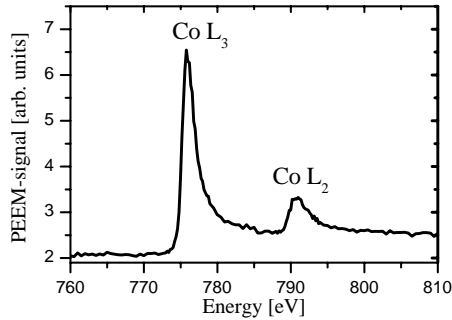


Figure 2.23: Energy dependence of the PEEM signal on a bombarded area of a pinned CoFe layer obtained by local spectroscopy on the spot indicated by the red square in Fig. 2.22. The values of the PEEM signal have been extracted from PEEM measurements with various photon energies.

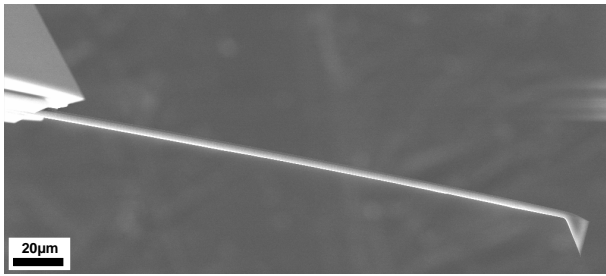


Figure 2.24: SEM image of a MFM probe (right lower corner) with cantilever and mounting device (upper left corner).

$2p_{1/2}$  and  $2p_{3/2}$  states, respectively.<sup>20</sup> This means that the spin magnetic moment of the electrons before the excitation is oriented antiparallel or parallel to the orbital magnetic moment and, therefore, the probability for a certain magnetic moment of the excited electron is different for a given photon polarization. Therefore, one can obtain a magnetic contrast by dividing or subtracting experimental results which describe the probability of this kind of electron excitation at the  $L_2$  and  $L_3$  edges. The PEEM signal provides this information for every point of the investigated area. Figure 2.22 shows an example of PEEM measurements carried out at a pinned CoFe layer with a checkered magnetic pattern and the resulting magnetic contrast.

References [140, 141, 142, 121, 143, 144, 145] describe the XMCD effect and its applications in more detail. For more information about the PEEM see Ref. [139, 146]. More information about the experimental setup at the Advanced Light Source, Lawrence Berkeley National Laboratory, Berkeley, CA including PEEM-tutorials can be found at [146]. This chapter is mainly based on the information given in the references cited above.

### 2.6.9 Magnetic force microscopy

Magnetic force microscopy (MFM) is a technique which makes it possible to investigate the strayfield of samples down to the range of a few nanometers. It is an extension of the non contact atomic force microscopy (AFM).

To obtain an AFM image, a probe (Fig. 2.24) is scanned over the sample surface. The force between the sample and the probe is measured, e.g., by vibrating the probe which is mounted at the end of a thin cantilever and detecting the change of

<sup>20</sup>For the investigated materials as, e.g., Co and Fe the measurements at the L edge (transition from  $2p$  to  $3d$  state) result in a good signal.

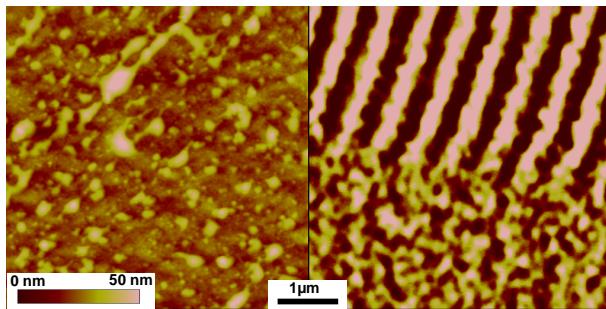


Figure 2.25: Left part: AFM image of a  $5\mu\text{m} \times 5\mu\text{m}$  large part of a DAT tape; right part: corresponding MFM image (lines in upper part: magnetized areas used for information storage)

the vibration frequency and phase due to the interaction between sample and probe. To obtain the information about the magnetic strayfields probes with a magnetic coating are used. When an MFM measurement is carried out, first a line is scanned with a smaller distance between probe and sample to obtain the height information. Then the probe is scanned the same line again with a constant height. But the second time the distance between probe and sample is larger and, therefore, mainly the long range magnetostatic interaction is detected.

An example of a MFM measurement can be found in Fig. 2.25. The right part shows a MFM measurement of a DAT tape with an alternating orientation of the magnetization of small lines which are visible in the upper part of the MFM image because their stray fields are detected. The corresponding AFM measurement is shown in the left part of the image.

In this work a Digital Instruments NanoScope microscope has been used.

More information about atomic- and magnetic force microscopy can be found in Ref. [147, 148, 149].

### 2.6.10 Scanning electron microscope

The scanning electron microscope (SEM) LEO 1530 allows to investigate samples over a wide range of magnifications down to a few nanometers. Furthermore, this tool has been used for electron beam lithography (compare chapter 2.6.2).

The basic principle of the scanning electron microscope is to focus a fine electron beam (primary electrons) on a sample and scan over the area of interest on the sample. To obtain an image, the backscattered electrons as well as secondary electrons resulting from inelastic scattering of the electron beam in the sample can be detected.

Other operation modes of SEMs are Auger electron spectroscopy (AES, [150, 151])<sup>21</sup> and energy dispersive x-ray spectroscopy (EDX, [152]).<sup>22</sup> X-rays and Auger electrons are emitted when a core electron is removed by a scattering primary electron. This event produces an atom in an excited state which can decay to its ground state by emitting x-rays or Auger electrons. As the energy of these photons or electrons depends on the material, element specific measurements can be carried out.

<sup>21</sup>AES has been carried out in a Physical Electronics scanning Auger microscope (model 660).

<sup>22</sup>These two modes have been used only during sample preparation and no measurements will be shown.



More details about this measurement method and the used experimental setup can, e.g., be found in [150, 123, 153, 151, 152].

### 2.6.11 Ion bombardment

All ion bombardment has been carried out by members of the group of Arno Ehresmann at the Kaiserslautern University of Technology and Kassel University.

In this work, only bombardment with He ions in the energy range from  $E_{IB}=4.5$  keV to  $E_{IB}=30$  keV has been used.

The ions are generated in a Penning ion source. Ions are extracted from the plasma in the ion source and the diverging ion beam is transferred into a parallel ion beam by electrostatic lenses. This beam hits the sample.

If nothing else is stated, a permanent magnetic field of 1000 Oe is used for ion bombardment in a magnetic field.

A sample holder which allows to apply magnetic fields of up to 6 kOe during the ion bombardment has been manufactured.

More details about the ion bombardment can, e.g., be found in [45, 79, 77, 78, 56].

## 2.7 Simulation programs

### 2.7.1 Stopping and range of ions in matter (SRIM)

The program package SRIM<sup>23</sup> (stopping and range of ions in solids) with its main component, the Monte-Carlo program TRIM (transport of ions in matter) enables an easy depth dependent calculation of the effect of ions as, e.g., the defect generation or energy deposition in a sample.

TRIM calculates the trajectory in a target for a high number of ions (usually, 30000 to 99999 ions have been calculated).

Furthermore, with the “*Detailed Calculation with full Damage Cascades*” calculation mode, which was used in all simulations shown in this work, the trajectories of the recoiling atoms including the details about the collisional damage are calculated until the energy of the recoiling atom is lower than the lowest displacement energy of any atom in the sample.

The impinging ion is defined by its element, its energy and its angle relative to the surface. All calculations have been carried out for ions hitting the target along the surface normal.

The target material consists of layers of different materials with a defined stoichiometry. The crystal structure is not defined. For the density of the materials the density obtained by x-ray diffraction measurements at calibration samples with a thickness in the range of a few ten nanometers has been used. For the displacement energy, the surface binding energy, and the lattice binding energy the default values given

---

<sup>23</sup>The program can be downloaded at [www.SRIM.org](http://www.SRIM.org).

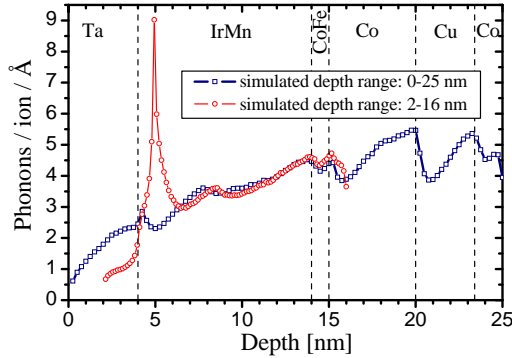


Figure 2.26: SRIM simulations of phonons produced per ion and  $\text{\AA}$  with identical parameters (stack  $SV_{3.4nmCu}$ , ion energy 10 keV, 99999 ions calculated) except the investigated depth range.

by SRIM have been used.

The program has some limitations which one should keep in mind when looking at the results.

The program does not include any information about changes to the structure due to earlier ions. Each ion hits a fresh system and, therefore, if a severe change of the sample due to ion bombardment occurs because, e.g., a large number of atoms is displaced and the average displacement energy is changed, this will not be included in the calculations. But for this work ion doses which destroy the sample significantly are not of large interest, because it can be expected that the exchange bias and especially the magnetoresistive effect would not survive this treatment.

A rough estimation shows that one can expect about 0.1 vacancies per ion and  $\text{\AA}$  in the CoFe/IrMn bilayer of a sample with stack  $hMTJ$  (compare Fig. 3.103 for simulation and appendix A for stack details). The maximum exchange bias after turning the EB direction by  $180^\circ$  has been observed for this stack at about  $1 \times 10^{14}$  ions/cm<sup>2</sup>. This results in about 1 vacancy per nm<sup>3</sup>. Therefore, for each vacancy several atoms are not moved (e.g., crystal constant of Fe:  $2.87 \text{\AA}$  [154]).

The detailed structure of the results of SRIM simulations will not be used to get information about the investigated sample as it is influenced by details of the calculation like, e.g., the depth range which is stored and displayed (always the full stack is simulated). An extreme example of this influence is shown in Fig. 2.26. These two simulations have been started with identical parameters except the investigated depth range.

The SRIM instruction manual [155] lists several reasons for artifacts at layer edges: They are due to the fact that the program calculates the trajectories of the ions in the full defined stack, but saves and displays only a defined region. This depth region is always divided into 100 equally sized bins. When an edge of a target layer does not fit to an edge of a bin, one bin consists of two materials and the program assumes the bin to consist of one or the other material based on the current ions trajectory.

Furthermore, problems can arise from the fact, that the program assumes a minimum distance (monolayer distance) between atoms in the target material calculated as the inverse cube root of the atomic density in units of atoms/cm<sup>3</sup>. This is the minimum distance which an ion has to move between two collisions and, therefore, this is the minimum distance which is used in the program. If a bin is less than one

monolayer wide, the program may not treat it correctly. This problem might with decreasing intensity also occur for thin bins up to about 2 nm (compare Fig. 2.26). This is a thickness range which is frequently used for our stacks. These problems might stretch over more than the one bin which is directly affected, because the program can "jump" many monolayers between collisions and approximate the intermediate collisions.

But although the high number of very thin layers in most of the samples investigated here induces some artifacts, the program is very useful to get an idea how the system of ions and sample might react when, e.g., the ion energy is changed or different capping layers are used.

For more details on the limitations and the calculation details of SRIM in general see [155, 156].

### 2.7.2 Downhill simplex minimization in multidimensions

The magnetization direction of a FM layer aligns in a way that minimizes the total energy. Therefore, the magnetization reversal process can be predicted by determining the magnetic configuration of a sample which results in the minimum total energy for all external magnetic fields of interest. The basic computational principle used for this kind of energy minimization calculations will be briefly described in the following lines. More details about the energy minimization can be found in chapter 3.3.

The downhill simplex method due to Nelder and Mead [157] can be used for finding the minimum of functions with more than one independent variable. This method does not require derivative calculations and makes almost no special assumptions about the investigated function. The storage requirement for an N-dimensional problem is  $N^2$  and it can be rather slow, but it can be extremely robust in some cases.

A simplex is a geometrical figure which in an N-dimensional space has N+1 corners. In two dimensions, e.g., the simplex is a triangle while in three dimensions the simplex is a tetrahedron (Fig. 2.27).

For a calculation with N variables a starting guess of N+1 values forming a non degenerated simplex is needed. When one point is chosen to be the origin the vectors pointing from this point to the others span an N-dimensional space. During the minimization the values of the function which has to be minimized are calculated for all points of the simplex. Then the point with the highest value is moved through the opposite face (gray area in Fig. 2.27) to a point with a lower value. This transformation is called reflection (Fig. 2.27 (a)). For reflections the nondegeneracy of the simplex is always conserved. Sometimes it is possible to use larger steps by expanding the simplex after the reflection (Fig. 2.27 (b)). When the simplex is close to a minimum, its volume is decreased by contracting the simplex in the direction of the point with the largest value (Fig. 2.27 (c)) or in all directions towards the lowest point (Fig. 2.27 (d)).

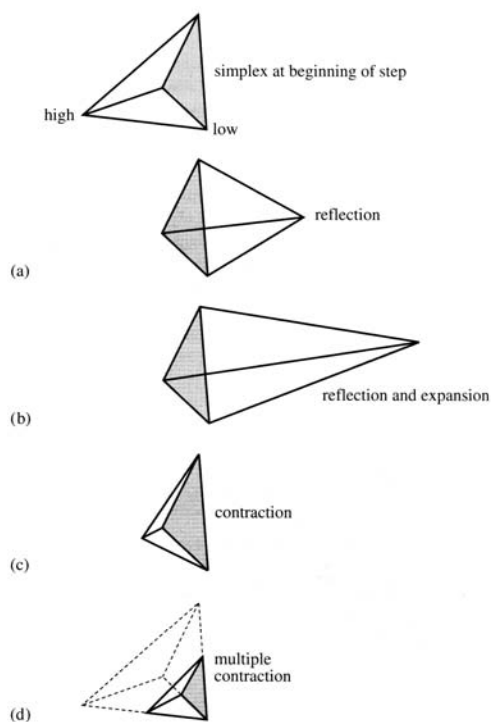


Figure 2.27: Possible results of one calculation step in the downhill simplex method: (top) simplex in three dimensions (tetrahedron) before calculation step and (a) after reflection of point with high value of investigated function (b) after reflection of point with high value and additional expansion (c) after contraction along one dimension from the point with high value and (d) after a contraction along all dimensions towards the point with the lowest value. (from [158])

A more detailed description and the code of the amoeba implementation<sup>24</sup> can be found in Ref. [159, 158] which was also the basis of this chapter.

<sup>24</sup>The program implementing the minimization method as described in [159] and the base of the program used for the energy minimization calculations shown in chapter 3.3 have been provided by Andy Thomas.

## Chapter 3

# Applicability of ion bombardment induced magnetic patterning

It is known that the exchange bias (EB) coupling can be manipulated in sign and magnitude by ion bombardment (IB) in a magnetic field for several combinations of ferromagnet (FM) and antiferromagnet (AF) (compare chapter 2.2).

This manipulation can be carried out selectively on parts of the sample (compare chapter 2.2.2). With this technique an arbitrary lateral exchange bias pattern can be produced (Fig. 3.1). This example shows a 3 nm thick CoFe layer which is pinned to an IrMn layer. The EB has been initialized homogeneously on the whole sample by field cooling (FC). Then, the sample has been covered with 4 layers PMMA and the resist has been exposed by the electron beam on the area of the letters. After the development the sample has been bombarded with 10 keV He ions in a magnetic field  $\mathbf{H}_{\text{IB}}$  antiparallel to the field during field cooling  $\mathbf{H}_{\text{FC}}$ . The whole area except the letters is protected by the resist against the ion bombardment. Therefore, only the EB on the area of the letters is manipulated. This treatment results in an opposite direction of the EB coupling and, therefore, an opposite orientation of the magnetization in remanence on the area of the letters compared to the rest of the sample. The remanence magnetization pattern, which has been measured in the photoelectron emission microscope, is shown in Fig. 3.1.

In the following chapters several other examples of a patterned exchange bias coupling will be shown.

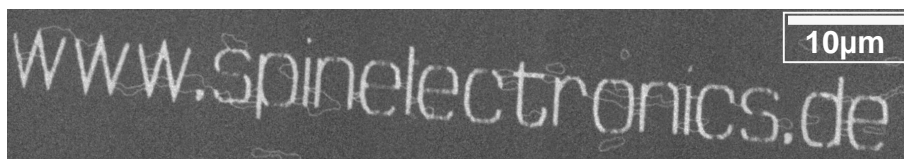


Figure 3.1: Photoelectron emission microscopy image of a CoFe layer pinned to an IrMn layer with a patterned EB coupling. Dark and bright contrast indicates an opposite direction of the remanence magnetization.

In the next sections the question of the applicability of this technique will be investigated. Especially the question of the applicability in combination with magnetoresistive effects will be answered in detail. During the description of this investigations several interesting physical effects will be discussed.

## 3.1 Switchable resonant x-ray Bragg scattering on a magnetic grating patterned by ion bombardment

### 3.1.1 Introduction

On the following pages another example of a magnetic pattern will be described. Here, additionally the question whether a pure magnetic pattern or a mixture of magnetic and topographic structures is present will be addressed. But the main topic is the interesting effect of manipulating soft x-rays with a flat sample by applying a magnetic field.

It will be shown that magnetic patterning opens the opportunity to build a magnetic grating showing a soft x-ray interference pattern based on the x-ray magnetic circular dichroism (XMCD) effect.

### 3.1.2 Experiment

The sample *CoFe-Xray* used in the present experiment consists of Cu 30 nm / Mn<sub>83</sub>Ir<sub>17</sub> 15 nm / Co<sub>70</sub>Fe<sub>30</sub> 3 nm / Al 1.4 nm +100 s electron cyclotron resonance plasma oxidation. A homogeneous EB was initialized by field cooling in an external magnetic field of  $H_{FC}=1500$  Oe. A resist mask with 1.6  $\mu\text{m}$  wide lines parallel to  $\mathbf{H}_{FC}$  and a periodicity of 5  $\mu\text{m}$  was patterned by electron beam lithography. Ion bombardment induced magnetic patterning (IBMP) with He ions (ion energy  $E_{IB}=10$  keV,  $1 \times 10^{14}$  ions/cm<sup>2</sup>) was carried out through this mask in an external magnetic field  $\mathbf{H}_{IB}$  (1000 Oe) oriented antiparallel to  $\mathbf{H}_{FC}$ . After the removal of the resist one can expect a magnetic grating with an approximately antiparallel orientation of the EB coupling at the bombarded lines and the area between them without a change of the topographical microstructure. The test of the magnetic grating has been done with the ALICE experimental setup [161] at beamline UE56/1-PGM-b at BESSY [162, 163]. A circular polarized x-ray beam (95% polarization [121]) was directed at the rotatable sample with a variable angle  $\Theta$  while the detector (GaAsP photodiode) was fixed at an angle of  $\phi=20^\circ$  relative to the incident beam (Fig. 3.2). The grating was tilted by about  $45^\circ$  relative to the plane of the incident/reflected beam. This made it possible to measure the interference pattern which results from the XMCD effect with a detector in the plane of the incident/reflected beam. The orientation of the external magnetic field has been fixed parallel to the direction of the incident photon beam. The magnetic structure of the sample has been investigated by magnetic force microscopy (MFM). All measurements have been carried out at room temperature.

---

<sup>1</sup>Parts of this chapter have been published in [160].

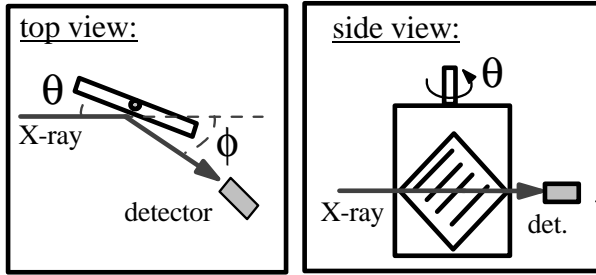


Figure 3.2: Experimental setup with angle  $\Theta$  between sample surface and incident photon beam and angle  $\phi$  between detector and incident photon beam, rotation axis perpendicular to scattering plane.

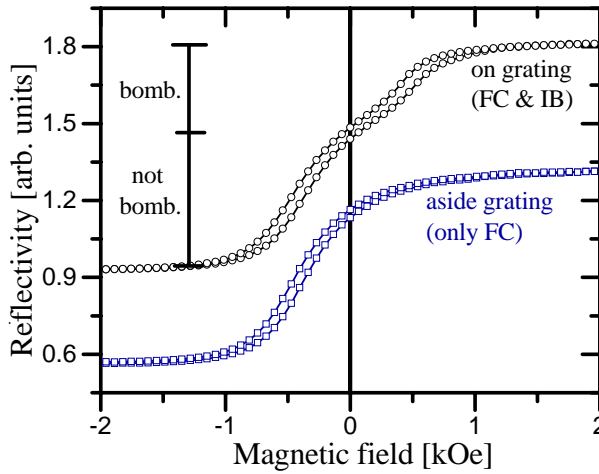


Figure 3.3: Hysteresis loops obtained by x-ray reflectivity measurements on the magnetic grating (superposition of signal from bombarded and not bombarded areas, black circles) and aside the magnetically patterned grating (blue squares) on sample *CoFe-Xray* (Co  $L_3$ -edge,  $\Theta=10^\circ$ ,  $\phi=20^\circ$ , loops shifted on y-axis for better visibility).

### 3.1.3 Results and Discussion

As it can be seen from the hysteresis loop measured on the magnetic grating in Fig. 3.3, bombarded as well as not bombarded lines are hit by the x-ray beam. The change in reflectivity due to the not bombarded area in between the lines is approximately twice as high as that for the bombarded lines. This corresponds to the fact that the average distance between the lines is nearly two times the width of the bombarded area. The hysteresis loop of the same layer system measured aside the magnetically patterned grating (only FC) can be seen in the lower part of Fig. 3.3. The shape of the hysteresis loops is rounded in both cases because the magnetic field during the measurement was not aligned parallel to the easy axis of the pinned ferromagnet.

Magneto optical Kerr effect (MOKE) measurements carried out parallel to the easy axis (Fig. 3.4) show a shift of the hysteresis loop due to EB of  $H_{EB} = 626$  Oe (630 Oe) for the bombarded (not bombarded) areas with an opposite direction of the shift for the bombarded and the not bombarded area.

Although the relation of the width of the bombarded lines to the width of the not bombarded area in between is approximately one to two, the factor between the change of the MOKE signal at negative magnetic fields (bombarded area) relative to that at positive magnetic fields (not bombarded area) is much larger than two. This is due to the fact that the information about the magnetization obtained by the MOKE signal is averaged over the area of the laser spot. In this measurement not only the grating but also a part of the surrounding not bombarded area is tested by the MOKE measurement resulting the smaller signal of the bombarded lines relative

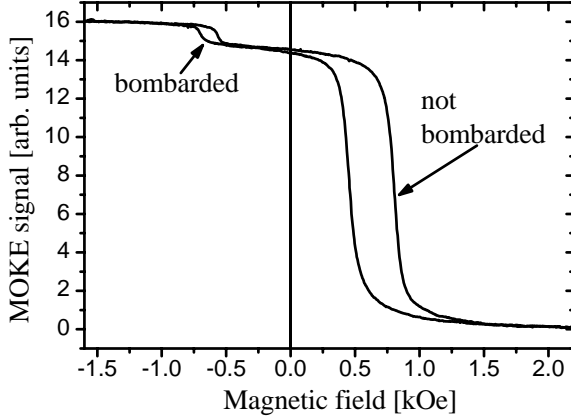


Figure 3.4: Hysteresis loops obtained by MOKE measurements on the magnetic grating on sample *CoFe-Xray*. (magnetic field during measurement parallel to  $\mathbf{H}_{FC}$ )

to the not bombarded area.

The values of the coercive field are 171 Oe for the not bombarded and 57 Oe for the bombarded area. A change of the coercive field due to IB has been reported before (see, e.g., Ref. [67]). It might be attributed to a decrease of the number of interfacial spins of the AFM layer which are loosely bound to the AFM and whose orientation, therefore, cannot be altered by thermal excitation but can be forced to rotate by the FM layer due to the exchange bias interaction [60].

Because the coercive field is in both cases much smaller than the shift of the hysteresis loop due to EB, one can assume an approximately antiparallel orientation of the FM magnetization in the bombarded and not bombarded areas in remanence. A small deviation of the antiparallel orientation of up to  $5^\circ$  might occur because of a possible small inaccuracy in the alignment of the directions of  $\mathbf{H}_{FC}$ ,  $\mathbf{H}_{IB}$  and the lines.

Apart from the charge scattering of the x-rays, which is independent of the IB-induced magnetic changes, a resonant magnetic scattering occurs at the  $L_{2,3}$  white lines of Co and Fe. When investigated in remanence, the part of the scattered x-rays which is due to resonant magnetic scattering will have a different intensity on areas with a magnetization direction oriented predominantly parallel to the incident beam than on areas with a predominantly antiparallel orientation of the magnetization. Therefore, a superposition of an interference pattern like that of a three dimensional reflective grating which is due to resonant magnetic scattering and the signal obtained by the field independent charge scattering can be expected.

Figure 3.5 shows a  $\Theta$  scan where the sample is rotated while the detector is fixed (Co  $L_3$ -resonance,  $\phi=20^\circ$ ). The difference between the two measurements for the sample saturated in the x-ray propagation direction and opposite to it shows the maximum possible magnetic signal. For the measurement without an external magnetic field the expected oscillation can be clearly seen [Fig. 3.5(b)]. This pattern vanishes when a magnetic field of  $\pm 2700$  Oe, which is sufficient to saturate the ferromagnetic layer (see Fig. 3.3), is applied. This shows that the observed oscillation at the measurement in remanence is due to interference at the magnetic pattern and not related to topographic structures.

For a selected range of angles  $\Theta$  scans have been performed with various magnetic fields (Fig. 3.6). The field values vary from saturation at -2700 Oe to saturation at



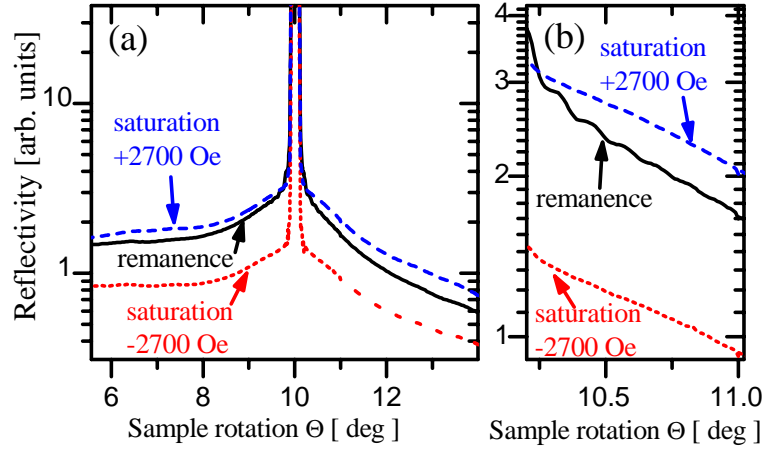


Figure 3.5: (a) Sample rotated by angle  $\Theta$  with fixed detector ( $\phi=20^\circ$ ) in a magnetic field of +2700 Oe (blue dashed line), -2700 Oe (red dotted line) and without an external magnetic field after saturation at -2700 Oe (black solid line). All measurements were done at the Co  $L_3$ -resonance. (b) Enlarged region of the same measurement.

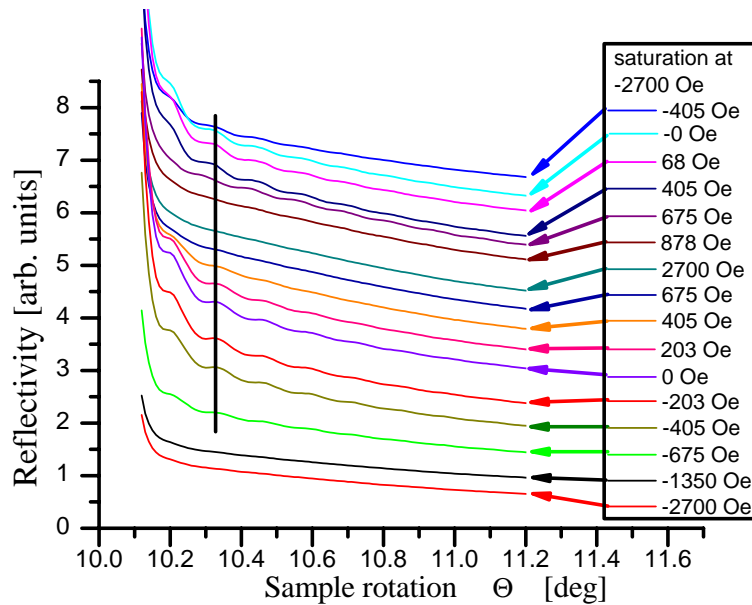


Figure 3.6:  $\Theta$  scan at the Co  $L_3$ -edge with fixed detector ( $\phi=20^\circ$ ) for various magnetic fields (-2700 Oe  $\rightarrow$  +2700 Oe  $\rightarrow$  -2700 Oe, measurements shifted on the y-axis for better visibility).

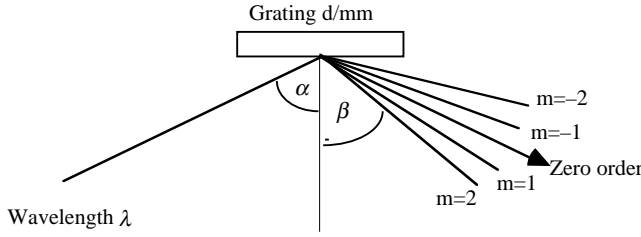


Figure 3.7: Sketch of notation for grating equation. (from [164])

+2700 Oe and back to saturation at -2700 Oe corresponding to a hysteresis loop. As it can be seen in Fig. 3.6 the angles of the individual maxima are not changed considerably by the magnetic field. The magnitude of the interference pattern of the magnetic grating decreases with increasing magnetic field and vanishes at a magnetic field larger than 675 Oe. This shows that it is possible to build a gradually tunable magnetic grating by this IBMP technique.

When the grating equation [164]  $m\lambda = d \times (\sin(\alpha) + \sin(\beta))$  (spectral order  $m$ , wavelength  $\lambda=1.59$  nm, angle  $\alpha$  between the incident beam and the surface normal, angle  $\beta$  between the scattered x-rays and the surface normal) is applied to the experimental results, the grating period  $d$  can be calculated.

The first visible maxima next to the specular peak at  $10.02^\circ$  are located at  $9.81^\circ$  and at  $10.32^\circ$ . The measured distance between adjacent maxima is  $0.12^\circ$  to  $0.13^\circ$ . Therefore, the maximum at  $10.32^\circ$  ( $9.81^\circ$ ) is of order -3 (2). The maxima of lower order are hidden by the specular peak. The superposition of the maxima due to interference and the specular peak can also shift the position of the maxima on the flank of the specular peak in the direction of the peak (compare Fig. 3.8).

By taking into account that the bombarded lines were tilted by  $45^\circ$  relative to the horizontal plane defined by the incident beam and the detector and that the measured angles represent the projection of the interference pattern on this plane, one gets values in the range of  $d=1.58 \mu\text{m}$  to  $d=1.92 \mu\text{m}$ . That result does not match with the periodicity of the magnetic grating of  $d = 5 \mu\text{m}$ , but it is in the range of the width of the bombarded lines. This is a hint that the Néel-wall-like boundaries between the bombarded and the not bombarded areas are of a great importance for the interference process. The maxima one would expect from the interference of x-rays scattered at Néel-wall-like boundaries with a distance of  $3.4 \mu\text{m}$  corresponding to the width of not bombarded areas have a smaller distance. Therefore, more maxima of this kind are hidden by the specular peak and only weaker maxima of a higher order can contribute to the observed interference pattern.

Figure 3.8 shows the angles at which maxima can be expected according to the grating equation for a grating with  $d=1.6 \mu\text{m}$ ,  $d=3.4 \mu\text{m}$ , and  $d=5 \mu\text{m}$ , which is tilted by  $45^\circ$  relative to the scattering plane. For an easier comparison with the experimental results, the difference between the  $\Theta$  scan measured in remanence and the one measured in saturation at +2700 Oe is printed in the same graph. This emphasizes the interference signal due to magnetic scattering. It can be seen that interference at a grating with a periodicity of  $d=5 \mu\text{m}$  can not explain the observed interference pattern.

The magnetic domain structure of the sample in remanence has been investigated by MFM measurements (Fig. 3.9). No topographic structures corresponding to the

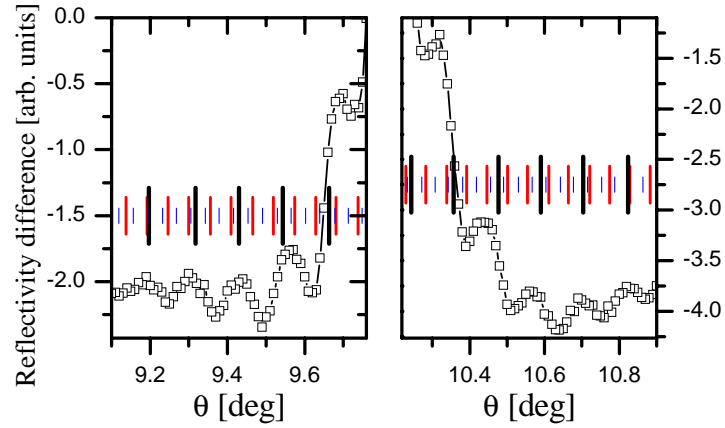


Figure 3.8:  $\Theta$  scan measured in remanence subtracted by the  $\Theta$  scan measured in saturation (+2700 Oe); vertical lines: angle at which a maximum is predicted by the grating equation for a grating with  $d=1.6\ \mu\text{m}$  (black big lines, shown up to  $m=7$ ),  $d=3.4\ \mu\text{m}$  (red medium lines, shown up to  $m=14$ ), and  $d=5\ \mu\text{m}$  (blue small lines, shown up to  $m=23$ ).

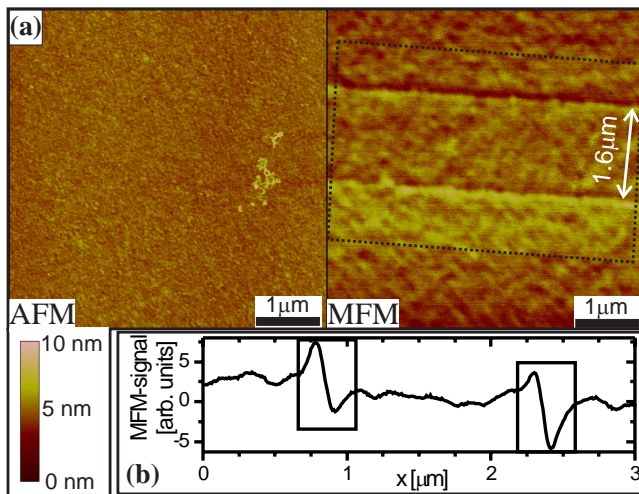


Figure 3.9: (a) MFM measurement (right) of a bombarded line (width indicated by arrow) with the corresponding AFM-measurement (left) and the color code for the AFM-image (b) spectrum of MFM image perpendicular to the bombarded line (boxes indicate Néel walls) averaged over the area indicated by the dotted box in the MFM image).

magnetically patterned lines are present.

It is striking that the Néel-wall-like boundaries on both sides of the bombarded line show a bright contrast below a dark contrast corresponding to the similar signature in the line scan (Fig. 3.9(b), boxes). This means that the magnetization is rotating in the same direction in both cases [165]. This effect has been observed at all investigated points of the magnetic grating. The direction of the rotation can be changed by saturating the sample with an angle of  $45^\circ$  relative to the lines as it has been done during the measurements at BESSY.

An example for this changed rotation direction can be seen in Fig. 3.10. The MFM measurements shown in this figure have been carried out after saturating the sample in a magnetic field pointing to the lower right [(a)/(b)], upper left [(c)/(d)], and again lower right [(e)/(f)] corner of the graph (red arrows in Fig. 3.10). In the first measurement [(a)/(b)] the bright contrast is at the right side while the dark contrast is at the left side of the boundary of the bombarded line (compare white and black arrows). On the second measurement [(c)/(d)] carried out after the sample has been saturated in an opposite direction compared to the first one the bright contrast is at the left side and the dark contrast is located at the right side. After a further saturation comparable to the first one, the situation of the first measurement has been reproduced [(e)/(f)].

As the rotational direction of the magnetization on the sample investigated at the BESSY switches at every investigated point of the sample in the same direction the observed interference pattern might be connected to the resonant scattering of x-rays at the magnetization of the Néel walls which is rotating in the same sense.

### 3.1.4 Summary

We have shown that it is possible to measure an x-ray interference pattern with a purely magnetic grating patterned by ion bombardment induced magnetic patterning. Regular topographical patterns as an origin of the interference pattern can be ruled out. Although the variation of the intensity is rather small, in principle a magnetically operated switch for x-rays has been produced.

A homogeneous rotational direction of the magnetization at the edges between bombarded and not bombarded areas has been observed. The rotational direction can be changed by saturating the sample with an angle of  $45^\circ$  between external field and the lines. Scattering at these edges as an important contribution for the observed interference pattern has been suggested.

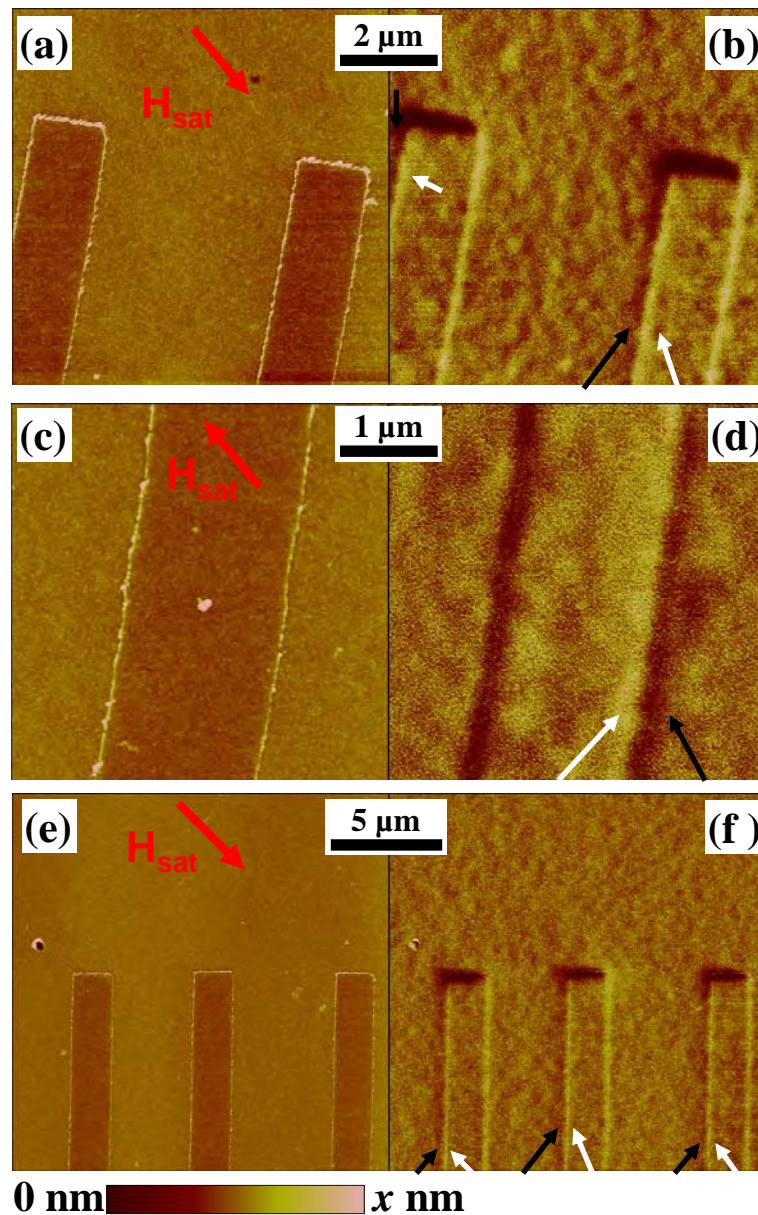


Figure 3.10: AFM [(a),(c),(e)] and corresponding MFM [(b),(d),(f)] measurements on a sample with stack *CoFe-Xray* and a magnetic grating produced by IBMP. The measurements have been carried out in remanence after the sample has been saturated in the a magnetic field  $H_{sat}$  pointing in the directions indicated by the red arrows. The color code for the AFM measurements is shown at the bottom of the figure. The maximum height  $x$  was 10 nm for part (a) and 15 nm for part (c) and (e). On the sample remained some resist rests at the boundaries of the bombarded lines indicating the bombarded lines in the AFM image. The white and black arrows point to the strayfield signature of the boundaries of the bombarded lines. The scan direction has been turned by  $10^\circ$  during the measurement e/f relative to the other measurements.

## 3.2 Thermal stability of magnetic patterns produced by ion bombardment induced magnetic patterning of pinned ferromagnetic layers

The examples on the last pages show that one can locally manipulate the exchange bias interaction resulting for small external fields in a corresponding arrangement of the magnetization of the pinned FM.

In giant magnetoresistance (GMR, Ref. [30]) or tunnel magnetoresistance (TMR, [167]) based devices the AF/FM-bilayer acts as a magnetic reference layer where it is important that the FM magnetization is stable. This stability should not be reduced by the application of the lateral magnetic patterning. For an application in a hot environment as, e.g., in the automotive industry, temperature stability can be a limiting factor. It is known, that the exchange bias vanishes above the blocking temperature  $T_B$  [38] limiting the thermal stability of every EB coupled layer system to this temperature.

Here, alternating gradient magnetometer (AGM) and x-ray photoemission electron microscopy (PEEM) measurements are presented which show how and at which temperature a magnetic pattern produced by ion bombardment on a typical reference electrode of a magnetic tunnel junction (MTJ) is changed by successive heating.

### 3.2.1 Experiment

Three kinds of magnetic layer systems were prepared for the tests of the thermal stability. The layer stack  $CoFe_{TS}^{PEEM3nm}$  is Cu 30 nm / Ir<sub>17</sub>Mn<sub>83</sub> 15 nm / Co<sub>70</sub>Fe<sub>30</sub> 3 nm / Al 1.4 nm +100s electron cyclotron resonance (ECR) plasma oxidation with -10 V bias voltage [168], and corresponds to the lower part of a typical MTJ [169]. The Cu layer is the lower conduction line. The CoFe layer (FM), which is pinned by the adjacent IrMn (AF), is used as the reference electrode of the MTJ. In this experiment the 1.8 nm thick Al-oxide tunnel barrier serves as an oxidation preventing capping layer.

Similar samples with a thicker CoFe layer ( Cu 30 nm / Ir<sub>17</sub>Mn<sub>83</sub> 15 nm / Co<sub>70</sub>Fe<sub>30</sub> 5 nm / Al 1.4 nm +ox.) are denoted as  $CoFe_{TS}^{PEEM5nm}$ .

Sample of type  $Co_{TS}^{PEEM}$  have a similar stack with the ferromagnet Co and an additional NiFe seed layer: Cu 30 nm / Ni<sub>80</sub>Fe<sub>20</sub> 1.9 nm / Ir<sub>17</sub>Mn<sub>83</sub> 25 nm / Co 3 nm / Al 1.4 nm +100s oxidation.

The detailed preparation of these samples for the various experiments is described in the following sections.

### 3.2.2 Alternating gradient magnetometer investigations on homogeneously bombarded samples

#### Experiment

Samples of type  $CoFe_{TS}^{PEEM3nm}$  and  $Co_{TS}^{PEEM}$  have been homogeneously bombarded and investigated by AGM measurements at several elevated temperatures.

Parts of two samples with stack  $CoFe_{TS}^{PEEM3nm}$  have been only annealed (1 h at 275°C)

---

<sup>2</sup>Parts of this chapter have been published in [166]

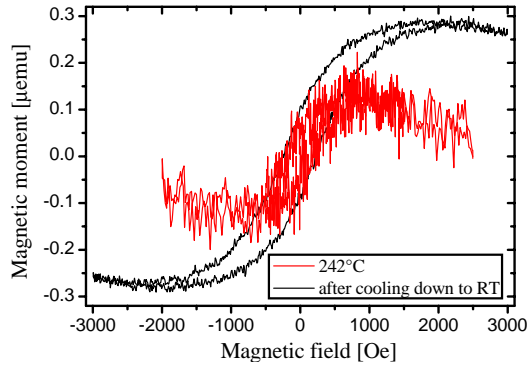


Figure 3.11: AGM measurement of sample holder without mounted sample at 242°C (after a sample has lost contact) and after cooling down to room temperature.

in an external magnetic field of  $H_{FC}=1.5$  kOe while another part of a sample of this kind has been annealed in the same way and additionally bombarded with  $1 \times 10^{14}$  ions/cm<sup>2</sup> in a magnetic field of  $H_{IB}=1000$  Oe antiparallel to  $H_{FC}$ . One part of the sample with stack  $Co_{TS}^{PEEM}$  has been annealed while another part has been bombarded with  $1 \times 10^{14}$  ions/cm<sup>2</sup> without an annealing step prior to the IB. The temperature dependence of the exchange bias for samples with stack  $CoFe_{TS}^{PEEM3nm}$  and  $Co_{TS}^{PEEM}$  has been investigated by AGM measurements.

To heat the samples while mounted in the AGM, hot He gas has been used. The measurements have been started some minutes after the temperature has been reached to allow the sample to adapt to the He temperature. The nominal temperature of the He is stated on the following pages. The absolute temperature of the sample might vary from this value by a few degree Celsius. The high temperature measurements in the AGM require the use of a special sample holder where the sample is fixed by a cement glue.<sup>3</sup> This cement glue turned out to produce a ferromagnetic signal itself after a sample has lost contact<sup>4</sup> (Fig. 3.11). This additional contribution has to be taken into account when interpreting the AGM measurements shown in this subsection but it has no influence on the possibility to investigate the temperature dependence of the exchange bias with these samples.

## Results and discussion

Figure 3.12 shows AGM measurements of a sample with stack  $CoFe_{TS}^{PEEM3nm}$  which has not been bombarded. At the measurement prior to heating (black line) the signature of the sample holder clearly can be seen at small magnetic fields. At the highest investigated temperature for this sample of 243°C the signature of the sample holder/FM particles is significantly smaller as it can be expected from Fig. 3.11. At this temperature the exchange bias has vanished. After cooling the sample

<sup>3</sup>On the sample holder used for all other AGM measurements shown in this work silicon grease has been used to fix the sample at the holder.

<sup>4</sup>The magnetic moment might be due to the cement itself or due to ferromagnetic particles which might have stuck under the sample because of the sample handling. An even larger magnetic moment of a few  $\mu$ emu can, e.g., be produced when the sample is handled with a nominally nonmagnetic metal tweezer.

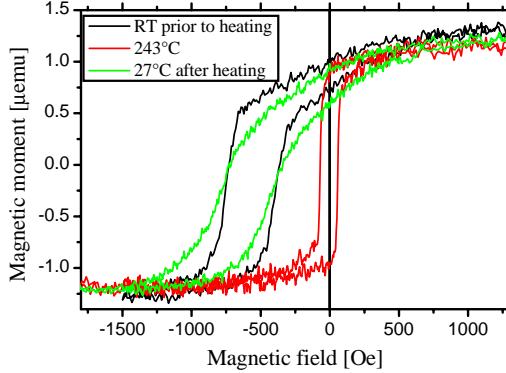


Figure 3.12: AGM measurements of a sample with stack  $CoFe_{TS}^{PEEM3nm}$  without ion bombardment at room temperature prior to heating, at  $243^{\circ}C$ , and at  $27^{\circ}C$  after cooling down.

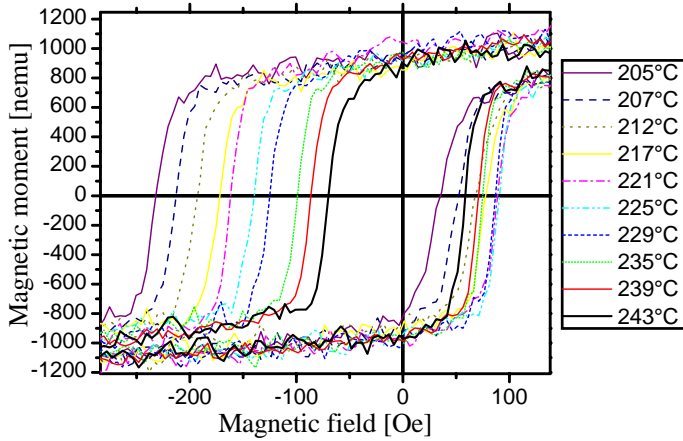


Figure 3.13: Selected AGM measurements of a sample with stack  $CoFe_{TS}^{PEEM3nm}$  without ion bombardment at temperatures in the range of  $205^{\circ}C$  to  $243^{\circ}C$ .

down to  $27^{\circ}C$  the old value of the EB has been restored. This can be explained by the fact that although some measurements have been carried out during the cooling process, the CoFe layer had a constant magnetization direction on the whole sample during the much longer time between the measurements.<sup>5</sup> Therefore, although the magnetic field was not present through the cooling process, effectively the sample has been field cooled. The altered shape of the hysteresis loop might be attributed to the details of this “*nearly field cooling*”.

To determine the detailed temperature dependence measurements at several temperatures have been carried out. Figure 3.13 shows selected measurements at this sample near the blocking temperature. The temperature dependence of the exchange bias resulting from this measurements is shown in Fig. 3.14 (a)/(b) by red diamonds.

It can be seen that the blocking temperature of sample  $CoFe_{TS}^{PEEM3nm}$  without IB is roughly in the range of  $250^{\circ}C$ . The experiment without ion bombardment has been reproduced with a second sample with an identical stack [blue circles in Fig. 3.14 (a)/(b)]. The temperature dependence during the heating fits good to the results obtained with the first sample.

<sup>5</sup>At the end of each AGM measurement the sample was saturated in the same direction. Because the temperature was significantly smaller than the Curie temperature of the FM layer and a significant remanence magnetization can be observed in this temperature range (compare Fig. 3.12), a roughly homogeneous alignment of the magnetization on the whole sample during the time between the measurements can be expected.



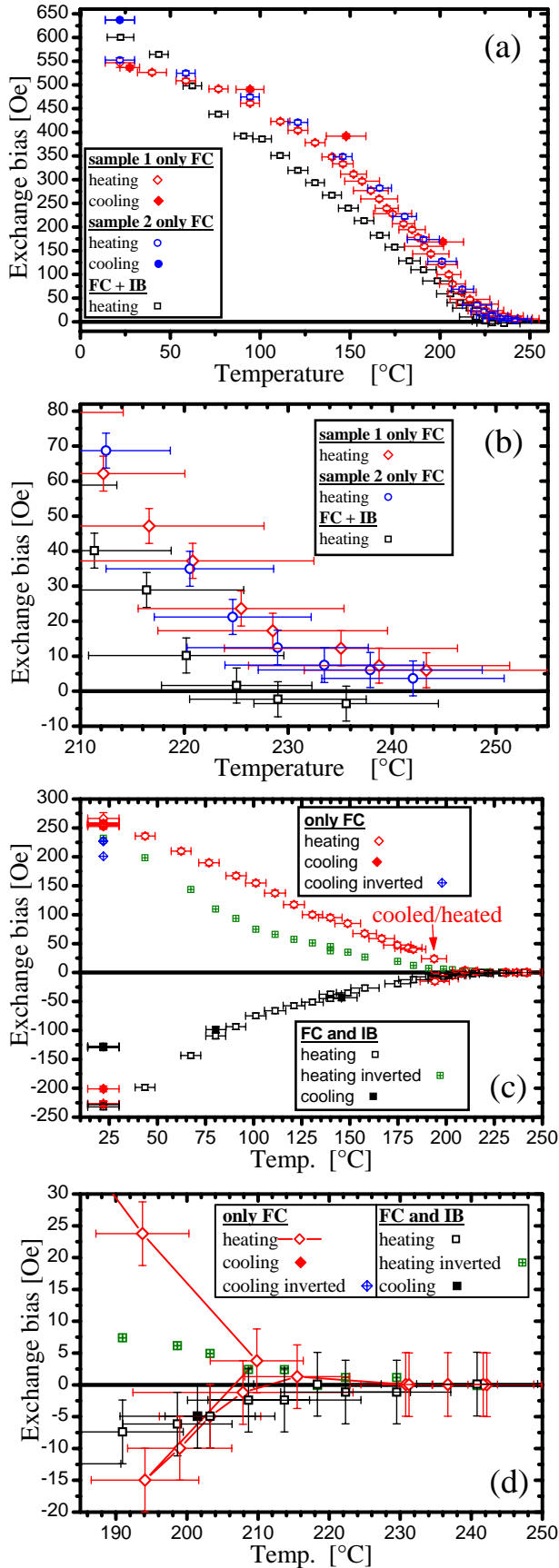


Figure 3.14: (a)/(b) Temperature dependence of EB for samples with stack  $CoFe^{PEEM3nm}$  with (black squares) and without (red diamonds and blue circles) IB. “Sample 1” (red diamonds) and “sample 2” (blue circles) are two identically treated samples. (b) shows an enlarged part of (a). (c)/(d) Temperature dependence of EB for samples with stack  $Co^{PEEM}_{TS}$  with (squares) and without (diamonds) IB. The red line in (d) connects measurements carried out while heating the not bombarded sample in a chronological order. Inverted measurements after cooling down on the sample without IB (blue diamond with cross) and during heating of the sample with IB (green square) have been added. (d) shows an enlarged part of (c). Values obtained while the temperature was increased (decreased) are symbolized by open (solid) symbols in all graphs.

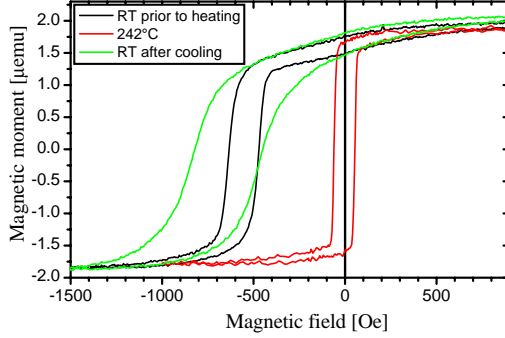


Figure 3.15: AGM measurements of a second sample with stack  $CoFe_{TS}^{PEEM3nm}$  without ion bombardment at room temperature prior to heating, at  $242^{\circ}C$ , and at  $22^{\circ}C$  after cooling down.

The EB after cooling down was even larger for the second sample compared to the measurements before heating (Fig. 3.15). This might be due to the longer time at an elevated temperature during the experiment compared to the field cooling.

The dependence of the EB on the time has been demonstrated in Ref. [170] for field grown NiO/NiFe bilayers. In these experiments the EB has been enlarged during the first 100 hours after deposition following a  $\ln(\text{time})$  law. This effect has been observed even at room temperature, but it was significantly stronger when the sample has been stored at elevated temperatures. Furthermore, it has been demonstrated that it is even at room temperature possible to turn the EB direction when the sample is kept directly after field growth for several hours saturated in a magnetic field antiparallel to  $\mathbf{H}_{\text{grow}}$ . This observations fit to the model of Fulcomer and Charap [44, 50], as in dependence of the temperature more or less grains can cross the barrier and change from the local minimum to the global minimum. When the sample is saturated in a magnetic field antiparallel to  $\mathbf{H}_{\text{grow}}$ , the local and global minima are interchanged. Now, the AF grains change from the new local (old global) minimum to the new global (old local) minimum and in total the EB direction changes. A similar process can be assumed for a sample kept with a defined direction of the magnetization for a longer time at an elevated temperature in the AGM.

The temperature dependence of the EB at low temperatures is larger for the bombarded sample compared to the not bombarded one. At higher temperatures close to the blocking temperature the difference between the EB values on the samples with and without IB is rather small when the accuracy of the measurement is taken into account [Fig. 3.14 (b)].

A similar relation of the temperature dependences can be observed for the bombarded and the not bombarded parts of sample  $Co_{TS}^{PEEM}$  [Fig. 3.14 (c)/(d)]. Up to about  $100^{\circ}C$  the temperature dependence of the EB on the bombarded sample is larger and for higher temperatures it is smaller than for the not bombarded sample [Fig. 3.14 (c)].

The change of the EB direction measured at the not bombarded sample at about  $200^{\circ}C$  is due to the fact that the sample has cooled down to about  $194^{\circ}C$  after the measurement at  $210^{\circ}C$  during an interruption of the measurement. This reduction of the temperature had the effect of a “*nearly field cooling*” as described above. The direction of the EB is defined by the the last saturation of the FM layer before the reduction of the temperature.

The EB of the bombarded and the not bombarded sample at temperatures above  $210^{\circ}C$  is nearly identical. The blocking temperature is independent of the bombard-

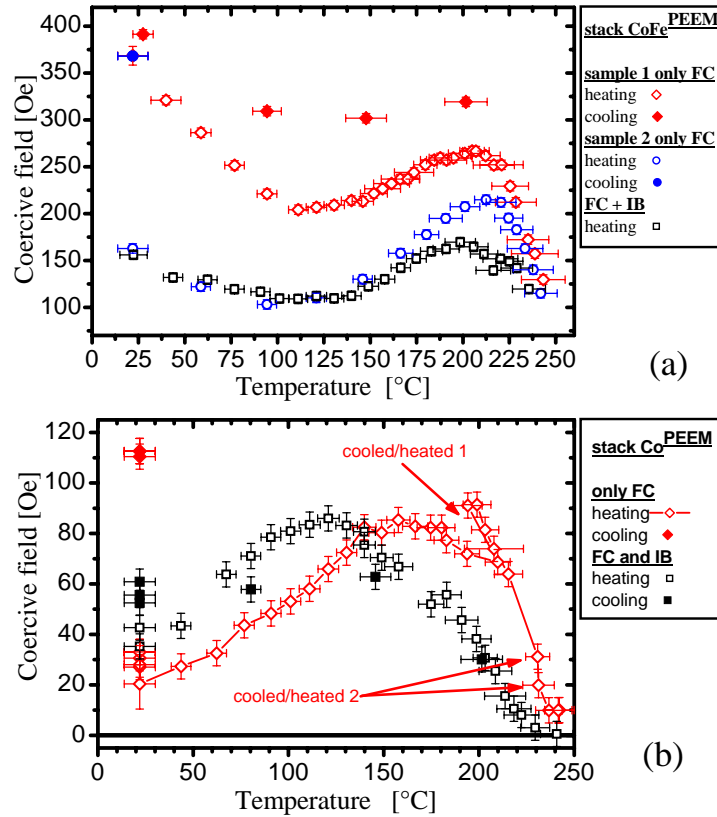


Figure 3.16: Temperature dependence of the coercive field of samples with stack  $CoFe_{TS}^{PEEM3nm}$  (a) and  $Co_{TS}^{PEEM}$  (b).

ment roughly 220°C.

Due to the small magnetic moment of the samples, the error is large relative to the measured magnetic signal. Therefore, a reasonable statement about the details of the temperature dependence of the magnetic moment can not be given. The observed changes were smaller than 20%.

The temperature dependence of the coercivity for both kinds of samples is shown in Fig. 3.16. The characteristic maximum has been observed for other systems as well (Fig. 3.17, Ref. [38] and references therein). To explain this effect one has to look at the anisotropy of the antiferromagnetic material [38]. When the magnetization of the ferromagnetic layer rotates and the anisotropy of the AF layer is small, the FM layer can drag AF spins. This results in an enlarged coercivity. In contrast to this, when the AF anisotropy is large enough to keep the direction of the AF spins fixed, the coercivity is smaller. When the anisotropy is decreased at elevated temperatures close to the blocking temperature, more AF spins can be dragged by the FM layer and the coercivity of the FM layer increases. On the other hand it is easier to turn the spins at higher temperatures resulting at a decreasing coercivity when the temperature approaches the blocking temperature.

A detailed discussion about the differences between the temperature dependence of the coercivity for the bombarded and the not bombarded sample does not appear

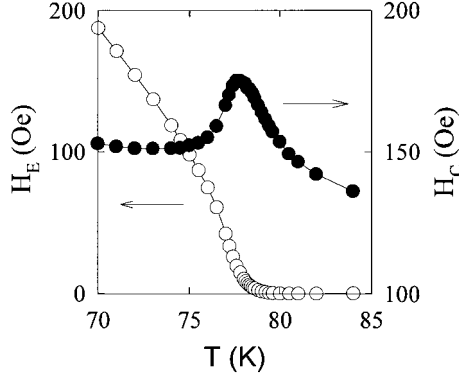


Figure 3.17: Exchange bias (open circles) and coercivity (solid circles) versus temperature for an  $\text{FeF}_2/\text{Fe}$  bilayer after field cooling. (from [38])

reasonable, because the difference between the two not bombarded samples with stack  $\text{CoFe}_{\text{TS}}^{\text{PEEM3nm}}$  is larger than the difference between the bombarded and the not bombarded sample [Fig. 3.16 (a)].

Furthermore, a modification of the samples can be observed. The coercivity measured after the heating experiment was for all samples in Fig. 3.16 significantly larger compared to the measurements carried out prior to the experiment. But it is unlikely that the main reason for this phenomenon can be found in diffusion processes although they can not be ruled out totally.

The cooling to about  $194^\circ\text{C}$  after the measurement at  $210^\circ\text{C}$  carried out at sample  $\text{Co}_{\text{TS}}^{\text{PEEM}}$  without IB (marked as *cooled/heated 1* in Fig. 3.16 (b), compare change of EB direction in Fig. 3.14) results in a strongly enhanced coercivity. But if this originated from a permanently altered sample, e.g., due to diffusion the coercivity should stay larger during the subsequent heating to higher temperatures compared to earlier measurements at the same temperature. A comparison of measurements in the range of  $208^\circ\text{C}$  to  $215^\circ\text{C}$  does not show this permanently enlarged  $H_C$ . Furthermore, this sample has been cooled down to room temperature (RT) after the first measurement ( $H_C=31$  Oe) at  $231^\circ\text{C}$  (*cooled/heated 2*). The coercivity of 19 Oe measured several hours later after the sample has been heated to  $231^\circ\text{C}$  again was even smaller than before. Therefore, the origin of the enlarged coercivity might be connected to the magnetic configuration (e.g., additional  $360^\circ$  walls) of the sample which is changed when the sample is heated and the domain pattern which developed at high temperatures is frozen during the cooling process.

This might also be the reason for the large difference of the two not bombarded samples with stack  $\text{CoFe}_{\text{TS}}^{\text{PEEM3nm}}$  as they have a very similar coercivity after the heating experiments [Fig. 3.16 (a)].

In summary, although the shape of the EB versus temperature graph is altered, no change of the blocking temperature due to the IB has been found. In the following sections the results of this temperature dependence of the EB coupling on the real magnetic pattern at elevated temperatures will be investigated.

### 3.2.3 X-ray photoemission electron microscopy investigations on only magnetically patterned samples

#### Experiment

Samples of type  $CoFe_{TS}^{PEEM3nm}$  and  $Co_{TS}^{PEEM}$  have been magnetically patterned without changing the sample topography.

The magnetically patterned part of sample  $CoFe_{TS}^{PEEM3nm}$  was annealed for 1 h at 275°C in an external magnetic field of  $H_{FC}=1.5$  kOe. No FC was carried out for the magnetically patterned sample with stack  $Co_{TS}^{PEEM}$ .

To define the area which was bombarded by ions, the samples were spin coated with an approximately 500 nm thick electron beam resist layer (four layers of PMMA, compare chapter 2.2.2). Then the resist was patterned by electron beam lithography.

On sample  $CoFe_{TS}^{PEEM3nm}$  amongst others a  $10.4\mu m \times 10.4\mu m$  large checkered pattern was produced.  $1.2\mu m \times 1.2\mu m$  large bombarded squares were arranged with a center to center distance of  $2\mu m$  resulting in  $0.8\mu m \times 0.8\mu m$  large quadratic not bombarded areas in between the bombarded squares. The edges of the squares have been oriented parallel/perpendicular to  $\mathbf{H}_{FC}$ . On sample  $Co_{TS}^{PEEM}$  as well as on sample  $CoFe_{TS}^{PEEM3nm}$   $1.6\mu m$  wide lines with a periodicity of  $5\mu m$  were patterned.

The samples were bombarded through the resist mask with He ions with an energy of  $E_{IB}=10$  keV and an ion dose of  $1 \times 10^{14}$  ions/cm<sup>2</sup>. The external magnetic field applied during IB was  $H_{IB}=1$  kOe for all samples. In the case of sample  $CoFe_{TS}^{PEEM3nm}$ ,  $\mathbf{H}_{IB}$  was oriented antiparallel to  $\mathbf{H}_{FC}$  while it was aligned parallel to the patterned lines during the bombardment of stack  $Co_{TS}^{PEEM}$ .

After IB, the resist mask was removed and the resulting magnetic pattern were investigated at room temperature by magneto-optical Kerr-effect magnetometry (MOKE).

PEEM measurements were carried out while heating the samples in situ at the PEEM-2 at beamline 7.3.1.1 at the Advanced Light Source, Berkeley, CA [139]. For the only magnetically patterned sample with stack  $CoFe_{TS}^{PEEM3nm}$  measurements were done while heating the sample from room temperature to 394°C. Sample  $Co_{TS}^{PEEM}$  was investigated while heating it up to 292°C and cooling it down to 75°C. All measurements were carried out in remanence with elliptically polarized x-rays with a degree of polarization of 75%. To visualize the domain pattern of the FM, the XMCD effect [144] was utilized. Therefore, at every investigated temperature PEEM images were taken at the Co L<sub>3</sub> edge and at the Co L<sub>2</sub> edge (Fig. 3.18). The ratio of the two images was calculated to gain information of the magnetic domains (compare Fig. 3.19). In the rest of this chapter the expression *PEEM image* always denotes this kind of processed image.

Magnetic force microscopy measurements at RT were carried out with another identically patterned part of sample  $CoFe_{TS}^{PEEM3nm}$  which has not been used for the PEEM heating experiment before.

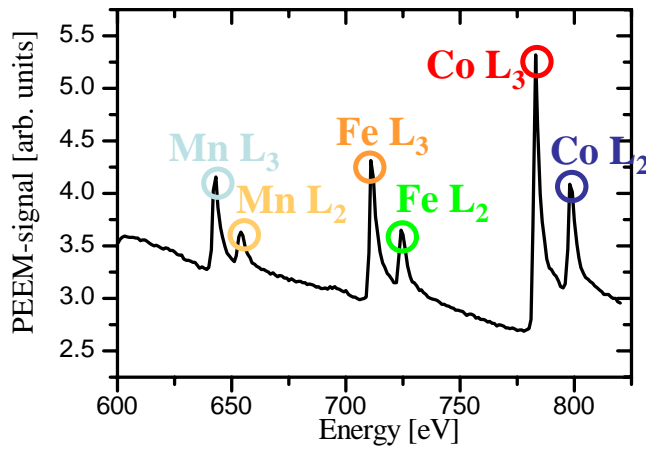


Figure 3.18: PEEM signal in dependence of the photon energy obtained by local spectroscopy on a sample with stack  $CoFe_{TS}^{PEEM3nm}$ .

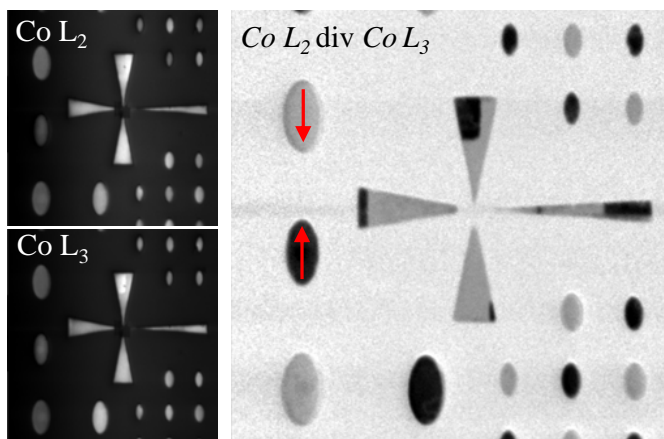


Figure 3.19: PEEM images of elliptic and triangular ferromagnetic structures with local magnetic patterning measured at the Co  $L_2$  and  $L_3$  white lines and the result of the division of both images showing the magnetic contrast due to the rotation of the EB direction by  $180^\circ$  at every second elliptic element.

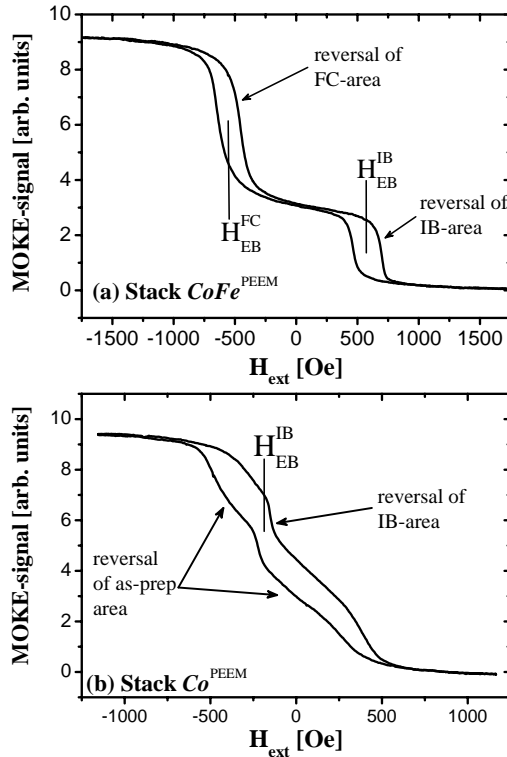


Figure 3.20: MOKE measurements at room temperature on the magnetically patterned areas of stack  $CoFe_{TS}^{PEEM3nm}$  (a) and stack  $Co_{TS}^{PEEM}$  (b) after IB.  $H_{EB}^{FC}$  is the EB field measured for the not bombarded but field cooled areas and  $H_{EB}^{IB}$  is the EB field measured in the bombarded areas.

## Results and discussion

The results of the MOKE-measurements on the magnetic pattern of stack  $CoFe_{TS}^{PEEM3nm}$  after IB can be seen in Fig. 3.20(a). The external field  $\mathbf{H}_{ext}$  during the measurement was aligned parallel to the axis defined by  $\mathbf{H}_{IB}/\mathbf{H}_{FC}$ . Because the diameter of the analyzed area on the sample of approx. 0.2 mm was larger than the single magnetic structures, a superposition of the signals originating from the bombarded and the not bombarded areas was obtained. The exchange bias field measured at the bombarded area of  $H_{EB}^{IB} = 570$  Oe has approximately the same absolute value as the one measured in the field cooled area ( $H_{EB}^{FC} = -550$  Oe) but is of the opposite sign. These values are comparable to other results obtained for the combination IrMn/CoFe in MTJs (compare, e.g., Tab. 3.4 or [169]).

Figure 3.20(b) shows a magnetization loop measured by MOKE on a magnetically patterned area of sample  $Co_{TS}^{PEEM}$ .  $\mathbf{H}_{ext}$  was aligned parallel to the axis defined by  $\mathbf{H}_{IB}$ . The curve shows again a superposition of the signals originating from the bombarded and the not bombarded area. The exchange bias field measured at the bombarded area is  $H_{EB}^{IB} = 190$  Oe. This value also is comparable to former results [171]. The shape of the signal of the as-prepared part can be explained by a local pinning of the Co to the IrMn with randomly distributed directions of the easy axis.

Figure 3.21 shows selected PEEM images of sample  $CoFe_{TS}^{PEEM3nm}$ . It can be seen in Fig. 3.21 (a) (RT) that domains with the magnetization oriented parallel to  $\mathbf{H}_{FC}$  appear bright while the bombarded domains with an opposite direction of the magnetization appear dark in the processed PEEM images. The rounded edges originate from a corresponding shape of the resist mask. Temperatures up to 180°C do not induce a considerable change of the magnetic pattern [Fig. 3.21(b)]. The

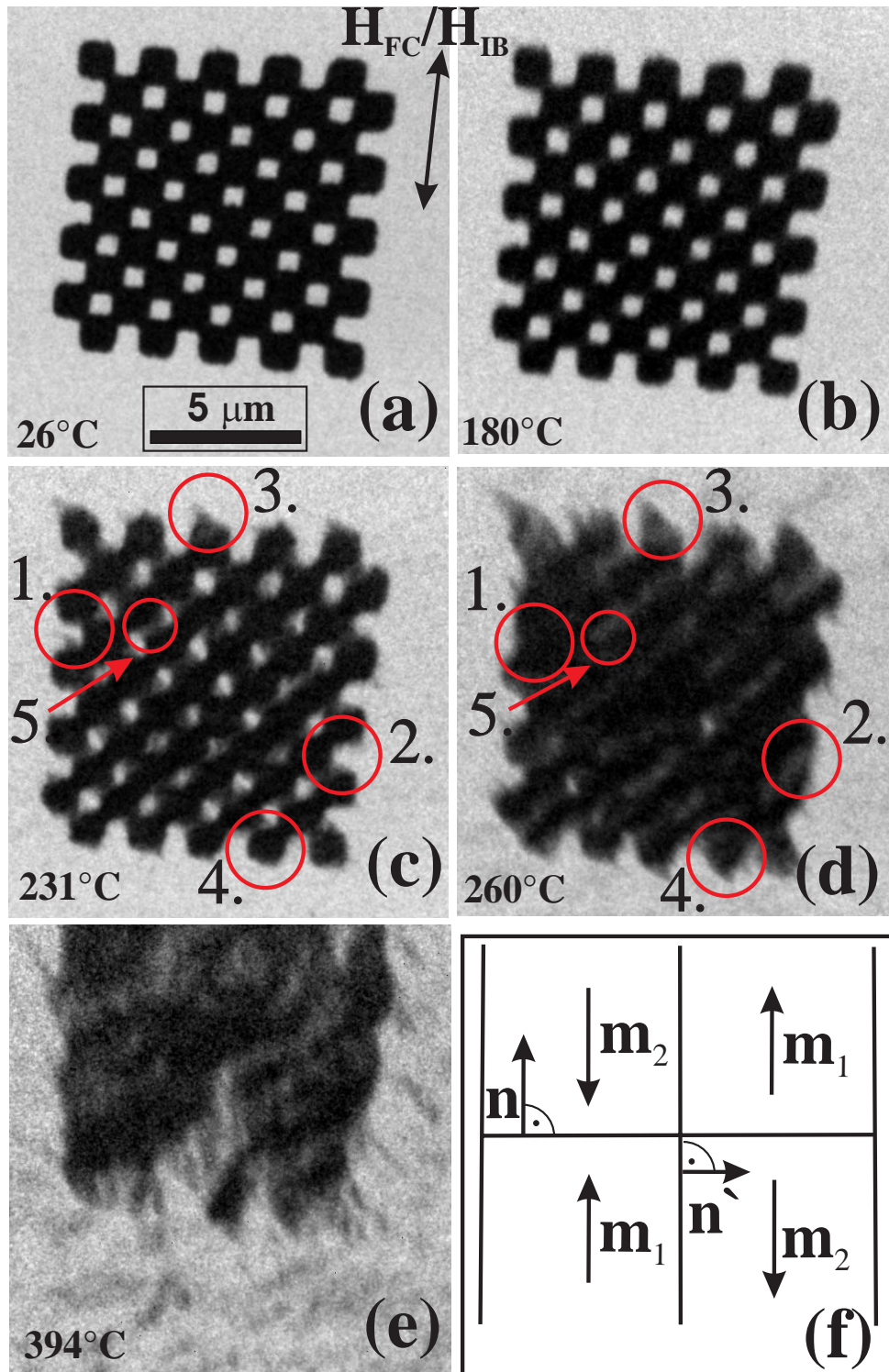


Figure 3.21: PEEM measurements of stack  $CoFe_{TS}^{PEEM3nm}$  ( $H_{IB} \uparrow \downarrow H_{FC}$ , magnetization  $\uparrow \uparrow H_{IB}$ : dark, magnetization  $\uparrow \uparrow H_{FC}$ : bright) at (a) 26°C, (b) 180°C, (c) 231°C, (d) 260°C, and (e) 394°C; (f) FM areas with different magnetization direction  $\mathbf{m}$ . The shift of the domain pattern to the upper part of the image is due to a thermal elongation of the sample holder.



blocking temperature at which the exchange bias coupling vanishes after a strong decrease over a wide temperature range was determined by AGM measurements to be in the range of 220°C to 250°C for other samples with the same layer stack (Fig. 3.14). The other energy terms contributing to the total free energy do not vanish at this temperature: in Ref. [172] a temperature dependence of the exchange stiffness energy proportional to the cube of the saturation magnetization ( $J_S(T)^3$ ) was found for FePd while a proportionality to  $J_S(T)^2$  is supposed in Ref. [173]. The strayfield energy follows  $J_S(T)^2$  [174]. AGM measurements at other samples with this layer stack have in all cases shown a decrease of the saturation magnetization  $J_S(T)$  between RT and  $T_B$  of less than 20%. In summary, one can see that while reaching the blocking temperature the influence of the latter two energy contributions grows relatively to the exchange bias coupling and, therefore, a degradation of the magnetic pattern in this temperature range and above can be observed. All samples were sputtered without an external field. Therefore, it can be expected that the FM layer does not show a macroscopic anisotropy.

Figure 3.21 (c) shows a PEEM measurement at 231°C where a change in the domain pattern easily can be seen. Between 180°C and 231°C bright domains begin to grow gradually into the dark ones and vice versa [Fig. 3.21 (c)]. One striking effect is that the prolate dark domains growing into the not bombarded area around the magnetic pattern only can be observed at those edges where the magnetization direction of the dark and the bright domains are oriented head to head (see, e.g., circles 1–3). This behavior can be seen even better at the measurement shown in Fig. 3.21 (d) (260°C). The indentations at the sides vanish (e.g. Fig. 3.21 (d), circles 1,2) and the domain walls which were oriented perpendicular to  $\mathbf{H}_{FC}/\mathbf{H}_{IB}$  after IB (head to head orientation of the magnetization) switch to a diagonal or frayed pattern (circles 3–5). In contrast to this the corners parallel to  $\mathbf{H}_{FC}/\mathbf{H}_{IB}$  on the outer sides of the magnetic pattern remain unchanged (circles 1, 2). This can be explained by the influence of strayfields resulting from interfacial magnetic charges with a reduced interface charge density of  $\sigma = (\mathbf{m}_1 - \mathbf{m}_2) \cdot \mathbf{n}$  [Ref. [174], reduced magnetization vector  $\mathbf{m}(\mathbf{r}) = \mathbf{J}(\mathbf{r})/J_S$  with  $\mathbf{J}$  = magnetization vector and  $J_S$  = saturation magnetization,  $\mathbf{n}$ : vector normal to pattern boundary, see Fig. 3.21 (f)]. At the domain walls with a head to head orientation of the magnetization, the vector  $(\mathbf{m}_1 - \mathbf{m}_2)$  is aligned parallel to the normal vector  $\mathbf{n}$  resulting in a maximum interface charge density while at the domain walls parallel to  $\mathbf{H}_{FC}/\mathbf{H}_{IB}$   $(\mathbf{m}_1 - \mathbf{m}_2)$  is oriented perpendicular to  $\mathbf{n}$ . Therefore, no magnetic charges occur in the latter case.

The magnetic force microscopy measurement of bombarded lines on another field cooled part of the same sample  $CoFe_{TS}^{PEEM3nm}$  which is shown in Fig. 3.22 confirms these considerations.  $\mathbf{H}_{IB}$  was oriented parallel to the lines and antiparallel to  $\mathbf{H}_{FC}$ . Therefore, the relative orientation of the magnetization at the end of the bombarded lines is head to head to the magnetization of the surrounding area. As expected this area shows the largest strayfield. According to the energy minimization principle it can be expected that the energetically unfavorable "head to head" domain walls in the heated sample will be altered at high temperatures when their existence is not enforced any longer by the exchange bias interaction. Furthermore a temperature induced nucleation of dark domains can be seen in the not bombarded (bright) area at the temperature of 260°C [Fig. 3.21 (d)]. They gain in size during the further

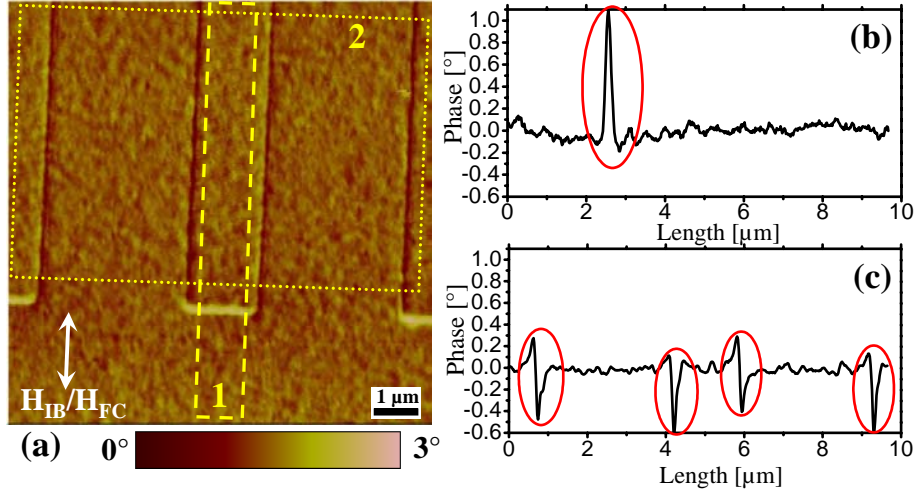


Figure 3.22: (a) MFM measurement of a second structure on stack  $CoFe_{TS}^{PEEM3nm}$  (bombarded lines,  $\mathbf{H}_{IB} \uparrow \downarrow \mathbf{H}_{FC}$ ), (b) line scan parallel to lines (averaged over area 1 indicated by dashed box in MFM image; head to head orientation of magnetization: large interface charge density), (c) line scan perpendicular to lines (averaged over area 2 indicated by dotted box in MFM image; low interface charge density); The ellipses in (b) and (c) mark the domain walls between bombarded and not bombarded areas. Different offsets have been applied to the line scans and the MFM image.

heating up to the maximum investigated temperature of  $394^{\circ}\text{C}$  [Fig 3.21(e)]. Even about  $160^{\circ}\text{C}$  above the blocking temperature the bombarded area is still visible by a darker average color in the PEEM image. This is due to an exchange length smaller than the size of the magnetic pattern. Note that the  $0.8\ \mu\text{m} \times 0.8\ \mu\text{m}$  large bright domains in the inner part of the magnetic pattern disappeared.

The magnetic structure of the sample with stack  $Co_{TS}^{PEEM}$  at RT with a uniform magnetization at the bombarded lines (bright) and small domains in the as-prepared area can be seen at the PEEM image in Fig. 3.23 (a). At a temperature of  $116^{\circ}\text{C}$  independent of the IB a thermally activated domain growth starts. This can be seen by comparing the marked area of the zoomed PEEM-image measured on a not bombarded part of the sample at  $111^{\circ}\text{C}$  [Fig. 3.23 (b)] with the image of the same area taken at  $116^{\circ}\text{C}$  [Fig. 3.23 (c)] where the dark domain has grown into the bright one. A growth of bright domains into dark ones can be observed as well (not shown). For rising temperatures the growth of the small domains in the as-prepared area continues [Fig. 3.23 (d)]. For  $T \geq 152^{\circ}\text{C}$  dark domains partly grow into the bombarded area, until at  $244^{\circ}\text{C}$  [Fig. 3.23 (e)] and for higher temperatures (not shown) no trace of the bombarded lines can be found. The same considerations about energy minimization as used for stack  $CoFe_{TS}^{PEEM3nm}$  can be applied here. The disappearance of the lines is due to the smaller size of the thin lines compared to the compact checkered pattern on sample  $CoFe_{TS}^{PEEM3nm}$ . After cooling the sample to  $76^{\circ}\text{C}$  the domain state is frozen. No specific features as, e.g., different domain sizes due to a change of the microstructure of the sample can be seen in the domain state of the bombarded area in comparison to the not bombarded area after the heating

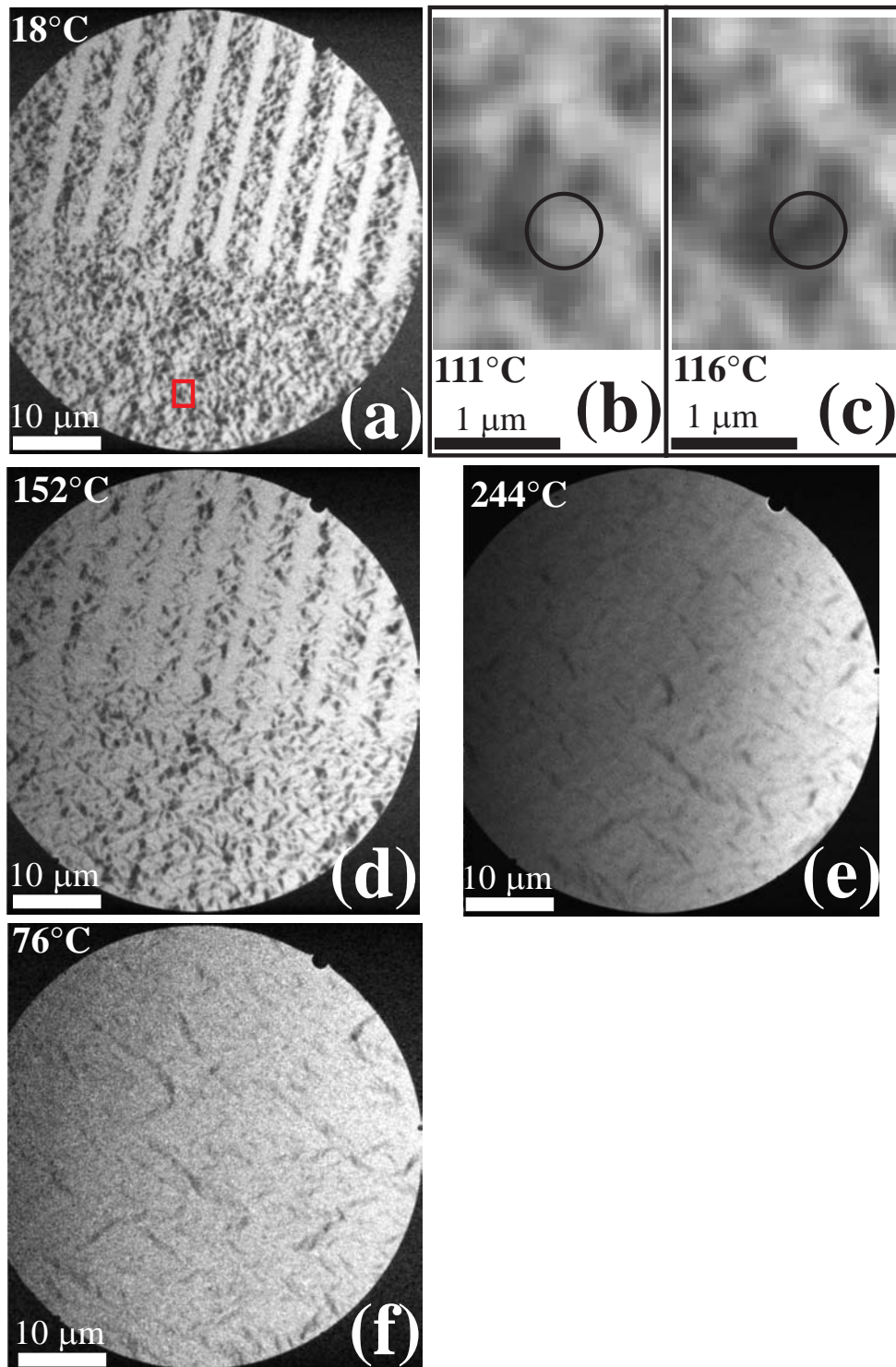


Figure 3.23: PEEM measurements of stack  $Co_{TS}^{PEEM}$  (no FC,  $\mathbf{H}_{IB} \uparrow$  to bombarded lines) while heating at (a) 18°C, (b) 111°C [area shown in part (b) and (c) indicated by red box in (a)], (c) 116°C, (d) 152°C, and (e) 244°C and (f) after cooling to 76°C. The shift of the lines is due to a thermal elongation of the sample holder.

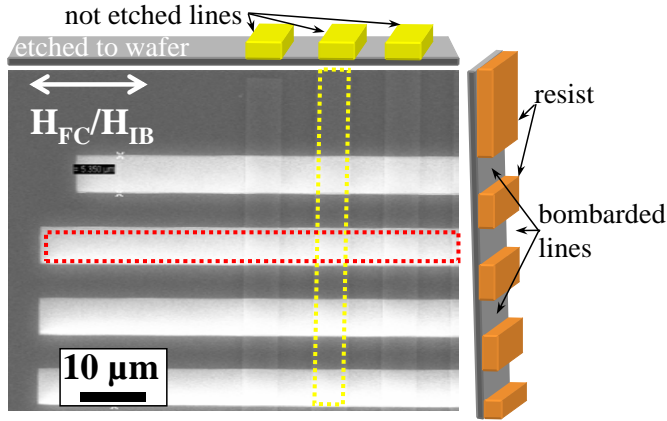


Figure 3.24: SEM image of a resist mask on a topographically and magnetically patterned sample with stack  $CoFe_{TS}^{PEEM5nm}$  after IB (bombarbed lines without resist capping: e.g., red rectangle; topographic grating with not etched topographic lines: e.g., yellow rectangle).

and cooling process. Therefore, no hint for a permanent change of the properties of the bombarbed areas by the applied ion bombardment has been found.

### 3.2.4 X-ray photoemission electron microscopy investigations on crossed topographic and magnetic gratings

#### Experiment

Samples with stack  $CoFe_{TS}^{PEEM5nm}$  have been patterned topographically as well as magnetically with lines. The samples have been annealed for 1 h at  $275^{\circ}C$  in a magnetic field  $H_{FC}$  of 1500 Oe to initialize the EB homogeneously on the whole sample. Afterwards, resist covered lines with a varying width in the range from about 100 nm to about  $5 \mu m$  have been defined by electron beam lithography. The sputtered layers on the surrounding area have been removed by ion beam etching. After the etching the resist has been removed. On the topographically patterned sample a resist mask (PMMA) with lines of varying width analogous to the etched topographic lines has been fabricated (Fig. 3.24). The lines of this resist mask are oriented perpendicular to the topographic lines. The EB direction on these lines has been turned by  $180^{\circ}$  by ion bombardment ( $E_{IB}=10 \text{ keV}$ ,  $1 \times 10^{14} \text{ ions/cm}^2$ ) in a magnetic field (1000 Oe) antiparallel to  $H_{FC}$  through the resist mask.

#### Results and discussion

The crossed topographic and magnetic gratings on samples with stack  $CoFe_{TS}^{PEEM5nm}$  result in various different rectangular regions with a predominantly homogeneous magnetization direction in remanence (Fig. 3.25). A wide range of areal sizes and ratios of the length of edges with opposite orientation of the magnetization and edges between the layer stack and the etched area is obtained.

The bright and dark contrast in Fig. 3.25 symbolize an opposite direction of the magnetization in the bombarbed and the not bombarbed areas. The bright lines in the not bombarbed areas are due to  $360^{\circ}$  walls. The fact that the  $360^{\circ}$  walls can only be observed in the not bombarbed area is due to the direction of the last saturation during the last measurement. This magnetic field was oriented parallel to the direction of the magnetization of the bombarbed field in remanence. Therefore,

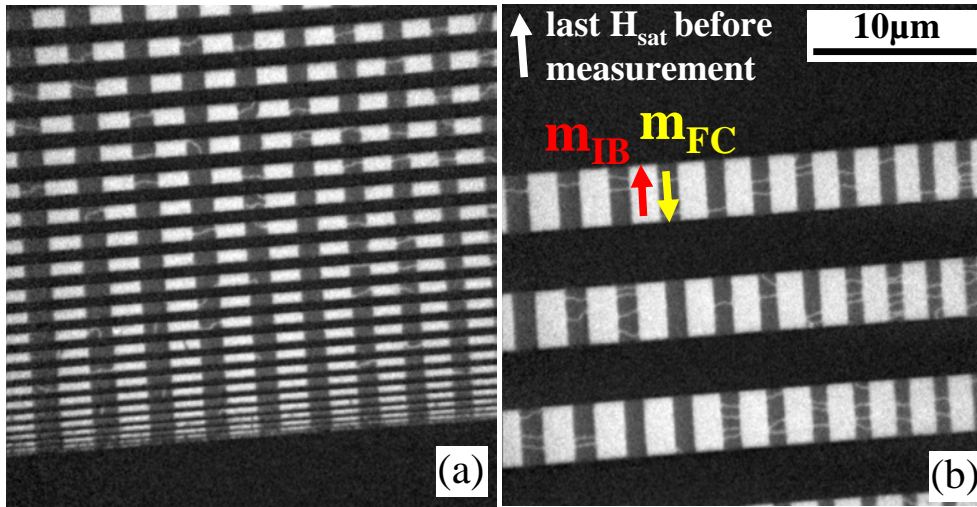


Figure 3.25: PEEM images of crossed topographic and magnetic gratings on a sample with stack  $CoFe_{TS}^{PEEM5nm}$ . These images have been obtained at room temperature prior to the heating experiments.

$360^\circ$  walls have been removed when the sample was saturated and since this time the magnetization of the bombarded area did not turn its direction what would enable the formation of new  $360^\circ$  walls. In contrast to this, the magnetization of the not bombarded areas has turned its direction when the external magnetic field was decreased after the measurements, enabling the creation of  $360^\circ$  walls during this process.

Some selected PEEM measurements obtained during the heating of this sample to  $345^\circ\text{C}$  and the subsequent cooling to RT can be seen in Fig. 3.26. A comparison of the images measured before heating and at  $255^\circ\text{C}$  shows that the first changes of the magnetic patterning due to the elevated temperature can be observed at the  $360^\circ$  walls in the not bombarded areas [circles in Fig. 3.26 (a)/(b)]. As the first change of the magnetic pattern was observed at not bombarded areas no hint for a reduction of the thermal stability in remanence due to IB has been found during the experiments with the crossed gratings. But one can not conclude from this that the thermal stability of the bombarded areas is higher, because the  $360^\circ$  walls which acted as a kind of nucleation sites for changes of the magnetization pattern have been present only in the not bombarded areas.

With rising temperature [ $255^\circ\text{C}$  (b) to  $345^\circ\text{C}$  (c)] the EB interaction gets weaker and vanishes at the blocking temperature while the exchange interaction and the dipole energy do not decrease as fast. Therefore, the artificial pattern induced by the patterning of the EB coupling vanishes and is replaced by the pattern of a demagnetized state. When the sample is cooled down to room temperature, the pattern of the demagnetized state is conserved. The shape of this pattern depends, e.g., on the width of the etched topographic lines (e.g., due to shape anisotropy) and the magnetic pattern before the heating. In the example measurements shown in Fig. 3.26 larger areas of the size of the bombarded/not bombarded regions with a

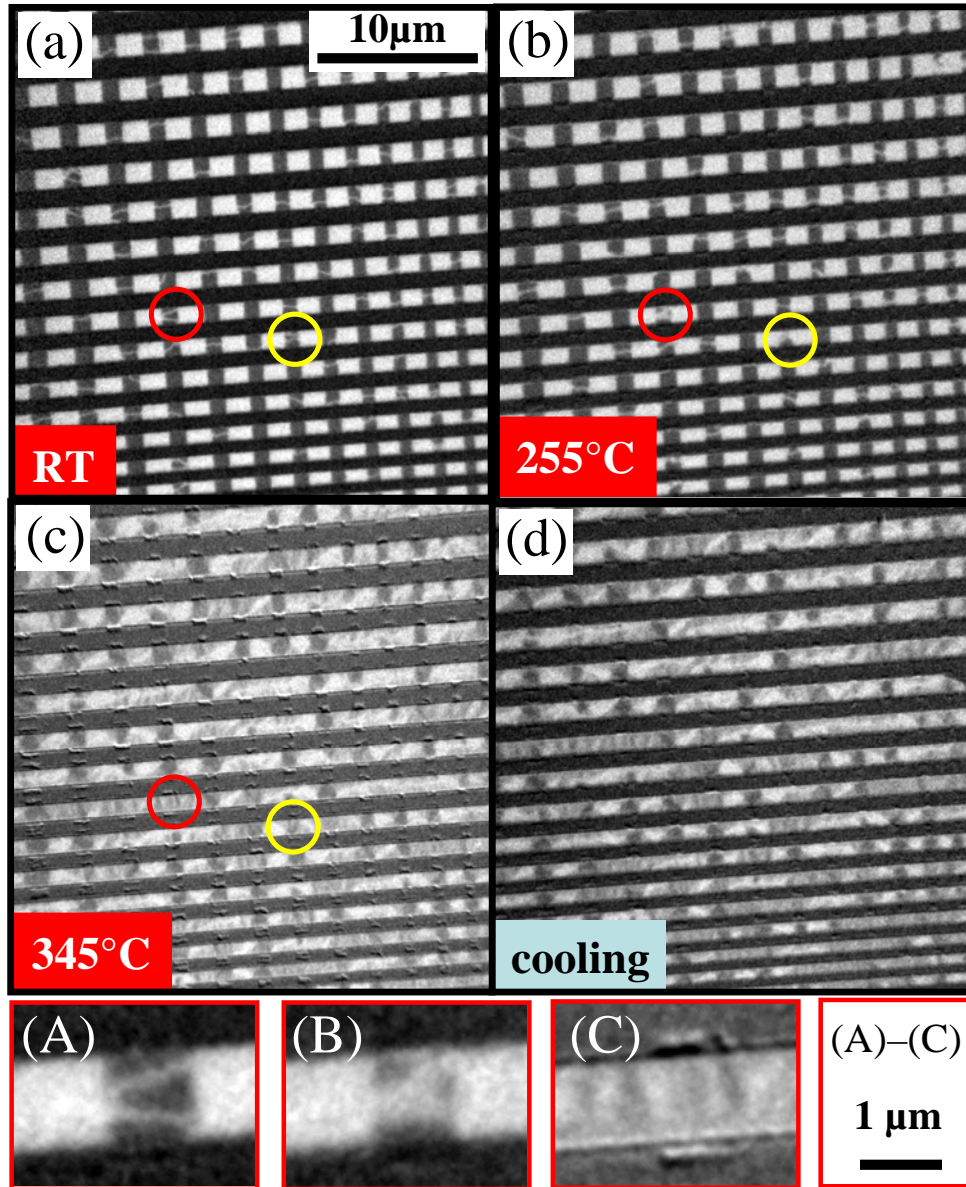


Figure 3.26: PEEM images of crossed topographic and magnetic gratings on a sample with stack  $CoFe_{TS}^{PEEM5nm}$  before (a) and during (b)/(c) the heating and after cooling the sample down to RT (d). (A), (B), and (C) show the regions indicated by red circles in (a), (b), and (c) with a larger magnification.

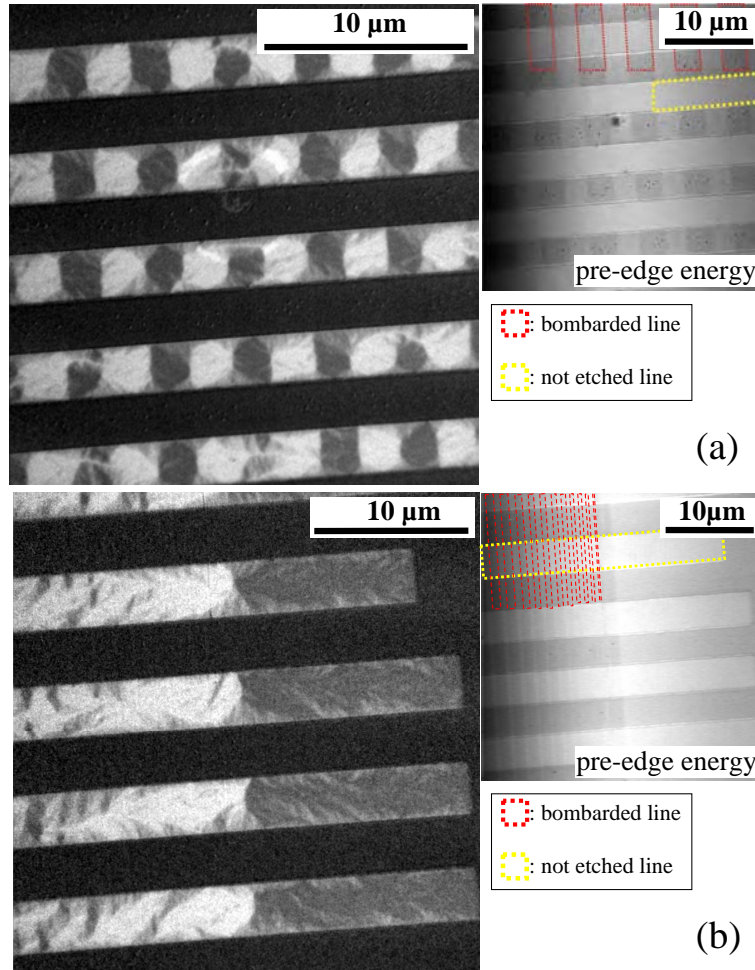


Figure 3.27: Large images: magnetic contrast obtained through PEEM measurements of crossed topographic and magnetic gratings on a sample with stack  $CoFe_{TS}^{PEEM5nm}$  after cooling the sample down to RT; small images: corresponding PEEM measurements carried out with x-rays with an energy slightly smaller than the Co white lines (topographic contrast).

rather homogeneous magnetization with the same orientation as before the heating can be found. But there are as well regions with a strongly fragmented pattern. Examples for the magnetic pattern after cooling down with larger bombarded/not bombarded areas and with thinner lines can be found in Fig. 3.27. A comparison of the position of the bombarded lines indicated by red boxes in the small pre-edge energy PEEM image with the domain pattern obtained for the thick bombarded lines in Fig. 3.27 (a) shows that the pattern remains visible after heating. At the edges of the etched topographic lines additional closure domains can be found. In contrast to this, the thin magnetic structures which have been created on the area depicted in part (b) can not be seen any more after the sample has been heated above the blocking temperature. This can be explained by the different size of the structures relative to the exchange length in the FM layer (compare the measurements for the

only magnetically patterned samples).

### 3.2.5 X-ray photoemission electron microscopy investigations on elliptic and triangular structures with partly manipulated exchange bias

#### Experiment

Samples with stack  $CoFe_{TS}^{PEEM3nm}$  have been patterned topographically with several elliptical and triangular structures with a subsequent magnetic patterning (compare, e.g., Fig. 3.28). The elliptical topographic structures have a long (short) axis of  $5.7 \mu\text{m}$  ( $2.6 \mu\text{m}$ ) and  $2.7 \mu\text{m}$  ( $1.2 \mu\text{m}$ ) length. This elliptic shape is the most likely shape for the application of small MTJs. Therefore, these heating experiments give an indication for the magnetic behavior of the reference layer of these MTJs, e.g., during a postannealing step without a magnetic field which can be used to decrease the side effects of the ion bombardment on full magnetic tunnel junctions (compare chapter 3.5).<sup>6</sup>

The sample preparation has been carried out in the same way and with the same parameters as described above for the sample with stack  $CoFe_{TS}^{PEEM5nm}$ .

#### Results and discussion

The elliptic structures have been alternating bombarded to turn the EB direction and not bombarded to maintain the EB direction initialized by the field cooling. The largest part of the triangular structures is not bombarded. The bombarded areas can be identified in Fig. 3.28 (a) by the PEEM signal. The magnetization direction in the bombarded areas before the heating results in a dark contrast in figures 3.28 and 3.29 (bombarded structures, e.g.: 1,3,b,d).

The magnetization direction of the large elliptic structures is not significantly altered for temperatures up to  $200^\circ\text{C}$  [Fig. 3.28 (a-d)].<sup>7</sup> At  $220^\circ\text{C}$  a slight variation of the measured magnetization direction can be guessed while at  $240^\circ\text{C}$  changes of the magnetic configuration in the large elliptic structures three (bombarded) and five (not bombarded) can be seen [Fig. 3.28 (d) and (e)]. This value fits good to the vanishing exchange bias field observed in this temperature range in the AGM investigations. Again, the temperature necessary for a first variation of the magnetic structure is independent of the IB.

At a temperature of  $360^\circ\text{C}$  the PEEM signal of all large elliptic structures turns together with all other structures to a predominantly dark contrast [Fig. 3.29 (j)]. This effect gets even stronger when the temperature is further enlarged [Fig. 3.29 (k)].

This effect results from the fact that for all images in Fig. 3.28 and 3.29 the brightness and contrast have been optimized to make the structure of the magnetic pattern visible. A comparison of the PEEM image measured at a temperature of  $200^\circ\text{C}$  [Fig.

<sup>6</sup>The effects of scaling the MTJs down are not covered in these experiments.

<sup>7</sup>The magnetic signal at this temperature is especially at the left side less good compared to, e.g., the measurement at  $175^\circ\text{C}$ . This is due to a slightly different fine tuning of the adjustment of the experimental setup during this measurement.



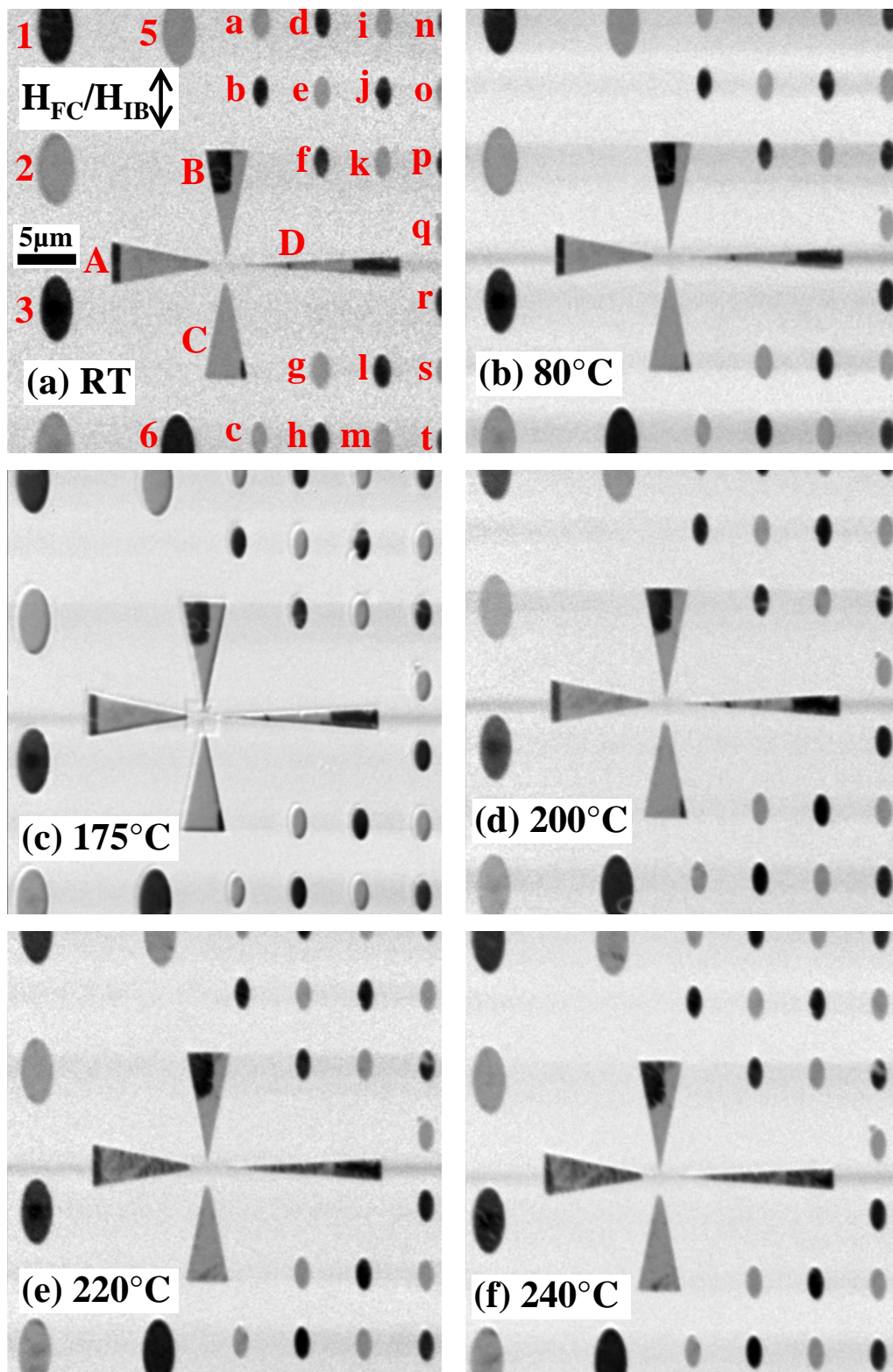


Figure 3.28: PEEM images of elliptic and triangular etched structures with an alternating EB direction on a sample with stack  $CoFe_{TS}^{PEEM3nm}$  before (a) and during (b)-(f) the heating. The brightness and the contrast of each image has been optimized separately for a good visibility of the magnetic pattern.

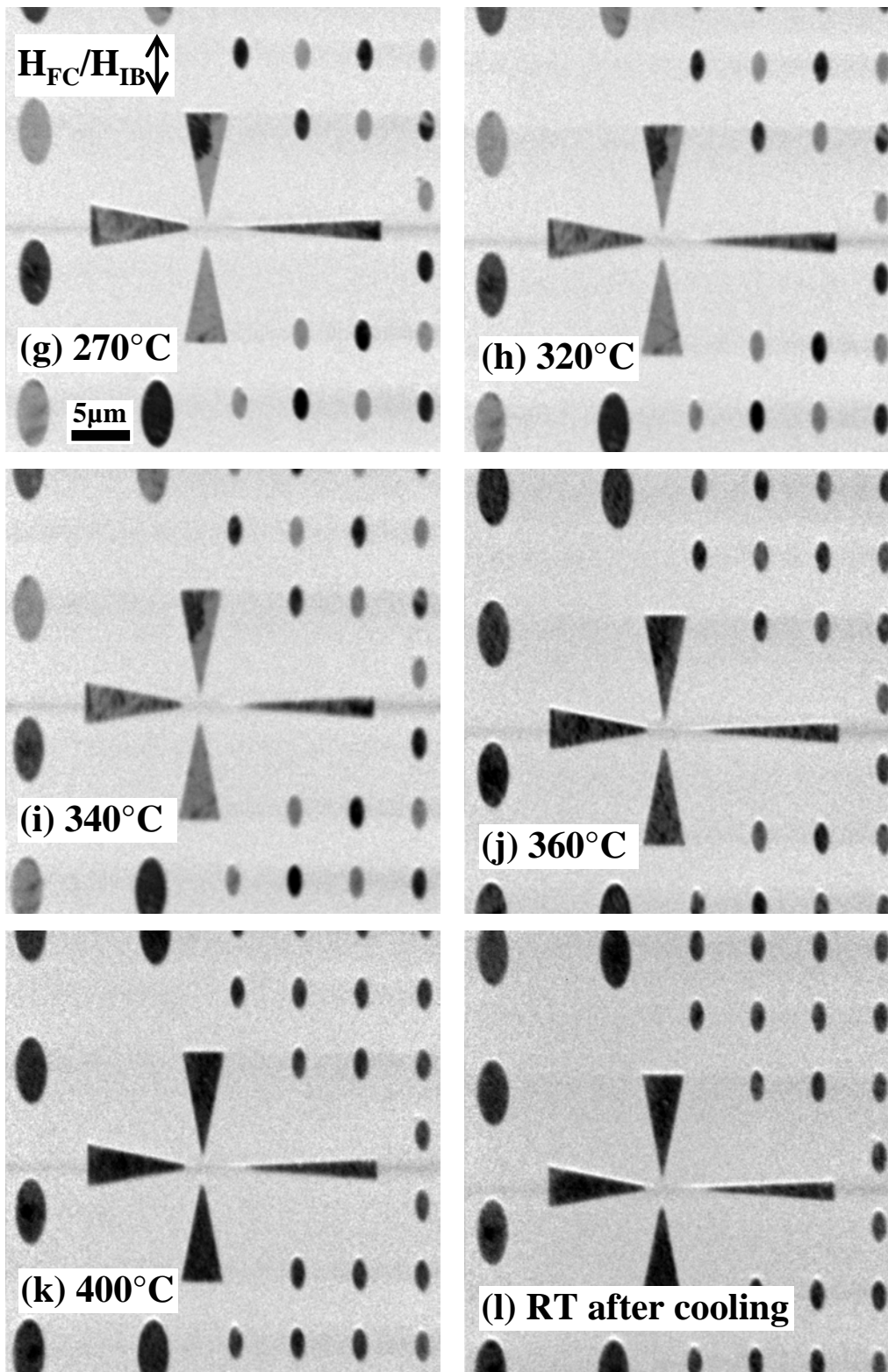


Figure 3.29: PEEM images of elliptic and triangular etched structures with an alternating EB direction on a sample with stack  $\text{CoFe}_{\text{TS}}^{\text{PEEM3nm}}$  during (g)-(k) the heating and after cooling the sample down to RT (l). The brightness and the contrast of each image has been optimized separately for a good visibility of the magnetic pattern.

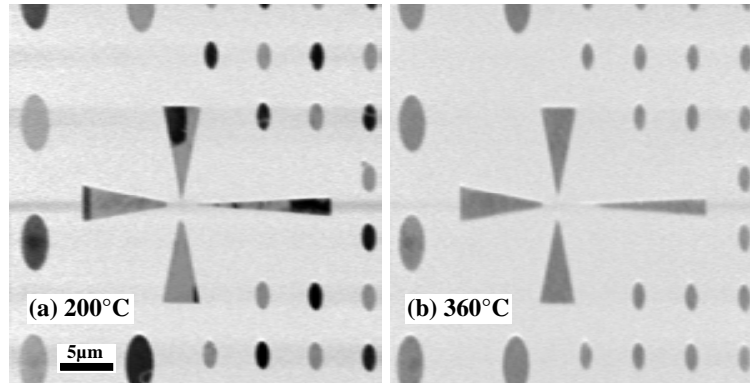


Figure 3.30: PEEM images on a sample with stack  $CoFe_{TS}^{PEEM3nm}$  (a) at  $200^{\circ}\text{C}$  with optimized brightness and contrast and (b) at  $360^{\circ}\text{C}$  with identical brightness and contrast parameters as used in part (a).

3.28(d) and 3.30 (a)] and the image measured at  $360^{\circ}\text{C}$  with the same brightness and contrast parameters as used for the  $200^{\circ}\text{C}$ -measurement [Fig. 3.30 (b)] shows that with identical parameters the brightness of the large elliptic structures heated to  $360^{\circ}\text{C}$  is somewhere between the values of the bombarded and not bombarded large elliptic structures heated to  $200^{\circ}\text{C}$ . This can be explained by an average direction of the magnetization which is less good aligned parallel or antiparallel to the axis which is probed by the PEEM, e.g., due to a pattern of small domains [compare, e.g., magnetic structure of large elliptic element 2 in Fig. 3.29 (j)].

The temperature dependence of the magnetization of the small elliptic structures is slightly different. Two of the small elliptic structures (f and p) contain  $360^{\circ}$  walls [visible, e.g., in Fig. 3.28 (b)] which produce a growing signal with increasing temperature [Fig. 3.28 (d)]. At a temperature of  $220^{\circ}\text{C}$  the  $360^{\circ}$  wall of element f disappears while the one at element p survives even at a temperature of  $340^{\circ}\text{C}$ . This might be due to, e.g., inhomogeneities of this element.

All other small elliptical elements keep their magnetization pattern constant up to a temperatures of about  $320^{\circ}\text{C}$ . This is significantly larger than the blocking temperature and has to be explained with the influence of the shape anisotropy which prevents that the magnetization direction is altered.

The triangular structures show a similar behavior as it has been described for the crossed etched and magnetic gratings. The small structures change their magnetic pattern when the temperature gets in the region of the blocking temperature [see, e.g., triangle D, Fig. 3.28 (d) & (e) or triangle C in Fig. 3.28 (d) & (e)] while large magnetic structures are mainly altered at their edges but remain visible (triangle B).

Similar measurements carried out at four of the larger elliptical structures with a larger magnification can be found in appendix B.

### 3.2.6 Summary

The temperature dependence of the exchange bias obtained by AGM measurements has a slightly different shape compared to the reference measurements obtained on not bombarded samples, but it is very similar in the range of the blocking temperature.

To determine the influence of the slightly changed temperature dependence on the thermal stability of magnetically patterned structures, e.g., on a reference layer of magnetic tunnel junctions consisting of CoFe or Co, PEEM investigations at elevated temperatures have been carried out. The magnetic pattern produced by IB in an external field on the field cooled stack  $CoFe_{TS}^{PEEM3nm}$  without topographic structures was stable up to about 175°C and changed its shape due to the growing influence of strayfields and a reduction of the stabilizing EB energy for higher temperatures. The alteration of the magnetic pattern occurs in the range of the blocking temperature. Therefore, no indication for a change of the thermal stability of magnetic structures in remanence due to the ion bombardment has been found in the experiment with this sample. On the as-prepared stack  $Co_{TS}^{PEEM}$  first changes of the domain structure in the as-prepared area were seen at 116°C independent of the IB, while the direction of the magnetization on the bombarded area was stable up to the temperature of about 150°C. As the as-prepared area showed a domain growth at lower temperatures than the bombarded area, again, no hint for an IB induced decrease of the thermal stability in remanence was found.

Additional experiments on samples which had experienced a topographic (lines, ellipses and triangles) as well as a magnetic patterning, again, showed no hint for a reduction of the thermal stability due to the magnetic patterning by ion bombardment.

Therefore, this investigation shows that the choice of IB for the manipulation of the EB does not influence the thermal stability in remanence and, therefore, does not limit the applicability of the magnetic pattern.

### 3.3 Applicability of ion bombardment induced magnetic patterning on samples containing pinned artificial ferrimagnets

#### 3.3.1 Introduction

It has been shown in the last chapters that the exchange bias interaction can be manipulated locally by ion bombardment in an external magnetic field (compare as well [28, 60, 50, 29]). Furthermore, the application of IBMP is possible for the reference electrodes of complete MTJs without a destruction of the magnetoresistive properties even if the ferromagnetic layer / antiferromagnetic layer bilayer is buried underneath the sensible alumina tunneling barrier (chapter 3.4 and 3.5 and [176, 167]). But during all these experiments only single FM layers have been used as reference electrodes. As it will be shown, e.g., in chapter 4.3 for some applications it is very useful to tune the magnetic moment of the FM layers. This can be done by using artificial ferrimagnets (AFi) consisting of two FM layers coupled antiferromagnetically by the interlayer exchange coupling (IEC, chapter 2.4). Therefore, the question whether a magnetic patterning of the EB with He ions is possible in systems including an AFi has to be addressed because the ion bombardment might destroy the antiferromagnetic coupling.

Several experiments addressing the influence of IB on the antiferromagnetic interlayer exchange coupling (IEC) of FM/spacer/FM sandwich structures have been reported. In Ref. [177] the interlayer coupling of a sandwich structure containing a Ru interlayer, which is frequently used in AFis for the application in MTJs (see, e.g., [88]), has been changed from antiferromagnetic to ferromagnetic by 60 keV Co bombardment. For He ions with an energy  $E_{IB}$  of 5 keV it has been demonstrated in Ref. [178] that the antiferromagnetic interlayer coupling in a Fe/Cr/Fe system can be increased, decreased and transformed into a ferromagnetic coupling depending on the thickness of the Cr interlayer and the ion dose. The conversion of similar systems from antiferromagnetic to ferromagnetic coupling by bombardment with 50 keV and 30 keV  $Ga^+$  ions has been described in Ref. [179] and [180], respectively. The manipulation of the EB interaction for a Co/Cu/Co/FeMn spin valve with a 2.4 nm thick Cu interlayer (no antiferromagnetic interlayer exchange coupling) with 10 keV He ions in an external magnetic field has been described in Ref. [27, 181] for several ion doses and orientations of the magnetic field during bombardment. In this case, again, a ferromagnetic coupling has been found for high ion doses. For the small ion doses which are sufficient to increase or reverse the EB, no ferromagnetic coupling has been found.

Here, the manipulation of the EB in an IrMn/CoFe/Ru/CoFe system as it can be used in MTJs [6] will be investigated. Of special interest is the effect of the IB on the combined system with EB and antiferromagnetic interlayer exchange coupling. Furthermore, the IBMP of an IrMn/Py/Co/Cu/Co stack with a Cu thickness in the range of the first maximum of the antiferromagnetic IEC will be tested. The

---

<sup>8</sup>Parts of this chapter have been published in [175]

attention is focused on the effect of the IB with an ion dose necessary to manipulate the EB on the AF interlayer exchange coupling.

### 3.3.2 Experiment

Different types of samples have been deposited. Samples of the type  $Ru_{AF}$  have a stack equal to the lower part of a typical MTJ with a pinned AFi up to the tunnel barrier (see inset in Fig. 3.31). The Ru interlayer has a thickness in the range of 0.9 nm to 0.95 nm corresponding to the second antiferromagnetic maximum of the IEC. A similar stack  $Ru_{AF}^{no\ IrMn}$  without the IrMn layer has been sputtered to test the AF interlayer coupling without EB. *hMTJ* denotes samples build like the lower half of a MTJ containing an antiferromagnet/ferromagnet reference layer without an AFi as described in Ref. [176]. Furthermore,  $Cu_{AF}$  samples with a Cu based AFi stack and a Cu spacer thickness of 1.05 nm corresponding to the first antiferromagnetic maximum of the IEC have been prepared.<sup>9</sup>

For a part of the samples the EB interaction has been initialized by field growth or field cooling. The following ion bombardment has been carried out in all cases by using 10 keV He ions in an external magnetic field  $H_{IB}$  with various ion doses up to  $4 \times 10^{14}$  ions/cm<sup>2</sup>. The detailed stacks and the parameters used for the EB initialization and the subsequent EB manipulation by IB can be found in table 3.1. The dependence of the magnetization on an external magnetic field has been investigated for all samples containing AFis by magneto optical Kerr effect or alternating gradient magnetometer measurements prior to and after ion bombardment. Furthermore, pinned FM layers with a varying thickness have been deposited with the same sputter deposition tool (CLAB 600). Their saturation magnetization has been determined by AGM measurements.

### 3.3.3 Results and discussion

In this section first the magnetization reversal process of samples with stack  $Ru_{AF}$  and  $Ru_{AF}^{no\ IrMn}$  without ion bombardment will be described and explained. Then the experimental results about the ion dose dependence of the magnetization reversal process for an IB induced increase of the EB will be shown. After a discussion of possible origins of this ion dose dependence, the question whether the EB direction can be turned by 180° has to be addressed. Finally, the influence of ion bombardment on the magnetization reversal process of samples with stack  $Cu_{AF}$  is investigated.

#### Ru-AFi: Magnetization reversal process

Figure 3.31 shows MOKE measurements carried out at an annealed sample with a  $Ru_{AF}$  stack including an IrMn layer and at a sample with a  $Ru_{AF}^{no\ IrMn}$  stack without IrMn layer which has not been annealed. Both samples have not been bombarded

<sup>9</sup>The questions whether the AF layer should be located below or on top of the interlayer and which ion energy should be used for the different possible stacks are not treated in this chapter. The reader is referred to chapter 3.8.2 for a detailed discussion of this question in the context of the location of the AF layer below or on top of the barrier. The results obtained there can also be applied for the optimization of AFis.

Sample name, EB manipulation by IB	Sputter deposition: Stack (layer thickness in nm)	Field cooling			Ion bombardment	
		Temp. [°C]	Time [min]	H <sub>FC</sub> [kOe]	Orientation <b>H</b> <sub>IB</sub>	H <sub>IB</sub> [kOe]
$Ru_{AF}^{1\text{ kOe, AP}}$ , EB enlarged	Cu 25/IrMn 15/CoFe 2/Ru 0.95/CoFe 3/Al 1.4 + ox.	275	30	6.5	<b>H</b> <sub>IB</sub> ↑↓ <b>H</b> <sub>FC</sub>	1
$Ru_{AF}^{5.4\text{ kOe, AP}}$ , EB turned	Cu 25/IrMn 15/CoFe 2/Ru 0.95/CoFe 3/Al 1.4 + ox.	275	30	6.5	<b>H</b> <sub>IB</sub> ↑↓ <b>H</b> <sub>FC</sub>	5.4
$Ru_{AF}^{5.4\text{ kOe, P}}$ , EB enlarged	Cu 25/IrMn 15/CoFe 2/Ru 0.95/CoFe 3/Al 1.4 + ox.	275	30	6.5	<b>H</b> <sub>IB</sub> ↑↑ <b>H</b> <sub>FC</sub>	5.4
$Ru_{AF}^{\text{no IrMn}}$ , no IB	Cu 25/CoFe 2/Ru 0.9/CoFe 3/Al 1.4 + ox.	no FC			no IB	
$Cu_{AF}$ , EB turned	Cu 25/IrMn 10/NiFe 2/Co 2/Cu 1.05/Co 2/Al 1.4	field growth			<b>H</b> <sub>IB</sub> ↑↓ <b>H</b> <sub>grow</sub>	1
$hMTJ$ , EB initialized	Cu 30/IrMn 15/CoFe 3/Al 1.4 + ox./NiFe 4/Ta 6	no FC			<b>H</b> <sub>IB</sub>	1
$hMTJ$ , EB enlarged	Cu 30/IrMn 15/CoFe 3/Al 1.4 + ox./NiFe 4/Ta 6	250	5	1.5	<b>H</b> <sub>IB</sub> ↑↑ <b>H</b> <sub>FC</sub>	1
$hMTJ$ , EB turned	Cu 30/IrMn 15/CoFe 3/Al 1.4 + ox./NiFe 4/Ta 6	250	5	1.5	<b>H</b> <sub>IB</sub> ↑↓ <b>H</b> <sub>FC</sub>	1
$FM-A_{\text{pinned}}^{x\text{IrMn}/y\text{FM}}$ , no IB	Cu 30/IrMn $x$ /FM $y$ /AlOx 1.8 (FM=CoFe/Py)	275	60	1.5	no IB	
$FM-B_{\text{pinned}}^{x\text{CoFe}/10\text{IrMn}}$ , no IB	Ta 5/CoFe $x$ /IrMn 10	275	30	1.5	no IB	
$FM-C_{\text{pinned}}^{x\text{Co}/10\text{IrMn}}$ , no IB	Cu 5/ Co $x$ /IrMn 10	275	30	1.5	no IB	
$FM-C_{\text{pinned}}^{x\text{Py}/10\text{IrMn}}$ , no IB	Cu 5/ Py $x$ /IrMn 10	275	30	1.5	no IB	

Table 3.1: Stack of investigated samples with layer thickness in nm and parameters of field cooling (max. temperature, heating duration and magnetic field  $H_{FC}$  applied during field cooling) and ion bombardment (orientation of magnetic field during IB ( $\mathbf{H}_{IB}$ ) relative to the field during field cooling ( $\mathbf{H}_{FC}$ ) or field during field growth ( $\mathbf{H}_{grow}$ ) and strength of  $H_{IB}$ ). The ion energy was always 10 keV.

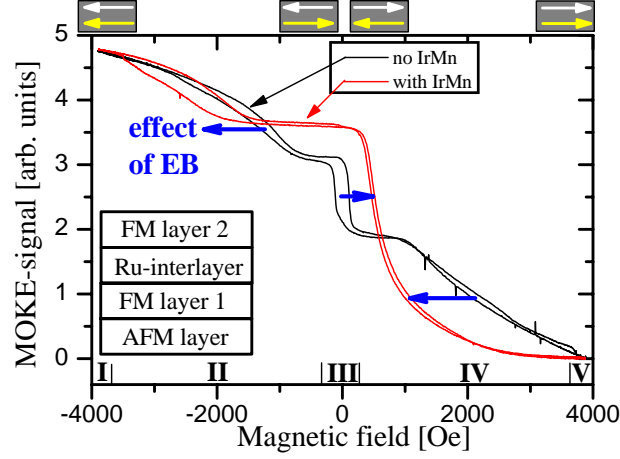


Figure 3.31: MOKE measurements done at an annealed sample with  $Ru_{AF}$  stack (no IB, a magnetic field labeled with positive values in this graph is aligned parallel to  $\mathbf{H}_{FC}$ ) and at a sample with a similar  $Ru_{AF}^{no\ IrMn}$  stack (no IB, no FC). The thick blue arrows indicate the change of the magnetic switching behavior due to EB. The arrows in the gray boxes at the top indicate the direction of the magnetization of the two FM layers for the sample without IrMn layer (white upper arrow: 3 nm upper CoFe layer, yellow lower arrow: 2 nm lower CoFe layer). The inset shows a sketch of the pinned AFi.

with ions prior to measurements. The arrows in the gray boxes at the top of the graph indicate the direction of the magnetization of the two CoFe layers in the case of the  $Ru_{AF}^{no\ IrMn}$  sample. The white upper (yellow lower) arrow symbolizes the direction of the magnetization of the 3 nm thick upper (2 nm thick lower) CoFe layer. The magnetization reversal process can be reproduced theoretically by considering the energy related to the interactions between the layers and the influence of the external magnetic field. The direction of the magnetizations will be oriented in a way that minimizes the total energy which can be described by the following approximation:

$$\begin{aligned}
 E = & -\mu_0 M_S^1 d_1 H \cos(\Theta_1) - \mu_0 M_S^2 d_2 H \cos(\Theta_2) \\
 & -K_u \cos(\Theta_1) - J_L \cos(\Theta_1 - \Theta_2) \\
 & -J_Q \cos^2(\Theta_1 - \Theta_2) + K_1 d_1 \sin^2(\Theta_1 - \Theta_{easy}) \\
 & +K_2 d_2 \sin^2(\Theta_2 - \Theta_{easy})
 \end{aligned} \tag{3.1}$$

with  $M_S^i$ : saturation magnetization of FM layer  $i$  (for a sketch of the stack see inset of Fig. 3.31),  $d_i$ : thickness of layer  $i$ ,  $\Theta_i$ : angle between magnetization of layer  $i$  and the external magnetic field,  $K_u$ : unidirectional anisotropy constant,  $J_L$ : bilinear interlayer exchange coupling constant,  $J_Q$ : biquadratic interlayer exchange coupling constant,  $K_i$ : uniaxial anisotropy constant of layer  $i$  and  $\Theta_{easy}$ : angle of easy axis relative to the external magnetic field. The first two terms denote the Zeeman areal energy density of the lower layer 1 and the upper layer 2, respectively [174]. The third term gives an expression for the exchange bias interaction [35] acting on layer 1 while the fourth and fifth ones give the areal energy density resulting from the



bilinear and biquadratic interlayer exchange interaction [99]. The last two terms describe the energy due to a uniaxial anisotropy which is in its minimum on an axis tilted by the angle  $\Theta_{easy}$  relative to the direction of the external magnetic field during measurement. The expressions given for the uniaxial anisotropy are valid for hexagonal and tetragonal crystals [174]. In our samples we have polycrystalline layers with not necessarily aligned easy axes of all grains. Therefore, for our samples the anisotropy terms should only be regarded as an approximative measure for several mechanisms inducing a hysteresis. The external magnetic field during the measurement is oriented parallel to the axis defined by  $\mathbf{H}_{FC}$ ,  $\mathbf{H}_{grow}$  and  $\mathbf{H}_{IB}$ . Therefore, for the calculation of the energy due to the EB and the energy due to the Zeeman energy, the same angle  $\Theta_1$  can be used.

Figure 3.32 shows a calculated magnetization reversal process which was obtained by minimizing equation 3.1 using the downhill simplex method with the *amoeba* implementation [159]<sup>10</sup> and adjusting the parameters for a good agreement with an AGM measurement of a sample of type  $Ru_{AF}^{no\ IrMn}$ . The values of the contributions of the single energy densities in Eq. 3.1 in dependence of the external magnetic field can be seen in Fig. 3.32 (a).

The angles of the magnetization of the two ferromagnetic layers resulting from the energy minimization calculation are shown in Fig. 3.32 (b). Even and odd multiples of  $\pi$  correspond to an orientation of  $\mathbf{M}_i$  parallel to the positive and negative external magnetic field during measurement, respectively.

The adjustment of the calculation to the experiment has been carried out by comparing the normalized experimental results and the normalized projection of the magnetization on the direction of the external magnetic field weighted by the layer thickness and the saturation magnetization  $[d_1 M_S^1 \cos(\Theta_1) + d_2 M_S^2 \cos(\Theta_2)]/[d_1 M_S^1 + d_2 M_S^2]$  (Fig. 3.32 (c)).

The influence of details of the change of the magnetization direction like, e.g., pinning of domain walls is not considered here. These neglected effects on the magnetization reversal as, e.g., the hysteresis could partly be covered by assuming the existence of an effective uniaxial anisotropy term.<sup>11</sup>

The FM layer thicknesses have been chosen according to stack  $Ru_{AF}^{no\ IrMn}$  ( $d_1=2$  nm,  $d_2=3$  nm).

To obtain the values of  $M_S$ , results of AGM measurements of samples with a similar FM layer thickness have been used as a starting point. Then these values have been fine tuned until a good agreement between the height of the single switching loops in the calculated and the measured magnetization reversal is observed. The resulting saturation magnetizations of  $M_S^1=1.07 \times 10^6$  A/m (1070 emu/cm<sup>3</sup>) for the 2 nm thick Co<sub>70</sub>Fe<sub>30</sub> layer 1 and  $M_S^2=1.24 \times 10^6$  A/m (1238 emu/cm<sup>3</sup>) for the 3 nm thick Co<sub>70</sub>Fe<sub>30</sub> layer 2 fit well to the thickness dependence of the saturation magnetization found experimentally by AGM measurements with samples of type  $FM-B_{pinned}^{x\ CoFe/10IrMn}$  (compare Fig. 3.33).<sup>12</sup> With the values a net saturation magnetization of the whole

<sup>10</sup>For this investigations a program provided by Andy Thomas which was based on the code published in Ref. [159] has been adjusted to fit to the described task.

<sup>11</sup>An example calculation including finite values of  $K_1$  and  $K_2$  to reproduce the hysteresis can be found in appendix D.

<sup>12</sup>During the deposition and measurement of this samples special attention has been payed to the fact that they do not have any contact to any kind of magnetic material which might influence the measured saturation magnetization.

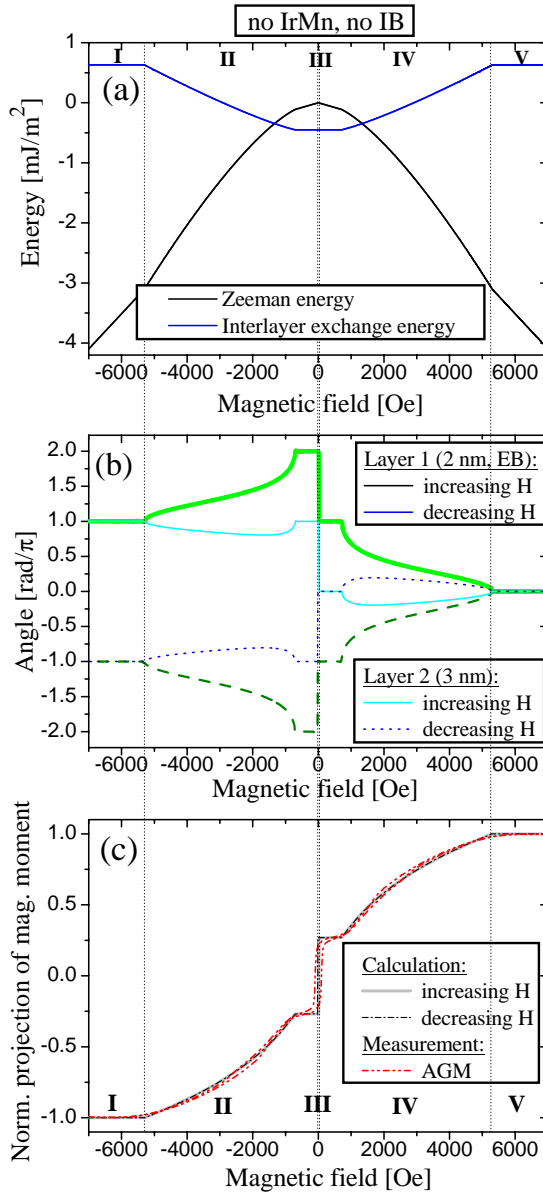


Figure 3.32: (a) Energy of Zeeman interaction and interlayer exchange interaction calculated for the angles of the magnetization of the two FM layers ( $\mathbf{M}_i$ ) which result in the minimum sum of this energies at each value of the external magnetic field. (b) Direction of  $\mathbf{M}_i$  described by the angle relative to the axis of the external magnetic field. Even (odd) multiples of  $\pi$  correspond to an orientation of  $\mathbf{M}_i$  parallel to the positive (negative) external magnetic field. (c) Calculated magnetization reversal and normalized AGM measurement for sample  $Ru_{AF}^{no\ IrMn}$ . The calculated magnetization reversal has been obtained with  $J_L = -5.4 \times 10^{-4} \text{ J/m}^2$ ,  $J_Q = -9 \times 10^{-5} \text{ J/m}^2$  and  $K_u = 0 \text{ J/m}^2$ .

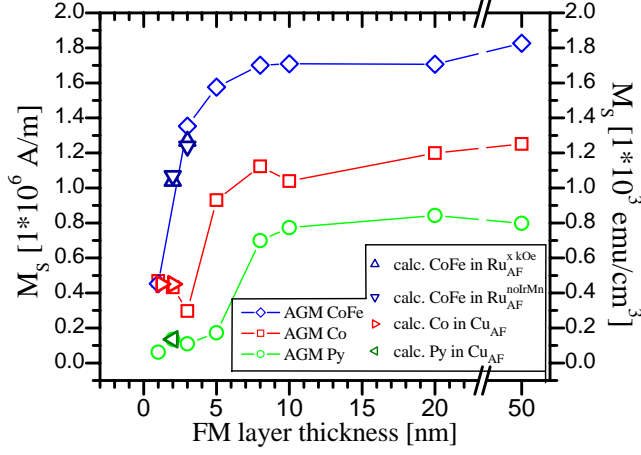


Figure 3.33: Saturation magnetization  $M_S$  of pinned  $\text{Co}_{70}\text{Fe}_{30}$ , Co and Py ( $\text{Ni}_{80}\text{Fe}_{20}$ ) layers in dependence of the FM layer thickness  $d$  (sample  $FM-B_{\text{pinned}}^x \text{CoFe}/10\text{IrMn}$ ,  $FM-C_{\text{pinned}}^x \text{Co}/10\text{IrMn}$  and  $FM-C_{\text{pinned}}^x \text{Py}/10\text{IrMn}$ , all samples without FC). The values obtained by AGM measurements are connected by lines as a guide to the eye. The not connected triangles symbolize the values of  $M_S$  used in the calculations of the magnetization reversal process.

sample of  $1.17 \times 10^6 \text{ A/m}$  ( $1170 \text{ emu/cm}^3$ ) can be expected. The values found experimentally for the net saturation magnetization of stack  $Ru_{\text{AF}}^{\text{no IrMn}}$  are in the range of  $1.19 \times 10^6 \text{ A/m}$  to  $1.27 \times 10^6 \text{ A/m}$ . The deviation to the value used in the calculations is smaller than the experimental uncertainty of approximately 10%.

The unidirectional anisotropy constant  $K_u$  has been set to zero as due to the lack of an antiferromagnetic layer no exchange bias is present.

The bilinear and biquadratic IEC constants resulting in the best fit between calculation and measurement for sample  $Ru_{\text{AF}}^{\text{no IrMn}}$  are  $J_L = -5.4 \times 10^{-4} \text{ J/m}^2$  and  $J_Q = -9 \times 10^{-5} \text{ J/m}^2$ .

Although the obtained value for the bilinear interlayer coupling is smaller than the values published by Wiese *et al.* [133] and Saito *et al.* [182] (Tab. 3.2) they are in the same order of magnitude.<sup>13</sup>

The fitting method has no significant influence on the result. When the biquadratic term is ignored and  $J_L$  is calculated with the equation used by Wiese [183, 133] ( $J_L = -\mu_0 H_{\text{sat}} M_1 t_1 M_2 t_2 / [M_1 t_1 + M_2 t_2]$ ) one gets  $J_L = -5.7 \times 10^{-4} \text{ J/m}^2$ . For this calculation  $H_{\text{sat}} = 5700 \text{ Oe}$  ( $453591 \text{ A/m}$ ),  $M_1 = 1.07 \times 10^6 \text{ A/m}$ ,  $t_1 = 2 \text{ nm}$ ,  $M_2 = 1.24 \times 10^6 \text{ A/m}$  and  $t_2 = 3 \text{ nm}$  have been used. Therefore, for sample  $Ru_{\text{AF}}^{\text{no IrMn}}$  a good agreement between the values obtained by the fit procedure ( $J_L = -5.4 \times 10^{-4} \text{ J/m}^2$ ) and by calculating  $J_L$  using  $H_{\text{sat}}$  ( $J_L = -5.7 \times 10^{-4} \text{ J/m}^2$ ) has been found.

The method to determine  $J_L$  by just measuring the saturation magnetization does not work when the shape of the magnetization reversal process is changed by exchange bias. Therefore, for all other samples only the energy minimization procedure is used.

The uniaxial anisotropy constants have been chosen to be  $K_1 = K_2 = 0$  as in the investigated samples due to the polycrystalline nature of the FM layers no uniform

<sup>13</sup>For the difference between measured values and literature values several reasons are possible. For example is the stoichiometry of the CoFe different, the thickness of the Ru layer is not exactly the same and the surrounding stack and, therefore, the growth conditions are different. But even if one would deposit the same stack with exactly the same sputter targets different results can be expected when the sputter parameters vary.

Stack [nm]	J [mJ/m <sup>2</sup> ]	Ref.	Determined by...
Co <sub>90</sub> Fe <sub>10</sub> 3 / Ru 0.95 / Co <sub>90</sub> Fe <sub>10</sub> 5	-1.05	Sai06	$J=H_{sat}M_{sat}t_1t_2 / (t_1+t_2)$ [cgs]
Co <sub>90</sub> Fe <sub>10</sub> 3 / Ru 1.05 / Co <sub>90</sub> Fe <sub>10</sub> 5	-0.78	Sai06	$J=H_{sat}M_{sat}t_1t_2 / (t_1+t_2)$ [cgs]
Co <sub>90</sub> Fe <sub>10</sub> 3 / Ru 1.15 / Co <sub>90</sub> Fe <sub>10</sub> 5	-0.52	Sai06	$J=H_{sat}M_{sat}t_1t_2 / (t_1+t_2)$ [cgs]
Co <sub>75</sub> Fe <sub>25</sub> 5 / Ru 0.9 / Co <sub>75</sub> Fe <sub>25</sub> 8	-1.18	Wie06	$J=-\mu_0H_{sat}((m_1m_2)/(m_1+m_2))$
Co <sub>75</sub> Fe <sub>25</sub> 7 / Ru 0.9 / Co <sub>75</sub> Fe <sub>25</sub> 10	-1.18	Wie06	$J=-\mu_0H_{sat}((m_1m_2)/(m_1+m_2))$
Co <sub>75</sub> Fe <sub>25</sub> 3 / Ru 0.9 / Co <sub>75</sub> Fe <sub>25</sub> 6	-1.11	Wie06	$J=-\mu_0H_{sat}((m_1m_2)/(m_1+m_2))$
Co <sub>75</sub> Fe <sub>25</sub> 3 / Ru 0.9 / Co <sub>75</sub> Fe <sub>25</sub> 7	-1.13	Wie06	$J=-\mu_0H_{sat}((m_1m_2)/(m_1+m_2))$
Co <sub>75</sub> Fe <sub>25</sub> 3 / Ru 0.9 / Co <sub>75</sub> Fe <sub>25</sub> 9	-1.16	Wie06	$J=-\mu_0H_{sat}((m_1m_2)/(m_1+m_2))$
Ni <sub>81</sub> Fe <sub>19</sub> 16 / Ru 0.8 / Co <sub>90</sub> Fe <sub>10</sub> 12	-1.2	Fas06	$J=-H_{sat}(M_{CoFe}d_{CoFe}+M_{NiFe}d_{NiFe})$
Co <sub>60</sub> Fe <sub>20</sub> B <sub>20</sub> 3.8 / Ru 1.1 / CoFeB 3	-0.06	Wie05	$J=-\mu_0H_{sat}((m_1m_2)/(m_1+m_2))$
Co <sub>60</sub> Fe <sub>20</sub> B <sub>20</sub> 4 / Ru 1.1 / CoFeB 3	-0.06	Wie05	$J=-\mu_0H_{sat}((m_1m_2)/(m_1+m_2))$
Co <sub>60</sub> Fe <sub>20</sub> B <sub>20</sub> 5 / Ru 1.1 / CoFeB 3	-0.04	Wie05	$J=-\mu_0H_{sat}((m_1m_2)/(m_1+m_2))$
Co <sub>60</sub> Fe <sub>20</sub> B <sub>20</sub> 3 / Ru 1.1 / CoFeB 3.8	-0.1	Wie05	$J=-\mu_0H_{sat}((m_1m_2)/(m_1+m_2))$
Co <sub>60</sub> Fe <sub>20</sub> B <sub>20</sub> 4 / Ru 0.7 / CoFeB 3	-0.12 to -0.15	Wie04	$J=-\mu_0H_{sat}M_1t_1M_2t_2/(M_1t_1+M_2t_2)$
Co <sub>60</sub> Fe <sub>20</sub> B <sub>20</sub> 4 / Ru 0.8 / CoFeB 3	-0.04 to -0.07	Wie04	$J=-\mu_0H_{sat}M_1t_1M_2t_2/(M_1t_1+M_2t_2)$
Co <sub>60</sub> Fe <sub>20</sub> B <sub>20</sub> 4 / Ru 0.9 / CoFeB 3	-0.01	Wie04	$J=-\mu_0H_{sat}M_1t_1M_2t_2/(M_1t_1+M_2t_2)$
Co <sub>60</sub> Fe <sub>20</sub> B <sub>20</sub> 4 / Ru 1.0 / CoFeB 3	-0.05 to -0.09	Wie04	$J=-\mu_0H_{sat}M_1t_1M_2t_2/(M_1t_1+M_2t_2)$
Co <sub>60</sub> Fe <sub>20</sub> B <sub>20</sub> 4 / Ru 1.1 / CoFeB 3	-0.07 to -0.09	Wie04	$J=-\mu_0H_{sat}M_1t_1M_2t_2/(M_1t_1+M_2t_2)$
Co <sub>60</sub> Fe <sub>20</sub> B <sub>20</sub> 4 / Ru 1.2 / CoFeB 3	-0.01 to -0.03	Wie04	$J=-\mu_0H_{sat}M_1t_1M_2t_2/(M_1t_1+M_2t_2)$
Co/Ru	-1	vdB75	
Co/Cu	-0.3	vdB75	
Co 1.2 / Cu 1 / Co 2	-0.4	vdB99	

Table 3.2: Literature values for interlayer exchange coupling. For details of the stack and the preparation see cited papers. Sai06: *JAP 99 (2006) 08K702*, Saito et al., Wie06: *Nils Wiese, PhD thesis, 2006*, Fas06: *JAP 99 (2006) 08G301*, Fassbender et al., Wie05: *JMMM 290 (2005) 1427*, Wiese et al., Wie04: *APL 85 (2004) 2020*, Wiese et al., vdB75: *JMMM 165 (1975) 524*, van den Berg et al., vdB75: *JMMM 165 (1975) 524*, van den Berg et al., vdB99: *IEEE TMag 35 (1999) 2892*, van den Berg et al.

anisotropy axis is present.

The values obtained with this kind of calculations for several measurements are shown in tab. 3.3.

A good agreement between the projection of the calculated magnetization vector on the direction of the external magnetic field and the experiment has been obtained with these values [Fig. 3.32 (c)].

Considering the energy contributions described above, the magnetization reversal for stack  $Ru_{AF}^{no-IrMn}$  can be explained as follows: At high magnetic fields, the Zeeman energy is the dominating term and both FM layers are aligned parallel to the external magnetic field (Figures 3.31 and 3.32 region *V*). For a decreasing magnetic field, the thinner, lower FM layer turns the direction of its magnetization  $\mathbf{M}_{2nmCoFe}$  due to the antiferromagnetic interlayer exchange coupling (*IV*). The direction of the magnetization  $\mathbf{M}_{3nmCoFe}$  of the thicker FM layer is slightly influenced during the switching of  $\mathbf{M}_{2nmCoFe}$  because of the IEC [Fig. 3.32 (b)]. The hysteresis loop at zero magnetic field (*III*) results from a switching of the net magnetic moment of the two coupled FM layers (compare, e.g., Ref. [177]). Here, the magnetization direction of both FM layers switches and the antiparallel orientation remains unchanged. With an increasing negative magnetic field the magnetization direction of the thinner FM layer turns parallel to the external field again due to the growing Zeeman interaction (*II*) until both FM layers are saturated (*I*).

In the comparison of the two MOKE measurements of the samples  $Ru_{AF}$  and  $Ru_{AF}^{no-IrMn}$  in Fig. 3.31 the effect of the EB on the shape of measurements clearly can be seen. The magnetic field represented by positive values of  $H_{ext}$  during the measurement in Fig. 3.31 is aligned parallel to  $\mathbf{H}_{FC}$ . Therefore, the EB interaction acts like an additional positive external field which can be sensed only by the thin FM layer. As a result of this, a smaller positive external field is sufficient to keep the thin pinned FM layer parallel to the external magnetic field. This results in a shift of the corresponding switching field to smaller values (right blue arrow in part *IV* of Fig. 3.31). When the net magnetic moment switches around zero magnetic field (*III*), the magnetization of the thin FM layer turns from an energetically unfavorable orientation with respect to the EB to a favorable one. Therefore, this switching is promoted by the EB and takes place at higher positive fields. In the range *II*, where in the not pinned, IrMn less stack only the AF interlayer exchange coupling has to be overcome by the Zeeman coupling, now additionally the EB interaction keeps the magnetization of the thin, pinned layer in the actual position. This results in a shift of the switching field to higher negative fields.

This open loop at negative magnetic fields in Fig. 3.31 is a good indicator for the strength of the EB interaction. In Fig. 3.41 (a) it is used to investigate the ion dose dependence of the EB on a  $Ru_{AF}^{1kOe,AP}$  sample qualitatively with MOKE measurements.

### Ru-AFi: Experiments on influence of ion dose

To determine the ion dose dependence of the interlayer exchange coupling and the exchange bias, parts of a sample with stack  $Ru_{AF}^{5.4kOe,P}$  have been investigated by

Sample	Ion dose [ions/cm <sup>2</sup> ]	H <sub>IB</sub> [kOe]	H <sub>IB</sub> ⇕ H <sub>FC</sub>	K <sub>u</sub> [μJ/m <sup>2</sup> ]	J <sub>L</sub> [μJ/m <sup>2</sup> ]	J <sub>Q</sub> [μJ/m <sup>2</sup> ]	M <sub>S</sub> <sup>1</sup> (Co/CoFe) [MA/m]	M <sub>S</sub> <sup>1</sup> (Py) [MA/m]	M <sub>S</sub> <sup>2</sup> (Co/CoFe) [MA/m]	Fig.
$Ru_{AF}^{no\ IrMn}$	0	-	-	0	-540	-90	1.07	-	1.24	3.32
$Ru_{AF}^{5.4kOe,P}$	0	-	-	220	-270	-72	1.04	-	1.27	3.34, C.1
$Ru_{AF}^{5.4kOe,P}$	$5.0 \times 10^{12}$	5.4	↑↑	235	-310	-60	1.04	-	1.27	C.2
$Ru_{AF}^{5.4kOe,P}$	$1.0 \times 10^{13}$	5.4	↑↑	238	-340	-40	1.04	-	1.27	C.3
$Ru_{AF}^{5.4kOe,P}$	$2.5 \times 10^{13}$	5.4	↑↑	240	-340	-40	1.04	-	1.27	C.4
$Ru_{AF}^{5.4kOe,P}$	$5.0 \times 10^{13}$	5.4	↑↑	260	-390	-40	1.04	-	1.27	3.35, C.5
$Ru_{AF}^{5.4kOe,P}$	$7.5 \times 10^{13}$	5.4	↑↑	230	-400	-36	1.04	-	1.27	C.6
$Ru_{AF}^{5.4kOe,P}$	$1.0 \times 10^{14}$	5.4	↑↑	245	-360	-30	1.04	-	1.27	C.7
$Ru_{AF}^{5.4kOe,P}$	$4.0 \times 10^{14}$	5.4	↑↑	120	-100	-	1.04	-	1.27	3.36, C.8
$Ru_{AF}^{5.4kOe,P}$	$4.0 \times 10^{14}$	5.4	↑↑	245	4000	-	1.04	-	1.27	3.36, C.8
$Ru_{AF}^{5.4kOe,P}$	$4.0 \times 10^{14}$	5.4	↑↑	245	-200	-	1.04	-	1.27	3.36, C.8
$Ru_{AF}^{1kOe,AP}$	$4.0 \times 10^{14}$	1	↑↓	<b>20</b>	-180	-60	1.04	-	1.27	3.43
$Ru_{AF}^{1kOe,AP}$	$4.0 \times 10^{14}$	1	↑↓	<b>20</b>	200	200	1.04	-	1.27	3.43
$Cu_{AF}$	0	1	↑↓	22.5	-11	-8	0.88	0.18	0.88	3.48, E.1
$Cu_{AF}$	$4.7 \times 10^{12}$	1	↑↓	12	-16.6	-4.8	0.88	0.18	0.88	E.1
$Cu_{AF}$	$9.4 \times 10^{12}$	1	↑↓	10	-15	-5	0.88	0.18	0.88	E.2
$Cu_{AF}$	$1.7 \times 10^{13}$	1	↑↓	<b>10</b>	-10	-3.4	0.88	0.18	0.88	E.2
$Cu_{AF}$	$2.5 \times 10^{13}$	1	↑↓	<b>17</b>	-3	-3	0.88	0.18	0.88	E.3
$Cu_{AF}$	$4.6 \times 10^{13}$	1	↑↓	<b>31</b>	400	-	0.88	0.18	0.88	E.3
$Cu_{AF}$	$6.3 \times 10^{13}$	1	↑↓	<b>27</b>	400	-	0.88	0.18	0.88	E.4
$Cu_{AF}$	$2.0 \times 10^{14}$	1	↑↓	<b>18.1</b>	400	-	0.88	0.18	0.88	E.4
$Cu_{AF}$	$3.0 \times 10^{14}$	1	↑↓	<b>13.5</b>	400	-	0.88	0.18	0.88	E.5

Table 3.3: Parameters obtained by fine tuning values to get optimum agreement between energy minimization calculation with Eq. 3.1 and measurement. The thickness of the FM layers is chosen according to the real thickness of the layers (see Tab. 3.1).  $K_1$  and  $K_2$  were set to zero for listed calculations. The calculation for stack  $Ru_{AF}^{no\ IrMn}$  with non zero  $K_i$  shown in App. D resulted in the same parameters  $J_L$ ,  $J_Q$ ,  $K_u$  and  $M_S^i$  as the listed calculation with zero  $K_i$ . The calculations for stack  $Ru_{AF}^{5.4kOe,P}$  after IB with  $4 \times 10^{14}$  ions/cm<sup>2</sup> and 5.4 kOe ( $\mathbf{H}_{IB} \uparrow \uparrow \mathbf{H}_{FC}$ ) approximate different parts of the magnetization reversal process (compare Fig. 3.36). A superposition of the two listed calculations for stack  $Ru_{AF}^{1kOe,AP}$  after IB with  $4 \times 10^{14}$  ions/cm<sup>2</sup> and  $H_{IB}=1$  kOe ( $\mathbf{H}_{IB} \uparrow \downarrow \mathbf{H}_{FC}$ ) is needed to approximate the measurement (compare Fig. 3.43). Bold values of  $K_u$  symbolize a rotated EB direction.

AGM and MOKE after FC and after a subsequent IB step with  $H_{IB}=5400$  Oe and  $\mathbf{H}_{IB}\uparrow\uparrow\mathbf{H}_{FC}$ . The ion bombardment has been carried out homogeneously on each part for several doses of 10 keV He ions. Selected measurements before and after IB and the corresponding calculated magnetization reversal processes adjusted to the measurement after IB are shown in Figures 3.34 to 3.36. The measurements with the corresponding calculations for all investigated ion doses can be found in appendix C (Fig. C.1 to C.8).

The reference sample without IB has been measured twice together with the other samples: once before the IB of the other samples and once afterward (Fig. 3.34).

In Fig. 3.35 and 3.36 and Fig. C.2 to C.8 the change of the magnetization reversal process for an increasing ion dose can be observed. The difference of the width of the hysteresis at a positive external magnetic field before and after ion bombardment is for no ion dose larger than the difference between the two measurements at the not bombarded reference sample. Therefore, no conclusions can be drawn from the variation of this feature. One reason for the variation of the hysteresis at positive magnetic fields can be a slight variation of the orientation of the sample in the AGM. The effect of a tilt of about  $10^\circ$  can be seen in Fig. 3.37. This slight variation of the angle can also partly explain the differences in the shape of the AGM measurements before IB shown in Figures 3.34 to 3.36 and C.1 to C.8. Additionally, small local variations in, e.g., the ruthenium thickness can result in local variations of the IEC and, therefore, change the shape of AGM measurements carried out at different parts of the same sample.

Some of the AGM measurements after IB show a different width of the hysteresis loop at negative values of the external magnetic field compared to the measurements before IB. But these differences do not show a clear dependence on the ion dose as, e.g., the width after IB is smaller for  $5 \times 10^{12}$  ions/cm<sup>2</sup> (Fig. C.2) but slightly larger for  $5 \times 10^{13}$  ions/cm<sup>2</sup> (Fig. 3.35 / C.5) and no difference is observed for most ion doses.

Therefore, here the focus is set to the shift of the switching fields. This can be reproduced by choosing the bilinear interlayer exchange constant  $J_L$ , the biquadratic interlayer exchange constant  $J_Q$  and the exchange bias anisotropy constant  $K_u$  in energy minimization calculations according to equation 3.1 as shown in Figures 3.34 to 3.36 and C.1 to C.8. The values obtained for  $K_u$ ,  $J_L$  and  $J_Q$  with sample  $Ru_{AF}^{5.4kOe,P}$  are summarized in Fig. 3.38.  $K_1$  and  $K_2$  have been set to zero during all calculations.

The strength of the EB without IB is in the same range as values calculated from the shift of the hysteresis loop  $H_{EB}$  of single pinned FM layers (Fig 3.39). The EB coupling constants shown in Fig. 3.39 have been calculated with the equation  $K_u = \mu_0 M_{sat} dH_{EB}$ . For details see table 3.4. Furthermore, the values of  $0.02$  mJ/m<sup>2</sup> ( $Cu_{AF}$ ) to  $0.22$  mJ/m<sup>2</sup> ( $Ru_{AF}$ ) obtained by energy minimization calculations (no IB) fit good to the range of  $0.01$  mJ/m<sup>2</sup> to  $0.19$  mJ/m<sup>2</sup> ( $0.01$  erg/cm<sup>2</sup> to

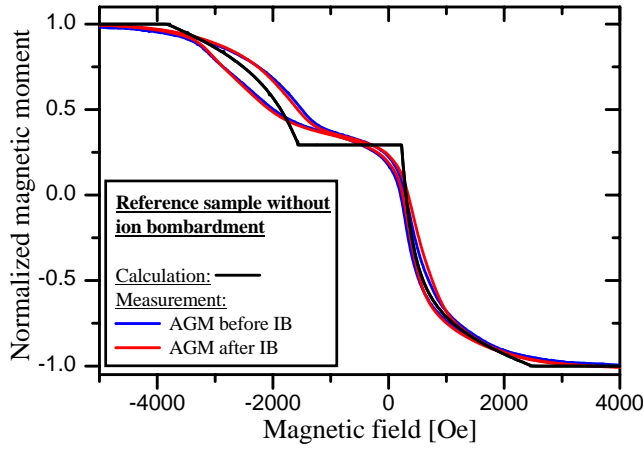


Figure 3.34: AGM measurements of not bombarded part of sample  $Ru_{AF}^{5.4kOe,P}$  carried out together with the measurements shown in Fig. 3.35, 3.36, and C.2 to C.8 before and after the other samples have been bombarded. The calculated magnetization reversal has been obtained with  $J_L = -2.7 \times 10^{-4} \text{ J/m}^2$ ,  $J_Q = -7.2 \times 10^{-5} \text{ J/m}^2$  and  $K_u = 2.2 \times 10^{-4} \text{ J/m}^2$ .

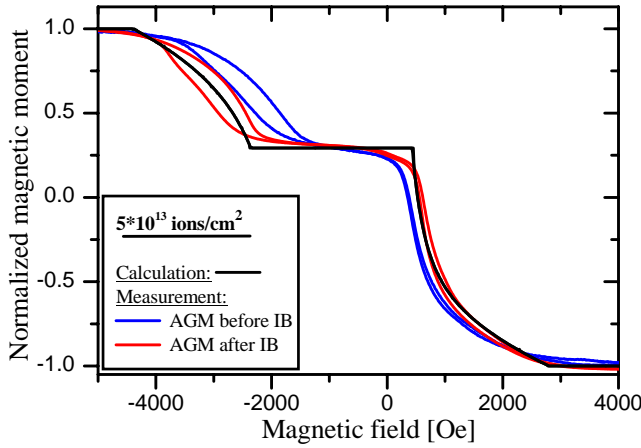


Figure 3.35: AGM measurements carried out before and after IB with  $5 \times 10^{13} \text{ ions/cm}^2$  and  $H_{IB} = 5.4 \text{ kOe}$ . The best agreement of the calculated magnetization reversal with the measurement after IB has been obtained with  $J_L = -3.9 \times 10^{-4} \text{ J/m}^2$ ,  $J_Q = -4.0 \times 10^{-5} \text{ J/m}^2$  and  $K_u = 2.6 \times 10^{-4} \text{ J/m}^2$ .

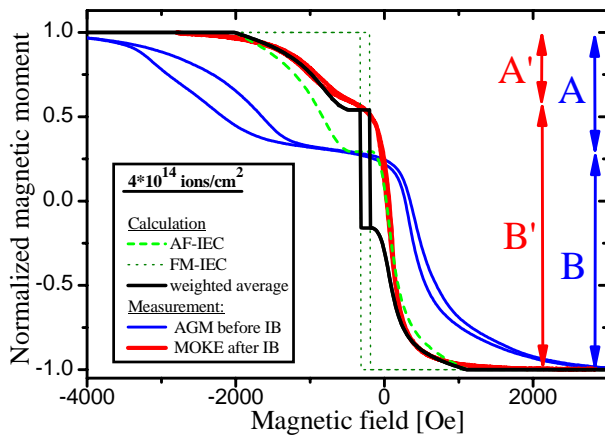


Figure 3.36: AGM measurements carried out before and MOKE measurements carried out after IB with  $4 \times 10^{14} \text{ ions/cm}^2$  and  $H_{IB} = 5.4 \text{ kOe}$ . The calculated magnetization reversals have been obtained for *antiferromagnetic inter-layer exchange coupling (IEC)* (dashed bright green line) with:  $J_L = -8.0 \times 10^{-5} \text{ J/m}^2$ ,  $J_Q = -6.0 \times 10^{-5} \text{ J/m}^2$  and  $K_u = 1.5 \times 10^{-4} \text{ J/m}^2$ , and for

*ferromagnetic IEC* (dotted dark green line) with:  $J_L = +4.0 \times 10^{-3} \text{ J/m}^2$ ,  $J_Q = 0 \text{ J/m}^2$  and  $K_u = 1.5 \times 10^{-4} \text{ J/m}^2$  and weighted superposition (black solid line) of both calculations with 65% antiferromagnetic IEC and 35% ferromagnetic IEC. A and B (A' and B') indicate the change of the normalized magnetic moment in the positive and negative magnetic field range, respectively.



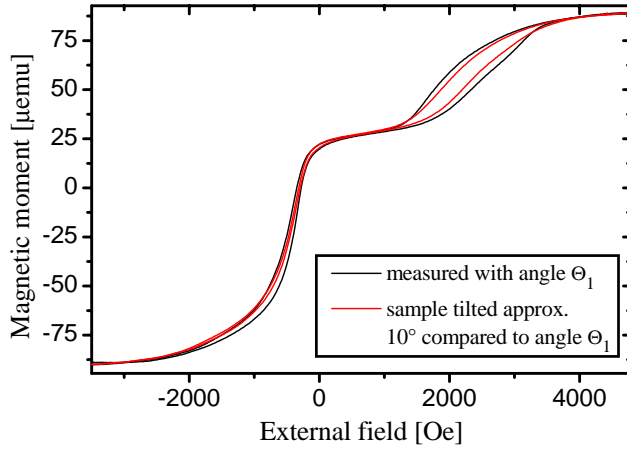


Figure 3.37: AGM measurement of sample  $Ru_{AF}$  (FC but no IB) at angle  $\Theta_1$  with an approximately parallel orientation of the magnetic field during measurement and the exchange bias direction imprinted by the magnetic field  $\mathbf{H}_{FC}$  during field cooling and approximately  $10^\circ$  tilted relative to angle  $\Theta_1$ .

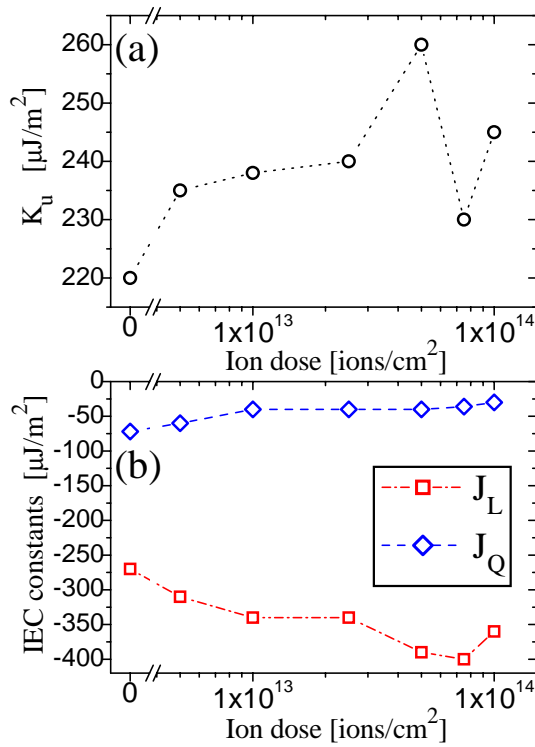


Figure 3.38: (a) Exchange bias anisotropy constant  $K_u$  and (b) interlayer exchange coupling (IEC) constants: bilinear interlayer exchange constant  $J_L$  and biquadratic interlayer exchange constant  $J_Q$  of sample  $Ru_{AF}^{5.4kOe,P}$  in dependence of the ion dose. ( $H_{IB}=5.4kOe$ ,  $\mathbf{H}_{IB}\uparrow\mathbf{H}_{FC}$ , He ion energy: 10keV)

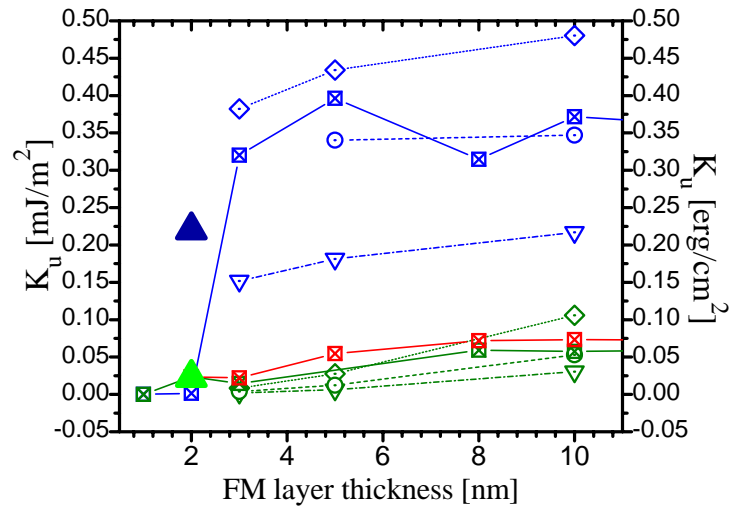


Figure 3.39: Unidirectional anisotropy constant  $K_u$  for pinned monolayers (open symbols) consisting of  $\text{Co}_{70}\text{Fe}_{30}$  (blue symbols), Co (red) and Py ( $\text{Ni}_{80}\text{Fe}_{20}$ , green). The antiferromagnetic layer was  $\text{Ir}_{17}\text{Mn}_{83}$  with a thickness of 8 nm ( $\diamond$ , dotted line), 10 nm ( $\square$ , solid line), 15 nm ( $\circ$ , dashed line) or 30 nm ( $\nabla$ , dash-dotted line). The constants represented by open symbols have been obtained with the equation  $K_u = \mu_0 M_{sat} dH_{EB}$ . For values represented by symbols with a cross (e.g.,  $\otimes$ )  $H_{EB}$  and the saturation magnetization  $M_{sat}$  have been obtained by AGM measurements. Symbols with a dot (e.g.,  $\odot$ ) represent constants where  $H_{EB}$  is obtained by MOKE measurements and  $M_{sat}$  is taken from Fig. 3.33. Results of fits to the magnetization reversal process of AFIs are symbolized by solid triangles pointing upwards (blue triangle:  $Ru_{AF}$ , IrMn 15 nm/CoFe 2 nm/Ru/CoFe 3 nm; green triangle:  $Cu_{AF}$ , IrMn 10 nm/Py 2 nm/Co 2 nm/Cu/Co 2 nm). All samples have been field cooled (see table 3.1 for details) but not bombarded.

Sample	FM	Exp. method	Thickness FM [nm]	Thickness IrMn [nm]	$H_{EB}$ [Oe]	$H_{EB}$ [A/m]	$M_{sat}$ [kA/m] [emu/cm <sup>3</sup> ]	$K_u$ [ $\mu$ J/m <sup>2</sup> ]
<i>FM-A</i> <sub>8IrMn/3CoFe pinned</sub>	Co <sub>70</sub> Fe <sub>30</sub>	MOKE	3	8	942	74962	1353	382
<i>FM-A</i> <sub>8IrMn/5CoFe pinned</sub>	Co <sub>70</sub> Fe <sub>30</sub>	MOKE	5	8	551	43847	1576	434
<i>FM-A</i> <sub>8IrMn/10CoFe pinned</sub>	Co <sub>70</sub> Fe <sub>30</sub>	MOKE	10	8	281	22361	1709	480
<i>FM-B</i> <sub>1 CoFe/10IrMn pinned</sub>	Co <sub>70</sub> Fe <sub>30</sub>	AGM	1	10	0	0	6	0
<i>FM-B</i> <sub>2 CoFe/10IrMn pinned</sub>	Co <sub>70</sub> Fe <sub>30</sub>	AGM	2	10	75.46	6005	101	2
<i>FM-B</i> <sub>3 CoFe/10IrMn pinned</sub>	Co <sub>70</sub> Fe <sub>30</sub>	AGM	3	10	856.8	68182	1245	320
<i>FM-B</i> <sub>5 CoFe/10IrMn pinned</sub>	Co <sub>70</sub> Fe <sub>30</sub>	AGM	5	10	500.7	39844	1583	396
<i>FM-B</i> <sub>8 CoFe/10IrMn pinned</sub>	Co <sub>70</sub> Fe <sub>30</sub>	AGM	8	10	232.3	18486	1693	315
<i>FM-B</i> <sub>10 CoFe/10IrMn pinned</sub>	Co <sub>70</sub> Fe <sub>30</sub>	AGM	10	10	203.3	16178	1828	372
<i>FM-B</i> <sub>20 CoFe/10IrMn pinned</sub>	Co <sub>70</sub> Fe <sub>30</sub>	AGM	20	10	95.5	7600	1733	331
<i>FM-B</i> <sub>50 CoFe/10IrMn pinned</sub>	Co <sub>70</sub> Fe <sub>30</sub>	AGM	50	10	25.23	2008	1893	239
<i>FM-A</i> <sub>15IrMn/3CoFe pinned</sub>	Co <sub>70</sub> Fe <sub>30</sub>	MOKE	3	15	675	53715	1353	274
<i>FM-A</i> <sub>15IrMn/5CoFe pinned</sub>	Co <sub>70</sub> Fe <sub>30</sub>	MOKE	5	15	432	34377	1576	340
<i>FM-A</i> <sub>15IrMn/10CoFe pinned</sub>	Co <sub>70</sub> Fe <sub>30</sub>	MOKE	10	15	203	16154	1709	347
<i>FM-A</i> <sub>30IrMn/3CoFe pinned</sub>	Co <sub>70</sub> Fe <sub>30</sub>	MOKE	3	30	374	29762	1353	152
<i>FM-A</i> <sub>30IrMn/5CoFe pinned</sub>	Co <sub>70</sub> Fe <sub>30</sub>	MOKE	5	30	230	18303	1576	181
<i>FM-A</i> <sub>30IrMn/10CoFe pinned</sub>	Co <sub>70</sub> Fe <sub>30</sub>	MOKE	10	30	127	10106	1709	217
<i>FM-C</i> <sub>2 Co/10IrMn pinned</sub>	Co	AGM	2	10	279.4	22234	421	24
<i>FM-C</i> <sub>3 Co/10IrMn pinned</sub>	Co	AGM	3	10	191.77	15261	385	22
<i>FM-C</i> <sub>5 Co/10IrMn pinned</sub>	Co	AGM	5	10	105.04	8359	1042	55
<i>FM-C</i> <sub>8 Co/10IrMn pinned</sub>	Co	AGM	8	10	73.45	5845	1222	72
<i>FM-C</i> <sub>10 Co/10IrMn pinned</sub>	Co	AGM	10	10	62.569	4979	1171	73
<i>FM-C</i> <sub>20 Co/10IrMn pinned</sub>	Co	AGM	20	10	28.399	2260	1232	70
<i>FM-A</i> <sub>8IrMn/3Py pinned</sub>	Py	MOKE	3	8	542	43131	51	8
<i>FM-A</i> <sub>8IrMn/5Py pinned</sub>	Py	MOKE	5	8	319	25385	173	28
<i>FM-A</i> <sub>8IrMn/10Py pinned</sub>	Py	MOKE	10	8	137	10902	774	106
<i>FM-C</i> <sub>1 Py/10IrMn pinned</sub>	Py	AGM	1	10	0		13	0
<i>FM-C</i> <sub>2 Py/10IrMn pinned</sub>	Py	AGM	2	10	461.88	36755	255	24
<i>FM-C</i> <sub>3 Py/10IrMn pinned</sub>	Py	AGM	3	10	285.24	22699	172	15
<i>FM-C</i> <sub>8 Py/10IrMn pinned</sub>	Py	AGM	8	10	98.25	7818	753	59
<i>FM-C</i> <sub>10 Py/10IrMn pinned</sub>	Py	AGM	10	10	80.31	6391	715	57
<i>FM-C</i> <sub>20 Py/10IrMn pinned</sub>	Py	AGM	20	10	39	3104	814	63
<i>FM-C</i> <sub>50 Py/10IrMn pinned</sub>	Py	AGM	50	10	14.798	1178	874	65
<i>FM-A</i> <sub>15IrMn/3Py pinned</sub>	Py	MOKE	3	15	248	19735	51	4
<i>FM-A</i> <sub>15IrMn/5Py pinned</sub>	Py	MOKE	5	15	141	11220	173	12
<i>FM-A</i> <sub>15IrMn/10Py pinned</sub>	Py	MOKE	10	15	68.4	5443	774	53
<i>FM-A</i> <sub>30IrMn/3Py pinned</sub>	Py	MOKE	3	30	124	9868	51	2
<i>FM-A</i> <sub>30IrMn/5Py pinned</sub>	Py	MOKE	5	30	74	5889	173	6
<i>FM-A</i> <sub>30IrMn/10Py pinned</sub>	Py	MOKE	10	30	39.4	3135	774	30

Table 3.4: Uniaxial anisotropy constant  $K_u$  for pinned monolayers of Co<sub>70</sub>Fe<sub>30</sub>, Co and Py (Ni<sub>80</sub>Fe<sub>20</sub>).  $K_u$  has been obtained with the equation  $K_u = \mu_0 M_{sat} dH_{EB}$ . *AGM*:  $H_{EB}$  and saturation magnetization  $M_{sat}$  obtained by same AGM measurement, *MOKE*:  $H_{EB}$  obtained by MOKE measurement and  $M_{sat}$  taken from Fig. 3.33.

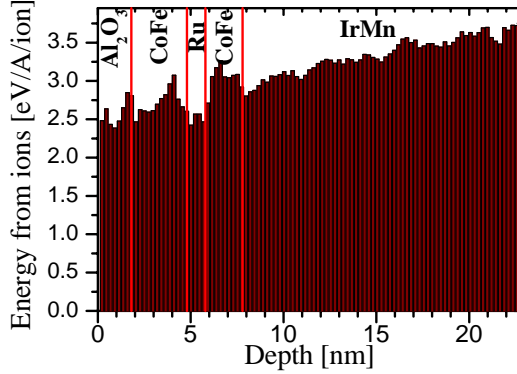


Figure 3.40: SRIM simulation of energy transferred per Å depth from one 10 keV He ion to sample  $Ru_{AF}$ .

0.19 erg/cm<sup>2</sup>) published in Ref. [38] for samples containing IrMn.<sup>14</sup>

The bombardment with 10 keV He ions has been done in a magnetic field of 5400 Oe oriented parallel to  $\mathbf{H}_{FC}$ . Therefore, the magnetization of the CoFe layer adjacent to the IrMn was oriented parallel to  $\mathbf{H}_{FC}$  and an enlargement of the EB can be expected [62]. This increasing strength of the EB interaction is confirmed by the increasing value of  $K_u$  up to  $5 \times 10^{13}$  ions/cm<sup>2</sup> in Fig. 3.38 (a).

When one observes the position of the switching field at negative magnetic fields in the calculated magnetization reversal it is possible to see changes of  $K_u$  as small as  $2 \mu\text{J}/\text{m}^2$  when all other parameters are fixed. But as the other parameters can be varied as well, an uncertainty of about  $15 \mu\text{J}/\text{m}^2$  should be assumed for the resulting value of  $K_u$ . Therefore, the increase of  $K_u$  is significantly larger than the experimental uncertainty.

For higher ion doses, a decreasing tendency of the EB strength is found. This is usually attributed to processes as intermixing at the FM/AF surface [29].

The bilinear interlayer exchange coupling constant  $J_L$  increases for ion doses up to  $7.5 \times 10^{13}$  ions/cm<sup>2</sup> and shows a decreasing tendency for higher ion doses up to  $1 \times 10^{14}$  ions/cm<sup>2</sup>. The biquadratic coupling constant  $J_Q$  shows a slight decrease.

To test the trends for high ion doses, the measurements carried out at a sample bombarded with  $4 \times 10^{14}$  ions/cm<sup>2</sup> are analyzed. Figure 3.38 does not show values for this ion dose as a reasonable fit was not possible, because the ratio between the change of the magnetization at positive and negative external magnetic field has changed. It is unlikely that this is due to a change of the ratio of the magnetic moments of the FM layers, because the FM layers are close to the interface and with the used ion energy of  $E_{IB}=10$  keV approximately the same amount of energy per unit depth is deposited in both layers (Fig. 3.40).

Another possible explanation is a locally varying coupling which is partly anti-ferromagnetic and partly ferromagnetic due to, e.g., the formation of ferromagnetic

<sup>14</sup>The strength of the EB coupling depends, e.g., on the thickness of the AF and the FM layer (compare Fig. 3.33), the choice of the AF and FM material and the sputter parameters. But also the method used for the EB initialization and the details of the initialization have an influence on the strength of the coupling as the enlargement of the EB by IB (Fig. 3.38) or the dependence of the EB on the annealing temperature during the field cooling step (Fig. 2.6) shows. Therefore, a value of  $K_u$  is always connected to a certain system with given materials, layer thicknesses and preparation procedures.

bridges [178] and which can not be resolved by the MOKE.<sup>15</sup> In Fig. 3.36 (C.8) a calculated magnetization reversal process is shown which approximately reproduces the magnetic fields at which the magnetization switches (bright green dashed line). As it is not possible to adjust the shape of the calculated magnetization reversal process to the measured one, an average value of  $J_Q$  has been used which does not necessarily fit to the real strength of the biquadratic coupling in this sample. To match the small change of the magnetization at negative magnetic fields (black solid line), it is necessary to assume that 35% of the sample are coupled ferromagnetically (dark green dotted line). The value of  $J_L = +4.0 \times 10^{-3} \text{ J/m}^2$  is an arbitrary value resulting in a ferromagnetic coupling as it is not possible to distinguish between different values of  $J_L$  from AGM or MOKE measurements once the coupling is ferromagnetic. The assumption of antiferromagnetically and ferromagnetically coupled parts is a strong simplification as in reality a superposition of several more or less (anti-)ferromagnetically coupled areas can be expected when this effect is due to a local variation of the coupling. Furthermore, adjacent areas with a dominating FM and AF coupling would be coupled, e.g., via the exchange coupling inside the FM layer and would not necessarily switch independently. When the constant  $J_L = -8 \times 10^{-5} \text{ J/m}^2$  obtained by the calculation with the antiferromagnetic coupling is used as an upper barrier, one can see that the strength of the IEC is significantly decreasing in this range of the ion dose as it is already indicated by the slightly smaller coupling observed with the ion dose  $1 \times 10^{14} \text{ ions/cm}^2$ . The strength of the EB coupling ( $K_u = 1.5 \times 10^{-4} \text{ J/m}^2$ ) is significantly decreased compared to the smaller ion doses.

A qualitative confirmation of the ion dose dependence of the interlayer exchange and exchange bias coupling with interesting effects at the ion dose of  $4 \times 10^{14} \text{ ions/cm}^2$  have been found in a similar experiment with the same kind of samples but with a magnetic field during IB of  $H_{IB} = -1000 \text{ Oe}$ .

In this case  $\mathbf{H}_{IB}$  is oriented antiparallel to the magnetic field during field cooling. This forces the magnetization of the 3 nm thick upper CoFe layer to turn into this direction. Because the field of  $-1000 \text{ Oe}$  is not large enough to overcome the antiferromagnetic IEC (compare Fig. 3.31), the magnetization of the 2 nm thick lower CoFe layer, which is adjacent to the IrMn layer, is oriented parallel to  $\mathbf{H}_{FC}$ . Therefore, again an enlargement of the EB due to IB and a shift of the loop at negative magnetic fields (turning of magnetization of thin FM layer against the IEC) to larger negative fields can be expected.

The maximum magnetic field during the MOKE measurements is not sufficient to saturate both FM layers of sample  $Ru_{AF}^{1kOe,AP}$  (Fig. 3.41). Therefore, it is not possible to determine  $J_L$ ,  $J_Q$  and  $K_u$  from this measurements. But nevertheless all important features of the magnetization reversal process and especially the qualitative change of the shift of the loop at negative magnetic field by the IB can be seen.

Only a small change was observed in MOKE measurements after an IB with  $5 \times 10^{12} \text{ ions/cm}^2$  (Fig. 3.41 (a)). With increasing ion dose an increase of the EB and/or IEC accompanied by an increasing shift of the loop at negative fields can be observed until a maximum is found for the range of  $5 \times 10^{13} \text{ ions/cm}^2$ . This dose dependence

<sup>15</sup>The signal of the MOKE is always averaged over the area of the laser spot with approximately 0.2 mm thickness.

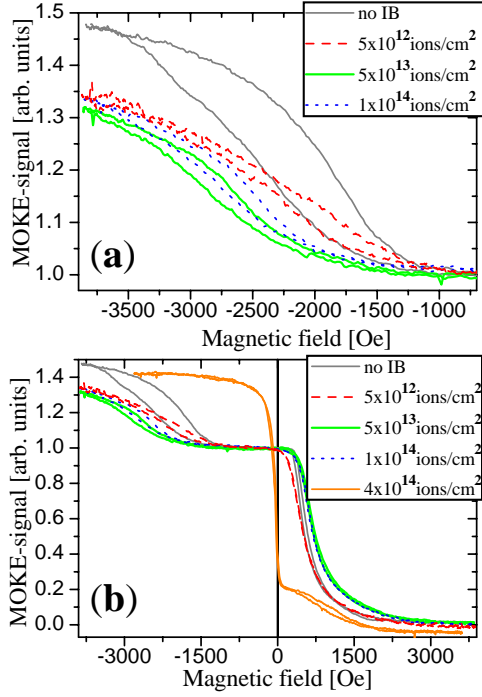


Figure 3.41: MOKE measurements on  $Ru_{AF}^{1kOe,AP}$  sample for several ion doses; (a) shows a magnification of a region in (b). All measurements except  $4 \times 10^{14}$  ions/cm<sup>2</sup> in part (b) have been set to zero at saturation at high positive fields and normalized to 1 at -350 Oe. ( $H_{IB}=1$  kOe,  $\mathbf{H}_{IB} \uparrow \downarrow \mathbf{H}_{FC}$ )

of the loop shift reproduces the ion dose dependence of  $K_u$  and  $J_L$  observed in the AGM measurements after the ion bombardment with  $H_{IB}=5400$  Oe and a parallel alignment of  $\mathbf{H}_{FC}$  and  $\mathbf{H}_{IB}$ . The decrease of the MOKE signal at the maximum field of -3850 Oe for an increasing shift of the loop to negative fields in Fig. 3.41 (a) is due to the fact that the maximum magnetic field applied during the MOKE measurements is not sufficient to saturate all magnetic layers totally.

When a degradation of the antiferromagnetic IEC occurs, a smaller external magnetic field is sufficient to align the magnetic moments of both ferromagnetic layers parallel. This would result in a shift of the loop in Fig. 3.41 (a) to smaller magnetic fields. As this can not be observed for doses up to  $5 \times 10^{13}$  ions/cm<sup>2</sup> a severe degradation of the AF coupling in this dose range can be ruled out. For larger ion doses of  $7.5 \times 10^{13}$  ions/cm<sup>2</sup> (not shown) and  $1 \times 10^{14}$  ions/cm<sup>2</sup> [Fig. 3.41 (a)] the shift starts to get smaller again. This slight decrease of the shift is a hint that a reduction of the AF interlayer coupling or the EB coupling occurs at this ion dose. This fits to the reduction of  $K_u$  for  $7.5 \times 10^{13}$  ions/cm<sup>2</sup> and  $1 \times 10^{14}$  ions/cm<sup>2</sup> and  $J_L$  for  $1 \times 10^{14}$  ions/cm<sup>2</sup> in Fig. 3.38. Therefore, the information about the ion dose dependence of the interlayer exchange coupling and the exchange bias which can be deduced from the MOKE measurements after IB with  $H_{IB}=1$  kOe and  $\mathbf{H}_{IB} \uparrow \downarrow \mathbf{H}_{FC}$  in Fig. 3.41 up to  $1 \times 10^{14}$  ions/cm<sup>2</sup> nicely reproduces the results of the experiments with  $H_{IB}=5.4$  kOe ( $\mathbf{H}_{IB} \uparrow \uparrow \mathbf{H}_{FC}$ ) in Figures 3.34 to 3.38 and C.1 to C.8.

A conspicuous change of the magnetization loop can be seen in Fig. 3.41 (b) for  $4 \times 10^{14}$  ions/cm<sup>2</sup>. The shape of this measurements can be explained by a pinning of the 2 nm thick FM layer in an opposite direction compared to all other measurements. Furthermore, the shift of the small loop (thin layer turning against AF

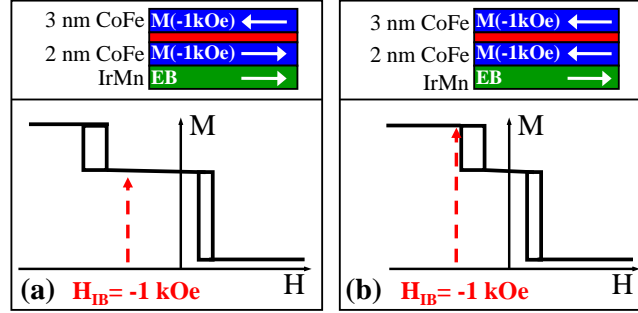


Figure 3.42: (a) Sketch of magnetization reversal process without IB (lower part) and orientation of magnetization at  $-1000$  Oe with parallel alignment of  $\mathbf{H}_{EB}$  and magnetization  $M$  of the 2 nm CoFe layer (upper part) and (b) sketch of magnetization reversal process with reduced interlayer exchange coupling and/or exchange bias (lower part) and corresponding orientation of magnetization at  $-1000$  Oe with antiparallel alignment of  $\mathbf{H}_{EB}$  and  $\mathbf{M}_{2nmCoFe}$  (upper part).

interlayer exchange coupling), which is found at positive fields now, is smaller than before. This effect results from a reduction of the AF interlayer exchange coupling and/or the exchange bias by the IB during the bombardment process.

The lower part of Fig. 3.42 (a) shows a sketch of a magnetization reversal process as it has been observed without IB (compare Fig. 3.34). The magnetization  $\mathbf{M}_{3nmCoFe}$  of the thicker FM layer is aligned parallel to the external field  $\mathbf{H}_{ext}$  of  $-1000$  Oe. The magnetization of the lower, 2 nm thick CoFe layer adjacent to the IrMn layer ( $\mathbf{M}_{2nmCoFe}$ ) is oriented antiparallel to  $\mathbf{M}_{3nmCoFe}$  at  $-1000$  Oe and, therefore, parallel to  $\mathbf{H}_{FC}$ . In this configuration the EB can be enlarged by IB. When the antiferromagnetic IEC and/or the exchange bias are significantly decreased during the IB, the loop at negative field is shifted towards zero field [lower part of Fig. 3.42 (b)]. This results in an antiparallel orientation of  $\mathbf{M}_{2nmCoFe}$  and  $\mathbf{H}_{FC}$  at  $H_{IB} = -1000$  Oe and the EB direction can be turned by the following ions.

A direct determination of the energy constants with the fitting method described above is not possible because the relative height of the loop of the thin layer compared to the thick layer has decreased (compare to  $4 \times 10^{14}$  ions/cm<sup>2</sup> with  $H_{IB} = 5400$  Oe and  $\mathbf{H}_{IB} \uparrow \uparrow \mathbf{H}_{FC}$ ). Again, a rough approximation of the magnetization reversal process can be obtained by assuming a superposition of the signal of ferromagnetically and antiferromagnetically coupled areas. The result of a calculation with one half of the sample with a ferromagnetic coupling and one half with an antiferromagnetic coupling is shown in Fig. 3.43. The step in the calculated magnetization reversal is again due to the fact that only two distinct values of  $J_L$  have been used while a superposition of several values for the different places of the sample is much more likely. The value of  $J_L$  of less than  $-1.8 \times 10^{-4}$  J/m<sup>2</sup> resulting from this calculation<sup>16</sup> fits well to the decrease of this quantity with increasing ion dose (Fig. 3.38) although it is higher than the value obtained in the calculation with  $4 \times 10^{14}$  ions/cm<sup>2</sup>,  $H_{IB} = 5400$  Oe and  $\mathbf{H}_{IB} \uparrow \uparrow \mathbf{H}_{FC}$  ( $J_L = -8 \times 10^{-5}$  J/m<sup>2</sup>).

<sup>16</sup>The values of  $J_L = 2 \times 10^{-4}$  J/m<sup>2</sup> and  $J_Q = 2 \times 10^{-4}$  J/m<sup>2</sup> used for the simulation of the part with FM coupling are, again, arbitrarily chosen due to the ferromagnetic coupling (compare page 93).

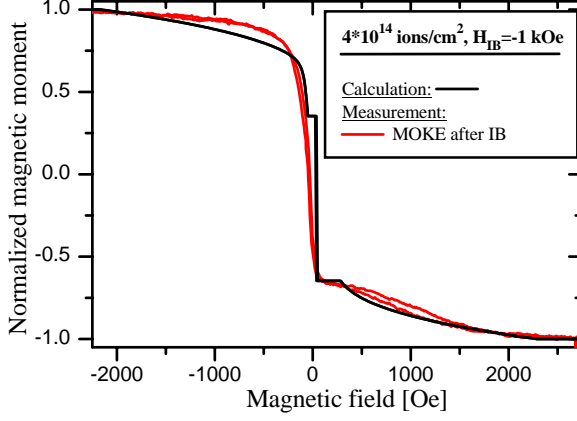


Figure 3.43: Normalized MOKE measurement of sample  $Ru_{AF}^{1kOe, AP}$  after IB with  $4 \times 10^{14}$  ions/cm<sup>2</sup> and  $H_{IB} = -1000$  Oe and calculated magnetization reversal with  $K_u = 2 \times 10^{-5}$  J/m<sup>2</sup> and one half of the sample with an antiparallel IEC ( $J_L = -1.8 \times 10^{-4}$  J/m<sup>2</sup>,  $J_Q = -6.0 \times 10^{-5}$  J/m<sup>2</sup>) and the other half of the sample with a ferromagnetic IEC ( $J_L = 2 \times 10^{-4}$  J/m<sup>2</sup>,  $J_Q = 2 \times 10^{-4}$  J/m<sup>2</sup>).

The value used for  $K_u$  of  $2 \times 10^{-5}$  J/m<sup>2</sup> is significantly smaller than the values obtained without IB and for smaller ion doses after bombardment with  $H_{IB} = 5400$  Oe and  $\mathbf{H}_{IB} \uparrow \uparrow \mathbf{H}_{FC}$  (Fig. 3.38) as well as the upper limit found for  $4 \times 10^{14}$  ions/cm<sup>2</sup>,  $H_{IB} = 5400$  Oe and  $\mathbf{H}_{IB} \uparrow \uparrow \mathbf{H}_{FC}$  ( $K_u = 1.5 \times 10^{-4}$  J/m<sup>2</sup>). As  $K_u$  was smaller after IB with  $4 \times 10^{14}$  ions/cm<sup>2</sup>,  $H_{IB} = 5400$  Oe and  $\mathbf{H}_{IB} \uparrow \uparrow \mathbf{H}_{FC}$  than for all other doses with this magnetic field, it can be assumed, that  $4 \times 10^{14}$  ions/cm<sup>2</sup> with  $E_{IB} = 10$  keV induce a significant amount of intermixing at the CoFe/IrMn interface. This should be valid independent on the size and orientation of  $\mathbf{H}_{IB}$  and reduce the EB for  $H_{IB} = -1000$  Oe as well. Usually the modulus of the EB for high ion doses does not depend significantly on the direction of  $\mathbf{H}_{IB}$  (e.g.,  $\uparrow \uparrow$  or  $\uparrow \downarrow \mathbf{H}_{FC}$ ). The reason for the fact that in this experiments the modulus of  $K_u$  after IB with  $4 \times 10^{14}$  ions/cm<sup>2</sup> and  $\mathbf{H}_{IB}(-1000 \text{ Oe}) \uparrow \downarrow \mathbf{H}_{FC}$  is significantly smaller than after IB with  $4 \times 10^{14}$  ions/cm<sup>2</sup> and  $\mathbf{H}_{IB}(5400 \text{ Oe}) \uparrow \uparrow \mathbf{H}_{FC}$  is that in the first case the first ions did not turn the EB but increased it in the original direction.

It is not possible to determine exactly at which ion dose  $\mathbf{M}_{2nmCoFe}$  has been turned by  $H_{IB} = -1000$  Oe on a significant part of the sample but because after IB with  $1 \times 10^{14}$  ions/cm<sup>2</sup> the FM layers were aligned clearly antiparallel at an external magnetic field of  $-1000$  Oe (Fig. 3.41), the rotation has to take place in the range of  $1 \times 10^{14}$  ions/cm<sup>2</sup> to  $4 \times 10^{14}$  ions/cm<sup>2</sup>.

A variation of the value of  $J_Q$  changes mainly the shape of the switching process and, therefore, this constant can not be determined here. An average value has been used for the calculations.

To summarize the experiments with stack  $Ru_{AF}$ , it can be said that an increase of the bilinear interlayer exchange coupling constant  $J_L$  for ion doses up to  $7.5 \times 10^{13}$  ions/cm<sup>2</sup> and a decrease for higher ion doses including  $4 \times 10^{14}$  ions/cm<sup>2</sup> was found in combination with a maximum of the enlarged EB coupling at  $5 \times 10^{13}$  ions/cm<sup>2</sup>.



### Ru-AFi: Influence of ion dose – theoretical considerations

The same effect of an increasing bilinear interlayer exchange coupling for low ion doses and a decrease for higher doses in combination with a decreasing  $J_Q$  for all doses has been observed by Demokritov *et al.* for the bombardment of epitaxial Fe/Cr/Fe samples (6 and 8 monolayers Cr) with 5 keV He ions [178]. Furthermore, a decreasing antiferromagnetic interlayer coupling has not only been observed for IB with high ion doses [177, 178, 179, 180] but also for annealing at high temperatures [184].

Four effects can contribute to the magnetic coupling between the two FM layers: the bilinear IEC which can be ferromagnetic or antiferromagnetic depending on the interlayer thickness, the biquadratic IEC which favors a  $90^\circ$  orientation of the magnetizations, the magnetostatic Néel coupling (ferromagnetic) and the coupling by ferromagnetic bridges (ferromagnetic) [95]. In the investigated samples in all cases an interlayer thickness resulting in an antiferromagnetic coupling of the two FM layers prior to IB has been chosen.

The ion bombardment can influence the sample properties by several mechanisms as, e.g., intermixing at the interfaces, creation of point defects and interstitials or effects of local heating.

Some heat related effects on interlayer exchange coupled systems have been proposed in Ref. [184]. To explain the decreasing antiferromagnetic coupling after annealing at high temperatures<sup>17</sup> an intermixing at the CoFe/Ru interface because of negative enthalpies of formation for FeRu and CoRu and an increase of the ferromagnetic coupling due to ferromagnetic bridges especially in the grain boundaries has been suggested [184].

In the following paragraphs, the influence of IB on the microscopic mechanisms resulting in a change of the coupling will be discussed.

The bilinear interlayer exchange coupling can be explained by spin dependent quantum well states resulting from spin dependent reflections of electron waves at the interfaces of the interlayer [110] (compare chapter 2.4 and references therein). As the structure of the interface is altered by the intermixing due to IB, it can be assumed that this has an effect on the reflectivity. When only a small number of atoms is moved to places close to the interface they may contribute to the incoherent scattering at the expense of the coherent scattering [110]. For a larger amount of intermixing the interface might be considered to be an averaged material and the incoherent scattering from each defect can decrease [110]. When the atoms are moved deeper into the interlayer, they can change the properties of the interlayer itself.

In this context it is interesting to look at similar samples deposited by molecular beam epitaxy (MBE) and sputter deposition (Fig. 3.44). For thin Ru layers in samples deposited by MBE a significantly larger saturation field compared to samples deposited by sputter deposition has been observed [185]. This is thought to be due to a larger amount of intermixing at the FM interlayer surface in the case of the sputtered samples resulting in a random component in the atom distribution near

---

<sup>17</sup>A similar effect has been observed for the annealing of stack  $MTJ_{\text{Ru}}^{\text{MgO inv.}}$ . Compare chapter 3.8.1.

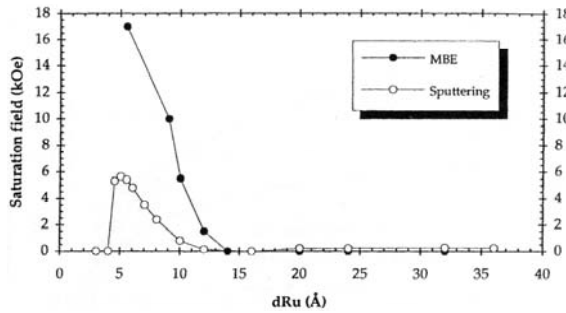


Figure 3.44: Saturation field as a function of Ru thickness in Co/Ru multilayers deposited by molecular beam epitaxy or sputter deposition. (Fig. adopted from [185])

the interface and a destructive interference of the electron waves [185].

Furthermore, the wavelength of the oscillation of the interlayer exchange coupling strength can be connected to extremal distances of the Fermi surface. When the shape of the Fermi surface is altered due to intermixing or the creation of defects, this might vary the wavelength and therefore influence whether the IEC for a given interlayer thickness is, e.g., at its maximum or not.

The interlayer thickness itself can be changed by IB when many atoms inside the interlayer are shifted from their location in the crystal and transferred to interstitials. A changed interlayer thickness would result in a change of the IEC but as many atoms have to be shifted for a significant variation of the thickness this would be accompanied with a variation of the electronic structure and a significant intermixing can be expected for such ion doses. Therefore, it is unlikely that this effect can be observed alone.

If the intermixing at the FM/interlayer interface is regarded as a reduction of the effective interlayer thickness [28] the interlayer coupling can be increased or decreased depending on the thickness of the interlayer.

The formation of alloys at the FM/interlayer interface due to local hyperthermal heating as it was described in Ref. [184] for the case of annealing, would as well change the electronic structure in the interlayer and therefore the IEC.

But as the detailed changes of the electronic structure or the reflection amplitudes by the IB via the mechanisms described in the last lines are not known, it is not possible to predict their influence on the bilinear IEC.

The origin of the biquadratic interlayer exchange coupling is thought to be connected to not intrinsic effects like roughness or magnetic impurities [99, 109, 110].

One approach to explain the biquadratic IEC is based on thickness fluctuations of the interlayer [111, 112]. In this theory, an increasing  $J_Q$  is predicted for an increasing area of monolayer high terraces of the FM layer at the interface to the interlayer as long as the formation of domains is not possible. An intermixing due to IB which would reduce the size of this terraces would then result in a reduced biquadratic IEC.

Another approach is based on the influence of loose spins of magnetic impurities in the interlayer where the coupling to the FM layers is mediated by the interlayer electrons [111, 112, 110]. Here, an increase of the biquadratic IEC for an increasing number of magnetic impurities has been predicted. A corresponding dependence of the biquadratic coupling on the amount of Fe in the interlayer of an Fe/Ag/Fe system has been reported in Ref. [115]. As the IB will increase the number of mag-

netic ions in the interlayer, an increase of the biquadratic IEC can be expected. On the other hand the IB can change the electronic structure of the interlayer as well as the interface structure what might influence the coupling of the loose spins via interlayer electrons to the FM interface. Furthermore, for high ion doses a formation of ferromagnetic bridges is likely. In this case, enough FM atoms are transferred into the interlayer at this ion doses to establish a chain of atoms connected by direct exchange coupling. Therefore, the spins connected to this structure or coupled in clusters inside the interlayer would be no longer “loose”.

Furthermore, a mechanism has been proposed which connects the biquadratic IEC and the magnetic strayfields due to uncorrelated roughness at the FM/interlayer interface [112, 110]. Here, a larger amplitude and/or a longer period of the not correlated roughness would result in a larger  $J_Q$ .

The strength of the Néel coupling depends on the thickness of the interlayer, it’s correlated roughness and the magnetization at the interface. As a result of the modification of the FM/interlayer interface the roughness of the two sides of the interlayer might be less correlated. This would reduce the ferromagnetic Néel coupling. Another effect that can reduce the Néel coupling is an enlargement of the interlayer thickness because of the change of the order of the interlayer atoms. Furthermore, the intermixing or formation of new alloys at the interface can change the magnetization in this region.

The formation of ferromagnetic bridges can be promoted by the transport of ferromagnetic material into the volume of the interlayer by direct momentum transfer to atoms in the FM layer or heat related effects.<sup>18</sup>

The assignment of the observed changes by IB to the microscopic effects is difficult as only the resulting direction of the magnetization and not the energies themselves can be detected. The differentiation between bilinear and biquadratic interlayer exchange coupling has been done by observing the shape of the magnetization reversal process as bilinear IEC promotes a parallel or antiparallel alignment while a large biquadratic IEC would result in a 90° type of coupling if  $J_L$  is small enough. But the effect of a variation of the ferromagnetic Néel coupling and/or ferromagnetic bridges can not be distinguished from a reduction or enlargement of the bilinear interlayer coupling. Therefore, the latter three effects are included in the experimentally determined  $|J_L|$ .

The increase of  $|J_L|$  at small ion doses might be connected to an increase of the IEC due to, e.g., changes of the electronic structure of the interlayer or a favorable change of the spin dependent reflection coefficients. Furthermore, a decrease of the ferromagnetic Néel coupling due to, e.g., a reduction of the correlated roughness or the magnetization at the interface might occur.

The reason for the decreasing shift for higher ion doses might be a combination of a decrease of the IEC because of the modification of the interface and of the elec-

---

<sup>18</sup>Experiments of Engel *et al.* showing a hysteresis loop at the Cu L<sub>3</sub> edge in x-ray resonant magnetic reflectivity measurements of a FeMn/Co/Cu/Co spin valve after bombardment with  $2 \times 10^{15}$  He ions per cm<sup>2</sup> in a magnetic field ( $E_{IB}=10$  keV) are another hint to the existence of a significant intermixing after IB [181].

tronic structure of the interlayer and an increasing coupling via the formation of ferromagnetic bridges. Demokritov *et al.* were able to reproduce 83% of the observed decrease of the antiferromagnetic coupling in their samples by an estimation of the coupling strength of ferromagnetic bridges. The area of these bridges has been determined out of the number of atoms which can be expected theoretically to be transferred by the bombardment with 5 keV He ions from the FM layer into the interlayer [178]. Therefore, it can be assumed that this mechanism is as well responsible for a significant part of the changed coupling at high ion doses in this experiments.

The decreasing tendency of  $J_Q$  with increasing ion dose observed in this experiments might be due to a decreasing size of terraces at the interface or a decreasing coupling between the loose spins and the FM layers. Furthermore, a formation of a direct exchange coupling between the FM atoms among each other or between FM atoms and the FM layers due to an increase of the density of FM atoms in the interlayer might reduce the number of loose spins and, therefore, reduce the strength of the coupling. A reduction of the period or the effective amplitude of the uncorrelated roughness due to intermixing might also play a role. Again, it is not possible to extract the information which of these effects or which combination of them is responsible for the observed dose dependence from the present measurements.

Depending on the microscopic distribution of the ion dose and the local variations of the sample properties, e.g., due to roughness and varying grain sizes, the effects of IB described above might influence the coupling at some places to a larger extent than on others. But as the MOKE measurements average over an area of the size of the laser spot (approx. 0.2 mm diameter) and the AGM measurements average over the whole sample, eventually existing inhomogeneities in the coupling can not be resolved.

### **Ru-AFi: Inversion of exchange bias direction**

In the last paragraphs it has been shown that the maximum possible increase of the EB can be obtained by IB without a significant decrease or even with an increase of the IEC for samples with stack  $Ru_{AF}$ .

Usually, the ion dose necessary to obtain the maximum EB after turning the EB direction usually is approximately the same as the dose necessary to obtain the maximum EB by IB with a parallel orientation of  $\mathbf{H}_{FC}$  and  $\mathbf{H}_{IB}$ . An example for the ion dose dependence of the exchange bias field  $H_{EB}$  measured at samples with stack  $hMTJ$  for three different relative orientations of  $\mathbf{H}_{FC}$  and  $\mathbf{H}_{IB}$  is shown in Fig. 3.45. The red diamonds symbolize  $H_{EB}$  after IB for a not annealed sample. The black boxes (green triangles) show measurements on an annealed sample with a parallel (antiparallel) alignment of  $\mathbf{H}_{FC}$  and  $\mathbf{H}_{IB}$ . For the case of an antiparallel orientation of  $\mathbf{H}_{FC}$  and  $\mathbf{H}_{IB}$ , the sign of  $H_{EB}$  has been inverted to enable an easier comparison with the other results. The larger ion dose necessary for the maximum EB in the case of sample  $hMTJ$  compared to sample  $Ru_{AF}$  is due to the larger amount of material above the IrMn/CoFe interface. Therefore, only a smaller percentage of the ions can reach the FM/AF bilayer at sample  $hMTJ$  and a higher ion dose is necessary to get the same result.

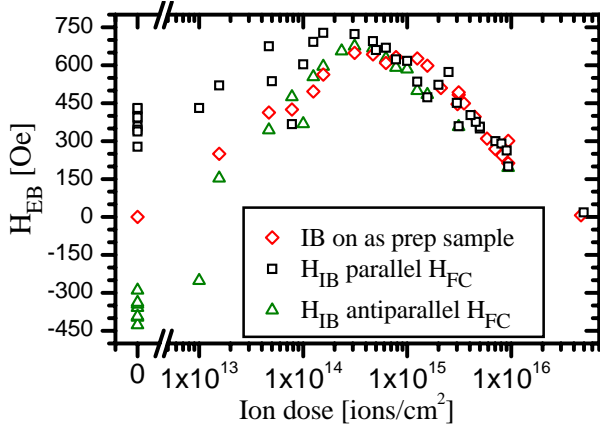


Figure 3.45: Shift of hysteresis loop of pinned FM layer due to EB ( $H_{EB}$ ) extracted from MOKE measurements on sample  $hMTJ$  for several ion doses and ( $\diamond$ ) IB without FC, ( $\square$ )  $H_{IB}$  parallel  $H_{FC}$  and ( $\triangle$ )  $H_{IB}$  antiparallel  $H_{FC}$ . The sign of the values of  $H_{EB}$  for the antiparallel case has been reversed to reach a better comparability of the maximum EB. (Ion energy 10 keV)

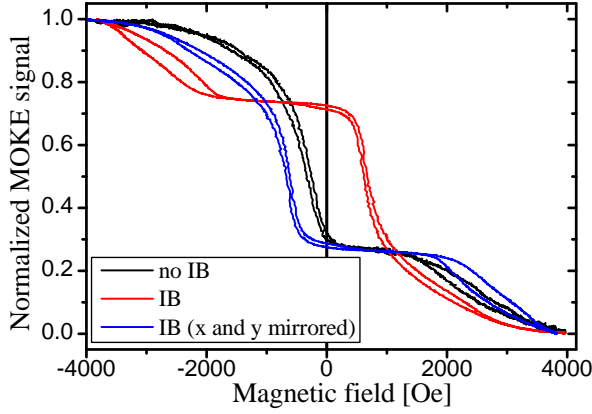


Figure 3.46: MOKE measurements on sample  $Ru_{AF}^{5.4kOe,AP}$  after IB with  $5 \times 10^{13}$  ions/cm<sup>2</sup> ( $E_{IB}=10$  keV) in a magnetic field of 5400 Oe antiparallel to  $H_{FC}$  on a not bombarded part of the sample (black), on a bombarded part of the sample (red) and inverted measurement on bombarded part of the sample with inverted sign of magnetic field (blue).

The mechanism responsible for the increase of the EB / reverse of the EB direction at small ion doses and the subsequent decrease for higher doses are discussed, e.g., in chapter 2.2 (compare Ref. [29, 50]).

A comparison of the measurements with different relative orientations of  $H_{FC}$  and  $H_{IB}$  shows that the dose responsible for the maximum enlargement of the EB with a parallel alignment of  $H_{FC}$  and  $H_{IB}$  and the dose necessary for the maximum EB after a 180° rotation with an antiparallel alignment of the two magnetic fields are nearly the same. Therefore, one can assume that it is as well possible to turn the EB direction by IB without destroying the antiferromagnetic interlayer exchange coupling.

This has been tested with sample  $Ru_{AF}^{5.4kOe,AP}$  which has been bombarded with  $5 \times 10^{13}$  ions/cm<sup>2</sup> ( $E_{IB}=10$  keV)<sup>19</sup> in a magnetic field of -5.4 kOe antiparallel to  $H_{FC}$ . In this magnetic field the magnetization of both FM layers during IB is aligned parallel to each other and antiparallel to  $H_{FC}$ . The measurements on a bombarded and a not bombarded sample for this IB configuration can be seen in Fig. 3.46. By comparing the measurements carried out on parts of the sample with and without IB it can easily be seen that the EB direction has been turned 180° (compare as well Fig. 3.41). For an easier comparison, the measurement with IB has been mirrored in x

<sup>19</sup>For this ion dose the maximum shift of the switching field has been observed in the case of  $H_{IB}(5600 \text{ Oe}) \uparrow \uparrow H_{FC}$  (Fig. 3.35 and 3.38) and  $H_{IB}(-1000 \text{ Oe}) \uparrow \downarrow H_{FC}$  (Fig. 3.41).

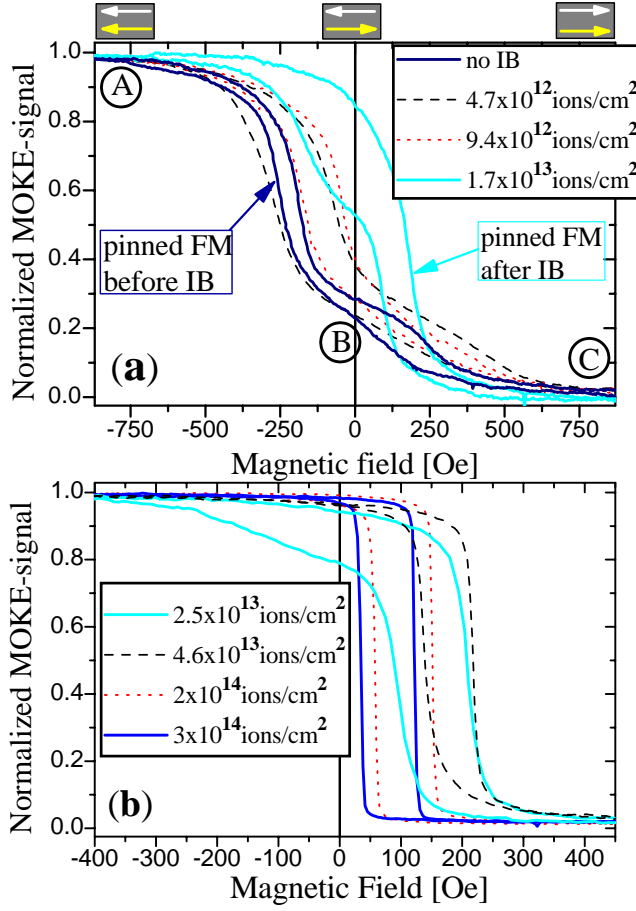


Figure 3.47: MOKE measurements on sample  $Cu_{AF}$  for different ion doses: (a) up to  $1.7 \times 10^{13}$  ions/cm<sup>2</sup> and (b)  $2.5 \times 10^{13}$  ions/cm<sup>2</sup> to  $3 \times 10^{14}$  ions/cm<sup>2</sup> ( $E_{IB}=10$  keV,  $\mathbf{H}_{IB}$  antiparallel to  $\mathbf{H}_{FC}$ , positive magnetic field during measurement parallel to  $\mathbf{H}_{FC}$ ). The arrows in the gray boxes at the top indicate the direction of the magnetization of the two FM layers for the not bombarded sample (white upper arrow: upper Co 2 nm layer, yellow lower arrow: lower pinned Py(2 nm)/Co(2 nm) layer).

and y direction (blue measurement in Fig. 3.46). It can be seen that the shift of the switching fields at positive as well as at negative magnetic fields is larger after IB. This shows, that not only the EB direction has been turned, but also the rotated EB and/or the antiferromagnetic IEC is larger after the IB than it was before.

Therefore, it has been shown that even for stack  $Ru_{AF}$ <sup>20</sup> it is possible to turn the EB direction without destroying the AF interlayer exchange coupling. This is an important requirement for the application of IBMP for, e.g., special kinds of magnetic logic [186].

### Cu-AFi: Influence of ion dose

Figure 3.47 shows MOKE measurements for various ion doses on a  $Cu_{AF}$  sample. On this sample the thicker FM layer is pinned. Therefore, a different effect of the EB on the magnetic switching behavior can be expected than described before. Here, the rotation of the thin magnetic layer against the antiferromagnetic IEC at high positive and negative external magnetic fields is not directly influenced by the EB.

<sup>20</sup>For different stacks where the pinned FM layer is located on top of the interlayer and an appropriate choice of the ion energy the influence of the IB on the interlayer coupling can be expected to be even smaller.

For the switching of the net magnetic moment around zero field a shift in the same direction (in this case to negative magnetic fields  $H_{\text{ext}}$ ) as usually observed for a single pinned FM layer annealed or grown in the same magnetic field as used for the growth of the  $Cu_{\text{AF}}$  sample can be expected. The strength of the interlayer exchange coupling can directly be estimated from the shift of the loop at positive values of  $H_{\text{ext}}$ . A comparison of the shift of the loops at positive magnetic fields measured at the  $Cu_{\text{AF}}$  sample [Fig. 3.47 (a)] with the shift of the loops at large magnetic fields measured at a  $Ru_{\text{AF}}^{\text{no IrMn}}$  sample without IrMn (Fig. 3.31) shows that the AF interlayer exchange coupling is significantly weaker in the case of the Cu interlayer.

To confirm this quantitatively the magnetization reversal process of sample  $Cu_{\text{AF}}$  without IB has been reproduced by energy minimization calculations (Fig. 3.48).<sup>21</sup> The best agreement between calculation and experiment has been found for  $J_L = -1.1 \times 10^{-5} \text{ J/m}^2$  and  $J_Q = -8 \times 10^{-6} \text{ J/m}^2$ . This is significantly smaller than the values of  $J_L$  and  $J_Q$  obtained without IB for sample  $Ru_{\text{AF}}^{\text{no IrMn}}$  with a 0.9 nm thick Ru layer and  $Ru_{\text{AF}}$  with a 0.95 nm thick Ru layer<sup>22</sup> (compare Fig. 3.32 and Fig. 3.34).

When the EB interaction is as strong as the AF IEC or even stronger as found for sample  $Cu_{\text{AF}}$  [compare Fig 3.48 (a)], it can be expected that the two loops for the switching of the net magnetic moment (compare III in Fig. 3.31) and the switching of the thin FM layer against the AF IEC at negative fields (II / IV in Fig. 3.31) merge. The orientation of the magnetization of the two FM layers on a not bombarded  $Cu_{\text{AF}}$  sample changes as follows when varying  $H_{\text{ext}}$  from large negative to large positive values: First, the direction of both magnetizations is aligned parallel to the external magnetic field by the Zeeman interaction (Fig. 3.47 (a), A). Then the thicker (pinned) FM layer switches due to EB, resulting in an antiparallel orientation (Fig. 3.47 (a), B). Finally, a switching of the thinner (not pinned) FM layer against the AF interlayer exchange coupling due to the increasing positive magnetic field can be observed and the magnetic moments of both FM layers are aligned parallel again (Fig. 3.47 (a), C). Without an IEC, the pinned FM layer would switch at negative fields and the not pinned FM would switch at about zero field.

After a bombardment with a small ion dose of  $4.4 \times 10^{12} \text{ ions/cm}^2$ , a part of the loop at positive external magnetic fields is extended to higher fields. This is a hint to an at least locally increased AF interlayer exchange coupling. This fits to the increased fitted coupling constant  $J_L$  (Fig. 3.49) and the results of the experiments with stack  $Ru_{\text{AF}}^{\text{Oe}}$ . Some explanations for this observation have been described above.

With further increasing ion dose ( $9.4 \times 10^{12} \text{ ions/cm}^2$ ) a further decrease of the EB can be observed (compare Fig. 3.47 and ion dose dependence of  $K_u$  in Fig. 3.49). At an ion dose of  $1.7 \times 10^{13} \text{ ions/cm}^2$  the EB has been reversed but it has not yet the same magnitude as prior to the IB. A comparison of the shape of the measurement done after bombardment with this minimum ion dose necessary for a reverse of the EB direction and the measurement carried out without IB shows

<sup>21</sup>The calculated magnetization reversal process for several ion doses can be found in appendix E.

<sup>22</sup>Values obtained without IB for sample  $Ru_{\text{AF}}^{\text{no IrMn}}$  with a 0.9 nm thick Ru layer (sample  $Ru_{\text{AF}}$  with a 0.95 nm thick Ru layer):  $J_L = -5.4 \times 10^{-4} \text{ J/m}^2$  and  $J_Q = -9.0 \times 10^{-5} \text{ J/m}^2$  ( $J_L = -2.7 \times 10^{-4} \text{ J/m}^2$  and  $J_Q = -7.2 \times 10^{-5} \text{ J/m}^2$ ).

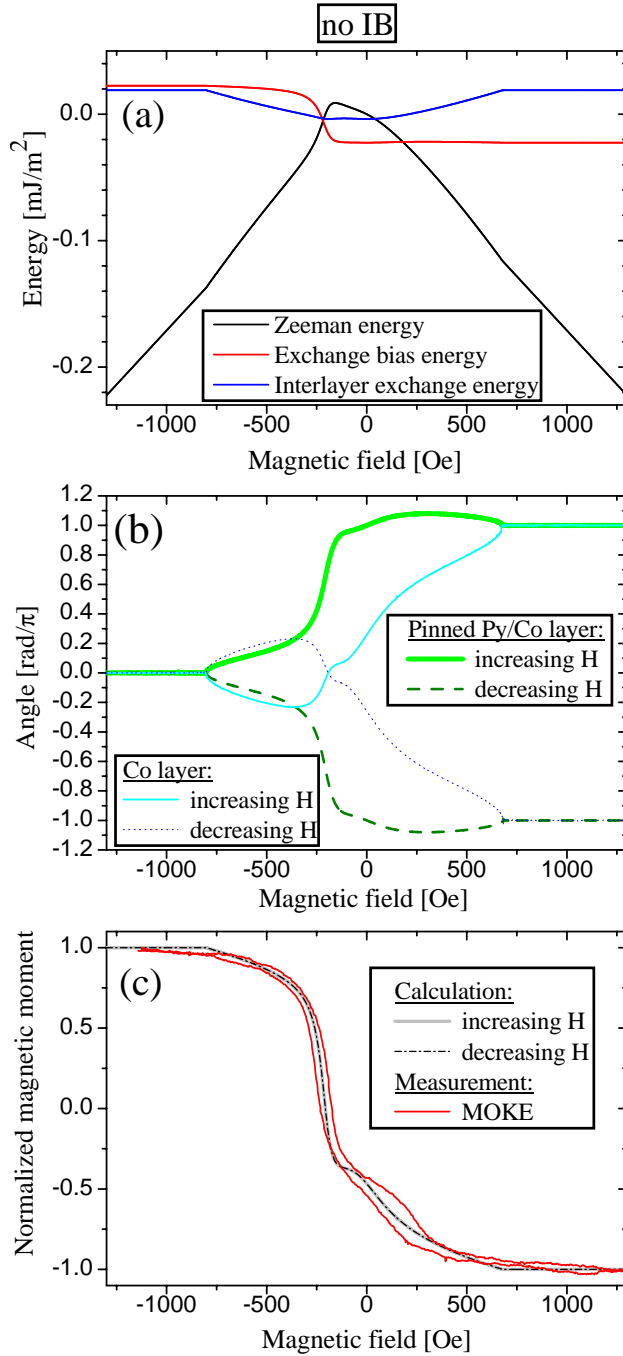


Figure 3.48: (a) Energy of Zeeman interaction, exchange bias interaction and interlayer exchange interaction calculated for the angles of the magnetization of the two FM layers ( $\mathbf{M}_i$ ) which result in the minimum sum of this energies at each value of the external magnetic field. (b) Direction of  $\mathbf{M}_i$  described by the angle relative to the axis of the external magnetic field. Even (odd) multiples of  $\pi$  correspond to an orientation of  $\mathbf{M}_i$  parallel to the positive (negative) external magnetic field. (c) Calculated magnetization reversal and normalized MOKE measurement for sample  $Cu_{AF}$ . The calculated magnetization reversal has been obtained with  $J_L = -1.1 \times 10^{-5} \text{ J/m}^2$ ,  $J_Q = -8 \times 10^{-6} \text{ J/m}^2$  and  $K_u = 2.2 \times 10^{-5} \text{ J/m}^2$ .



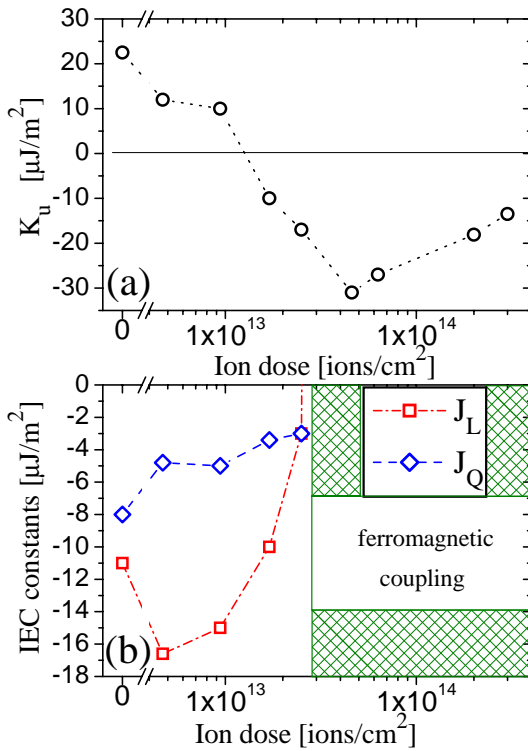


Figure 3.49: (a) Unidirectional anisotropy constant  $K_u$  and (b) bilinear and biquadratic interlayer exchange coupling constants of sample  $Cu_{AF}$  in dependence of the ion dose. All values have been obtained by varying the constants until a good agreement between the shape of the calculated magnetization reversal process and the measurement was obtained.

that after IB a larger part of the magnetic moment of the sample turns in the range around zero magnetic field. This is a sign for a degradation of the AF interlayer coupling on a part of the sample. This observation is also confirmed by the decreasing IEC constant  $J_L$  obtained by energy minimization calculations (Fig. 3.49). With increasing ion dose, a further decrease of the AF interlayer coupling can be observed [ $2.5 \times 10^{13} \text{ ions}/\text{cm}^2$ , Fig. 3.47 (b)] until at  $4.6 \times 10^{13} \text{ ions}/\text{cm}^2$  the whole sample shows a ferromagnetic interlayer coupling. At this ion dose the maximum shift observed for the combined hysteresis loop can be observed. Although the value of  $K_u$  of  $3.1 \times 10^{-5} \text{ J}/\text{m}^2$  after IB is larger than before IB ( $2.25 \times 10^{-5} \text{ J}/\text{m}^2$ ) the shift of the loop of about 180 Oe is slightly smaller than the shift of the loop of the 3 nm thick pinned FM layer prior to IB of about 210 Oe. This can be explained by an effectively thicker pinned FM layer after the AF interlayer exchange coupling has been turned into a FM coupling and both FM layers switch like one layer. Now the same external magnetic field results in a larger Zeeman energy. For higher ion doses a decrease of the EB has been found (Fig 3.47 (b)).

The ion dose dependence of the magnetization reversal process has been reproduced with a second sample with an identical stack (Fig. 3.50). Although the IEC of the second sample without IB is significantly smaller<sup>23</sup> than the one measured at the first sample (compare Figures 3.48 and 3.50), the shape of the measurement after IB with about  $5 \times 10^{12} \text{ ions}/\text{cm}^2$  is very similar for both samples. Therefore, the effect which was responsible for the lower IEC in the second sample has been

<sup>23</sup>The fact that the IEC of the two nominally identically samples which have been deposited on the same day with the same equipment and the same procedure is significantly different underlines the sensitivity of the IEC on tiny changes in the sample composition.

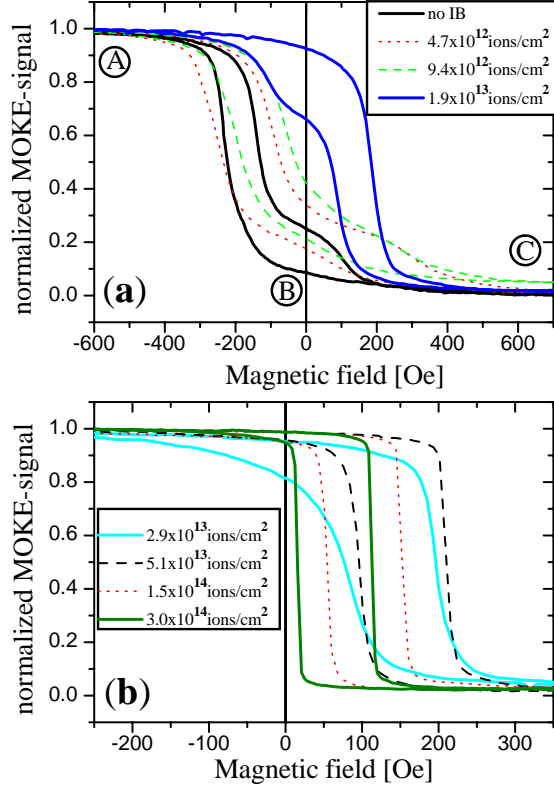


Figure 3.50: Ion dose dependence of second sample with stack  $Cu_{AF}$ . This sample shows less biquadratic IEC before IB.

reduced by the IB.

In Ref. [178] a stronger decrease of the AF interlayer exchange coupling was found for a smaller interlayer thickness after IB with the same ion dose. Furthermore, in Ref. [178] calculations have been shown which suggest an exponential decrease of the probability for the formation of magnetic bridges due to IB with increasing interlayer thickness. Therefore, it might be expected that for a higher antiferromagnetic maximum of the IEC of the  $Cu_{AF}$  stack the transformation from an antiferromagnetic to a ferromagnetic coupling occurs not as easy as it has been observed with the first maximum which has been investigated here.

The effect of a significantly thicker interlayer can be observed in the investigation of spin valves with a 2.4 nm thick Cu interlayer published in Ref. [27, 45]. With this interlayer thickness no antiferromagnetic IEC can be observed but for high ion doses the formation of a ferromagnetic coupling can also be observed (Fig. 3.51). This FM coupling is indicated by an enlargement of the absolute value of the shift of the not pinned FM layer ( $H_e$ , triangles in Fig. 3.51) until the switching of both FM layers can not be distinguished after bombardment with high ion doses.

Figure 3.51 shows this kind of investigations [45] for spin valves with an  $Fe_{50}Mn_{50} / Co / Cu / Co$  (a) and a  $Co / Cu / Co / Ir_{50}Mn_{50}$  (b) stack. The ion dose necessary to obtain the maximum EB after the IB is in the same range as observed with stack  $Cu_{AF}$  (compare Fig. 3.49). But in contrast to stack  $Cu_{AF}$  no significant ferromagnetic coupling has been observed in [45] (constant  $H_e$  in Fig. 3.51).

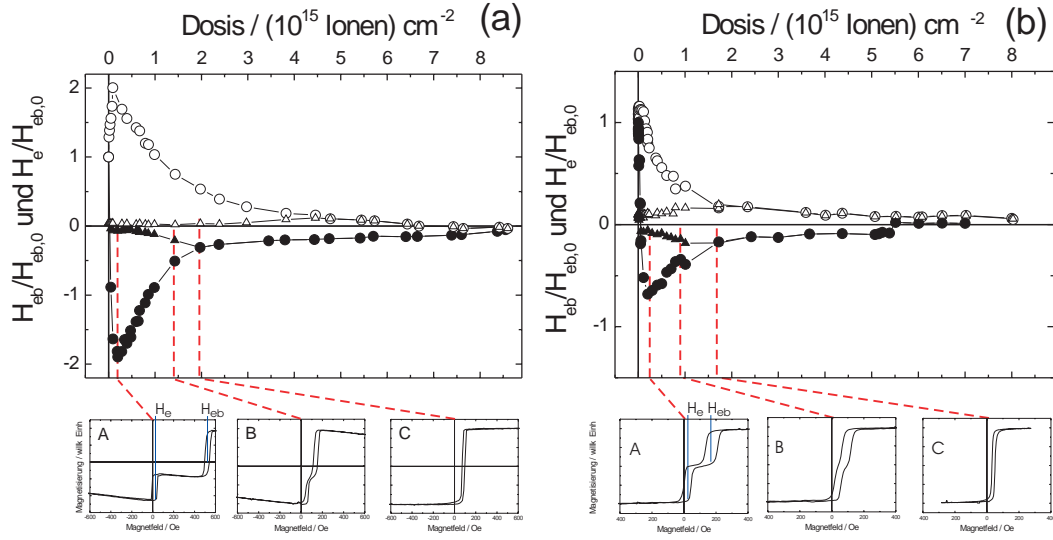


Figure 3.51: Shift of the pinned FM layer ( $H_{eb}$ , circles) and shift of the not pinned layer ( $H_e$ , triangles) after bombardment with  $H_{IB}$  parallel to  $H_{grow}$  (open symbols) and  $H_{IB}$  antiparallel to  $H_{grow}$  (solid symbols). All values are normalized to the EB field without IB. The small show hysteresis loops measured after bombardment with selected ion doses indicated by the dashed lines. (a) shows experiments carried out with a Fe<sub>50</sub>Mn<sub>50</sub>/Co/Cu/Co spin valve. (b) shows experiments carried out with a Co/Cu/Co/Ir<sub>50</sub>Mn<sub>50</sub>. (from[45])

This confirms the observation published in Rev. [178] that a higher ion dose is necessary to obtain a FM coupling when the interlayer is thicker.

### 3.3.4 Summary

The influence of ion bombardment on the interlayer exchange coupling in pinned artificial ferrimagnets has been investigated. It has been demonstrated that the exchange bias of a IrMn/CoFe/Ru/CoFe artificial ferrimagnet with a 1 nm thick Ru interlayer can be increased by bombardment with 10 keV He ions in a magnetic field without a destruction or even with an enlargement of the antiferromagnetic interlayer exchange coupling. Furthermore, it has been shown that a reversal of the exchange bias direction by ion bombardment is also possible for this system without a significant degradation of the interlayer exchange coupling. Therefore, an important prerequisite for the application of ion bombardment induced magnetic patterning for, e.g., special kinds of magnetic logic has been shown.

The IrMn/Py/Co/Cu/Co system is much more sensitive to damage produced by ion bombardment than the Ru based artificial ferrimagnet although the interlayer thickness in the case of the  $Ru_{AF}$  stack is even thinner than in the case of the  $Cu_{AF}$  stack. This observation fits to the fact that without IB the AF interlayer exchange coupling of the Ru based AFi is much stronger than the one of the Cu based AFi.

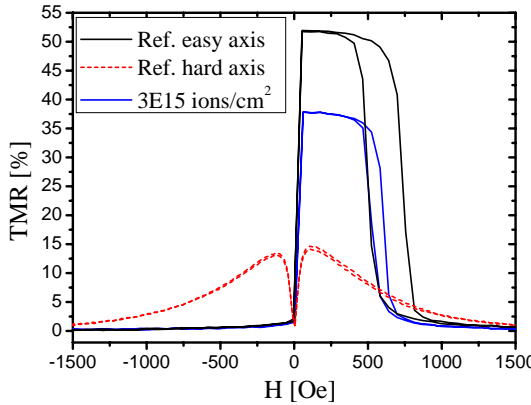


Figure 3.52: Major loops measured at a sample with stack  $MTJ_{AlOx}^{std}$  without an ion bombardment (reference measurements) and after a bombardment with 20 keV He ions with an ion dose of  $3 \times 10^{15}$  ions/cm<sup>2</sup>.  $\mathbf{H}_{IB}$  was perpendicular to  $\mathbf{H}_{FC}$ . The magnetic field during the measurement after IB was oriented parallel to the hard axis before IB and parallel to  $\mathbf{H}_{IB}$ .

### 3.4 Application of ion bombardment induced magnetic patterning on the reference layer of magnetic tunnel junctions with $Al_2O_3$ barrier

In the last chapters the ion bombardment induced magnetic patterning of the magnetic properties of pinned layers has been discussed. On the following pages the influence of the ion bombardment on the magnetoresistance of magnetic tunnel junctions will be described.

First, some results of investigations of the ion bombardment of MTJs obtained during the work for my diploma thesis [66] will be summarized, before additional experiments addressing this subject will be shown.

#### 3.4.1 Ion bombardment of standard alumina based magnetic tunnel junctions

##### Experiment

The question whether the tunnel magneto resistance survives the IB has been tested with sample  $MTJ_{AlOx}^{std}$  which has the following stack: wafer with 100 nm thermal Si oxide / Cu 25 nm /  $Ir_{17}Mn_{83}$  12 nm /  $Co_{70}Fe_{30}$  3.1 nm / Al 1.3 nm + 100 s oxidation /  $Ni_{80}Fe_{20}$  3.6 nm / Ta 3.1 nm / Cu 47 nm / Au 26 nm. It has been annealed for 1 h at 275°C in a magnetic field  $H_{FC}$  of 1500 Oe. The ion bombardment with  $E_{IB}=10$  keV,  $E_{IB}=20$  keV, and  $E_{IB}=30$  keV He ions has been carried out in a magnetic field  $\mathbf{H}_{IB}$  (1000 Oe) perpendicular to the magnetic field during field cooling ( $\mathbf{H}_{FC}$ ).

##### Results and discussion

With this sample, it has been shown that it is possible to rotate the exchange bias direction of the pinned reference layer in a magnetic tunnel junction with alumina barrier (Fig. 3.52). The black and the red major loops show measurements on not

<sup>24</sup>Some results described in this chapter are published in [169].

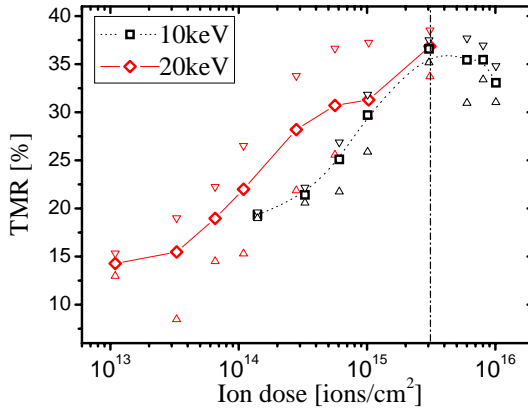


Figure 3.53: Ion dose dependence of the TMR measured on sample  $MTJ_{AlOx}^{std}$  for bombardment with 10 keV and 20 keV He ions in a magnetic field  $\mathbf{H}_{IB}$  perpendicular to  $\mathbf{H}_{FC}$ . Squares and diamonds symbolize averaged values. Triangles symbolize the smallest and the largest value measured at MTJs bombarded with a certain dose. The lines are a guide to the eye.

bombarded parts of the sample carried out with a magnetic field parallel to the easy and hard axis of the reference layer, respectively (reference measurements). The measurement after ion bombardment with  $3 \times 10^{15}$  ions/cm<sup>2</sup> has been carried out in a magnetic field parallel to the hard axis of the reference layer prior to the IB (red to blue major loop in Fig. 3.52). Therefore, it can be seen that the EB direction has been rotated by 90° and still a tunnel magnetoresistance is present.

The ion dose dependence of the TMR during the rotation of the EB direction by 90° is shown in Fig. 3.53.

For ion doses up to  $3 \times 10^{15}$  ions/cm<sup>2</sup>, the TMR amplitude increases with increasing dose (Fig. 3.53). This is due to the rotation of the exchange bias direction from the  $\mathbf{H}_{FC}$  to the  $\mathbf{H}_{IB}$  direction and the resulting better “antiparallel” alignment of the magnetization of the two FM layers.

The decrease in TMR for higher ion doses points to progressive structural degradation processes in the barrier region counteracting the increase in the TMR by rotating the exchange bias direction.

An important ion bombardment induced structural degradation process is, e.g., intermixing at the barrier interface which reduces the polarization of the tunneling electrons and therefore the TMR. Furthermore, a defect formation in the barrier may increase the density of defect states in the barrier band gap and, therefore, reduces the effective barrier height and can open additional conductance channels as, e.g., hopping via localized states. A decreasing resistance with increasing ion dose which results from this kind of effects has been observed experimentally at high ion doses (not shown).

During similar experiments with 30 keV He ions (not shown) similar results have been obtained.

A comparison of the easy axis measurement without IB and the major loop with IB show a reduction of the TMR amplitude due to the ion bombardment. A maximum TMR of 37.7% is obtained for an ion energy of  $E_{IB}=10$  keV instead of >50% prior to IB. Furthermore, the area resistance product is increased by IB with high ion doses (Fig. 3.54).

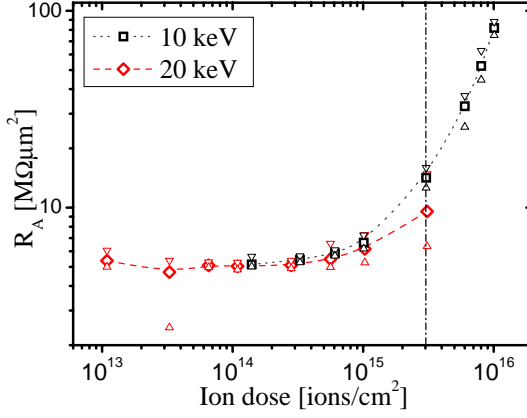


Figure 3.54: Ion dose dependence of the area resistance product  $R_A$  measured on sample  $MTJ_{AlOx}^{std}$  for bombardment with 10 keV and 20 keV He ions in a magnetic field  $\mathbf{H}_{IB}$  perpendicular to  $\mathbf{H}_{FC}$ . Squares and diamonds symbolize averaged values. Triangles symbolize the smallest and the largest value measured at MTJs bombarded with a certain dose. The lines are a guide to the eye.

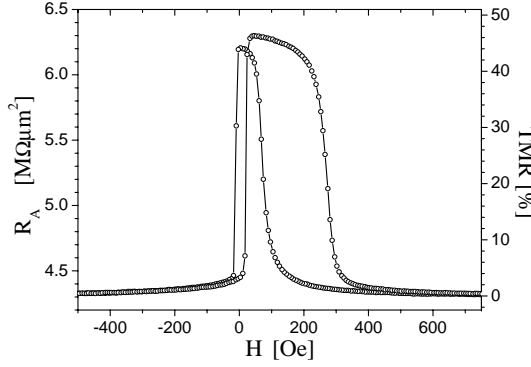


Figure 3.55: Major loop measured at a not bombarded sample with stack  $MTJ_{AlOx}^{inv}$ .

### 3.4.2 Ion bombardment of inverted alumina based magnetic tunnel junctions

#### Experiment

One approach to reduce this disadvantageous effects is to reduce the amount of energy deposited by the ions in the region of the barrier. This is difficult to achieve with stack  $MTJ_{AlOx}^{std}$  because every ion has to cross the barrier first before it can influence the EB coupling in the ferromagnet/antiferromagnet (AF) bilayer. Therefore, a stack with an inverted structure has been tested.

This sample  $MTJ_{AlOx}^{inv}$  consists of the following layers: wafer with 100 nm thermal oxide / Cu 30 nm / Ta 5 nm /  $Ni_{80}Fe_{20}$  5 nm /  $Co_{70}Fe_{30}$  2 nm / Al 1.4 nm + 100 s oxidation /  $Co_{70}Fe_{30}$  4 nm /  $Ir_{17}Mn_{83}$  12 nm / Ta 5 nm / Cu 35 nm / Ta 5 nm / Au 20 nm. It has been annealed for 1 h at a temperature of 275°C in a magnetic field of 1500 Oe. The effect of the ion bombardment on these samples has been tested with 10 keV and 20 keV He ions ( $\mathbf{H}_{IB} \perp \mathbf{H}_{FC}$ ).

#### Results and discussion

Without IB, 46.2% TMR have been obtained with this sample. The corresponding major loop can be found in Fig. 3.55. The shift of the hysteresis loop of the reference layer due to the EB is significantly smaller for this sample compared to the sam-

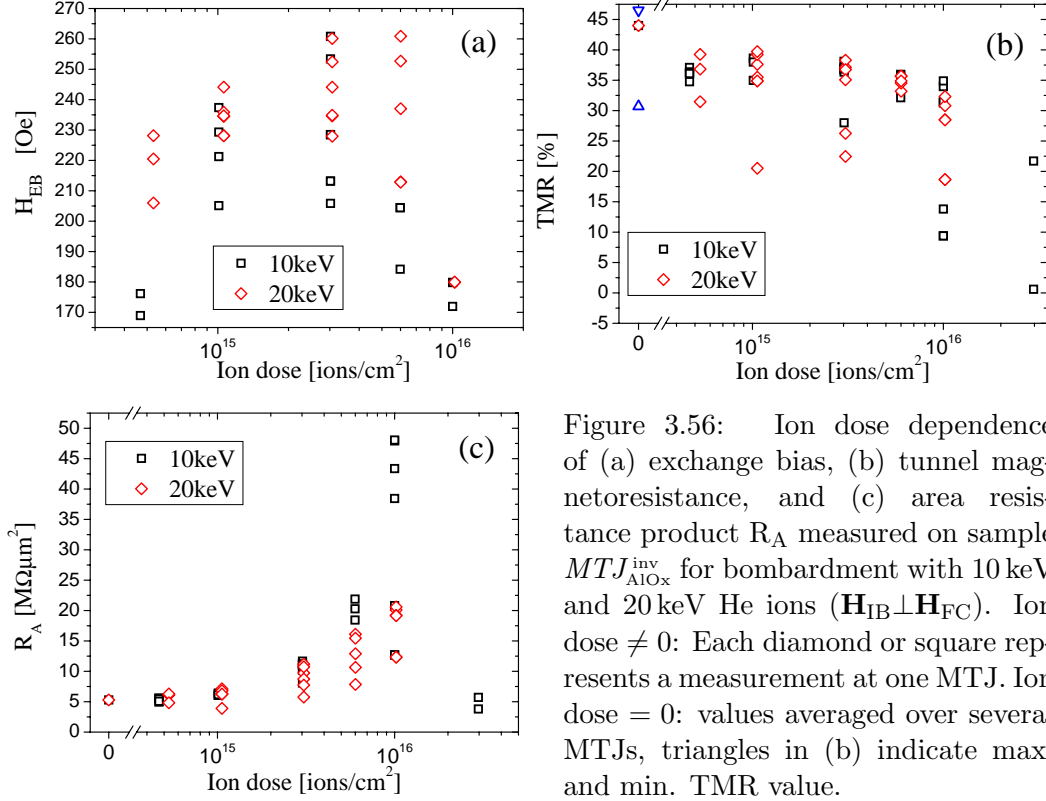


Figure 3.56: Ion dose dependence of (a) exchange bias, (b) tunnel magnetoresistance, and (c) area resistance product  $R_A$  measured on sample  $MTJ_{AlOx}^{inv}$  for bombardment with 10 keV and 20 keV He ions ( $\mathbf{H}_{IB} \perp \mathbf{H}_{FC}$ ). Ion dose  $\neq 0$ : Each diamond or square represents a measurement at one MTJ. Ion dose = 0: values averaged over several MTJs, triangles in (b) indicate max. and min. TMR value.

ple with stack  $MTJ_{AlOx}^{std}$  (Fig. 3.52). Therefore, the plateau with a high resistance due to the antiparallel alignment of the FM layer magnetizations is smaller and an incomplete EB rotation to the direction of the external magnetic field during the measurement can result in a reduced TMR amplitude more easily.

SRIM simulations suggest that for stack  $MTJ_{AlOx}^{std}$  the number of defects created per ion and Å depth by 10 keV He ions is approximately the same in the barrier and in the IrMn. In contrast to this, for stack  $MTJ_{AlOx}^{inv}$  about three times more defects in the IrMn are predicted compared to the barrier. The number of defects can be regarded as a measure for the different kinds of modification as, e.g., more energy deposition, more intermixing at interfaces, more defect creation, or more energy deposition as phonons are usually closely connected.<sup>25</sup>

The results of the experimental test of this prediction can be seen in Fig. 3.56. The ion dose dependence of the exchange bias measured in the direction of the field during ion bombardment  $\mathbf{H}_{IB}$  is shown in part (a). It is striking that the EB at high ion doses in the range of  $1 \times 10^{16}$  ions/cm<sup>2</sup> is already decreasing. This can be, e.g., due to an intermixing at the FM/AF interface and shows that the interesting ion doses for this stack are in the range of  $3 \times 10^{15}$  ions/cm<sup>2</sup>. At this ion dose, the maximum TMR has also been found for sample  $MTJ_{AlOx}^{std}$  (Fig. 3.53). The large statistical spread might be due to variations of the ion dose or sample

<sup>25</sup>More detailed SRIM simulations including, e.g., the influence of the ion energy will be shown for a stack with an MgO barrier in chapter 3.8.2.

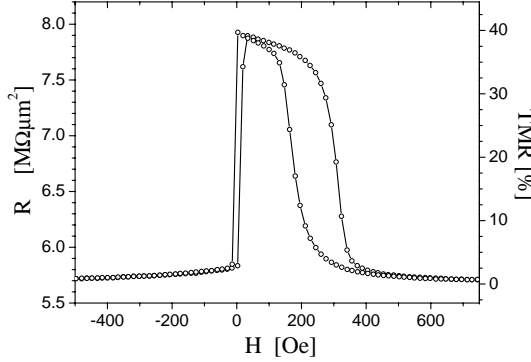


Figure 3.57: Major loop measured at a sample with stack  $MTJ_{AlOx}^{inv}$  after IB with  $E_{IB}=20$  keV,  $1 \times 10^{15}$  ions/cm<sup>2</sup> and  $\mathbf{H}_{IB}$  perpendicular to  $\mathbf{H}_{FC}$ .

properties like the roughness. The shift of the hysteresis due to EB has been determined by magnetoresistance measurements and, therefore, averages only over a small area in the range of  $100 \mu\text{m} \times 100 \mu\text{m}$  to  $300 \mu\text{m} \times 300 \mu\text{m}$ .

During these magnetoresistance measurements it was difficult to get a good electrical contact because at this sample the gold capping layer has suffered significantly during the lithography (including removal of resist in the ultrasonic bath) and the ion bombardment processes. This does not have any influence on the conclusions drawn from the experiments, but it can result in a larger scattering of the obtained resistance and TMR values [Fig. 3.56 (b)/(c)] as, e.g., the relatively high force used to press the gold needle on the MTJ to get a stable electrical contact might have damaged some of the sensible barriers. It can be seen that most MTJs in the interesting ion dose range up to  $3 \times 10^{15}$  ions/cm<sup>2</sup> still have a TMR value of about 90% of the value obtained without IB.

This is a significantly better result than it was obtained with stack  $MTJ_{AlOx}^{std}$ . This experimental result fits good to the predictions made with respect to the SRIM simulations above.<sup>26</sup>

An example of a major loop measured after IB with  $1 \times 10^{15}$  ions/cm<sup>2</sup> is shown in Fig. 3.57. The reorientation of the EB coupling at this ion dose is good enough to result in a larger high resistance plateau than it was observed after the field cooling without IB.

Furthermore, the relatively high ion energy of  $E_{IB}=10$  keV /  $E_{IB}=20$  keV has not been optimized for the application with the inverted stack. Several SRIM simulations dealing with the question of the optimum ion energy for inverted stacks will be shown in chapter 3.8.2.

On the following pages it will be demonstrated that even for stack  $MTJ_{AlOx}^{std}$  it is possible to reverse the decrease of the TMR due to IB totally.

<sup>26</sup>For a more detailed discussion of the influence of the stack and the ion energy see chapter 3.8.2 and 3.8.1.



### 3.5 Postannealing of alumina based magnetic tunnel junctions with ion bombardment modified exchange bias

In the last chapter it has been shown that the ion bombardment technique for setting the exchange bias direction in complete magnetic tunnel junctions has some side effects on the tunnel magnetoresistance amplitude as well as the resistance when ion doses ensuring a well defined EB are used. In this chapter, it will be shown how this side effects of the ion bombardment can be reduced while maintaining the IB induced EB direction in the magnetic tunnel junction.

#### 3.5.1 Postannealing of standard alumina based magnetic tunnel junctions

##### Experiment

The layer stack of the MTJs used for the following experiment is Cu 25 nm /  $Mn_{83}Ir_{17}$  12 nm /  $Co_{70}Fe_{30}$  3.1 nm / Al 1.3 nm +100 s ECR plasma oxidation with -10 V bias voltage [168] /  $Ni_{80}Fe_{20}$  3.6 nm / upper conduction line. The upper conduction line consists of Ta 3.1 nm / Cu 47 nm / Au 26 nm (stack  $MTJ_{AlOx}^{std}$ , compare chapter 3.4) or Ta 6 nm / Cu 47 nm / Ta 6 nm / Au 26 nm (stack  $MTJ_{AlOx}^{std+}$ ). The additional Ta layer in stack  $MTJ_{AlOx}^{std+}$  serves as a diffusion barrier, as the Cu and the Au in stack  $MTJ_{AlOx}^{std}$  tend to mix at higher temperatures.

After deposition, all samples are annealed for 60 min at  $T_{FC}=275^\circ C$  in a magnetic field of  $H_{FC}=1500$  Oe. These oxidation and initial annealing parameters are optimized with respect to the TMR amplitude [55, 187, 188].

After the initial annealing, the samples are bombarded with He ions (ion energy  $E_{IB}=10$  keV, ion dose  $1 \times 10^{14}$  ions/cm<sup>2</sup> to  $1 \times 10^{16}$  ions/cm<sup>2</sup>) in a magnetic field of  $H_{IB}=1000$  Oe. Two different orientations of  $\mathbf{H}_{FC}$  and  $\mathbf{H}_{IB}$  are used:  $IB^{\parallel}$ :  $\mathbf{H}_{FC}$  and  $\mathbf{H}_{IB}$  are aligned parallel and  $IB^{\perp}$ :  $\mathbf{H}_{FC}$  is perpendicular to  $\mathbf{H}_{IB}$ .

Square MTJs of  $S_J = 10\,000 \mu m^2$  to  $S_J = 90\,000 \mu m^2$  size are patterned after IB by optical lithography and ion beam etching. During this process step, the sample is heated with a resist capping for 30 min to  $95^\circ C$ .

The last preparation step is the postannealing of the patterned junctions in an ultra-high vacuum furnace up to  $300^\circ C$  without an external field, whereas the remanent magnetization of the pinned CoFe (FM1) and the free NiFe (FM2) layer is always aligned parallel prior to this postannealing step. The transport properties of the junctions are measured before and after postannealing at RT with 10 mV bias voltage as a function of the external magnetic field  $\mathbf{H}_{ext}$ .

The heating experiments are divided into two parts.

First, the effect of postannealing for 60 min at a fixed temperature  $T_p=275^\circ C$  on the transport properties of stack  $MTJ_{AlOx}^{std}$  as a function of the ion dose in the  $IB^{\perp}$  configuration has been investigated. This choice of the postannealing parameters is motivated by the fact, that the optimized initial annealing has to be carried out at  $T_{FC} = 275^\circ C$ .

<sup>27</sup>Parts of this chapter have been published in [167].

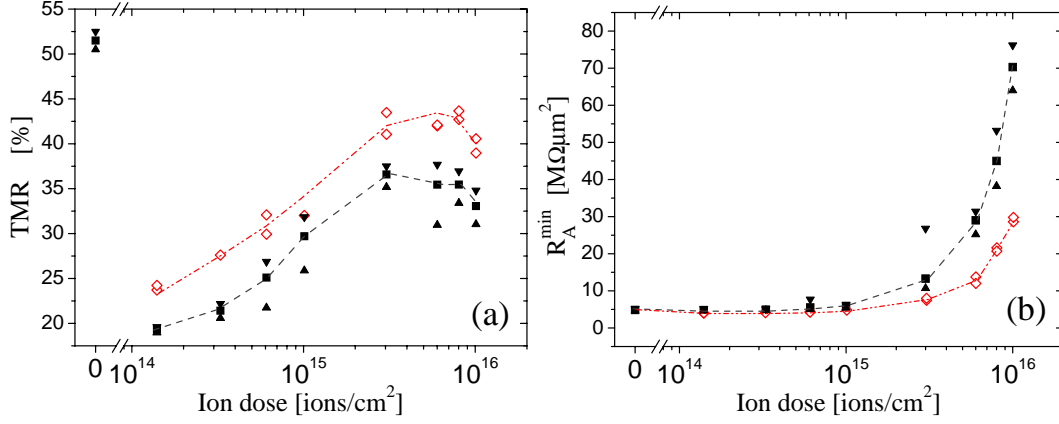


Figure 3.58:  $R_A^{\min}$  and TMR of MTJs with stack  $MTJ_{\text{AlOx}}^{\text{std}}$  for different ion doses before (■: average TMR/resistance, ▼/▲: max. / min. measured values) and after postannealing for 60 min at 275°C (red ◇: single measurements). Measurements with ion dose 0:  $\mathbf{H}_{\text{ext}} \uparrow \uparrow \mathbf{H}_{\text{FC}}$ , measurements with ion dose  $\neq 0$ :  $\mathbf{H}_{\text{ext}} \uparrow \uparrow \mathbf{H}_{\text{IB}}$ . The lines are a guide to the eye.

Then, the postannealing parameters have been optimized for selected ion doses. For the variation of  $T_p$  stack  $MTJ_{\text{AlOx}}^{\text{std+}}$  is used to rule out diffusion in the upper conduction line. The IB of stack  $MTJ_{\text{AlOx}}^{\text{std+}}$  sample is done in the IB $^{\parallel}$  configuration ( $\mathbf{H}_{\text{IB}} \uparrow \uparrow \mathbf{H}_{\text{FC}}$ ) at fixed ion doses of  $3 \times 10^{15}$  ions/cm $^2$  where the maximum of the TMR after IB of the stack  $MTJ_{\text{AlOx}}^{\text{std}}$  sample has been observed and with  $1 \times 10^{16}$  ions/cm $^2$ , where severe alterations of the transport properties after IB occurred. In this configuration of the magnetic fields, it is possible to investigate nonmagnetic effects more easily. The sample is successively annealed with temperatures between 150°C and 300°C in 25°C steps for 60 min per heating step.<sup>28</sup>

## Results and discussion

The dependence of the TMR and the resistance on the ion dose before and after postannealing is shown in Fig. 3.58 (compare chapter 3.4). A maximum TMR of 37.7% is obtained for an ion energy of  $E_{\text{IB}}=10$  keV instead of  $>50\%$  prior to IB.

As it can be seen in Fig. 3.58 (open symbols), postannealing at 275°C leads for all ion doses to a larger TMR and especially for higher doses to a reduction of the resistance. This points to a regression of the unintentional ion induced changes in the barrier region. One example might be a healing of defects in the barrier or at the barrier/electrode interfaces as it has been suggested in [187] for the initial annealing process.

<sup>28</sup>Magnetoresistance measurements have been carried out after each heating step. After annealing with 300°C, new MTJs have been structured and tested. No significant difference between these measurements and that carried out after this heating step at MTJs structured directly after the ion bombardment has been found. Therefore, a thermally induced degradation of, e.g., the MTJ edges has not been observed. Another part of the same sample has been heated in one step to 250°C. The TMR values and the resistance of this sample are comparable to that measured at the part heated up successively to this temperature.

Furthermore, Fe oxide, which might have been created due to the IB induced intermixing can be reduced as it has been found for the initial annealing step in Ref. [188].

The comparison with the initial mean transport properties ( $TMR = 51.5\%$ ,  $R_A^{\min} = 4.9 M\Omega\mu m^2$ ) shows, however, that the structural degradations seem to be only partially regenerated by postannealing at  $275^\circ C$  for 1 h. As the magnetization of the CoFe and NiFe layers are aligned parallel during postannealing without an external field, the EB direction set by IB is preserved (Fig. 3.59). Therefore, in the follow-

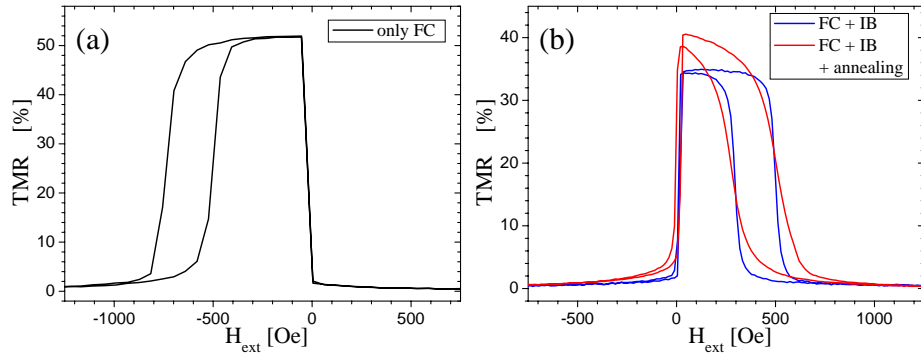


Figure 3.59: TMR major loop measured at stack  $MTJ_{AlOx}^{std}$  (a) after the initial field cooling ( $H_{ext} \uparrow \uparrow H_{FC}$ , black line) and (b) after IB with  $1 \times 10^{16}$  ions/cm<sup>2</sup> ( $H_{ext} \uparrow \uparrow H_{IB}$ , blue line), and after an additional postannealing with  $275^\circ C$  ( $H_{ext} \uparrow \uparrow H_{IB}$ , red line).

ing the influence of the postannealing temperature  $T_p$  on the regression of the ion bombardment induced structural degradation is discussed.

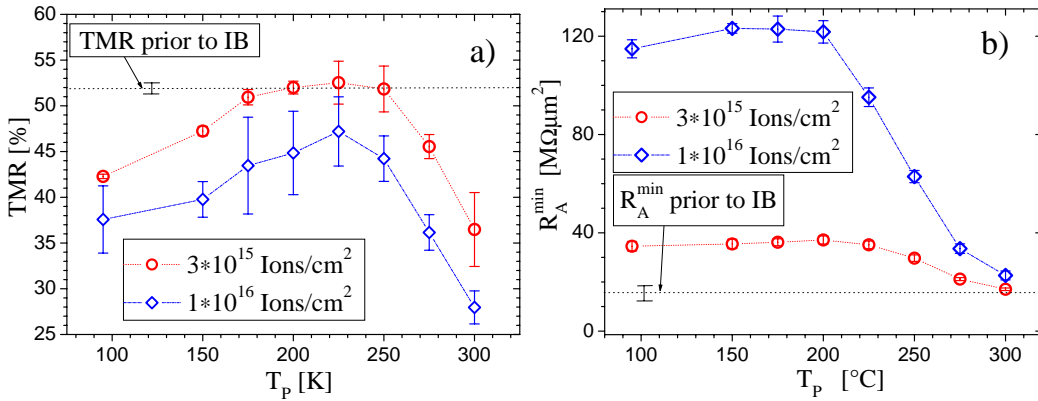


Figure 3.60: TMR (a) and  $R_A^{\min}$  (b) of stack  $MTJ_{AlOx}^{std+}$  after postannealing for fixed ion doses of  $3 \times 10^{15}$  ions/cm<sup>2</sup> ( $\circ$ ) and  $1 \times 10^{16}$  ions/cm<sup>2</sup> ( $\diamond$ ). The dashed horizontal lines correspond to the mean transport properties measured after initial annealing prior to IB. The error bars indicate the standard deviation. The values at  $95^\circ C$  have been measured after IB and structuring of the junctions but prior to postannealing. The value of  $95^\circ C$  is due to a heating step (30 min) during lithography.

Up to  $225^\circ C$  the successive postannealing results in an increase in the TMR

[Fig. 3.60 (a)]. For temperatures between 200°C and 250°C and an ion dose of  $3 \times 10^{15}$  ions/cm<sup>2</sup>, the TMR of more than 50% is comparable to that measured prior to IB. As also found for the stack  $MTJ_{\text{AlOx}}^{\text{std}}$  samples discussed above, the EB direction of the stack  $MTJ_{\text{AlOx}}^{\text{std+}}$  samples set by IB is preserved during the postannealing which is an important prerequisite to use this technique in future applications. Furthermore, it has to be stressed, that with the postannealing temperature  $T_p=225^\circ\text{C}$  the full recovery of the TMR amplitude unintentionally lowered during the IB preparation step has been obtained. Because the reasons for the reduced TMR after IB are structural degradation processes in the barrier region the full recovery of the TMR may also be expected for other relative orientations of  $\mathbf{H}_{\text{FC}}$  and  $\mathbf{H}_{\text{IB}}$ .

For temperatures higher than 250°C, the TMR decreases significantly with increasing temperature while the resistance monotonically decreases for temperatures above 200°C, finally reaching the value which was found prior to IB at 300°C. A decrease in the TMR amplitude by annealing is usually seen for our MTJs above 275°C because of the diffusion of Mn and Cu towards the barrier [188, 55]. As the TMR-decrease of stack  $MTJ_{\text{AlOx}}^{\text{std+}}$  starts at a temperature which is only 25°C lower than the temperature for which Mn and Cu diffusion was reported in Ref. [188, 55], a similar main reason for the TMR decrease may be proposed here.

Although it is not really understood on a micro structural basis so far, the decrease in the resistance to the initial value prior to IB suggests that this mainly reflects the recovery of the unintentional structural degradation processes induced by IB. The same holds for the TMR increase after postannealing up to 225°C.

### 3.5.2 Postannealing of inverted alumina based magnetic tunnel junctions

Because of the good results obtained by heating sample  $MTJ_{\text{AlOx}}^{\text{std+}}$  to temperatures in the range of 200°C to 250°C, similar experiments in this temperature range have been carried out with sample  $MTJ_{\text{AlOx}}^{\text{inv}}$ .

Figure 3.61 shows the result of a postannealing step with a temperature of 200°C carried out at sample  $MTJ_{\text{AlOx}}^{\text{inv}}$  after bombardment with 10 keV (a)/(c) and 20 keV (b)/(d) ions. Independent of the ion dose, the TMR is significantly increased after the postannealing [black squares in Fig. 3.61 (a) and (b)] compared to the measurements directly after the IB [red diamonds (averaged value for each ion dose) and red triangles (max./min. value measured at each dose) in Fig. 3.61 (a) and (b)]. This reproduces the TMR increase observed for the samples with the not inverted standard stack ( $MTJ_{\text{AlOx}}^{\text{std}} / MTJ_{\text{AlOx}}^{\text{std+}}$ ).

In contrast to the results obtained with stack  $MTJ_{\text{AlOx}}^{\text{std}}$  after the postannealing (Fig. 3.58), the resistance is increased for all investigated ion doses. This can at least partly be explained by the lower temperature used for this postannealing experiment of stack  $MTJ_{\text{AlOx}}^{\text{inv}}$  (200°C) compared to the experiment with one temperature and several ion doses carried out at stack  $MTJ_{\text{AlOx}}^{\text{std}}$  (275°C, Fig. 3.58). The postannealing of stack  $MTJ_{\text{AlOx}}^{\text{std+}}$  with a temperature of 200°C after bombardment with  $3 \times 10^{15}$  ions/cm<sup>2</sup> and  $1 \times 10^{16}$  ions/cm<sup>2</sup> also resulted in a slightly elevated resistance compared to the measurement directly after IB (Fig. 3.60).

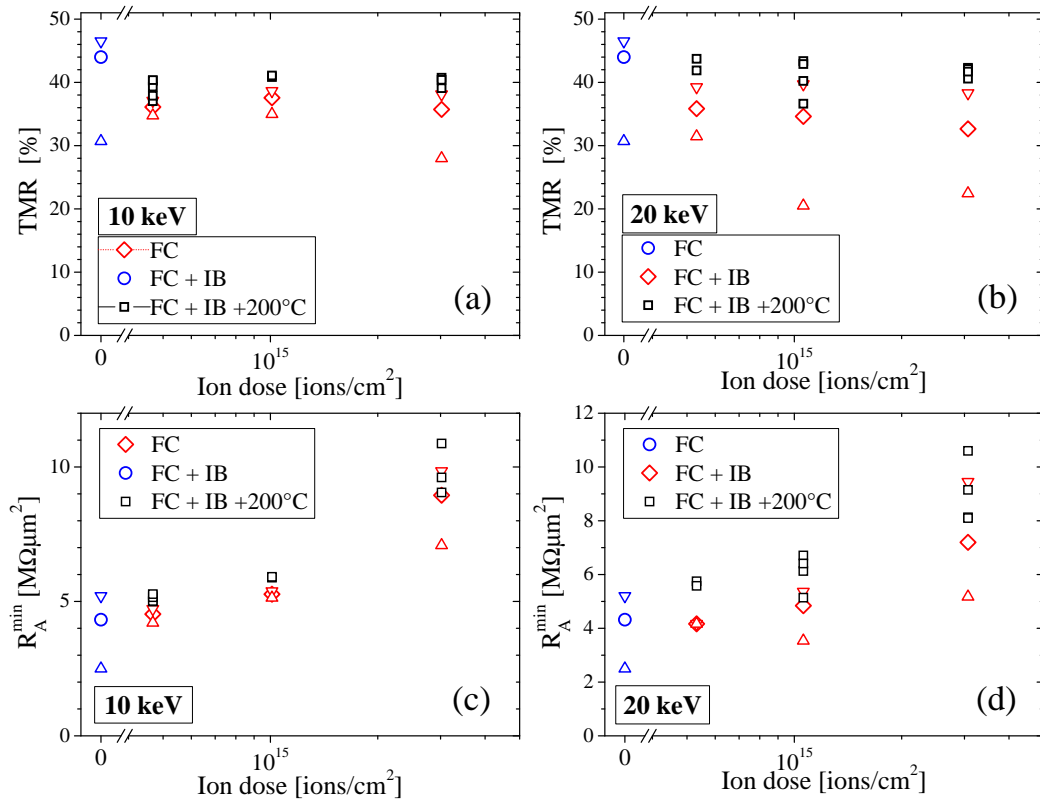


Figure 3.61: Ion dose dependence of the TMR (a)/(b) and the area resistance product in saturation  $R_A^{\min}$  (c)/(d) for a sample with stack  $MTJ_{AlOx}^{inv}$  without IB (blue circle), after bombardment with 10 keV (a)/(c) and 20 keV (b)/(d) He ions (red diamonds), and after IB with an additional postannealing without a magnetic field for 1 h at 200°C (black squares). Circles and diamonds symbolize average values for a certain ion dose. Triangles represent the smallest/largest measured values for a certain ion dose for all measurements without postannealing. Each square stands for a measurement at one MTJ after postannealing.

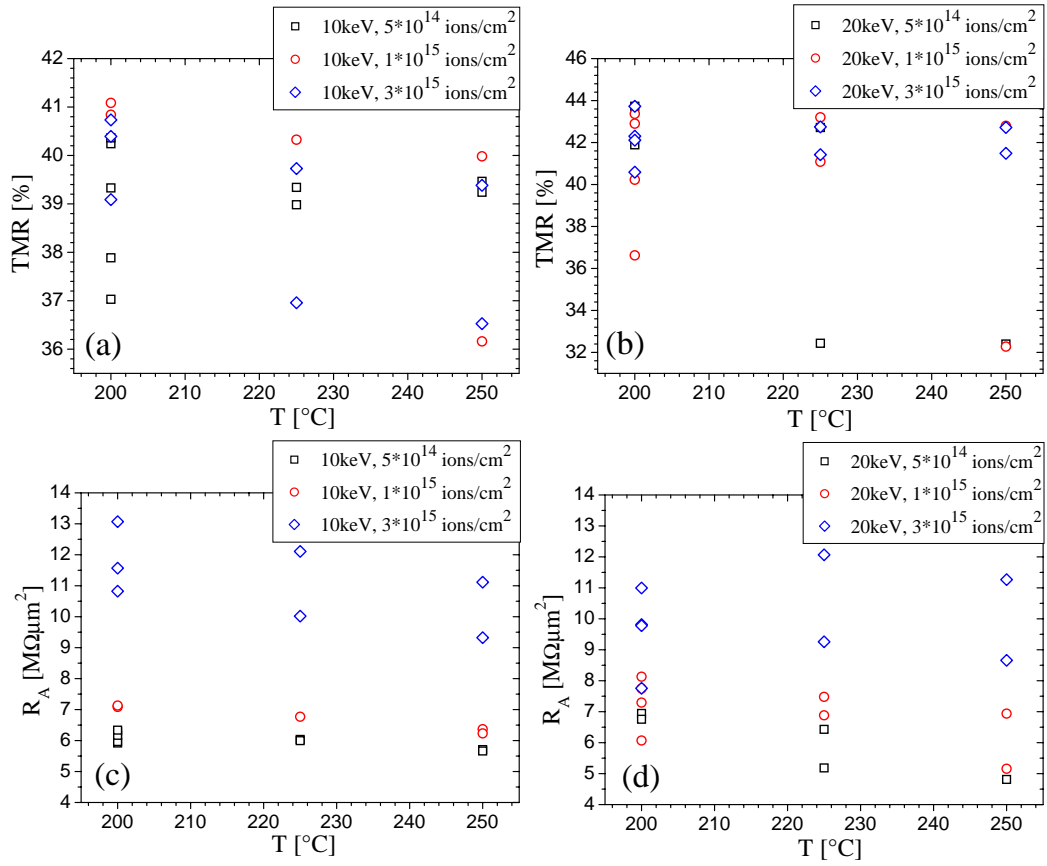


Figure 3.62: Postannealing temperature dependence of the TMR (a)/(b) and the area resistance product  $R_A$  for a sample with stack  $MTJ_{AlOx}^{inv}$  after bombardment with 10 keV (a)/(c) and 20 keV (b)/(d) He ions. Each symbol represents a measurement at one MTJ after postannealing.

After a subsequent heating to higher temperatures in the range of 200°C to 250°C, a nearly constant TMR with a partly decreasing tendency has been observed for stack  $MTJ_{AlOx}^{inv}$  (Fig. 3.62). No significant differences can be found for the postannealing after IB with different ion doses and energies. This fits to the nearly constant TMR found for sample  $MTJ_{AlOx}^{std+}$  in this temperature range (Fig. 3.60).

The variation of the area resistance product of sample  $MTJ_{AlOx}^{inv}$  after heating to temperatures of 200°C to 250°C is approximately in the same range as the scattering of the single measurements. But especially for the samples bombarded with  $E_{IB}=10$  keV, a decreasing tendency can be observed. This tendency is more pronounced for higher ion doses as on this samples more ion bombardment induced changes of the microscopic structure are present which can be removed by the annealing. The same effect has been observed for stack  $MTJ_{AlOx}^{std+}$  (compare measurements after IB with  $3 \times 10^{15}$  ions/cm<sup>2</sup> and  $1 \times 10^{16}$  ions/cm<sup>2</sup> ( $E_{IB}=10$  keV) in Fig. 3.60).

For the sample bombarded with 20 keV He ions no clear tendency can be found. After the heating to 250°C new MTJs have been structured. They do not show significant differences compared to the MTJs which have been structured before and measured between the subsequent heating steps.<sup>29</sup>

Figure 3.63 shows the evolution of the magnetic switching properties of a MTJ on a sample with stack  $MTJ_{AlOx}^{inv}$  after it has been treated by field cooling (a), after an additional ion bombardment with  $3 \times 10^{15}$  ions/cm<sup>2</sup> ( $E_{IB}=20$  keV,  $\mathbf{H}_{IB} \perp \mathbf{H}_{FC}$ ) (a), after an additional subsequent postannealing without an external magnetic field at 200°C (b),<sup>30</sup> and 250°C (c), and after an additional annealing step with 200°C in a magnetic field parallel to  $\mathbf{H}_{IB}$  (d).

A comparison of the major loops measured before and after IB shows that the shift of the reference layer hysteresis loop is increased from about 170 Oe to about 250 Oe during the rotation of the EB direction by 90° by bombardment with  $3 \times 10^{15}$  ions/cm<sup>2</sup> while the TMR amplitude is decreased from 46.1% to 38.3% [Fig. 3.63 (a)].

The postannealing of this MTJ with 200°C increases its TMR to 42.1%. But at the same time the shift of the hysteresis loop decreases from about 250 Oe to about 205 Oe. Furthermore, the shape of the switching is more rounded than it was before the postannealing. Because of this changed magnetic behavior the magnetization directions are not aligned perfectly antiparallel at small negative magnetic fields any longer. Therefore, the obtained TMR amplitude is smaller than it could be with a better antiparallel alignment. For an application one should use a stack with a larger shift of the reference layer due to EB ( $H_{EB}$ ). These samples would be less sensible to variations of the magnetization reversal process (compare Table 3.4).

The rounded shape was also observed after the postannealing of stack  $MTJ_{AlOx}^{std}$  although for this sample the EB did not decrease during the additional heating step (Fig. 3.59).

<sup>29</sup>In contrast to this, MTJs with a standard stack which have been structured first and then have been bombarded with ions did show significantly larger side effects of the IB than MTJs which have been structured on an equally bombarded area after the IB was finished. This might be due to the influence of the ions on the sides of the structured MTJ-“tower”.

<sup>30</sup>Between the heating steps with 100°C and 250°C an additional heating step to 225°C has been carried out which is omitted in graph 3.63 for the sake of clarity.

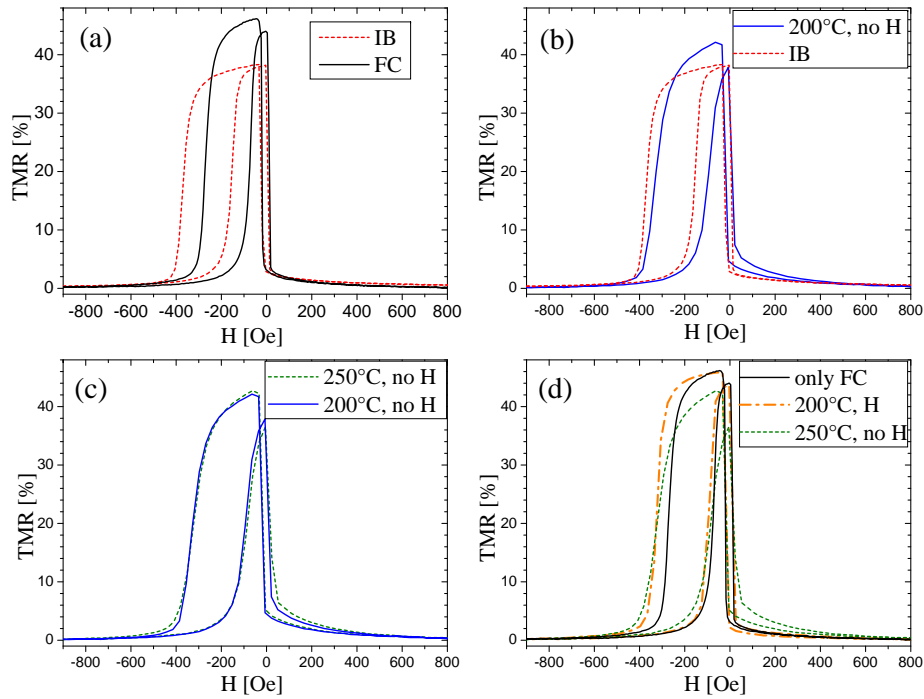


Figure 3.63: Major loops measured at a sample with stack  $MTJ_{AlOx}^{inv}$  after field cooling (FC) (a), after an additional ion bombardment (IB) with  $3 \times 10^{15}$  ions/cm<sup>2</sup> ( $E_{IB}=20$  keV,  $\mathbf{H}_{IB} \perp \mathbf{H}_{FC}$ ) (a), after additional subsequent postannealing without an external magnetic field at 200°C (b), and 250°C (c), and after an additional annealing step with 200°C in a magnetic field parallel to  $\mathbf{H}_{IB}$  (d). For each major loop the last treatment of the sample before the measurement was carried out is stated in the graph.



The basic principle which enables the postannealing without significant changes of the magnetic pattern is that the magnetization of the reference layer in remanence is given by the EB direction and, therefore, the magnetization direction during the additional annealing is the same as during the last field cooling or ion bombardment treatment when moderate temperatures are used for the postannealing. As long as this is true, the postannealing acts like a field cooling and the EB direction is conserved. Therefore, the change of the major loop shape after the postannealing might be connected to a not perfectly uniform magnetic alignment of the reference layer during the postannealing step at  $200^\circ\text{C}$ . This occurs when the temperature approaches the blocking temperature and the strength of the EB coupling decreases relative to, e.g., the exchange coupling at boundaries of bombarded areas (compare, e.g., chapter 3.2.3). When the temperature is in the range of the blocking temperature or even higher, a domain pattern can develop which prevents that at the whole area of the sample an antiparallel alignment of the FM layer magnetizations adjacent to the barrier can be obtained. This has been observed, e.g., for pinned ferromagnetic layers without a topographic patterning in the same temperature range as it has been used here for the postannealing (see, e.g., Fig. 3.21). Once a domain pattern is present at high temperatures, this pattern will be conserved when the temperature is decreased again (compare chapter 3.2).

Two additional postannealing steps with a temperature of  $225^\circ\text{C}$  and  $250^\circ\text{C}$  and a duration of one hour each, slightly advanced the change of the magnetization reversal process at sample  $MTJ_{AlO_x}^{inv}$  [Fig. 3.63 (c)].

An additional annealing step in a magnetic field at a temperature of  $200^\circ\text{C}$  restores the more squared kind of switching for the pinned reference layer while the enlarged EB after the IB is conserved [Fig. 3.63 (d)]. This results in a better antiparallel alignment of the magnetizations of the two electrodes for small negative magnetic fields compared to the reference measurement carried out before the IB. Furthermore, the original TMR amplitude is restored again. This shows that the reduced TMR amplitude after the postannealing step without magnetic field compared to the measurements carried out before the EB direction was turned by  $90^\circ$  by IB is due to the incomplete antiparallel alignment of the FM electrode magnetizations.

For an industrial application much smaller MTJs would be used. Furthermore, an elliptic shape is more likely than the squared shape of the MTJs investigated here. The temperature dependence of the magnetic pattern of some magnetic structures which are closer to this design than the MTJs used here is described in chapter 3.2.5. The constant magnetic pattern up to temperatures of about  $320^\circ\text{C}$  observed while heating the elliptic pinned FM layers [long (short) axes:  $2.6\ \mu\text{m}$  ( $1.2\ \mu\text{m}$ )] in the PEEM suggests that the magnetization of the reference layer of small elliptic MTJs would be better aligned during the postannealing due to the shape anisotropy. Furthermore, the application of an artificial ferrimagnet would decrease the strayfield of the reference electrode which contributes to the formation of a domain pattern at high temperatures. Therefore, an at least smaller if not even vanishing change of the magnetic behavior during the postannealing step can be expected for this kind of MTJs.

### 3.5.3 Summary

The influence of postannealing on the transport properties of MTJs with a He ion bombardment modified IrMn/CoFe electrode has been investigated. It is possible to reduce the unintentional negative side effects of ion bombardment, namely deteriorated TMR and increased resistance, significantly by a postannealing step after IB. Because no external field is needed for this postannealing, the direction of the EB anisotropy remains unchanged for moderate annealing temperatures. After annealing for 60 min, at 225°C the TMR of samples with stack  $MTJ_{\text{AlOx}}^{\text{std}}$  reaches the value measured prior to ion bombardment. Therefore, postannealing after ion bombardment can help to pattern complete MTJs magnetically and keep large TMR values. This can open the way to prepare MTJs with a magnetically patterned reference electrode.

The postannealing of a sample with stack  $MTJ_{\text{AlOx}}^{\text{inv}}$  results in very similar variations of the electrical properties. Variations of the magnetic switching behavior observed especially at the sample with stack  $MTJ_{\text{AlOx}}^{\text{inv}}$  can be expected to be at least significantly reduced for the small elliptic magnetic tunnel junctions which are likely to be used in industrial applications.

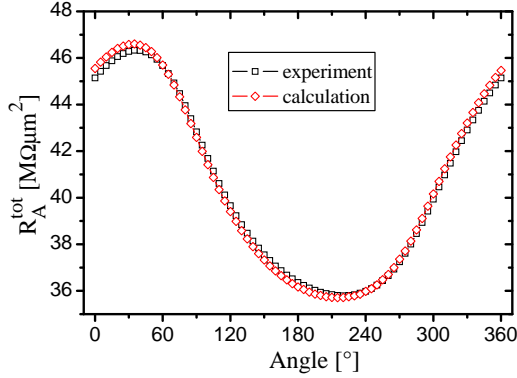


Figure 3.64:  $\square$ : Area resistance product in dependence of the direction of the external magnetic field (150 Oe) measured with 10 mV bias voltage at a half bombarded MTJ (EB direction on bombarded part rotated  $90^\circ$ ) and  $\diamond$ : the corresponding resistance versus field direction graph calculated from measurements carried out at one homogeneously bombarded MTJ and one not bombarded MTJ. A parallel wiring of these MTJs has been assumed.

## 3.6 Magnetic patterning of single magnetic tunnel junctions

### 3.6.1 Experiment

In the last tests the area of the whole magnetic tunnel junctions has been homogeneously bombarded or not bombarded. Additional tests have been carried out with  $200\ \mu\text{m} \times 200\ \mu\text{m}$  sized partly bombarded MTJs.

The tunnel junctions with stack  $MTJ_{\text{AlOx}}^{\text{std}+}$  have been annealed for 60 minutes at a temperature of  $275^\circ\text{C}$  in a magnetic field  $H_{\text{FC}}$  of about 1500 Oe to initialize the exchange bias. After MTJs have been structured by laser lithography and ion beam etching, resist masks covering one half of several MTJs have been produced by laser lithography. The direction of the EB on the not resist covered parts of these MTJs has been turned by  $90^\circ$  by bombardment with 10 keV He ions in a magnetic field  $H_{\text{IB}}$  perpendicular to  $H_{\text{FC}}$ . Furthermore, at some MTJs the not bombarded part has been removed with the usual lithography and ion beam etching procedures. The remaining part of these MTJs is identical to a homogeneously bombarded MTJ. The resistance of these partly bombarded, homogeneously bombarded and not bombarded MTJs has been investigated for several directions and sizes of the magnetic field.

### 3.6.2 Results

The partly bombarded MTJs act like it can be expected from two independent MTJs with a parallel wiring. Obviously, the interaction at the edge between the bombarded and the not bombarded parts of the MTJs is not large enough for a significant influence on the magnetic behavior of these large tunnel junctions.

As an example for these experiments a measurement of the resistance of a partly bombarded MTJ in dependence of the direction of the external magnetic field is shown in Fig. 3.64. The calculated graph has been obtained by calculating the total resistance  $R_A^{\text{tot}}$  of two parallel wired MTJs in dependence of the angle of the external magnetic field from corresponding measurements carried out with one

homogeneously bombarded and one not bombarded MTJ:

$$R_A^{\text{tot}} = \frac{A}{1/R_{IB}^{20000} + 1/R_{ref}^{20000}} \quad (3.2)$$

$A$  denotes the area of the magnetically patterned MTJ ( $A=40000 \mu\text{m}^2$ ) while  $R_{IB}^{20000}$  and  $R_{ref}^{20000}$  stand for the resistance of a homogeneously bombarded MTJ and a not bombarded reference MTJ, respectively. The latter two MTJs had an area of  $20000 \mu\text{m}^2$ . In the calculation, the measured resistance of the not bombarded MTJ has been enlarged by 9% for all angles for a good agreement between experiment and calculation. This is in the range of the variation of the resistance observed experimentally for reference MTJs on different parts of the investigated sample. The good agreement between the two graphs shows that in applications which need a parallel wiring of MTJs with different EB directions, this structure can be replaced by a single magnetically patterned MTJ. This result is valid for MTJs in the range of  $40000 \mu\text{m}^2$  and larger. For smaller MTJs additional tests are necessary as the exchange coupling in the single layers gets more important relative to the EB coupling.

### 3.7 Application of IBMP in MTJs with pinned electrode below the MgO barrier

In the last chapters the application of ion bombardment induced magnetic patterning in combination with magnetic tunnel junctions with alumina barrier has been described. At the time when the experimental work for this thesis has been started, this was the type of MTJs with the maximum TMR amplitude.

Recently, very high TMR amplitudes of up to 500% at room temperature have been reported for MTJs with an MgO barrier [25]. Therefore, on the following pages the applicability of IBMP on MTJs of this new type will be described.

#### 3.7.1 Effect of ion bombardment on standard MgO based magnetic tunnel junctions

##### Experiment

A sample with the following stack ( $MgO_{std}$ ) has been used for the first experiments with bombarded MgO MTJs:<sup>31</sup> wafer / Ta 5 nm / Cu 30 nm / Ta 5 nm / Cu 5 nm / Ir<sub>17</sub>Mn<sub>83</sub> 12 nm / Co<sub>40</sub>Fe<sub>40</sub>B<sub>20</sub> 4 nm / Mg 0.75 nm / MgO 1.5 nm / Co<sub>40</sub>Fe<sub>40</sub>B<sub>20</sub> 6 nm / Ta 5 nm / Cu 40 nm / Au 30 nm. This kind of stack with the pinned electrode located underneath the barrier is called *standard stack* on the following pages corresponding to the *standard* and *inverted* stack with alumina barrier in the last chapters.

The sample has been field cooled for one hour at 325°C in a magnetic field  $H_{FC}$  of about 1500 Oe.<sup>32</sup>

The sample has been bombarded with 10 keV He ions with doses in the range of  $1 \times 10^{14}$  ions/cm<sup>2</sup> to  $4 \times 10^{16}$  ions/cm<sup>2</sup>. The magnetic field during the ion bombardment ( $H_{IB}$ ) was aligned antiparallel to  $H_{FC}$ .

Square MTJs with a size of  $500 \mu\text{m}^2$  have been produced by the UV lithography and ion beam etching.

A postannealing has been carried out with various temperatures.

The electrical and magnetic properties of this sample have been investigated with and without postannealing by measuring major loops, IV curves and inelastic electron tunneling spectroscopy (IETS).

##### Results and discussion: TMR and resistance

Examples of major loops measured on a sample with stack  $MgO_{std}$  without ion bombardment and after the bombardment with several ion doses in a magnetic field antiparallel to  $H_{FC}$  are shown in Fig. 3.65. The exchange bias field extracted from several measurements of this kind in dependence of the ion dose can be found in Fig. 3.66. The EB direction is turned in the range of about  $1 \times 10^{15}$  ions/cm<sup>2</sup> (green mesh in Fig. 3.66) and the coupling reaches its maximum strength at  $6 \times 10^{15}$  ions/cm<sup>2</sup>.

<sup>31</sup>This stack and the used annealing parameters result from optimization experiments carried out by Xinli Kou who also deposited this sample.

<sup>32</sup>For this annealing temperature the maximum TMR can be expected for this stack [189]. (compare Fig. 3.83)

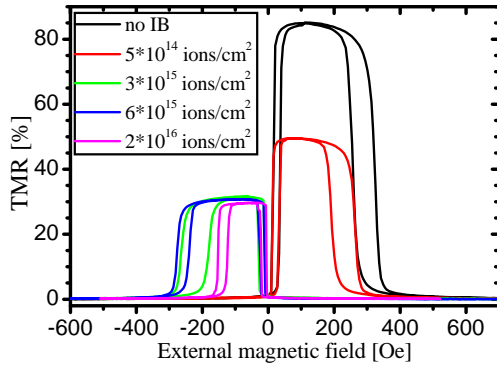


Figure 3.65: Major loops measured on a sample with stack  $MgO_{std}$  on one part of the sample without IB and on other parts which have been bombarded with ion doses of  $5 \times 10^{14}$  ions/cm<sup>2</sup> to  $2 \times 10^{16}$  ions/cm<sup>2</sup> ( $E_{IB}=10$  keV,  $\mathbf{H}_{IB} \uparrow \downarrow \mathbf{H}_{FC}$ ).

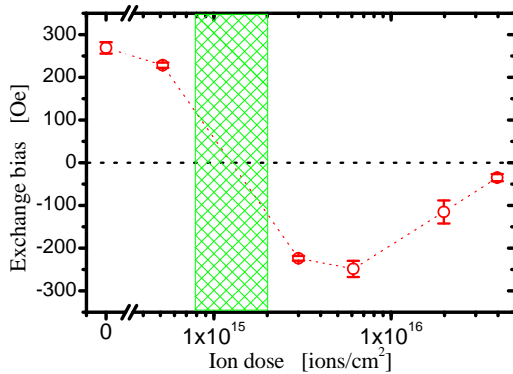


Figure 3.66: Exchange bias in dependence of the ion dose extracted from major loops measured at a sample with stack  $MgO_{std}$  after bombardment with 10 keV He ions ( $\mathbf{H}_{IB} \uparrow \downarrow \mathbf{H}_{FC}$ ). The circles indicate averaged EB values while the error bars indicate the corresponding standard deviation. The green mesh indicates the ion dose range in which the EB changes its direction. The error bars indicate the standard deviation. All lines are a guide to the eye.

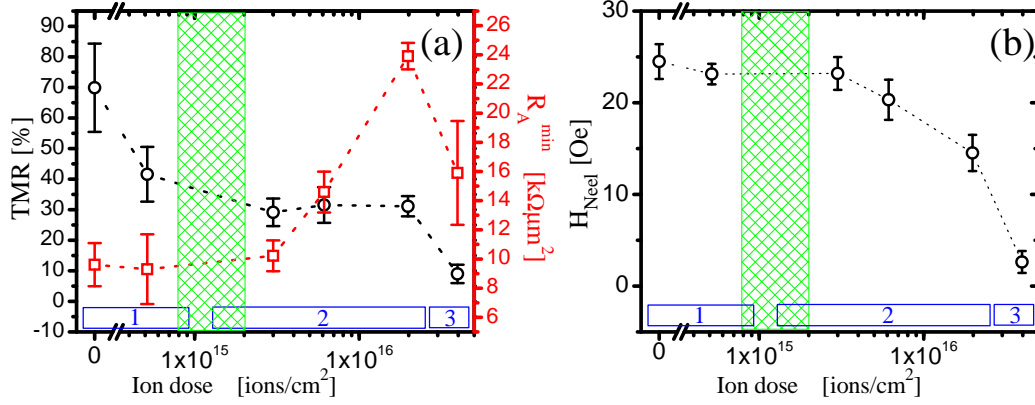


Figure 3.67: (a) TMR amplitude, area resistance product in saturation ( $R_A^{\min}$ ) and (b) absolute value of Néel coupling in dependence of the ion dose ( $E_{\text{IB}}=10$  keV). The green checked pattern indicates the ion dose range at which the exchange bias switches the direction. The error bars indicate the standard deviation. All lines are a guide to the eye.

For higher ion doses the EB decreases. This ion dose dependence of the EB fits well to the expectations for the IBMP with a magnetic field during IB antiparallel to  $\mathbf{H}_{\text{FC}}$  (compare chapter 2.2).

The TMR amplitude observed in the major loop measurements is even for small ion doses significantly decreased (Fig. 3.65). The ion dose dependence of the TMR amplitude, the area resistance product in saturation ( $R_A^{\min}$ ), and the shift of the hysteresis loop of the not pinned FM layer due to the Néel coupling<sup>33</sup> ( $H_{\text{Néel}}$ ) are shown in Fig. 3.67.

One can divide the investigated ion dose range into three regions. The first one ranges from zero to  $5 \times 10^{14}$  ions/cm<sup>2</sup>. For this ion doses the EB is not turned and the area resistance and Neel coupling are nearly constant. The TMR is significantly reduced with increasing ion dose. The second range follows up to  $2 \times 10^{16}$  ions/cm<sup>2</sup>. Here, the EB is turned, the resistance is increasing and the Néel coupling is decreasing. The TMR is nearly constant for this ion doses. Finally, the last range can be found above  $2 \times 10^{16}$  ions/cm<sup>2</sup>. For the ion dose  $4 \times 10^{16}$  ions/cm<sup>2</sup> all measured parameters are degrading.

The reason for the strong TMR decrease in region one might be connected with a partial destruction of the CoFeB/MgO crystal structure and a resulting destruction of a coherent tunneling which is characteristic for MTJs with MgO barrier if this type of tunneling is present in this sample. Because of the relatively small TMR amplitude of about 70% prior to IB this is not necessarily the case.

But Schmalhorst *et al.* found for samples of the same series hints for a crystallization

<sup>33</sup>This shift is denoted as Néel coupling because for these MTJs this ferromagnetic interaction is dominating over the antiferromagnetic strayfield coupling. If the strayfield coupling was the origin of the shift of the hysteresis loop, the loop would not be shifted in the same direction as the hysteresis loop of the pinned FM layer.

of the CoFeB electrodes after annealing to temperatures above 275°C accompanied with an increasing TMR amplitude which they attributed to an enhancement of coherent tunneling [190].

Another possible reason for the decrease of the TMR amplitude after IB is a formation of Fe oxide at the barrier / electrode interface due to intermixing. This oxide has been found directly after the deposition of this kind of MTJs [190]. The reduction of the Fe oxide during annealing to temperatures up to 275°C was accompanied by an increasing TMR amplitude [190]. Therefore, it can be expected that a formation of Fe oxide by IB would also decrease the TMR amplitude. This material might be reduced by a postannealing step.

Furthermore, the intermixing and local heating due to IB might result in the formation of a B oxide as it has been observed after annealing this kind of MTJs to high temperatures in the range of 350°C [190]. This also can reduce the TMR amplitude. As the formation of the B oxide has been observed during heating, it is unlikely that this effect can be reversed by postannealing.

When one assumes that only processes which reduce the TMR and have an increasing effect with increasing number of IB induced changes like, e.g., intermixing or defect production are present, many possible explanations for the decreasing TMR amplitude can be excluded.

In this case, the TMR decrease can not be caused by the generation of additional not spin polarized electron channels because this would decrease the resistance and for ion doses above  $1 \times 10^{15}$  ions/cm<sup>2</sup> a further decrease of the TMR and the resistance can be expected. Both of these effects have not been observed.

Furthermore, when the TMR decrease are due to processes which induce a spin flip and, therefore, can reduce the polarization of the tunneling electrons without increasing their number, it can be expected that a further increase of the ion dose also increases the number of this events. This would also result in a decrease of the TMR in range two. But in the experimental data this decrease has not been found. In the context of inelastic electron tunneling spectroscopy measurements this topic will be investigated again and hints will be presented that these effects should not be excluded.

One effect has been described in the literature which might weaken the argument that no processes which result in a decreasing spin polarization of the tunnel current can take place in region 1 because then in region 2 a further decrease would be observable. This effect might explain an increasing TMR amplitude which might neutralize the TMR decreasing effects of an increasing not spin polarized current, e.g., via hopping.

Jang *et al.* [191] found that at about 0.3 V a minimum appeared in their conductance versus voltage plots (parallel alignment of magnetizations) when the sample was heated to temperatures above 300°C (compare arrows in Fig. 3.68). They explained this by the formation of a minority Bloch state in the lower electrode due to the crystallization of the CoFeB.<sup>34</sup>

The asymmetry of the measurement despite the fact that both electrodes consist of

---

<sup>34</sup>The investigated stack in [191] was: Ta 30 nm / IrMn 15 nm / Co<sub>60</sub>Fe<sub>20</sub>B<sub>20</sub> 3 nm / MgO 1.8 nm / Co<sub>60</sub>Fe<sub>20</sub>B<sub>20</sub> 3 nm / Ta 5 nm / Ru 10 nm.



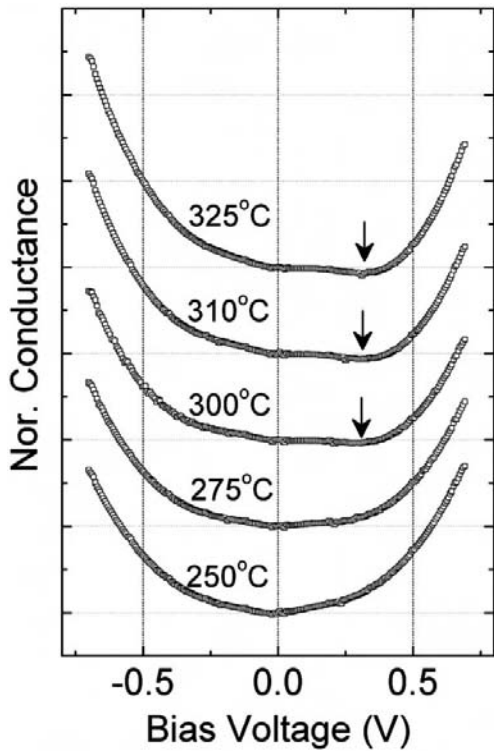


Figure 3.68: Normalized conductance ( $dI/dV$ ) in dependence of the applied bias voltage measured by Jang *et al.* in the parallel state after annealing with various temperatures at sputtered CoFeB/MgO/CoFeB based MTJs. (from [191])

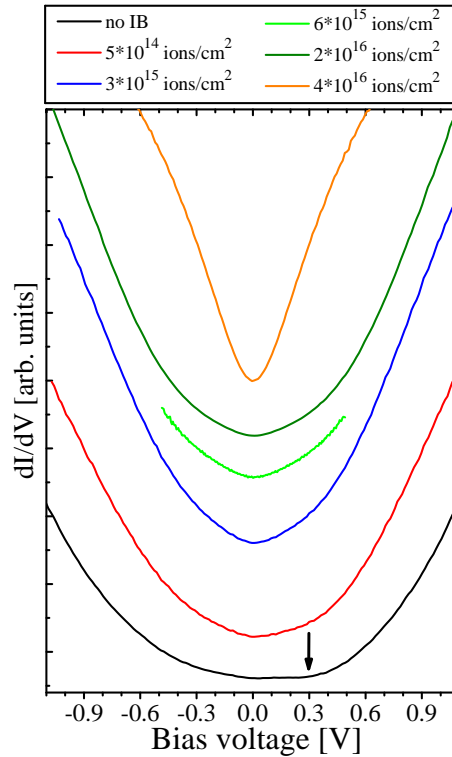


Figure 3.69:  $dI/dV$  calculated from current versus voltage measurements in saturation carried out at room temperature at MTJs with stack  $MgO_{std}$  after IB with various ion doses (increasing ion dose from bottom to top of graph). The measurements have been shifted on the y-axis for clarity.

the same material has been explained in Ref. [191] by a formation of iron oxide in the lower electrode of their MTJs during the sputter deposition which was reduced during the heating to higher temperatures in combination with the formation of boron oxide. No iron oxide has been found at the top electrode.

Furthermore, the different growth conditions of the lower and the upper electrodes due to the different last layer underneath the two FM layers can result in an asymmetric behavior.

The conductance over voltage measurements carried out at not bombarded MTJs with stack  $MgO_{\text{std}}$  carried out with parallel aligned FM layer magnetizations show a dip (deviation from parabola) at about 300 mV. A similar process might be involved during the sputter deposition and annealing of our samples, too. This can be seen especially clear in the measurements carried out with the lock in amplifier at about 12 K (Fig. 3.71 (e)) but is as well visible for measurements carried out at room temperature (arrow in Fig. 3.69).

The dip is easy to find in the measurement without IB and is not visible in the measurement done at a MTJ which has been bombarded with  $4 \times 10^{16}$  ions/cm<sup>2</sup>. If minority Bloch states which have a large decay length in the barrier [192] were removed during the bombardment, this would result in an increasing resistance. As tunneling via the minority Bloch states reduces the TMR, the TMR plateau might be at least partly be explained by a TMR increase due to a destruction of the minority Bloch states and competing TMR reducing effects like, e.g., scattering at magnetic atoms or hopping. The fact that the plateau in the TMR versus ion dose plot and the increasing resistance can be observed in the same ion dose range [range 2 in Fig. 3.67 (a)] fits well to this suggestion.

The increasing resistance due to a destruction of minority Bloch states will be superpositioned by the usual resistance increase, e.g., due to scattering at IB induced defects.

The decreasing shift of the hysteresis loop of the not pinned FM layer in the ion dose range from  $3 \times 10^{15}$  ions/cm<sup>2</sup> to  $2 \times 10^{16}$  ions/cm<sup>2</sup> in Fig. 3.67 (b) might be related to an increase of the barrier thickness due to a change of the order in the crystal. This could also explain the increasing resistance in this ion dose range.

Furthermore, a less correlated roughness at the barrier interfaces due to intermixing might be a reason for the decreasing Néel coupling.

A strong decrease of the saturation magnetization at the FM/barrier interface as an explanation for the decreasing Néel coupling is unlikely because this would result in a decreased spin polarization and, therefore, a decreased TMR amplitude.

The strong decrease of the TMR amplitude and the resistance at  $4 \times 10^{16}$  ions/cm<sup>2</sup> points to the formation of pinholes at this ion dose. Furthermore, other additional electron channels like hopping via defects in the barrier might have been opened by the IB at this ion dose, reducing the TMR and the resistance. The polarization of the tunneling electrons might be reduced by scattering at magnetic defects in the barrier resulting in a reduced TMR amplitude. Other mechanisms which might be involved at this ion dose are the reduction of the spin polarization at the FM interface (lower TMR) and the correlated roughness of the barrier interfaces (reduced  $H_{\text{Néel}}$ ) due to intermixing at the barrier / FM interfaces.

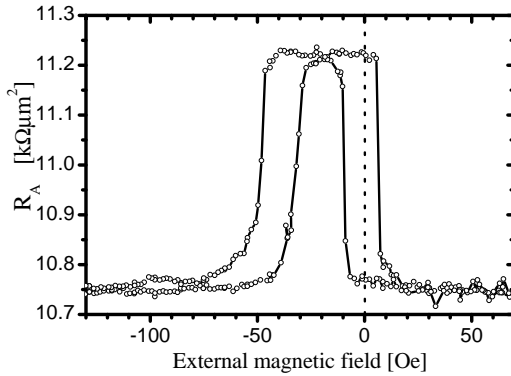


Figure 3.70: Major loop measured at a  $500 \mu\text{m}^2$  MTJ on a sample with stack  $\text{MgO}_{\text{std}}$  after bombardment with  $4 \times 10^{16}$  ions/ $\text{cm}^2$ .

Although the EB coupling is significantly reduced at this ion dose, a plateau with a high resistance is still visible in the major loop (Fig. 3.70). This shows that the reduced EB is not responsible for the reduction of the TMR amplitude at this ion dose.

### Results and discussion: Inelastic electron tunneling spectroscopy

To learn more about the mechanisms involved in the variation of the electric properties of this MgO based MTJs, inelastic electron tunneling spectroscopy (IETS) measurements at low temperatures have been carried out. Here,  $dI/dV$  has been measured in dependence of the bias voltage. These measurements have been differentiated to obtain the IETS-signal proportional to  $dI^2/dV^2$ . A more detailed description of this technique and the used experimental setup can be found in chapter 2.6.5.

Figure 3.71 (a) shows IETS measurements carried out at a not bombarded MTJ with stack  $\text{MgO}_{\text{std}}$  at a temperature of 12.5 K.<sup>35</sup>

This MTJ shows a TMR amplitude of 121 % at 14 K [Fig. 3.71 (b)] and 72 % at room temperature (RT) [Fig. 3.71 (d)]. It has an area resistance product in saturation ( $R_A^{\text{min}}$ ) of  $8.6 \text{ k}\Omega\mu\text{m}^2$  and  $9.7 \text{ k}\Omega\mu\text{m}^2$  at 14 K and RT, respectively.

The IETS measurements have been carried out in a magnetic field of -118 Oe [blue line in Fig. 3.71 (a)] and +118 Oe [red line in Fig. 3.71 (a)]. The minor loops measured at this MTJ at a temperature of 13 K [Fig. 3.71 (c)] show that a parallel and antiparallel alignment of the FM layer magnetizations can be assumed for +118 Oe and -118 Oe, respectively, when these two external magnetic fields are applied in an alternate order for subsequent measurements.<sup>36</sup>

The large peaks in the IETS-signal ( $dI^2/dV^2$ ) at about  $\pm 18$  Oe [blue A and A' in Fig. 3.71 (a)] and about  $\pm 10$  Oe [red A and A' in Fig. 3.71 (a)] for the

<sup>35</sup>All temperatures given here for measurements in the cryostat are nominal temperatures. In some cases, the real temperature of the sample might vary a few K from this value. When a temperature of 12.5 K or lower is stated, the cryostat usually has cooled with maximum power for a relatively long time (about 3 hours to 3 days) and it can be assumed that no significant temperature gradient between the sample and the temperature sensor is present.

<sup>36</sup>The values of the magnetic fields applied for bombarded MTJs have been adjusted to the varied magnetic properties of these samples.

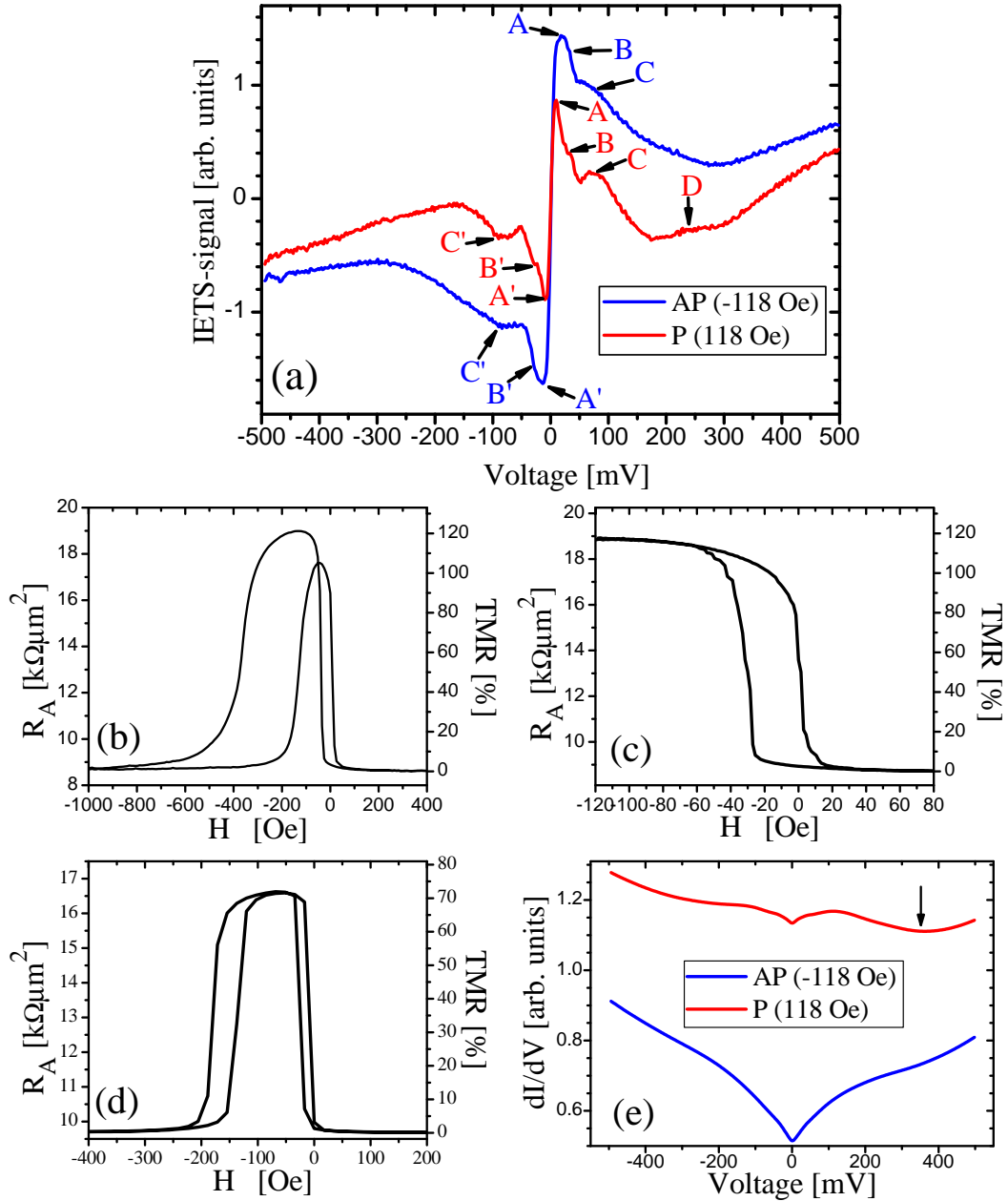


Figure 3.71: (a) Inelastic electron tunneling spectra (IETS,  $dI^2/dV^2$ ) measured at a not bombarded MTJ with stack  $MgO_{std}$  at 12.5 K (A/A': zero bias anomaly, B/B': magnon excitation, C/C': phonon excitation) and the corresponding (b) major (14K) and (c) minor (13K) loops. (d) corresponding major loop at room temperature. The magnetization of the two electrodes was aligned antiparallel and parallel during the IETS measurements at -118 Oe (blue) and +118 Oe (red), respectively. The  $dI/dV$  measurement from which the IETS measurement in (a) has been derived is shown in (e). The arrow in (e) indicates the minimum similar to [191] (compare Fig. 3.68 and 3.69 and page 128).

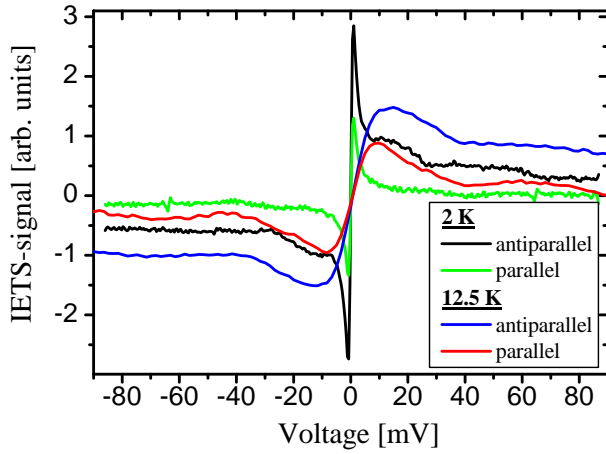


Figure 3.72: IETS measurements carried out at about 2 K and about 12.5 K with a parallel (P) and antiparallel (AP) alignment of the FM layer magnetizations at a MTJ with stack  $MgO_{std}$ . The given bias voltage and relative IETS signal should be regarded as approximations.

antiparallel and parallel alignment, respectively, are usually denoted as zero bias anomaly [128, 193]. This effect is frequently attributed to magnetic impurity scattering [128, 193].

This interpretation is supported by the temperature dependence of the zero bias anomaly shown in Fig. 3.72. Instead of one rather broad peak in the range below 30 mV as observed at 12.5 K, the measurement at about 2 K<sup>37</sup> shows one larger and sharper peak at nearly zero bias voltage and, especially in the case of the antiparallel alignment of the magnetizations, one wider peak at about 17 mV. The change from a broad low peak to a sharper higher peak with decreasing temperature is consistent with the observations described in [193] and with a zero bias anomaly resulting from magnetic impurity scattering [193].

The peak at about 17 mV in the measurements carried out at 2 K fits well to the peak observed by Moodera *et al.* [195] in IETS measurements carried out at 1 K with  $Co/Al_2O_3/Ni_{80}Fe_{20}$  MTJs. It has been explained by magnon generation in the FM electrodes [195].

Therefore, it can be assumed that the low voltage peak denoted as zero bias anomaly in the measurements carried out at 12.5 K consists of contributions due to scattering at magnetic impurities as well as tunneling including magnon generation. It is not possible to distinguish between these contributions at 12.5 K.

It is striking that for all bias voltages a higher IETS signal is observed for the antiparallel alignment. This will also be the case in all other IETS measurements shown in this work. This might be connected to the fact that scattering at magnetic impurities as well as tunneling with the participation of a magnon induces a spin flip. Therefore, minority electrons can tunnel into majority states and vice versa. This results in a larger conductance (lower resistance) in the case of antiparallel aligned magnetizations. Therefore, the IETS signal, which is the derivative of the conductance, can be expected to be larger at the voltages where processes including

<sup>37</sup>The resistance of the He cryostat setup is higher than the resistance of the Oxford cryostat which has been used for all other low temperature measurements. For  $500\mu m^2$  MTJs with stack  $MgO_{std}$  the resistance of the He cryostat setup is of the same order of magnitude as the resistance of the sample [194]. Therefore, in Fig. 3.72 the displayed voltage as well as the IETS signal has been modified to remove the influence of the setup resistance to enable a direct comparison of the measurements. This adjustment should be regarded as an approximation ( $\Delta V \approx 5$  mV).

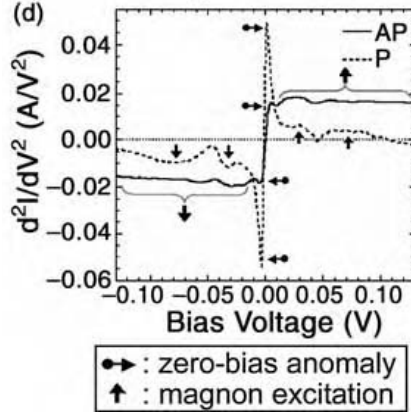


Figure 3.73: IETS measurements carried out at 4.3 K with a parallel (P) and antiparallel (AP) alignment of the FM layer magnetizations at a CoFeB/MgO/CoFeB based MTJ published by Matsumoto *et al.* (from [193])

a spin flip take place when the magnetizations are aligned antiparallel.

The shoulders at about  $\pm 25$  mV [ $B$  and  $B'$  in Fig. 3.71 (a)] and the peaks (shoulders) at about 80 mV ( $C$  and  $C'$ ) match good to IETS measurements (4.3 K) at samples with a CoFeB/MgO/CoFeB stack<sup>38</sup> published by Matsumoto *et al.* in Ref. [193] (Fig. 3.73). In both cases the IETS-signal with parallel aligned magnetizations is smaller compared to the antiparallel alignment. Because of their strong dependence on the magnetic configuration, these two peaks have been attributed to magnon excitation in Ref. [193]. The peak at about 25 mV is usually denoted as magnon peak [192, 196]. Higher order peaks (compare [128]) have not been observed.

The position of the second peak at about 80 mV ( $C/C'$  in Fig. 3.71) matches good the energy of phonons in bulk single crystal MgO (resonance frequency  $(651 \pm 2)$  cm<sup>-1</sup> [197]) of 80.7 meV [192].

The small peak at about 250 mV (D in Fig. 3.71) has also been found for CoFeB/MgO systems in the references [196, 130] but no detailed explanation has been given so far.

In Fig. 3.71 (a) a dip can be observed at smaller bias voltages. The measurement carried out in the parallel configuration shows even negative values. The fact, that the dip is located at smaller values might be connected with a peak at higher voltages which influences the signal at lower voltages.

Matsumoto *et al.* found significantly large dips at about  $\pm 400$  mV which they attributed to the electronic structure of CoFeB or MgO because this kind of dips has not been observed for MTJs with an AlOx barrier. This interpretation is supported by a comparison between IETS measurements of samples with MgO and alumina barrier which are identical apart from the barrier material published in Ref. [198]. These dips in the range of about 300-400 mV have been found by several groups for CoFeB/MgO/CoFeB [193, 192, 198, 130, 196] as well as Fe/MgO/Fe [199] stacks.

<sup>38</sup>The full stack of the sputter deposited sample presented in [193] is: Si substrate / Ta 10 nm / PtMn 15 nm / Co<sub>70</sub>Fe<sub>30</sub> 2.5 nm / Ru 0.85 nm / Co<sub>60</sub>Fe<sub>20</sub>B<sub>20</sub> 3 nm / MgO 1.8 nm / Co<sub>60</sub>Fe<sub>20</sub>B<sub>20</sub> 3 nm / Ta 10 nm / Ru 7 nm. The sample has been annealed for 2 hours at 360°C in a magnetic field of 8 kOe.

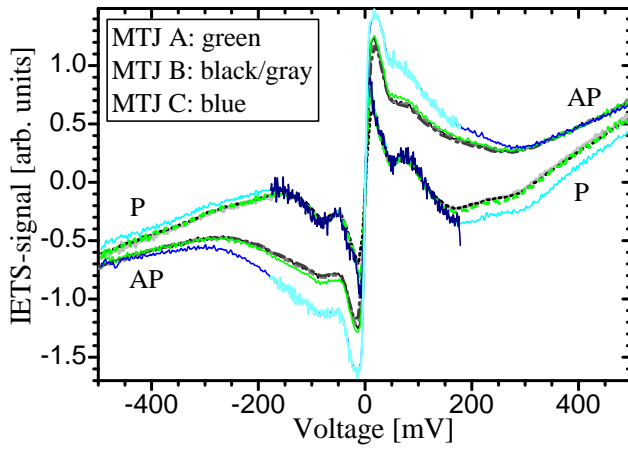


Figure 3.74: IETS measurements carried out with various voltage step sizes at 12.5 K at not bombarded MTJs with stack  $MgO_{std}$  on different parts of the sample. (MTJ A and B: field 8, MTJ C: field 1 in Fig. 3.75)

High voltage peaks at about 1 V have been found in Fe/MgO/Fe MTJs with thick MgO barriers which have never been found in MTJs with alumina barrier [199]. They have been attributed by Ando *et al.* to the band structure of Fe electrodes. Ono *et al.* found corresponding peaks at about 600 mV for CoFeB/MgO/CoFeB MTJs and suggested that these peaks are due to coherent tunneling in combination with the band structure of the CoFeB electrodes [196].

In some measurements carried out at MTJs with stack  $MgO_{std}$  also peaks at high voltages have been found. But it is unlikely that they result from a coherent scattering as suggested by Ono *et al.* for their MTJs because it will be shown on the following pages that the peaks get larger with increasing ion dose. This topic will be discussed in detail in the context of the bombardment with high ion doses. Furthermore, the high voltage peaks will be discussed again in the context of the investigation of the bias voltage dependence of the TMR and resistance of inverted MTJs with MgO barrier.

Figure 3.74 shows repeated IETS measurements carried out with various measurement point densities and ac voltages<sup>39</sup> at MTJs located on different parts of the sample.<sup>40</sup> MTJs A and B are located at one side of the sample (field 8 in Fig. 3.75) while C is located on the opposite side of the sample (field 1 in Fig. 3.75).

It is striking, that MTJ A and B show a very similar behavior. In contrast to this, a significant difference between the measurements done at MTJs A and B on one side and MTJ C on the other side can be observed, e.g., at low bias voltages. This is correlated to their location on the sample.

A less good antiparallel alignment of the magnetizations in the case of MTJs A and B which would result in a reduced IETS signal as well can be ruled out. In this case the IETS signal would be smaller for all bias voltages, but, e.g., the measurements with antiparallel aligned magnetizations (higher IETS signal) are nearly identical for all MTJs at high positive voltages but differ significantly for small voltages. Ad-

<sup>39</sup>The good agreement between the measurements carried out with different parameters at the same MTJs indicates the good reliability of the obtained information.

<sup>40</sup>The IETS measurements are carried out for one to three MTJs per ion dose. The values given, e.g., for the resistance or TMR amplitude in dependence of the ion dose are averaged over about 4-15 MTJs per ion dose, except when a name of certain MTJs is stated.

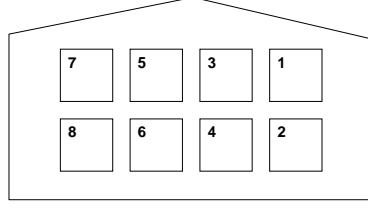


Figure 3.75: Sketch of the location of the bombarded regions on the sample with stack  $MgO_{\text{std}}$  which was used for the IETS measurements. Field 1 and 8 have not been bombarded and are used for reference measurements. Field 2:  $5 \times 10^{14}$  ions/cm<sup>2</sup>, field 3:  $3 \times 10^{15}$  ions/cm<sup>2</sup>, field 4:  $6 \times 10^{15}$  ions/cm<sup>2</sup>, field 5:  $2 \times 10^{16}$  ions/cm<sup>2</sup>, field 6:  $4 \times 10^{16}$  ions/cm<sup>2</sup>, field 7:  $8 \times 10^{16}$  ions/cm<sup>2</sup>.

Sample	TMR	$R_A^{\text{min}}$	TMR	$R_A^{\text{min}}$
	room temperature	room temperature	12.5 K	12.5 K
MTJ A	76.6%	12.3 k $\Omega\mu\text{m}^2$	118.6%	11.8 k $\Omega\mu\text{m}^2$
MTJ B	66.9%	12.1 k $\Omega\mu\text{m}^2$	101.9%	11.7 k $\Omega\mu\text{m}^2$
MTJ C	72.3%	9.7 k $\Omega\mu\text{m}^2$	121.5%	8.6 k $\Omega\mu\text{m}^2$

Table 3.5: Transport properties of the not bombarded magnetic tunnel junctions used for the IETS measurements shown in Fig. 3.74.

ditionally, the minor loops measured at these three MTJs (not shown) do not show a different magnetic behavior.

Furthermore, the resistance of MTJ C is smaller compared to the other two MTJs although the TMR value at room temperature is between the TMR amplitudes of the two MTJs located in field 8 and the TMR amplitude at low temperature is even higher. The transport properties of these three MTJs are listed in Tab. 3.5. This shows that the low resistance can not be due to a larger amount of not spin polarized conductance channels as hopping over defects or small pinholes. It can be assumed that the reason for the lower resistance of MTJ C is connected to a thickness gradient of the MgO barrier over the sample.

Therefore, the location of MTJs on the sample has to be taken into account when comparing IETS measurements of bombarded MTJs with reference measurements.

Figure 3.76 shows IETS measurements carried out at two MTJs which have been bombarded with  $5 \times 10^{14}$  ions/cm<sup>2</sup> and one not bombarded MTJ. The measurements without IB have been carried out at MTJ C (compare Fig. 3.74 and Tab. 3.5). This MTJ is located in the field next to the field bombarded with  $5 \times 10^{14}$  ions/cm<sup>2</sup>. MTJ C showed the largest zero bias anomaly and had the lowest signal with parallel aligned magnetizations (compare Fig. 3.74).

No new peaks which might indicate the creation of new conductance channels appear in the range up to 0.5 V [Fig. 3.76 (a)]. The zero bias anomaly with the magnon shoulder is increased for parallel as well as for antiparallel aligned magne-



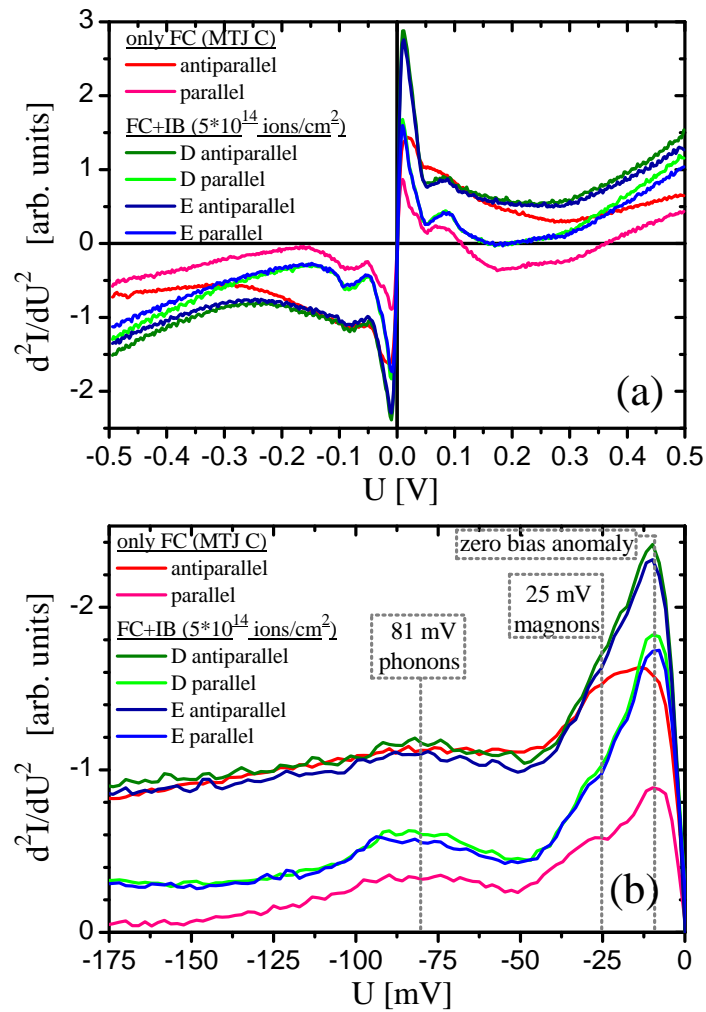


Figure 3.76: IETS measurements carried out at 12.5K at not bombarded and bombarded ( $5 \times 10^{14}$  ions/cm $^2$ ) MTJs with stack  $MgO_{std}$ . (b) shows an enlarged region of (a) which has been mirrored with respect to IETS-signal=0.

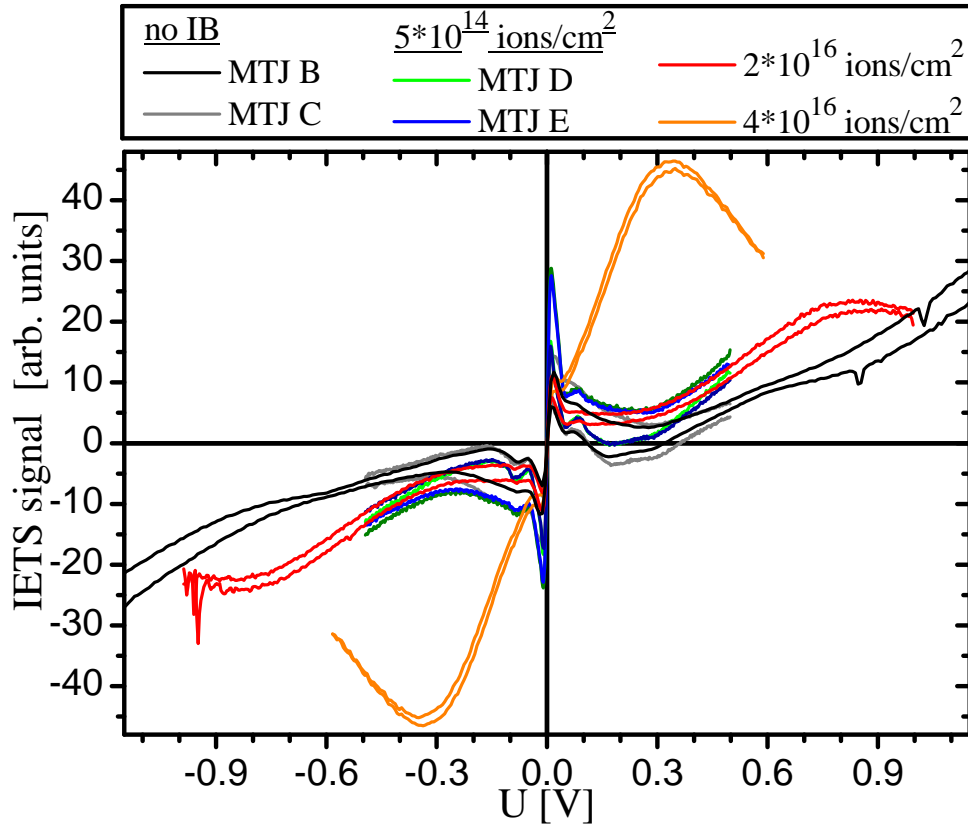


Figure 3.77: IETS measurements carried out at 12.5K at not bombarded and bombarded MTJs with stack  $MgO_{\text{std}}$ . Reference MTJ B (field 8) is located closer to field 5 and 6 ( $2 \times 10^{16}$  ions/cm<sup>2</sup> and  $4 \times 10^{16}$  ions/cm<sup>2</sup>). Reference MTJ C (field 1) is located closer to field 2 ( $5 \times 10^{14}$  ions/cm<sup>2</sup>). At each MTJ the IETS measurement with the higher signal has been measured with an antiparallel alignment of the magnetizations.

tizations even relative to the reference measurement [Fig. 3.76 (b)]. This indicates an increasing amount of magnetic impurity scattering which can be explained by an intermixing at the ferromagnet (FM) / barrier interface.

The phonon peak at about 81 mV at negative bias voltage has in the parallel as well as the antiparallel case a similar peak height relative to the surrounding region independent on the ion bombardment. Therefore, no significant change of the atomic order in the barrier has been detected.

At large bias voltages the IETS signal of the bombarded MTJs is significantly larger compared to the not bombarded MTJ [Fig. 3.76 (a)]. This effect also seems to have an influence on the IETS signal at lower voltage as, e.g., at the dip at about 200 mV.

For the not bombarded MTJs at voltages up to 1.2 V an increasing IETS signal but no maximum can be observed (Fig. 3.77).

For a MTJ which has been bombarded with  $2 \times 10^{16}$  ions/cm<sup>2</sup>, at higher voltages a peak can be found. This peak will be called *high voltage peak* in the following

considerations.

The difference of the slope at -500 mV of the IETS measurements of the two MTJs which have been bombarded with  $5 \times 10^{14}$  ions/cm<sup>2</sup> is larger than the difference between these two MTJs and the MTJ which has been bombarded with  $2 \times 10^{16}$  ions/cm<sup>2</sup>. Furthermore, these three measurements have a large similarity at +500 mV, too. Therefore, one might assume that a similar peak might exist for samples bombarded with  $5 \times 10^{14}$  ions/cm<sup>2</sup>, too. The MTJ with the highest ion dose of  $4 \times 10^{16}$  ions/cm<sup>2</sup> shows the largest high voltage peak at the lowest bias voltage.

In the following lines the experimental observations regarding this peak which gains in size while moving to smaller voltages with increasing ion dose will be compared to the predictions one can make for hopping over localized states in the barrier. The temperature dependence of the average zero bias conductance due to hopping via two localized states  $G_2^{hop}(T)$  is described by Xu *et al.* [200] for the low bias limit ( $eV \ll k_B T$ ) by

$$G_2^{hop}(T) = \nu_{2,T}(gS\alpha^{-1}k_B T)(g\alpha^{-2}dk_B T) \left(\frac{e^2/\hbar}{k_B T}\right) \times \left(\lambda \frac{k_B T}{E_0}\right)^{1/3} E_0 \exp\left(-\frac{2\alpha d}{3}\right) \quad (3.3)$$

$$\propto g^2(k_B T)^{4/3} \quad (3.4)$$

The prefactor  $\nu_{2,T}$  is approximately 50,  $g$  represents the density of localized states in the barrier,  $S$  is the area of the MTJ,  $\alpha^{-1}$  denotes the localization length,  $E_0$  is the binding energy of the localized states and  $d$  stands for the barrier thickness. The dimensionless quantity  $\lambda$  is defined as

$$\lambda \equiv \frac{\Lambda^2 E_0^2}{\hbar^3 \rho v_s} \quad (3.5)$$

with the average deformation potential of the barrier material  $\Lambda$ , the mass density  $\rho$  of the barrier and the speed of sound  $v_s$ .

From these expressions Xu *et al.* derived the following equation for the conductance due to hopping via  $N$  localized states  $G_N^{hop}(T)$  relative to the conductance due to resonant tunneling via one localized state  $G_1^{res}$  which is regarded as temperature independent for these calculations:

$$\frac{G_N^{hop}(T)}{G_1^{res}} = \nu_{N,T}(g\alpha^{-2}dk_B T)^{N-1} \left(\lambda \frac{k_B T}{E_0}\right)^{(N-1)/(N+1)} \exp\left(\frac{N-1}{N+1}\alpha d\right) \quad (3.6)$$

$$\propto g^{N-1}(k_B T)^{(N^2+N-2)/(N+1)}. \quad (3.7)$$

The total conductance due to direct tunneling ( $G_0^{dir}$ ), resonant tunneling via one defect state ( $G_1^{res}$ ) and hopping via up to  $X$  states ( $G_2^{hop}$  -  $G_X^{hop}$ ) can be described as

$$G^{tot} = G_0^{dir} + G_1^{res} + \sum_{N=2}^X G_N^{hop}(T). \quad (3.8)$$

Because of the limited number of available hopping sites, the probability of the existence of chains with a certain number of defect states in a MTJ is smaller for higher

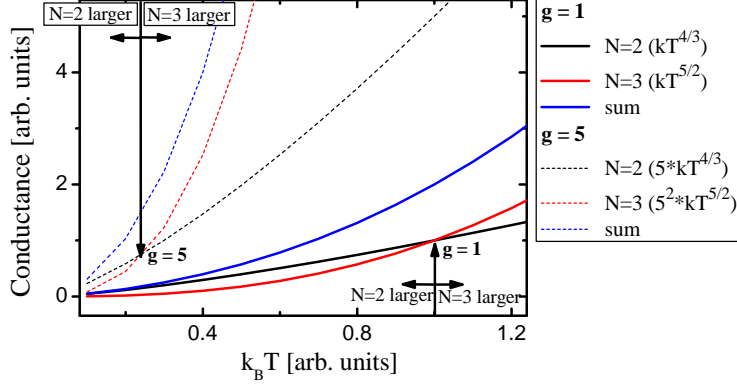


Figure 3.78: Sketch of temperature dependence of conductance due to hopping via  $N=2$  (black) or  $N=3$  (red) defect states and sum of both conductances (blue). The temperature dependence of the hopping conductance over  $N$  defect states is described by  $G_N^{hop,approx.}(T) = g^{N-1}(k_B T)^{(N^2+N-2)/(N+1)}$  to illustrate the principle of the temperature dependence.

numbers and vanishes at some point  $X$ .

When the defect density is increased by IB, two effects can be expected. The number of chains with a given number of states  $N$  grows and the maximum number of hopping sides per chain which can be observed in a MTJ can increase.

The expected effect of an IB on the temperature dependence of the conductance is sketched in Fig. 3.78. Here, it has been assumed that with increasing ion dose the density of defects increases, e.g., due to intermixing, but the other material constants as, e.g., the speed of sound or the density of the barrier are not altered. As only the qualitative change of the conductance is discussed to illustrate the principle of the temperature dependence of the conductance, in Fig. 3.78 the contributions of direct and resonant tunneling have been neglected and all constants except  $g$  and  $k_B T$  have been set to one. Therefore, the temperature dependence of the conductance due to hopping via  $N$  states is described by  $G_N^{hop,approx.}(T) = g^{N-1}(k_B T)^{(N^2+N-2)/(N+1)}$ . Black and red lines represent  $G_2^{hop,approx.}(T)$  and  $G_3^{hop,approx.}(T)$ , respectively. Hopping via more than 3 defects is not considered in Fig. 3.78. The blue lines show the sum of  $G_2^{hop,approx.}(T)$  and  $G_3^{hop,approx.}(T)$ . The solid lines in Fig. 3.78 represent a low density of defects ( $g$  set to one) while for the dashed lines a five times larger value of  $g$  has been used.

It can be seen that for small temperatures the conductance via  $N=2$  is predominant while at higher temperatures hopping via  $N=3$  states is the dominant mechanism. The point where the dominant mechanism changes to hopping via chains with more defect states is shifted to lower temperatures. Therefore, it can be expected that the temperature dependence is significantly increased by the ion bombardment induced increase of the density of defect states in the barrier.

This expectation can be confirmed by comparing the resistance measured at low temperature (12.5 K) and at room temperature in Fig. 3.79. One should look at the region at about zero voltage to compare the experimental results with the expect-

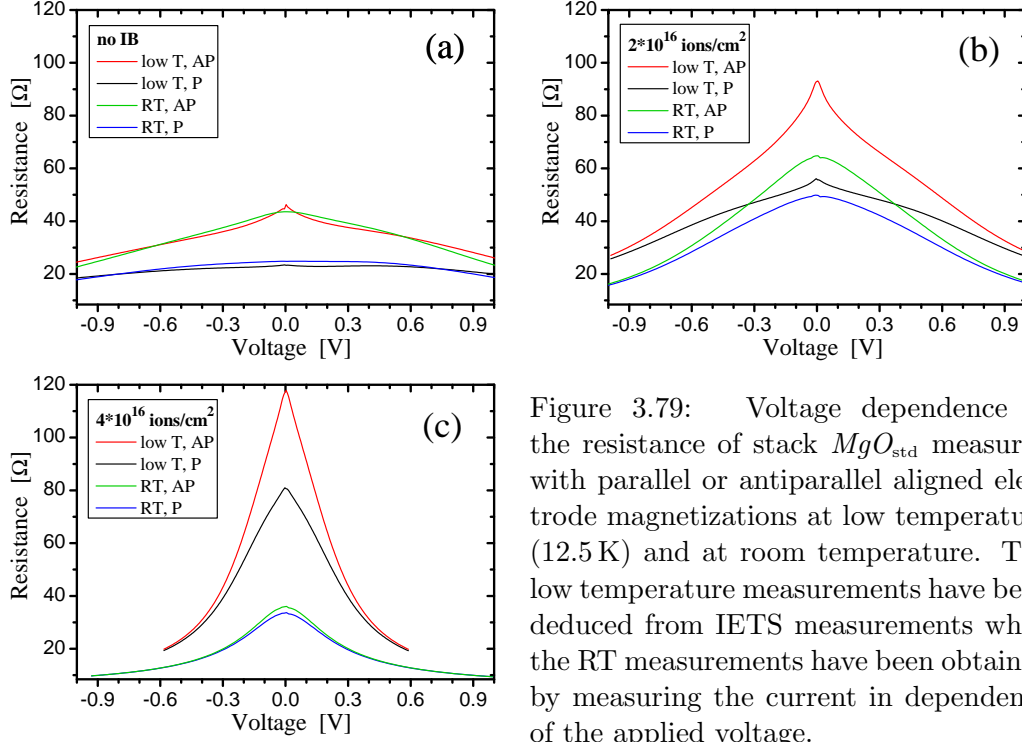


Figure 3.79: Voltage dependence of the resistance of stack  $MgO_{std}$  measured with parallel or antiparallel aligned electrode magnetizations at low temperature (12.5 K) and at room temperature. The low temperature measurements have been deduced from IETS measurements while the RT measurements have been obtained by measuring the current in dependence of the applied voltage.

taions from the theory obtained in the low bias limit. Without IB, the temperature dependence is rather small<sup>41</sup> [Fig. 3.79 (a)] while it is significantly larger after bombardment with  $2 \times 10^{16}$  ions/cm<sup>2</sup> [Fig. 3.79 (b)] and  $4 \times 10^{16}$  ions/cm<sup>2</sup> [Fig. 3.79 (c)].

Furthermore, the difference between the resistance in the AP and the P configuration depends with increasing ion dose much more on the temperature. This increase of the temperature dependence of the magnetoresistance by IB fits to a not spin polarized current with a strong temperature dependence as it is predicted by the hopping process. The much higher resistance at low temperatures and bias voltages, where hopping processes do not contribute so much to the current across the barrier, in the case of  $4 \times 10^{16}$  ions/cm<sup>2</sup> makes clear that an additional effect as, e.g., an increase of the barrier thickness or the scattering at defects in the lower conduction line around the MTJs or in the electrodes themselves is present after IB with high ion doses. Additionally, it can be expected that, e.g., spin scattering at the defects contributes to the reduced TMR amplitude.

Furthermore, the voltage dependence of the resistance measured at low temperatures shown in Fig. 3.79 can be compared with the expectations from hopping processes for the low temperature limit ( $eV \gg k_B T$ ). Xu *et al.* propose for the

<sup>41</sup>The resistance at low temperature has been obtained by integrating the  $dI/dV$  signal obtained during IETS measurements and shifting the result to obtain a zero current at zero voltage. The resistance obtained in this way at about 10 mV differs by  $0.6 \Omega$  to  $5 \Omega$  from the resistance obtained for the parallel and antiparallel configuration by measuring major loops at a similar temperature. Therefore, effects as the overlapping measurements in Fig. 3.79 (a) are only artifacts and will not be discussed.

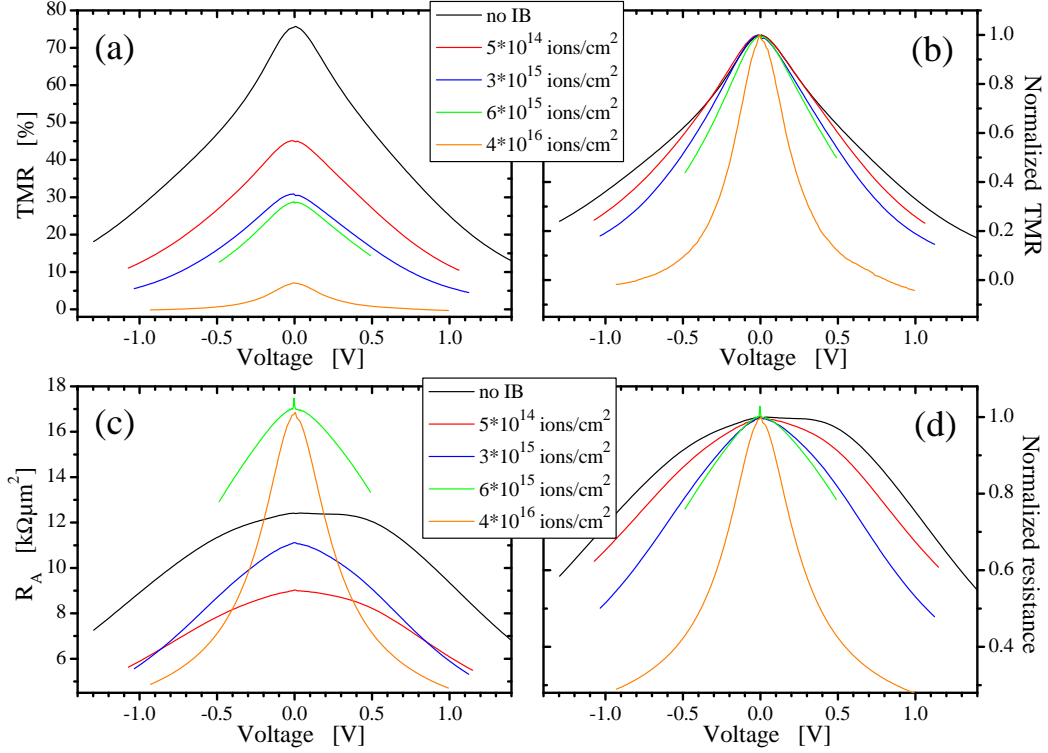


Figure 3.80: (a) TMR, (b) normalized TMR, (c) resistance, and (d) normalized resistance in dependence of the bias voltage measured at  $500 \mu\text{m}^2$  sized square MTJs with stack  $MgO_{\text{std}}$ . The resistance has been measured with parallel aligned magnetization directions. All measurements have been carried out at room temperature.

bias voltage dependence of the conductance an equation equivalent to Eq. 3.6 with  $k_B T$  interchanged by  $eV$ .

$$\frac{G_N^{\text{hop}}(V)}{G_1^{\text{res}}} = \nu_{N,V} (g\alpha^{-2} deV)^{N-1} \left( \lambda \frac{eV}{E_0} \right)^{(N-1)/(N+1)} \exp\left(\frac{N-1}{N+1} \alpha d\right) \quad (3.9)$$

$$\propto g^{N-1} (V)^{(N^2+N-2)/(N+1)}. \quad (3.10)$$

Therefore, Fig. 3.78 and the discussion concerning the strongly increased temperature dependence for an increasing ion dose due to an increasing number of longer chains contributing to the current through the barrier is also valid for the bias voltage dependence. The expected increase of the voltage dependence resulting from this discussion fits well to the observed increase of the voltage dependence with increasing ion dose at low temperature in Fig. 3.79.

Figure 3.80 shows the bias voltage dependence of the area resistance product and the TMR<sup>42</sup> for several ion doses. As these measurements have been carried out

<sup>42</sup> To obtain the bias voltage dependence of the TMR amplitude, the current has been measured in dependence of the voltage with a parallel and an antiparallel orientation of the magnetization directions on both sides of the barrier. From these measurements the TMR has been calculated with the equation  $TMR = 100 \times (R_{AP} - R_P)/R_P$  [ $R_P$  ( $R_{AP}$ ): resistance measured with parallel (antiparallel) aligned magnetizations adjacent to the barrier].

at room temperature, the condition  $eV \gg k_B T$  is only fulfilled for very large bias voltages. But nevertheless the tendency can be discussed for these measurements. It can be seen that the tendency to show a stronger bias voltage dependence with increasing ion dose can be observed also for smaller ion doses than shown in Fig. 3.79. This is good visible for the normalized resistance in Fig. 3.80 (d). Furthermore, also the normalized TMR shows a stronger bias voltage dependence with increasing ion dose.

As a peak in the IETS measurement stands for an additional current path through the barrier (compare chapter 2.6.5), a correlation between a strong decrease of the resistance and TMR and the high voltage peak in the IETS measurements can be expected. Especially in the case of the MTJ bombarded with  $4 \times 10^{16}$  ions/cm<sup>2</sup>, it can be seen that the voltage of the IETS high voltage maximum fits well to the voltage at which the TMR amplitude and the resistance decrease fast.

The IETS signal is the derivative of the conductance. Therefore, from the equations 3.9 and 3.8 the influence of the hopping on the IETS signal can be estimated. When the contribution of direct and resonant tunneling are neglected again, one obtains that the IETS signal is proportional to  $\frac{4}{3}V^{1/3} + \frac{5}{2}V^{3/2} + \dots$ \* This shows that with increasing ion dose and, therefore, increasing number of hopping sites in the longest available chains the IETS signal can be expected to increase faster and at smaller voltages. This fits to the observation of the larger high voltage IETS peak observed at lower voltages at the MTJ bombarded with  $4 \times 10^{16}$  ions/cm<sup>2</sup> compared to the one bombarded with  $2 \times 10^{16}$  ions/cm<sup>2</sup>. But with this expression it is not possible to explain the observed maximum in the IETS spectra (Fig. 3.77). Instead the equation suggests an “unlimited” increase of the conductance with increasing defect density. The reason for the existence of a maximum might be connected to the low absolute resistance of the investigated MTJs with stack  $MgO_{\text{std}}$  (Fig. 3.79). As the measured resistance can not fall below a value determined by the resistance of the experimental setup including bond wires and the contact between wire and sample (about 2-4  $\Omega$ ) and the lower conduction line and the electrodes themselves. When the resistance of the tunnel barrier is approaching this value, the decrease of the tunnel resistance does not to the same amount reduce the measured total resistance of the sample.

Ono *et al.* found a broad peak at about 600 meV in IETS spectra measured at CoFeB/MgO/CoFeB MTJs [196]. They attributed this peaks to coherent tunneling. Similar peaks have been observed by Ando *et al.* at about 1000 mV for Fe/MgO/Fe MTJs [199]. These peaks have never been observed in alumina based tunnel junctions and were attributed to coherent tunneling, too.

The high voltage peaks observed here do not result from a coherent tunneling. If this would be the case, the tunneling was more coherent after IB with increasing ion dose and the best coherent tunneling was present after the IB with  $4 \times 10^{16}$  ions/cm<sup>2</sup>. But at this ion dose the TMR amplitude is significantly decreased. Furthermore all investigations in the literature show that a well defined barrier/electrode interface and a small number of defects in the barrier is a fundamental prerequisite for a high TMR in MgO based magnetic tunnel junctions (e.g., [201, 202, 203, 204]).

---

\*Erratum: The correct equation is  $\xi_2 \frac{4}{3}V^{1/3} + \xi_3 \frac{5}{2}V^{3/2} + \dots$  with  $\xi_i$ : factor independent of V.

Figure 3.81 shows an enlarged low voltage region of Fig. 3.77. The measurement at MTJ D is omitted in this graph as no significant difference to MTJ E was observed in this voltage range.

After IB with  $2 \times 10^{16}$  ions/cm<sup>2</sup> and especially  $4 \times 10^{16}$  ions/cm<sup>2</sup>, the high voltage peak strongly influences the signal at low voltages and partly masks the phonon peak.

The zero bias anomaly increases for bombardment with  $5 \times 10^{14}$  ions/cm<sup>2</sup> (compare MTJ C and MTJ E in Fig. 3.81). After IB with  $2 \times 10^{16}$  ions/cm<sup>2</sup> the zero bias anomaly for parallel aligned magnetizations is only slightly larger than the not bombarded reference measurement (compare measurements with smaller IETS signal of MTJ B and  $2 \times 10^{16}$  ions/cm<sup>2</sup>). The zero bias anomaly in the case of antiparallel aligned magnetizations is even slightly smaller than the reference measurement.

The IETS measurements at the MTJ which has been bombarded with  $4 \times 10^{16}$  ions/cm<sup>2</sup> have a comparable small zero bias anomaly.

This does not fit to an explanation of the zero bias anomaly solely by scattering at magnetic defects as the increasing ion dose should result in a larger amount of intermixing and, therefore, in an increasing zero bias anomaly. In the measurements carried out at 12.5 K the origin of the peak at small voltages is a superposition of scattering at magnetic defects and magnon excitation (compare Fig. 3.72). At very high ion doses the barrier/electrode interface might be changed so much by intermixing that the magnon generation might at least partly be suppressed.

If the barrier/electrode interface at  $2 \times 10^{16}$  ions/cm<sup>2</sup> is changed by the IB so severely compared to  $5 \times 10^{14}$  ions/cm<sup>2</sup> that the magnetic properties are changed significantly and much less magnons are generated, one would expect a strong decrease of the TMR amplitude between this two ion doses. The observed decrease from about 40% to about 30% is rather small (Fig. 3.67). This would fit to the existence of a TMR increasing effect as described above.

In summary, the zero bias anomaly as it is observed at 12.5 K has been explained by a superposition of the influence of scattering at magnetic impurities and magnon generation. Its increase at small ion doses and subsequent decrease at larger ion doses might be connected to an increasing defect generation in the barrier and at high ion doses a severe degradation of the interface.

No clear change of the phonon peak has been observed.

Hopping over chains of defects has been suggested for the origin of the high voltage peak. This explanation fits qualitatively to the observed voltage and temperature dependence of TMR, resistance, and IETS signal, but other effects might also contribute to the observed ion dose dependences.

### 3.7.2 Postannealing of standard MgO based MTJs

In chapter 3.5 it has been shown for alumina based MTJs that the reduction of the TMR amplitude by the ion bombardment can be reduced by an additional annealing step without an external magnetic field. This treatment has also been applied for the sample with stack  $MgO_{\text{std}}$  which has been used for the IETS measurements (Fig. 3.82).



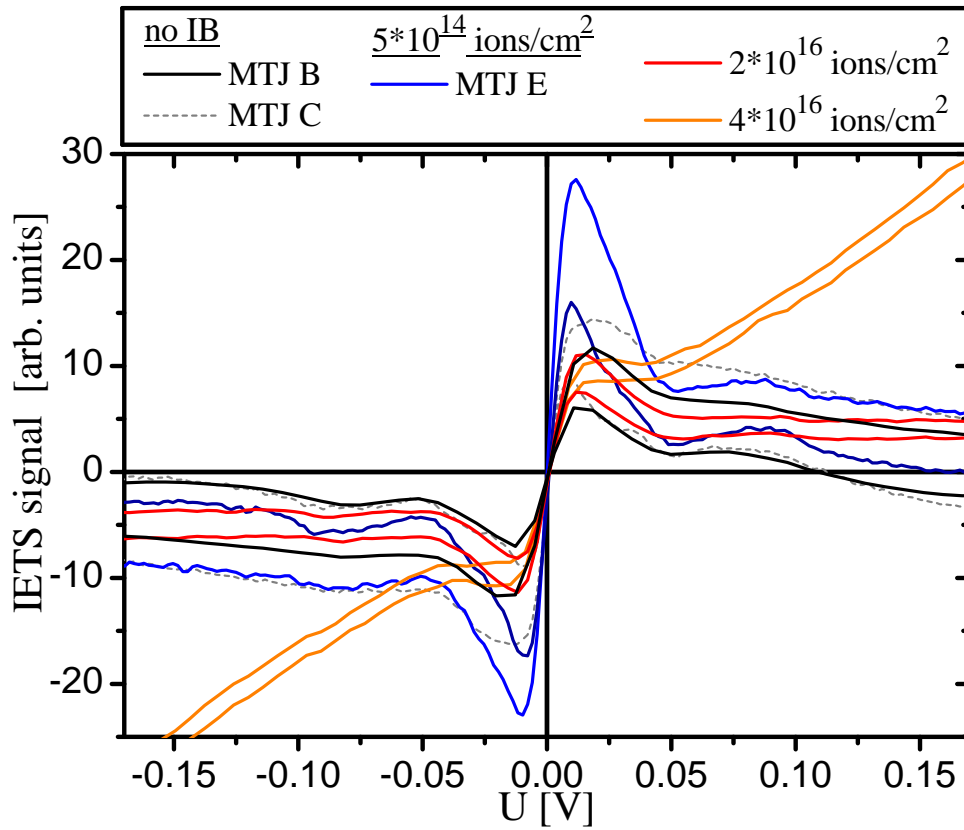


Figure 3.81: IETS measurements carried out at 12.5 K at not bombarded and bombarded MTJs with stack  $MgO_{\text{std}}$ . Reference MTJ B (field 8) is located closer to field 5 and 6 ( $2 \times 10^{16}$  ions/cm<sup>2</sup> and  $4 \times 10^{16}$  ions/cm<sup>2</sup>). Reference MTJ C (field 1) is located closer to field 2 ( $5 \times 10^{14}$  ions/cm<sup>2</sup>). (For the purpose of clarity the measurement carried out at MTJ D is omitted.) At each MTJ the IETS measurement with the higher signal has been measured with an antiparallel alignment of the magnetizations.

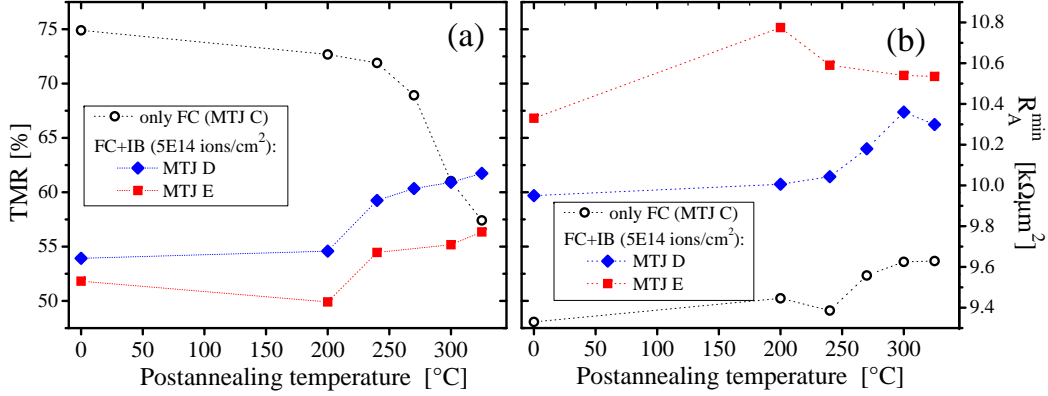


Figure 3.82: (a) TMR and (b) resistance in saturation ( $R_A^{\min}$ ) in dependence of the postannealing temperature measured at MTJs with stack  $MgO_{\text{std}}$ . All lines are a guide to the eye.

A part of the sample has been subsequently annealed to temperatures of 200°C to 325°C (compare Fig.3.82). Each heating step had a duration of 60 minutes. During the heating, the sample was mounted on an IC socket which is necessary for the low temperature measurements.

The annealing temperature dependence of the TMR amplitude and resistance in saturation can be found in Fig. 3.82. All measurements have been carried out at room temperature.

After heating to 200°C only small changes of the TMR amplitude have been observed. The TMR amplitude of the not bombarded MTJ C and of the bombarded MTJ E are slightly reduced while the bombarded MTJ D shows a slightly larger magnetoresistance effect.

After heating to 250°C and higher temperatures, the TMR amplitude of the bombarded MTJs increases due to the reduction of ion bombardment induced defects. Xinli Kou found a maximum TMR amplitude for an initial annealing in a magnetic field to 325°C with samples with stack  $MgO_{\text{std}}$  (Fig. 3.83). For higher temperatures the TMR amplitude was decreasing again.

Schmalhorst *et al.* [190] detected with x-ray absorption spectroscopy (XAS) measurements the formation of Fe-O at the lower surface of the barrier in this kind of MTJs. The Fe-O was found directly after the deposition of the samples and was reduced during the annealing to temperatures up to 275°C. Higher temperatures up to 325°C resulted in a recrystallization of the CoFeB electrode<sup>43</sup> which enhances the coherent tunneling [190]. Therefore, one might assume that apart from removing defects in the barrier, a recrystallization of the CoFeB layers can happen during the postannealing with sufficiently high temperatures if these have been damaged by the IB. Furthermore, if the intermixing due to IB induces the formation of Fe-O, this might be reduced during the postannealing. These two effects can increase the TMR amplitude in the bombarded MTJs.

<sup>43</sup>This observation fits to results obtained by Matsumoto *et al.* [193] at  $Co_{60}Fe_{20}B_{20}$  3 nm /  $MgO$  1.8 nm /  $Co_{60}Fe_{20}B_{20}$  3 nm samples. No crystalline peak in x-ray diffraction measurements was found for these samples after annealing to 270°C. A partial crystallization was found at samples annealed to 300°C and 360°C.

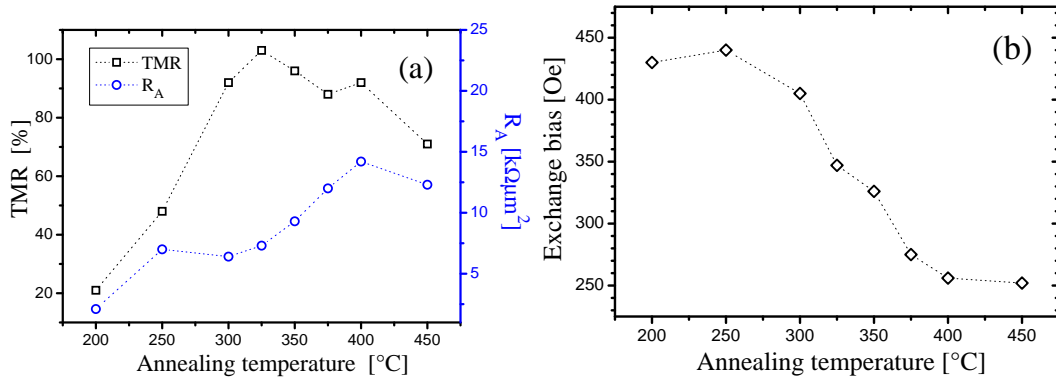


Figure 3.83: (a) TMR and area resistance product and (b) exchange bias field in dependence of the annealing temperature measured at MTJs with stack  $MgO_{std}$ . The measurements have been provided by Xinli Kou [189, 190]. All lines are a guide to the eye.

A possible formation of B-O might decrease the TMR amplitude in all MTJs. This effect might contribute to the decrease of the TMR amplitude of the not bombarded reference MTJ when the sample is heated to 250°C or higher and reduce the TMR increase at the bombarded MTJs.

A similar TMR amplitude versus annealing temperature dependence with a peak at 275°C was also observed for MTJs with alumina barrier [188]. The decreasing TMR amplitude for high temperatures in these samples has been explained in Ref. [188] by diffusion of Mn from the IrMn and  $Cu^{44}$  from the seed layer to the barrier. Furthermore, the highest TMR amplitude obtained so far with CoFeB/MgO based MTJs of 500% at room temperature has been obtained with Mn free MTJs and a high annealing temperature [25]. As both materials are as well used in stack  $MgO_{std}$ , similar processes can be assumed to happen here, too, although the details might be different because the investigations in [188] have been carried out with polycrystalline CoFe electrodes while the CoFeB layers used in stack  $MgO_{std}$  can be expected to be amorphous after deposition and have been observed to get crystalline starting at the MgO/CoFeB boundary [25].

The decreasing exchange bias observed when annealing the samples with stack  $MgO_{std}$  to temperatures above 250°C [Fig. 3.83 (b)] fits well to the diffusion of a part of the antiferromagnetic layer into the pinned ferromagnetic layer.

A diffusion of Ru from a seed layer and Mn from the AF layer has also been observed for CoFeB/MgO/CoFeB based MTJs [205]. For high temperatures, the increasing TMR amplitude due to the improvement of the crystal structure in the CoFeB/MgO/CoFeB region (compare [25, 205, 190]) is more than compensated by this kind of diffusion processes.

Therefore, it can be assumed that the additional heating for one hour at each temperature during the postannealing experiments with stack  $MgO_{std}$  has continued diffusion processes which have been started during the initial annealing of this sample.

Furthermore, extrinsic effects as the formation of tiny shorts at the sides of the

<sup>44</sup>A Cu diffusion was found in [187, 188] after annealing to temperatures of 350°C and higher.

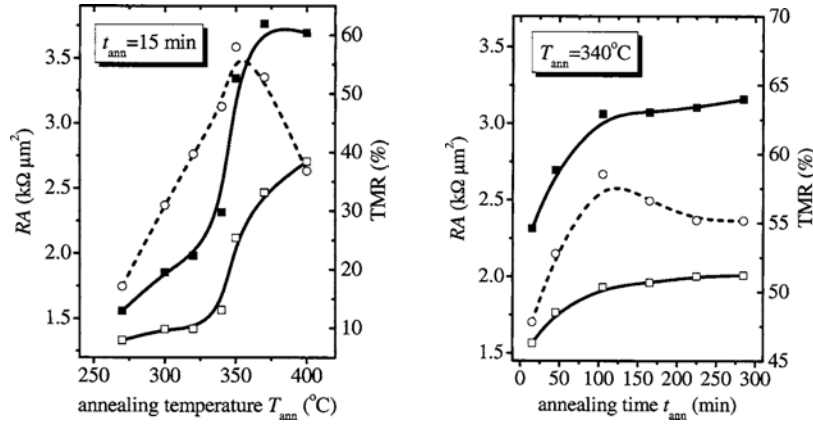


Figure 3.84: (*left*) Area resistance product for parallel (empty squares) and antiparallel (solid squares) aligned magnetizations and TMR amplitude (circles) in dependence of the annealing temperature after 15 min annealing of a CoFe/MgO/CoFe based sample (*right*) corresponding measurements for heating to  $340^{\circ}\text{C}$  for various annealing times. (from [206])

MTJs might contribute to the decreasing TMR amplitude of the reference MTJ and reduce the TMR increase of the bombarded MTJs.

The increasing resistance of the bombarded MTJs during the postannealing tests [Fig. 3.82 (b)] might be due to a decreasing number of IB induced electron paths across the barrier.

The increasing tendency of the resistance of the bombarded MTJs coincides with the increasing tendency of the resistance with increasing temperature during the test of the initial annealing (Fig. 3.83). Therefore, the postannealing might induce the same kind of ordering processes as the initial annealing.

This expectation is supported by annealing tests published by Dimopoulos *et al.* [206]. For the investigated CoFe/MgO/CoFe based system a maximum TMR amplitude has been reported for annealing to  $340^{\circ}\text{C}$  (Fig. 3.84, [206]). The resistance of the sample increased for increasing annealing temperature as it has been observed for stack  $\text{MgO}_{\text{std}}$  (compare Fig. 3.83 (a) and left part of Fig. 3.84). Longer annealing times at a temperature of  $340^{\circ}\text{C}$  led to a further increase of the resistance (right part of Fig. 3.84, [206]) as it has been observed during the postannealing of the bombarded MTJs with stack  $\text{MgO}_{\text{std}}$  [Fig. 3.82 (a)]. The decreasing TMR for long annealing times in Fig. 3.84 fits to the decreasing TMR of the not bombarded MTJ C in Fig. 3.82. It might be connected to diffusion processes.

As it is very likely that the bombarded MTJs are subject to the same diffusion processes as the not bombarded MTJ, it can be assumed that the maximum obtainable TMR amplitude of magnetically patterned MTJs after postannealing is significantly higher when these diffusion processes can be suppressed. Therefore, the possibility to use a high annealing temperature without inducing diffusion processes is not only of great interest for obtaining a high TMR amplitude directly after deposition [25] but it would also increase the possibility to repair the unwanted side effects of bombarding full MTJs with ions.

The influence of the postannealing on the IETS signal of a not bombarded reference measurement is shown in Fig. 3.85. No significant changes are observed up to 240°C. This fits to the fact that the largest part of the TMR amplitude reduction happened after heating the sample to 270°C and 300°C (Fig. 3.82).

The IETS measurements carried out with an antiparallel alignment (larger signal compared to parallel alignment) after heating to 270°C and 300°C show a reduced signal for all bias voltages up to 500 mV. The measurements done after this heating steps with a parallel alignment of the magnetizations adjacent to the barrier show a reduced signal only at small voltages (zero bias anomaly). Therefore, it is not likely that the reduced IETS signal in the antiparallel case is due to changes of, e.g., the experimental setup or the contact between the MTJ and the wire. A reduction of a special conduction channel should reduce the signal only at certain defined voltages. Therefore, it is likely that the origin of the reduced IETS signal for high temperatures is a decreasing antiparallel alignment resulting from the heating of the MTJs to temperatures significantly above the blocking temperature (e.g., blocking temperature of the system CoFe/IrMn: about 230°C).

All measurements with *antiparallel* alignment have been carried out at -118 Oe while a *parallel* alignment has been obtained in all cases by applying a magnetic field of +118 Oe. A comparison of the major and minor loops measured at MTJ C before postannealing and after the annealing to 240°C, 270°C, and 325°C (Fig. 3.86) shows that after the annealing to 240°C at -118 Oe still the best antiparallel alignment (highest resistance/TMR) can be found with an increasing resistance/TMR for decreasing magnetic field.<sup>45</sup> In contrast to this, after annealing to 270°C the shape of the minor loop has slightly changed (flat resistance/TMR versus magnetic field plateau) and after heating to 325°C the resistance at -118 Oe is already decreasing again with a decreasing magnetic field. This confirms the assumption that the less good antiparallel alignment is the reason for the decreased IETS signal at high temperatures for the “antiparallel” case.

The exact height of the zero bias anomaly in the parallel case is to some extent subject to noise resulting in an alternating increasing and decreasing height of the peak with increasing temperature.

When a decreasing tendency of the zero bias anomaly with increasing temperature is assumed for the parallel and maybe as well (masked by the magnetically induced reduction of the signal) for the antiparallel case, this might be explained by a small thermally induced reduction of number of magnetic defects. But this does not explain the monotonically decreasing TMR with increasing temperature.

The lack of evidence for additional current paths across the barrier in the IETS spectra suggests that the reason for the decreasing TMR amplitude with increasing postannealing temperature of the not bombarded MTJ C might be a reduction of the spin polarization at the interface due to the formation of, e.g., Mn oxide or B oxide at the barrier/electrode interface.

The postannealing of the bombarded MTJ D ( $5 \times 10^{14}$  ions/cm<sup>2</sup>) results in larger

---

<sup>45</sup> *Decreasing magnetic field* stands for an increasing negative field.

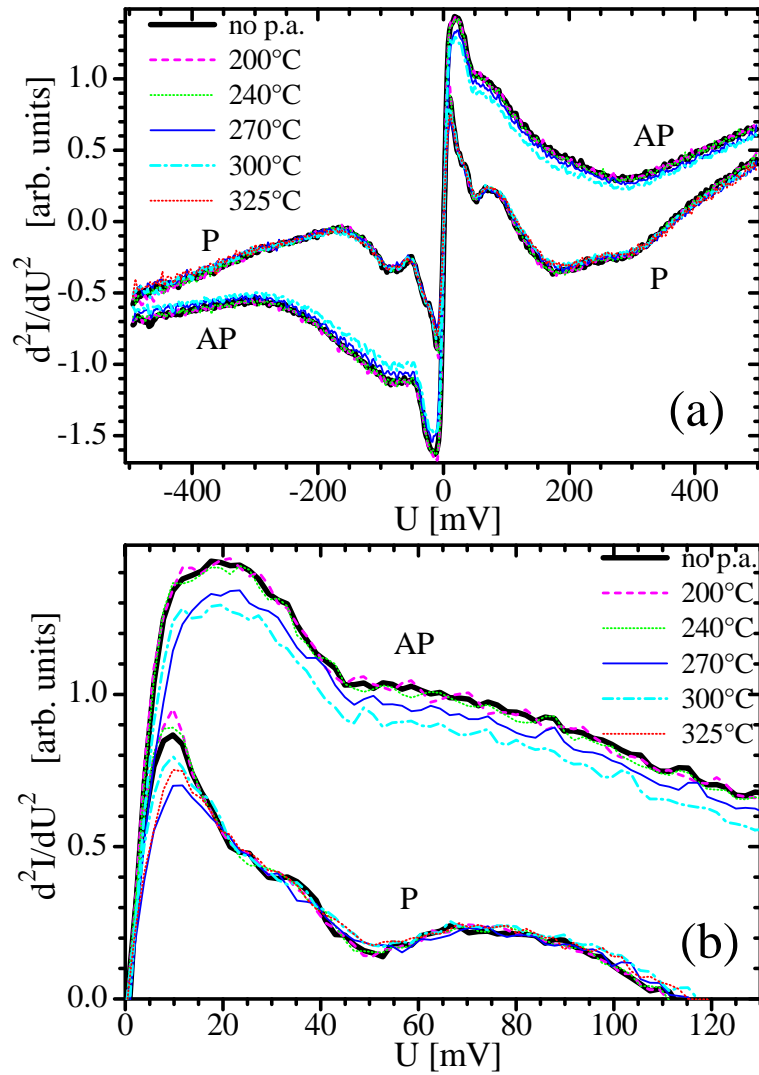


Figure 3.85: IETS measurements carried out at 12.5 K at reference MTJ C without postannealing (p.a.) and with subsequent postannealing steps with increasing temperatures (one hour each). (b) shows an enlarged region of (a). (No measurement with antiparallel alignment is available in case of 325°C.)

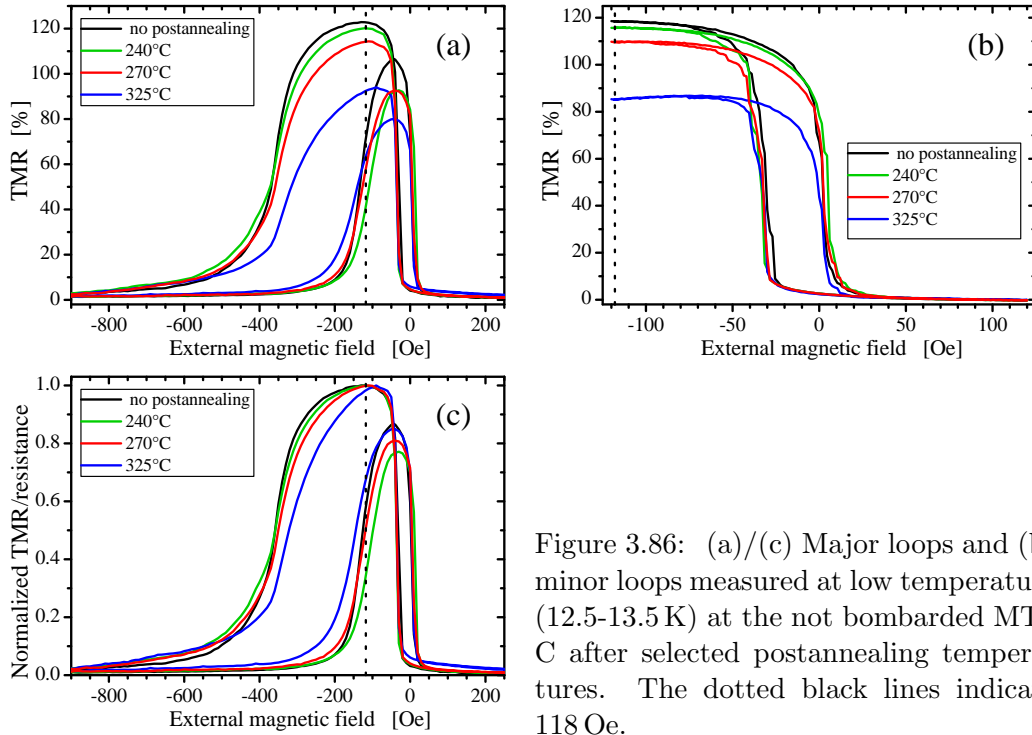


Figure 3.86: (a)/(c) Major loops and (b) minor loops measured at low temperature (12.5-13.5 K) at the not bombarded MTJ C after selected postannealing temperatures. The dotted black lines indicate 118 Oe.

changes of the IETS measurements (Fig. 3.87).

The zero bias anomaly, which was significantly enlarged by the ion bombardment is decreasing with increasing temperature for temperatures higher than 200°C. After heating to 325°C the zero bias anomaly is very similar to the measurements done at the not bombarded MTJ C. This fits good to the fact that the TMR amplitude of both MTJs after heating to 300°C is nearly the same.

The IETS signal at larger bias voltages close to 500 mV is also decreasing significantly with increasing temperature. This is a hint that the high voltage peak is reduced and/or shifted to higher bias voltages. According to the suggestions about the origin of the high voltage peak given above, a decreased/shifted high voltage peak would indicate that defects which enabled additional hopping processes are removed during the heating. This fits good to the increasing TMR amplitude with increasing temperature.

### 3.7.3 Summary for ion bombardment of magnetic tunnel junctions with pinned ferromagnetic layer below MgO barrier

The used MTJ with stack  $MgO_{std}$  shows a TMR amplitude of about 72% at room temperature and about 121% at 12.5 K. These values raise the question whether a significant coherent tunneling occurs in this sample which would allow to explain the strong decrease of the TMR amplitude after bombardment with only  $5 \times 10^{14}$  ions/cm<sup>2</sup> by the loss of the coherent tunneling.

The enlarged zero bias anomaly observed in the IETS measurement after bombard-

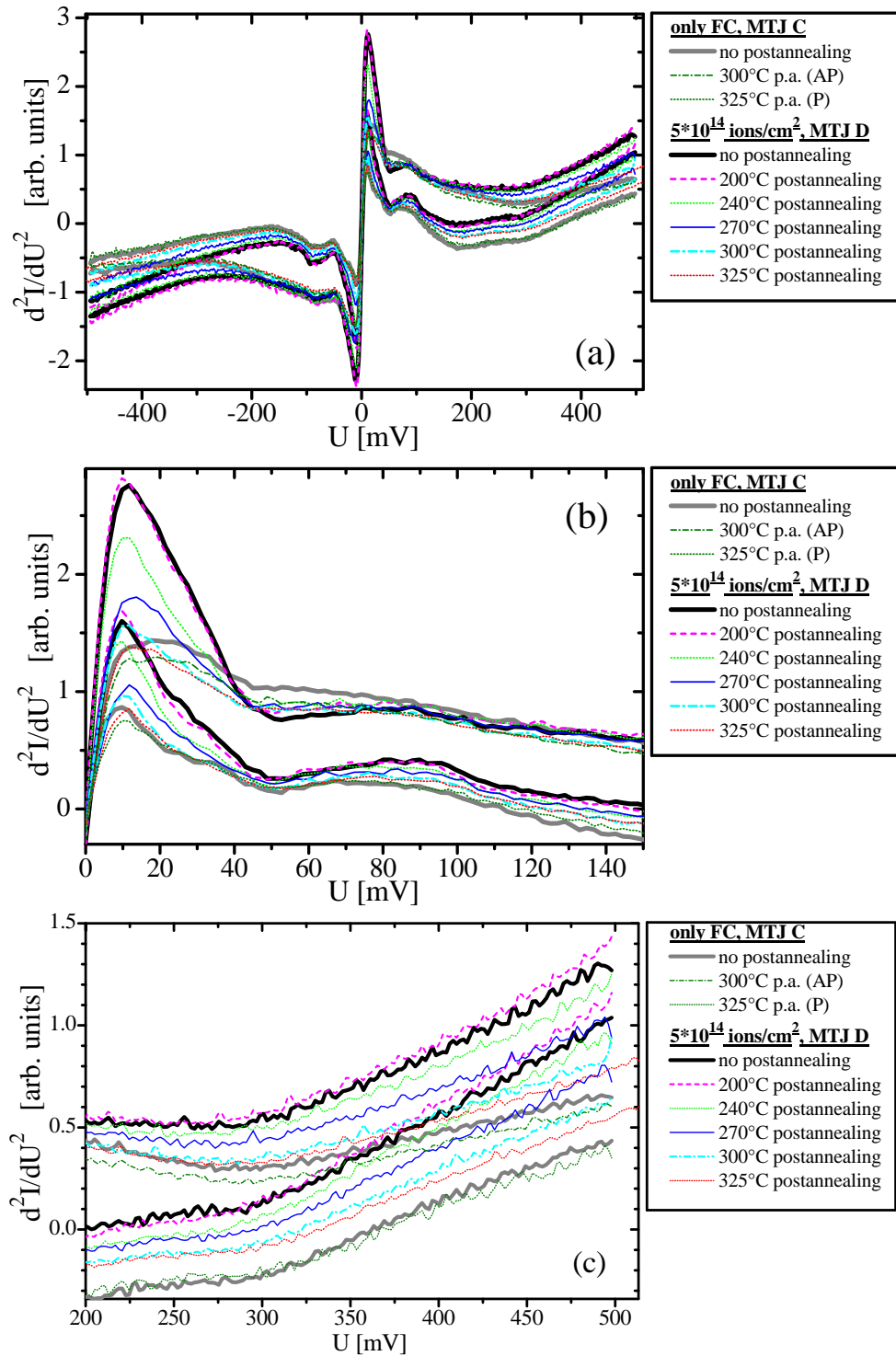


Figure 3.87: IETS measurements carried out at 12.5 K at the bombarded MTJ D ( $5 \times 10^{14}$  ions/cm<sup>2</sup>) without postannealing (p.a.) and after subsequent postannealing steps with increasing temperatures (one hour each). The reference MTJ C has been annealed in the same way as MTJ D but only selected temperatures are shown (compare Fig. 3.85). (b) and (c) show enlarged regions of (a).



ment with  $5 \times 10^{14}$  ions/cm<sup>2</sup> points to a larger amount of scattering at magnetic impurities and the increasing IETS signal at 0.5 V points to an increased amount of hopping at high bias voltages. This suggests that the loss of the coherent tunneling is at least not the only reason for the decreased TMR amplitude.

But when, e.g., more defects allowing hopping processes and spin flip scattering are present after bombardment with  $5 \times 10^{14}$  ions/cm<sup>2</sup> it can be expected that even more of them occur after bombardment with  $3 \times 10^{15}$  ions/cm<sup>2</sup> or  $2 \times 10^{16}$  ions/cm<sup>2</sup> and that this would reduce the TMR amplitude as well as the resistance with increasing ion dose. Furthermore, the decreasing Néel coupling in the range of  $3 \times 10^{15}$  ions/cm<sup>2</sup> to  $2 \times 10^{16}$  ions/cm<sup>2</sup> also indicates that a significant change of the barrier/electrode occurs which reduces the correlated roughness or the magnetic moment at the interface or that the structure of the barrier is changed strong enough to increase the effective barrier thickness. These large changes in the sensible barrier region should change the TMR amplitude.

In contrast to the expectation described above, the TMR amplitude does not change significantly between  $3 \times 10^{15}$  ions/cm<sup>2</sup> and  $2 \times 10^{16}$  ions/cm<sup>2</sup> and the resistance even increases. If the effective barrier thickness is increased this would also increase the resistance.

To explain this ion dose dependence of the TMR, an IB induced effect is necessary which increases the TMR and the resistance and therefore compensates for the decreasing TMR amplitude and resistance due to additional not spin polarized current channels. This effect might be the destruction of minor Bloch states which have a large decay length.

After bombardment with  $4 \times 10^{16}$  ions/cm<sup>2</sup>, the height of the "high voltage peak" in the IETS measurement is increased and it is shifted to lower voltages. This points to an increase of the number of defects in the barrier which allows an additional current via hopping processes. Furthermore, TMR, resistance, and Néel coupling are decreasing indicating a severely damaged MTJ.

The TMR amplitude of MTJs bombarded with  $5 \times 10^{14}$  ions/cm<sup>2</sup> has been increased by an additional subsequent postannealing steps to temperatures up to 325°C by up to 14.5% of the value after IB but the original value has not been reached. After heating the sample to the highest tested temperature the decreasing TMR amplitude of the not bombarded reference MTJ was as large as the increasing TMR amplitude of the bombarded MTJs. This suggests that the postannealing of the squared  $500 \mu\text{m}^2$  large MTJs with stack  $MgO_{\text{std}}$  is limited by diffusion effects and a reduced antiparallel magnetic alignment after heating the MTJs to temperatures of about 100°C above the blocking temperature.

The magnetic tunnel junction with MgO barrier is significantly more sensible to the side effects of ion bombardment induced magnetic patterning than magnetic tunnel junctions with alumina barrier. Therefore, an adjustment of the stack to the special needs of this kind of patterning has been investigated. Some experiments dealing with this will be shown in the next section.

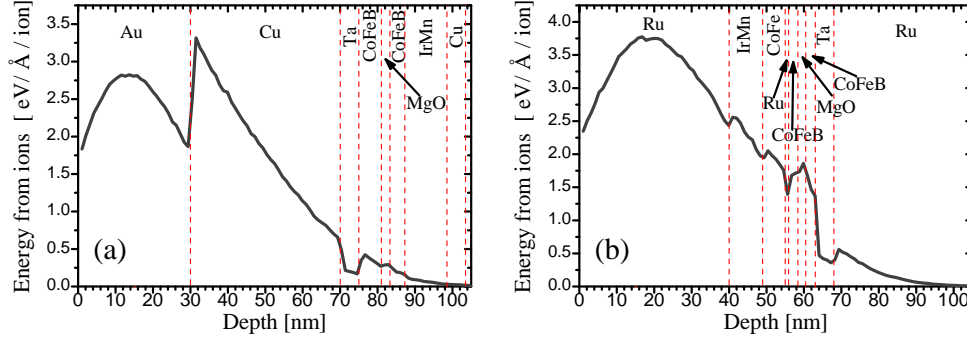


Figure 3.88: Energy transferred from 10 keV He ions to samples with (a) stack  $MgO_{std}$  and (b)  $MTJ_{IB}^{MgO^{inv}}$  in dependence of the depth.

### 3.8 Application of ion bombardment induced magnetic patterning in MTJs with pinned electrode located on top of the MgO barrier

#### 3.8.1 General considerations about an optimized layer stack for the application of ion bombardment induced magnetic patterning

As it has been shown in chapter 3.4 for magnetic tunnel junctions with alumina barrier, an optimization of the layer stack for ion bombardment induced magnetic patterning of the pinned magnetic electrode can reduce the side effects of ion bombardment significantly.

The most important adjustment is to place the FM/AF bilayer which has to be manipulated by IB above the sensible tunneling barrier. This design of the layer stack makes it possible that not every ion which is used to manipulate the EB has to cross the barrier first. The advantage of this modification for the depth distribution of the energy deposition is demonstrated by SRIM simulations.

Fig. 3.88 shows the energy transferred from the ions to the sample calculated with SRIM for sample  $MgO_{std}$  (pinned FM layer below barrier) and the inverted stack  $MTJ_{IB}^{MgO^{inv}}$  with the AF/FM bilayer located on top of the barrier. In both cases a bombardment with 10 keV He ions has been simulated. In the inverted stack about 1.3 times more energy per ion and Å is deposited in the IrMn layer compared to the MgO barrier. In contrast to this, for the "standard" stack  $MgO_{std}$  four times more energy has been deposited in the MgO barrier than in the IrMn layer. This shows the advantage one can expect when an inverted stack is used.

With a good choice of the seed layer, the shift of the antiferromagnetic IrMn layer from the lower part of the MTJ to the top does not have a negative effect on the growth of the FM/barrier/FM layers. That very good crystalline structures can be archived without IrMn underneath the barrier can be seen, e.g., in the work of Hayakawa *et al.* [205] where 472% TMR have been measured at room temperature with a Ta/Ru/Ta seed layer without an antiferromagnetic layer underneath the barrier. Therefore, this type of seed layer has been utilized for the inverted MgO based MTJ in this work.

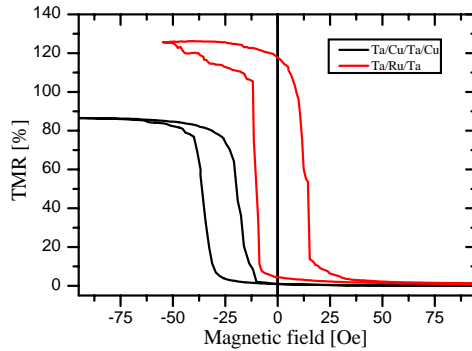


Figure 3.89: Minor loops measured at  $500 \mu\text{m}^2$  sized MTJs on sample  $MgO_{\text{std}}$  with Ta/Cu/Ta/Cu seed layer and on sample  $MgO_{\text{Ru seed}}^{\text{thin FM pinned}}$  with Ta/Ru/Ta seed layer.

A further advantage of this seed layer compared to the Cu based conduction line is a small correlated roughness which results in a smaller Néel coupling. An example of minor loops measured for a MTJ with a Ta/Cu/Ta/Cu seed layer and a pinning of the lower magnetic layer (stack  $MgO_{\text{std}}$ ) and for a MTJ with a Ta/Ru/Ta seed layer and a pinned upper magnetic layer (stack<sup>46</sup>  $MgO_{\text{Ru seed}}^{\text{thin FM pinned}}$ ) can be seen in Fig. 3.89. The used MTJs with a size of  $500 \mu\text{m}^2$  are too large for a significant shift of the hysteresis loop due to strayfield coupling.<sup>47</sup> The barrier of the two samples has a similar thickness. The free FM layer of stack  $MgO_{\text{std}}$  is significantly thicker than the one used in stack  $MgO_{\text{Ru seed}}^{\text{thin FM pinned}}$  resulting in a larger Zeeman energy. Therefore, for an identical correlated roughness and an identical strength of the Néel coupling a larger shift of the hysteresis loop would be expected for stack  $MgO_{\text{Ru seed}}^{\text{thin FM pinned}}$ . The fact that nearly no shift has been observed for this stack while the minor loop of the MTJ with stack  $MgO_{\text{std}}$  is shifted about 27 Oe is a hint, that the roughness at the barrier in samples prepared with the used sputter deposition tool<sup>48</sup> is strongly reduced with the Ta/Ru/Ta seed layer compared to the Ta/Cu/Ta/Cu seed layer. This observation fits to transmission electron microscopy experiments at a Ta/Cu/CoFe/ Ru/ CoFe/ Al-O/ NiFe/ Ta stack published in Ref. [187]. In these experiments the roughness of the full stack results mainly from the roughness of the Cu conduction line.

A common tool to manipulate the strayfield coupling which gets more important with a decreasing size of MTJs is the use of artificial ferrimagnets. An additional advantage of a low effective magnetic moment of an Afi with a similar thickness of the two antiferromagnetically coupled FM layers is a larger shift of the switching field of the pinned FM layer due to EB for a specific strength of the EB coupling. It has been shown in chapter 3.3 that the AF interlayer coupling in AFis with a Ru interlayer can survive the ion doses necessary to turn the direction of the EB coupling. Cu based AFis are much more sensible to IB induced defects. Therefore, a Ru based Afi is used in the inverted MgO based MTJ. A test of the strength of the interlayer exchange coupling in MTJs with stack

<sup>46</sup>layer stack  $MgO_{\text{Ru seed}}^{\text{thin FM pinned}}$ : Ta 5 nm / Ru 40 nm / Ta 5 nm / CoFeB 2.5 nm / MgO 2.1 nm / CoFeB 4 nm / Ru 0.9 nm / CoFe 2 nm / IrMn 9 nm / Ru 40 nm, annealed for 60 min at 325°C

<sup>47</sup>With stack  $MgO_{\text{Ru seed}}^{\text{thin FM pinned}}$ , e.g., no shift of the free magnetic layer hysteresis loop has been found for  $500 \mu\text{m}^2$  as well as  $56 \mu\text{m}^2$  sized MTJs.

<sup>48</sup>The following sputter parameters have been used: 115 W, 20 sccm Ar-flow, shutter at turbo molecular pump 21%, all materials on 4" sputter sources.

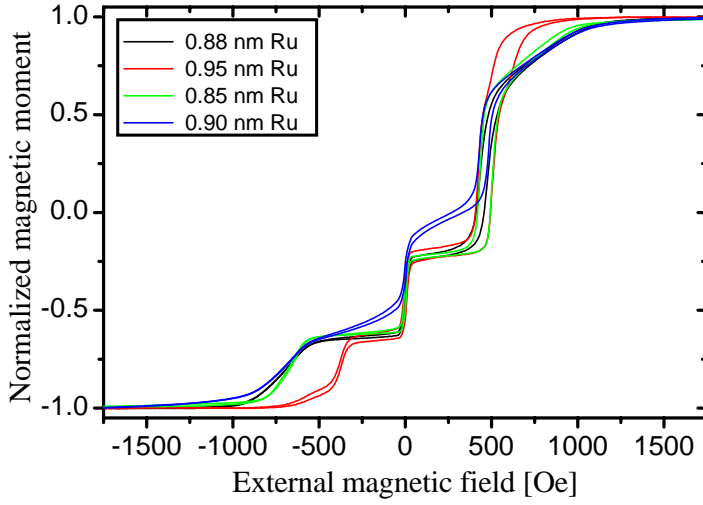


Figure 3.90: AGM measurements of stack  $MTJ_{Ru\text{ var.}}^{MgO\text{ inv}}$  with varying Ru-interlayer thickness. The sample with 0.9 nm Ru has been annealed at  $325^\circ\text{C}$  while all other samples have been annealed at  $350^\circ\text{C}$ .

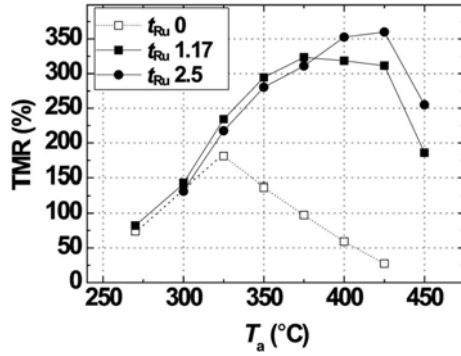


Figure 3.91: TMR amplitude in dependence of the annealing temperature  $T_a$  for CoFeB/MgO/CoFeB MTJs with an AFi with a Ru layer thickness  $t_{Ru}$  of 0, 1.17 nm, and 2.5 nm. (from [207])

$MTJ_{Ru\text{ var.}}^{MgO\text{ inv}}$ <sup>49</sup> in dependence of the Ru interlayer thickness is shown in Fig. 3.90. The largest interlayer exchange coupling has been found for an interlayer thickness of 0.88 nm to 0.9 nm. Therefore, this Ru layer thickness will be used for the AFi in all MgO based MTJs with an inverted stack.

Because of good results obtained in the past with the pinning of CoFe by an IrMn layer on top of the FM layer, CoFe is chosen for the FM layer adjacent to the IrMn in the AFi.

An additional advantage of artificial ferrimagnets in MTJs is that the Ru interlayer enables higher annealing temperatures resulting in higher TMR amplitudes ([207]). This can be due to a blocking of Mn diffusion from the IrMn layer towards the barrier [207]. Lee *et al.* found a maximum TMR of 361% after annealing a stack containing an AFi with a 2.5 nm Ru interlayer to  $425^\circ\text{C}$  while for a similar stack without the Ru interlayer a TMR decrease has been observed for temperatures higher than  $325^\circ\text{C}$  restricting the TMR to 181%. Therefore, the temperature dependence of the TMR amplitude has been tested for an inverted stack including the suggested improvements.

The samples used for the investigation of the temperature dependence of the TMR differ only in the thickness of the Ru interlayer in the AFi of 0.88 nm and 0.9 nm.

<sup>49</sup>  $MTJ_{Ru\text{ var.}}^{MgO\text{ inv}}$  stands for samples with the following stack: Ta 5 nm / Ru 40 nm / Ta 5 nm / CoFeB 2.5 nm / MgO 2.1 nm / CoFeB 2.5 nm / Ru variable / CoFe 6 nm / IrMn 9 nm / Ru 40 nm.

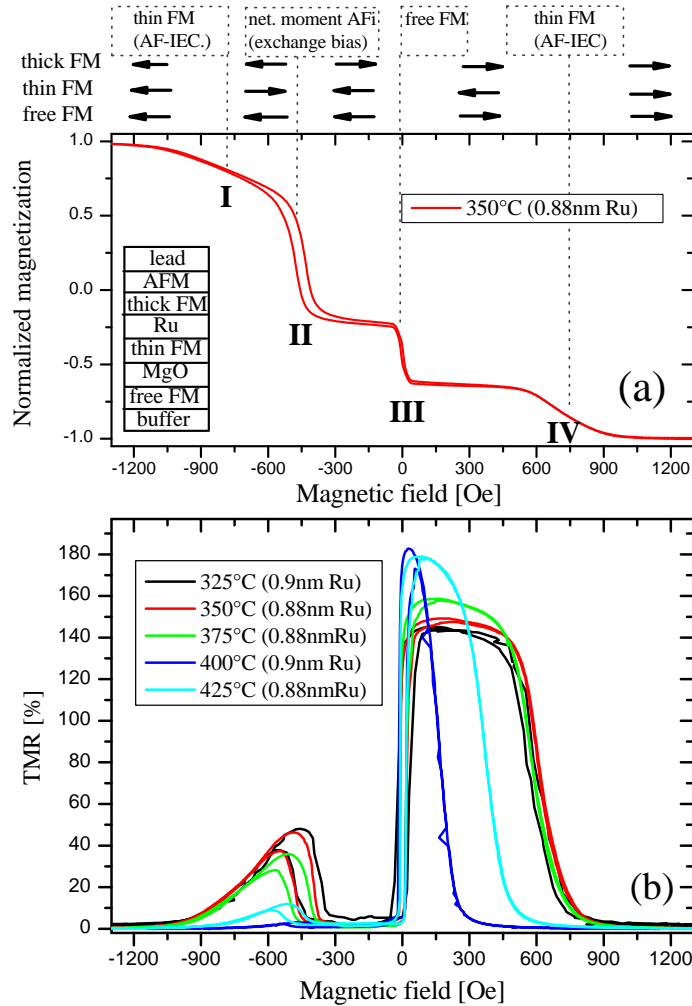


Figure 3.92: (a) AGM measurement of stack  $MTJ_{Ru \text{ var.}}^{MgO \text{ inv}}$  with about 0.88 nm Ru-interlayer thickness. The sample has been annealed at 350°C. The inset shows a sketch of the used layer stack. The direction of the magnetization of the three FM layers in dependence of the external magnetic field is indicated by the arrows at the top. Every rotation of a FM layer is indicated by a dotted line. In the boxes on top of each line, first the layer which is turning is listed. In the second line of each box the interaction which is mainly responsible for the position of this magnetization rotation is stated. Part (b) shows the corresponding TMR major loops measured after heating parts of this and other similar samples for about one hour to several temperatures.

This does not significantly change the magnetic properties and as the AFi is located above the barrier the growth conditions of the CoFeB/MgO/CoFeB layers are not altered. Therefore, the TMR values obtained with this samples can be compared without difficulty.

The direction of the magnetization of the two FM layers in the AFi and the free FM layer in dependence of the external magnetic field is indicated by the arrows at the top of the AGM measurement in Fig. 3.92 (a). In the boxes on top of the dotted lines the FM layer or AFi which is changing its magnetization direction at about this external magnetic field is listed in the first line. The interaction which is mainly responsible for the external magnetic field at which this magnetization rotation can be observed is stated in the second line.

The conductivity measurements corresponding to the AGM measurements described above can be seen in Fig. 3.92 (b).

In the following lines the magnetization reversal process is described starting at a large negative external magnetic field.

In the magnetic field range marked as **I** in Fig. 3.92 (a), the not pinned thin FM layer of the AFi starts to align antiparallel to the pinned layer because of the antiferromagnetic interlayer exchange coupling (IEC). As in stack  $MTJ_{\text{Ru var.}}^{\text{MgO inv}}$  the thicker FM layer in the AFi is pinned (see inset of Fig. 3.92 (a) for a sketch of the stack), the switching of the thin FM layer is not directly influenced by the EB interaction. Because the thin FM layer in the AFi is located adjacent to the barrier, its switching results in an increasingly antiparallel orientation of the magnetization direction of the two FM layers adjacent to the barrier and, therefore, the resistance increases.

In the region **II**, the pinned layer switches due to the exchange bias interaction. Now, for the not pinned layer of the AFi, it is with regard to the IEC as well as the Zeeman energy energetically more favorable to be aligned parallel to the external magnetic field again and, therefore, it changes its magnetization direction as well. This switching of both FM layers at the same time will be denoted as switching of the net magnetic moment of the AFi in the following considerations. It results in a parallel alignment of both FM layers adjacent to the barrier and, therefore, one can measure a low resistance between **II** and **III**.

Because in the range between **I** and **II** the switching of the AFi net magnetization (**II**) and the parallelization of the magnetization of the two FM layers (**I**) merges, no good antiparallel alignment of the two magnetizations occurs and only a small region with an elevated resistance can be observed.

At **III** the free layer switches and an antiparallel alignment of the magnetizations adjacent to the barrier (high resistance) is obtained until at **IV** the magnetization of the not pinned FM layer in the AFi is turned parallel to the external magnetic field and the resistance decreases again.

The switching behavior described above shows that a variation of the strength of the interlayer exchange coupling can be detected by observing the variation of the switching field **I** or **IV** while a changed strength of the exchange bias coupling shifts the switching field **II**.

The antiferromagnetic interlayer coupling is constant for temperatures up to 375°C but is significantly decreased for higher temperatures. This results in a narrower resistance maximum **III-IV** and may limit the TMR in the case of 400°C. Furthermore, a decrease of the resistance in region **I-II** can be observed. This observation coincide with the results of Lee *et al.* in Ref. [207]. They found for an interlayer thickness of 1.17 nm a strong decrease of the antiferromagnetic interlayer coupling at an annealing temperature of 375°C relative to 270°C. With an annealing temperature of 425°C they even observed a ferromagnetic coupling. In contrast to this, they found for samples with a 2.5 nm thick Ru interlayer an antiferromagnetic coupling at 425°C. Furthermore, the maximum TMR with the thin Ru interlayer was reported to be at 375°C while with a 2.5 nm thick interlayer an increasing TMR has been observed up to 425°C. Therefore, an AFi with a thicker interlayer might be more robust concerning annealing and ion bombardment. This is an interesting question for further investigations.

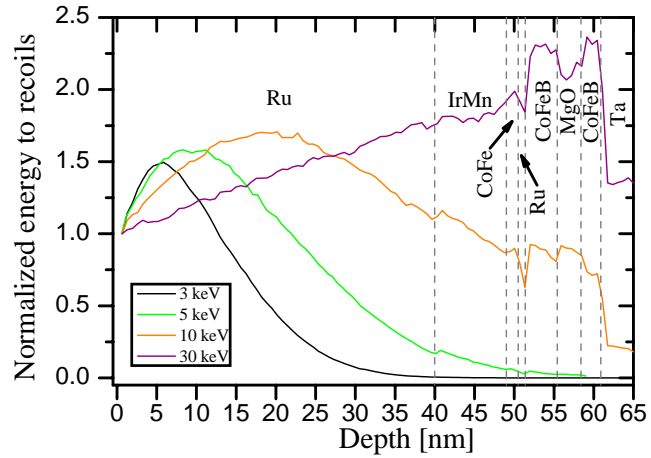
Although the interlayer coupling is decreasing for high temperatures, the TMR amplitude increases with increasing temperature up to 400°C. This can be attributed to a better crystalline ordering of the CoFeB/MgO/CoFeB layers. After heating to this temperature, a TMR amplitude of 180% has been obtained. As this is the highest TMR amplitude achieved so far with the present laboratory equipment, the considerations described on the last pages turned out to be successful. The maximum TMR amplitude obtained with stack  $MTJ_{\text{Ru var.}}^{\text{MgO inv}}$  is more than two times larger than the TMR amplitude of the MTJ with standard stack ( $MgO_{\text{std}}$ ) and suggests that a coherent tunneling is present in this samples.

A comparison with the annealing temperature dependence found for stack  $MgO_{\text{std}}$  shows an increase of the temperature which results in the maximum TMR amplitude from 325°C (Fig. 3.83, [189]) to 400°C (Fig. 3.92 (b)). This might be due to the described effect of the Ru-layer.

Because it is difficult to predict how an AFi with an interlayer exchange coupling which is already damaged by high annealing temperatures behaves during IBMP, an annealing temperature of 375°C will be used in the experiments with an inverted MgO based stack although not the optimum TMR amplitude is obtained with this temperature.

To obtain a good result with the proposed stack, the ion bombardment parameters should be adjusted to the stack. Some investigations regarding this aspect will be shown in the following section.

Figure 3.93: Energy transferred per ion and  $\text{\AA}$  depth from ions to target atoms normalized to the value at the surface for a stack similar to stack  $MTJ_{IB}^{MgOinv}$  and several initial ion energies.



### 3.8.2 Optimization of ion bombardment parameters for inverted stacks

For the application of ion bombardment induced magnetic patterning in magnetic tunnel junctions it is important to reduce the number of defects in the barrier and the intermixing at the barrier interfaces while depositing energy in the AF/FM bilayer. Therefore, it has been suggested in the last sections that an inverted stack, where the pinned FM layer is located on top of the barrier, should be used and some examples have been shown.

In this chapter, some SRIM simulations used for the determination of the appropriate ion energy and dose will be presented.

In the simulations shown in Fig. 3.88 for one standard and one inverted stack, the ion energy 10 keV has been used for both stacks. It can be expected that the depth distribution of the energy deposited by ions depends on their initial energy. The same is certainly also true for, e.g., the number of defects produced at a certain depth. Therefore, SRIM simulations have been carried out to find the best ion energy for the bombardment of stack  $MTJ_{IB}^{MgOinv}$ .<sup>50</sup>

The results of selected simulations with different ion energies for a stack similar to stack  $MTJ_{IB}^{MgOinv}$ <sup>51</sup> are shown in Fig. 3.93. It can be seen that large ion energies are not favorable for this inverted stack. This is demonstrated in Fig. 3.94 (a). Here, the energy transferred per ion and  $\text{\AA}$  from ions to target atoms at the middle of the MgO barrier and in the middle of the Ru interlayer of the artificial ferrimagnet normalized to the energy transferred to recoils in the middle of the IrMn layer in dependence of the energy of the impinging He ions is shown. As one wants to deposit energy in the range of the IrMn layer with a minimum of side effects in the barrier and for the interlayer exchange pinning, small values are favorable. These

<sup>50</sup>The optimum energy can be different for different stacks as, e.g., for stack  $MTJ_{IB}^{MgOinv}$  a strong decrease of the deposited energy with increasing depth in the range from 40 nm to 1000 nm is good while the opposite would be good for stack  $MgO_{std}$ . (compare Fig. 3.88)

<sup>51</sup>The simulated sample has the following stack: Si wafer / SiO<sub>2</sub> 50 nm / Ta 5 nm / Ru 40 nm / Ta 5 nm / Co<sub>40</sub>Fe<sub>40</sub>B<sub>20</sub> 2.5 nm / MgO 3 nm / Co<sub>40</sub>Fe<sub>40</sub>B<sub>20</sub> 4 nm / Ru 0.9 nm / Co<sub>70</sub>Fe<sub>30</sub> 1.5 nm / Mn<sub>83</sub>Ir<sub>17</sub> 9 nm / Ru 40 nm.



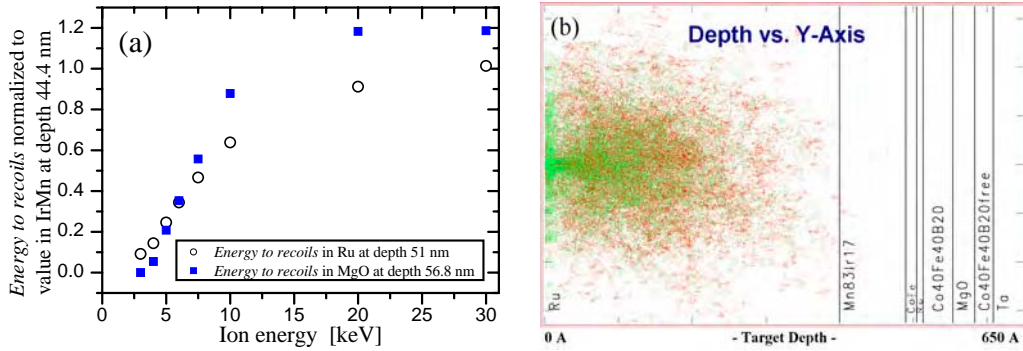


Figure 3.94: (a) Energy transferred per ion and  $\text{\AA}$  depth from ions to target atoms at the middle of the MgO barrier and in the middle of the Ru interlayer of the AFi normalized to the energy transferred to recoils in the middle of the IrMn layer in dependence of the energy of the impinging He ions. (b) Ion trajectories of He-ions (red) and recoils (Ru: green, Mn: blue, Ir: purple) for an ion energy of 3 keV.

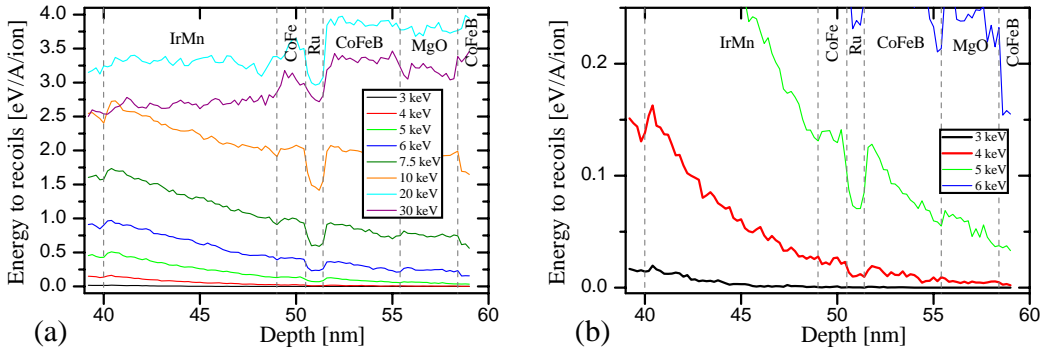


Figure 3.95: Energy transferred from ions to recoils independence of the depth in sample  $MgO_{\text{inv}3}$  for several ion energies. Part (b) shows the simulations for the lower ion energies in more detail.

can be found for small ion energies.

But when the initial ion energy gets smaller, the remaining energy of the ions at a larger depth as, e.g., in the IrMn layer gets smaller relative to the initial value at the top of the sample (Fig. 3.93). In combination with the smaller initial ion energy this effect results in a significantly reduced absolute value of the deposited energy in, e.g., the IrMn layer (Fig. 3.95). For small energies like 3 keV nearly no ions reach the IrMn layer [Fig. 3.94 (b)] and, therefore, nearly no energy is deposited there [Fig. 3.95 (b)]. This would make very high ion doses necessary to manipulate the exchange bias coupling.

Therefore, as a compromise the ion energy 4.5 keV has been chosen for the experimental tests with stack  $MTJ_{\text{IB}}^{\text{MgOinv}}$ .

When for a new stack no experimental results for the ion dose necessary to manipulate the exchange bias are available, SRIM simulations can be used to get an approximated range where the tests should be carried out. In the following lines

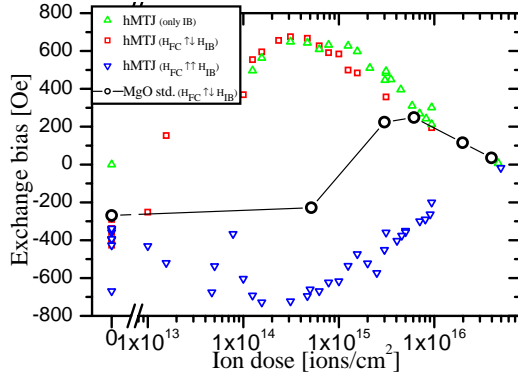


Figure 3.96: Exchange bias in dependence of the ion dose for stack *hMTJ* (AF/FM interface 14.8 nm below surface) and for stack *MgO<sub>std</sub>* (AF/FM interface 87.25 nm below surface). The ion energy was 10 keV for all shown measurements.

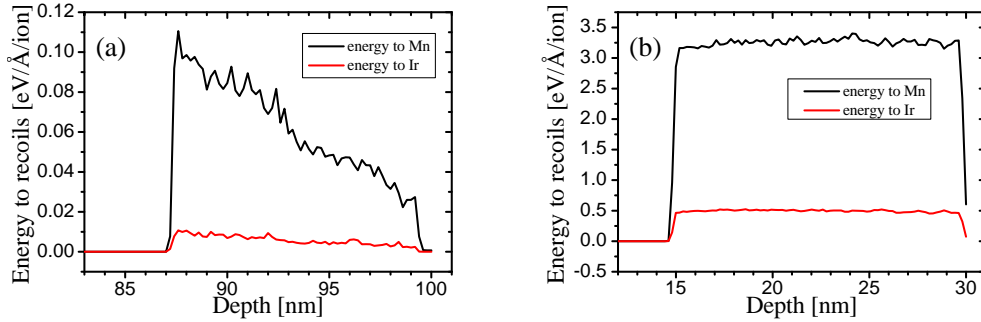


Figure 3.97: SRIM simulation of energy transferred per Å and ion to Mn and Ir recoils in the IrMn layer (a) of stack *MgO<sub>std</sub>* (averaged values: 0.006 eV/Å/ion to Ir recoils, 0.063 eV/Å/ion to Mn recoils, 0.069 eV/Å/ion in total) and (b) of stack *hMTJ* (averaged values: 0,50 eV/Å/ion to Ir recoils, 3,26 eV/Å/ion to Mn recoils, 3,76 eV/Å/ion in total).

this kind of calculations and some corresponding experiments will be introduced.

As it clearly can be seen in Fig. 3.96, the ion dose dependence of the exchange bias varies strongly for different stacks. The ion dose which is necessary to turn the EB direction is much higher for stack *MgO<sub>std</sub>* than for stack *hMTJ*. This can be explained with the different thickness of material above the AF / FM bilayer in these two stacks and the resulting differences in the energy absorption of the upper layers.

The relative strength of this shielding effect of the higher layers can be estimated by SRIM simulations of the energy deposited in the AF / FM bilayer. This can be described, e.g., by the sum of the energy transferred from the ions to Mn and Ir atoms.<sup>52</sup> This kind of simulations for the samples used in the measurements shown in Fig. 3.96 can be seen in Fig. 3.97. For both kinds of samples He ions with an energy of 10 keV have been used but in the case of stack *MgO<sub>std</sub>* a larger part of the ions has been stopped in the layers above the AF / FM bilayer (Fig. 3.98) and the remaining ions have lost more energy. Therefore, the amount of energy transferred from the ions to Mn and Ir atoms per Å depth is 56 times larger for stack *hMTJ* compared to stack *MgO<sub>std</sub>* (Fig. 3.97).

<sup>52</sup>According to the theories explaining the EB effect, the surface between FM and AF layer and the AF layer itself are the key regions for the EB.

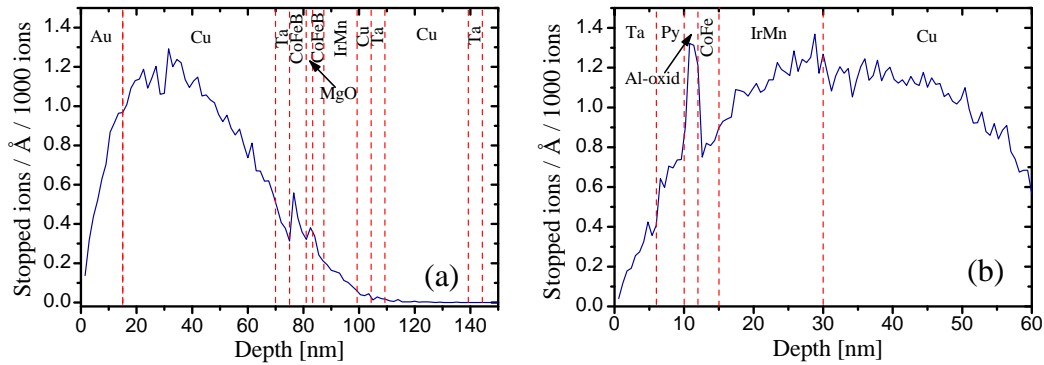


Figure 3.98: SRIM simulation of the range of 10 keV He ions (a) in stack  $MgO_{std}$  and (b) in stack  $hMTJ$

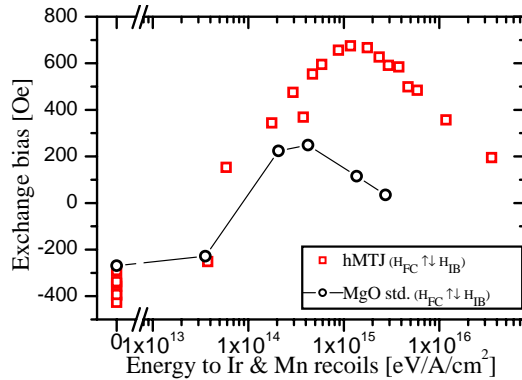


Figure 3.99: Exchange bias in dependence of the average energy transferred per  $\text{\AA}$  depth and  $\text{cm}^2$  sample area to Mn and Ir recoils in the IrMn layer of stack  $hMTJ$  ( $3,76 \text{ eV}/\text{\AA}/\text{ion}$ ) and of stack  $MgO_{std}$  ( $0.067 \text{ eV}/\text{\AA}/\text{ion}$ ).

As mentioned above, another possible measure of the energy deposited in the AF / FM bilayer is the number of phonons resulting from the ion bombardment. The detailed structure of the depth distributions of SRIM simulations will not be investigated in detail as it is influenced by details of the calculation like, e.g., the depth range which is stored (always the full stack is simulated, for details compare chapter 2.7.1).<sup>53</sup> Therefore, only average values will be used in the following investigations.

With the knowledge gathered with the simulations shown in Fig. 3.97, the ion dose in Fig. 3.96 can be replaced by the sum of the average energies transferred per  $\text{\AA}$  depth and  $\text{cm}^2$  sample area to Ir and Mn recoils in the IrMn layer (3.99). A comparison of Fig. 3.99 with Fig. 3.96 shows especially at small ion doses a much better agreement between the measurements for both stacks when the simulated energy deposition is used instead of the ion dose. The dependence of the EB on the transferred energy to Ir and Mn atoms is nearly identical for both stacks for ion doses up to  $2 \times 10^{14}$  ions/ $\text{cm}^2$ , which is just sufficient to turn the EB. But at higher ion doses a strong deviation can be observed. While for stack  $hMTJ$  the maximum value of the rotated EB was found at about  $1.5 \times 10^{15} \text{ eV}/\text{\AA}/\text{cm}^2$  and is significantly higher than the value before IB, for stack  $MgO_{std}$  the maximum at  $4 \times 10^{14} \text{ eV}/\text{\AA}/\text{cm}^2$  is even slightly lower than before IB.

<sup>53</sup>An extreme sample of an artifact calculated for stack  $SV_{3.4nmCu}$  is shown in chapter 2.7.1.

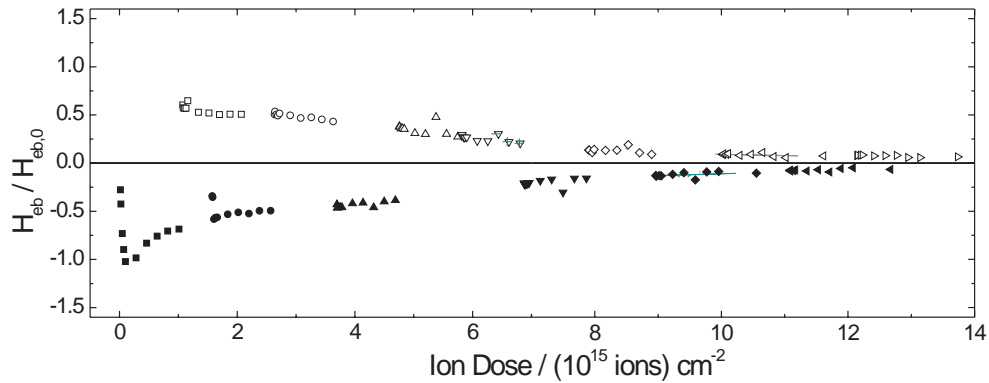


Figure 3.100: Exchange bias in dependence of the ion dose after successive IB steps with for a NiO (50 nm)/NiFe (5 nm)/Ta (2 nm) system. The sample has been bombarded successively with 10 keV He ions with an alternating direction of the magnetic field during ion bombardment (full (open) symbols:  $\mathbf{H}_{IB}\uparrow\downarrow$  ( $\mathbf{H}_{IB}\uparrow\uparrow$ ) initial EB direction). (from [60])

The position of the maximum EB after the rotation of the EB direction is determined by two competing mechanisms. One is the rotation and/or the enlargement of the EB direction in dependence of the direction of the external magnetic field during IB. It is due to, e.g., the local heating (compare chapter 2.1).

The other mechanism is decreasing the EB with increasing ion bombardment. The superposition of these two effects can easily be seen in an experiment of subsequent rotations of the EB direction induced by ion bombardment in magnetic fields with an alternating orientation published in Ref. [60] (Fig. 3.100). Here, the decreasing mechanism reduces the “amplitude” of the oscillating EB.

The EB decrease at large ion doses is usually attributed to ion bombardment induced defects at the antiferromagnet / ferromagnet interface as, e.g., intermixing (compare, e.g., [56, 28, 29, 69]).

The intermixing at high ion doses has been experimentally demonstrated by x-ray absorption measurements for samples with a pinned Co layer (stack  $Co_{TS}^{PEEM}$ , compare [171]).<sup>54</sup> A part of the sample has been annealed in a magnetic field  $H_{FC}$  for 60 min to a temperature of 200°C. Then an annealed and a not annealed sample with the same stack have been bombarded ( $\mathbf{H}_{IB}\uparrow\uparrow\mathbf{H}_{FC}$ ) with 10 keV He ions. The resulting exchange bias coupling can be seen in Fig. 3.101. For these samples x-ray absorption measurements at the Co  $L_2/L_3$  white lines and the Mn  $L_2/L_3$  white lines have been carried out (Fig. 3.102). As the Mn is located underneath the Co in stack  $Co_{TS}^{PEEM}$ , the Mn signal is much smaller than the Co signal. If Mn is transferred closer to the top of the sample or Co is transferred to lower regions, the ratio of the signals will be altered. Therefore, the ratio of the maximum  $L_3$ -signals of the Mn and the Co  $\xi = \text{intensity}(\text{Mn-}L_3) / \text{intensity}(\text{Co-}L_3)$  can be used as an indicator for the intermixing at the Co/IrMn interface. Figure 3.102 (c) shows this ratio in dependence

<sup>54</sup>The full stack of the sample is Cu 30 nm /  $Ni_{80}Fe_{20}$  1.9 nm /  $Ir_{17}Mn_{83}$  25 nm / Co 3 nm / Al 1.4 nm + oxidation.

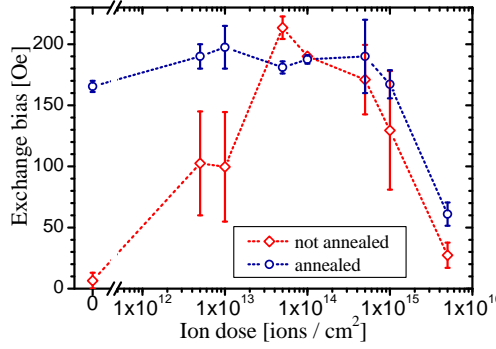


Figure 3.101: Exchange bias in dependence of the ion dose after bombardment with 10 keV He ions in a magnetic field of  $H_{IB}=1000$  Oe for samples with stack  $Co_{TS}^{PEEM}$  with ( $H_{IB} \uparrow H_{FC}$ ) and without field cooling. The error bars indicate the standard deviation of the mean value. The dotted lines are a guide to the eye. (compare [171])

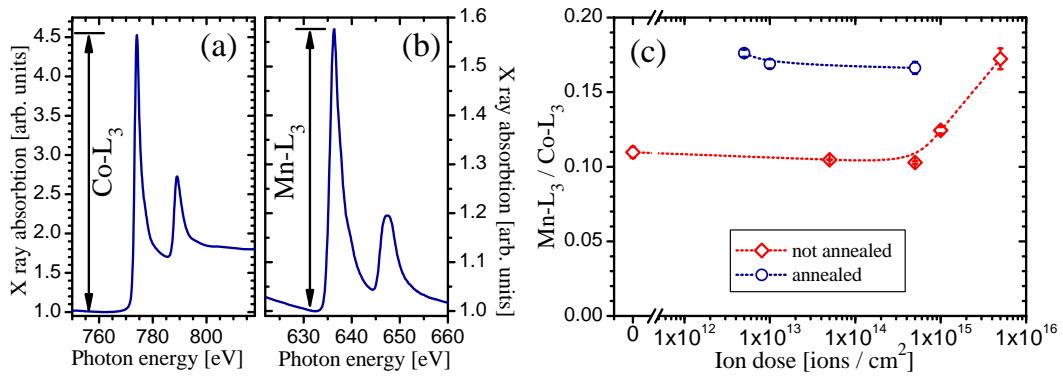


Figure 3.102: X-ray absorption of Co (a) and Mn (b) in dependence of the photon energy measured at an annealed sample with stack  $Co_{TS}^{PEEM}$  after IB with  $5 \times 10^{12}$  ions/cm<sup>2</sup> (average of signal with parallel and antiparallel alignment of photon spin and projection of the magnetization on the x-ray propagation direction) and (c)  $\xi = \text{intensity}(\text{Mn-L}_3) / \text{intensity}(\text{Co-L}_3)$  in dependence of ion dose (compare [171])

of the ion dose. The higher value for the annealed sample can be explained by Mn diffusion in the grain boundaries of the Co to the capping layer as it has frequently been observed in magnetic tunnel junctions [121, 188].

In the ion dose range around  $1 \times 10^{14}$  ions/cm<sup>2</sup>, where the largest exchange bias has been observed, no enlargement of  $\xi$  has been found. Therefore, no intermixing can be detected for this ion doses. In contrast to this, for high ion doses where the EB is reduced, an increasing ratio of the Mn and Co L<sub>3</sub> intensities is found. This correlation suggests that an intermixing at the interface is connected to the EB decrease at high ion doses.

For more details see Ref. [171].

One might think that the the energy deposited in the IrMn is altered by a different factor between the two samples than the intermixing at the interface and that, this is the reason for the observation that the maximum of the EB versus "energy transferred to Ir and Mn recoils" graph is not at the same value for both samples. This might happen, e.g., if ions with a smaller energy can transfer energy to the target atoms but the target atoms and the atoms hit by these recoiling atoms do not have enough energy to cross the interface .

The total number of vacancies / recoiling atoms produced per ion in the AF / FM bilayer is 42 times larger in the case of stack *hMTJ* than in stack *MgO<sub>std</sub>*. 25 times more vacancies per Å and ion have been calculated for the CoFe layer of stack *hMTJ* compared to the CoFeB layer of *MgO<sub>std</sub>* and 50 times more vacancies per Å and ion in the IrMn layer of stack *hMTJ* than in the corresponding layer of stack *MgO<sub>std</sub>* [Fig. 3.103 (a)/(b)]. These values are close to the values obtained for the energy transfer per Å and ion [factor of 18.5 between the energy transferred per Å and ion from the ions to Co and Fe atoms in Stack *hMTJ* and the energy transferred to Co, Fe and B atoms in the pinned FM layer of stack *MgO<sub>std</sub>* (Fig. 3.104), factor of 56 for the energy per ion and Å to Ir and Mn atoms (Fig. 3.97)].

Figure 3.103 (c) and (d) show the final distribution of recoiled atoms produced by one ion during the creation of the vacancies described above. An overlap of the atom distributions for CoFe(B) and IrMn clearly can be seen.<sup>55</sup> The area under the distribution of, e.g., Ir in the CoFeB layer describes the average number of Ir atoms that have crossed the interface. The total number of atoms which have crossed the barrier can be used as a measure for the intermixing. In Fig. 3.103 (e) and (f) the average numbers of atoms which have crossed the AF/FM interface have been determined for both stacks. In stack *MgO<sub>std</sub>* 0.0095 atoms have been shifted per ion while in the case of stack *hMTJ* in average 0.36 atoms per ion cross the barrier. That means 38 times more atoms per ion cross the surface in stack *hMTJ* than in stack *MgO<sub>std</sub>* while according to the simulations shown in Fig. 3.97 about 56 times more energy is transferred to recoils in the IrMn. The small difference between the factor for the degree of intermixing and the factor for the amount of energy deposition in the IrMn shows the uncertainties in this kind of calculations but it is not sufficient to explain the earlier decrease of the EB in Fig. 3.99. This can easily be seen in Fig. 3.105. Here, the exchange bias is shown in dependence of the total

<sup>55</sup>One has to keep in mind that especially at the interface between two layers the simulations should be regarded as approximations due to the limitations discussed in chapter 2.7.1.

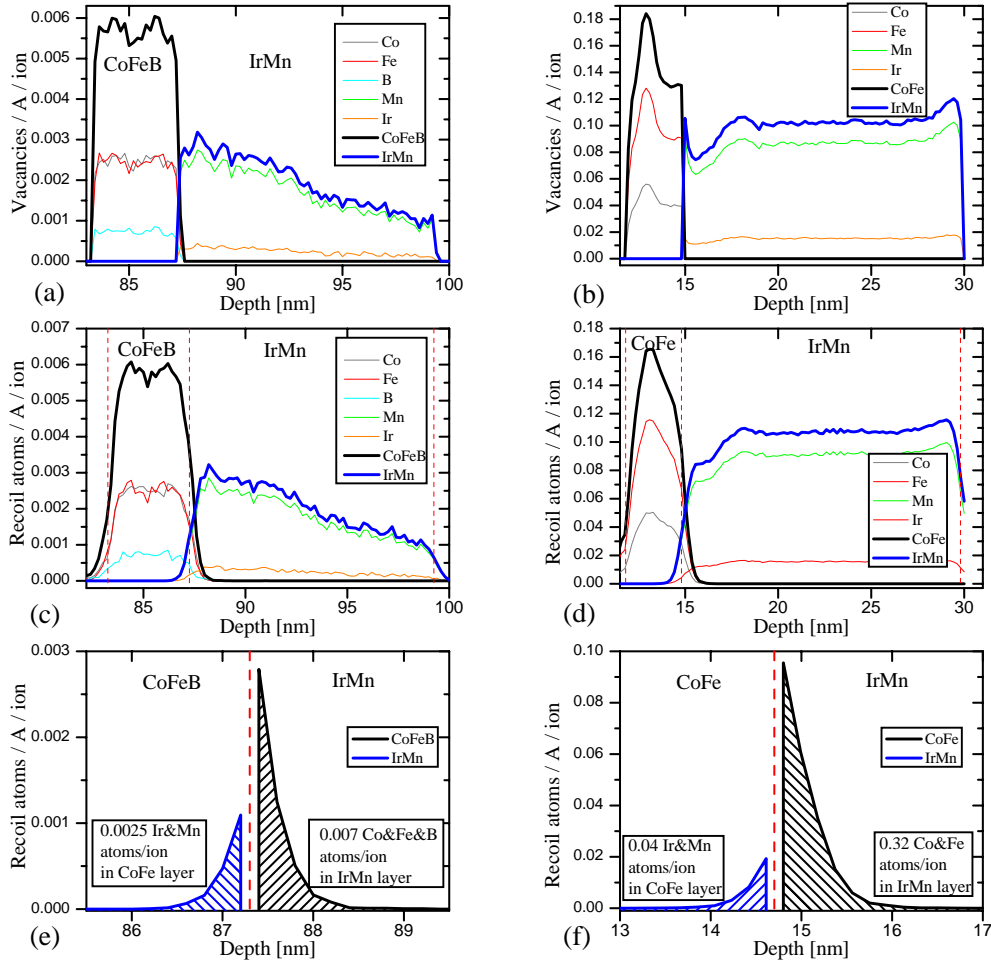


Figure 3.103: SRIM simulation of (a) vacancies generated by IB with stack  $MgO_{std}$  (averaged values: CoFeB: 0.0057 vacancies per ion and  $\text{\AA}$ , IrMn: 0.0020 vacancies per ion and  $\text{\AA}$ , in total 0.46 vacancies per ion in whole bilayer) and (b) with stack  $hMTJ$  (averaged values: CoFe: 0.14 vacancies per ion and  $\text{\AA}$ , IrMn: 0.10 vacancies per ion and  $\text{\AA}$ , in total 19.5 vacancies per ion in whole bilayer), (c) final recoil atom distribution with stack  $MgO_{std}$  and (d) with stack  $hMTJ$  and (e) final distribution of recoil atoms which have displaced into another layer representing the amount of intermixing produced by IB with stack  $MgO_{std}$  (total number of atoms that are shifted by one ion from CoFeB to IrMn and vice versa: 0.0095 atoms/ion) and (f) with stack  $hMTJ$  (total number of atoms that are shifted by one ion from CoFeB to IrMn and vice versa: 0.36 atoms/ion).

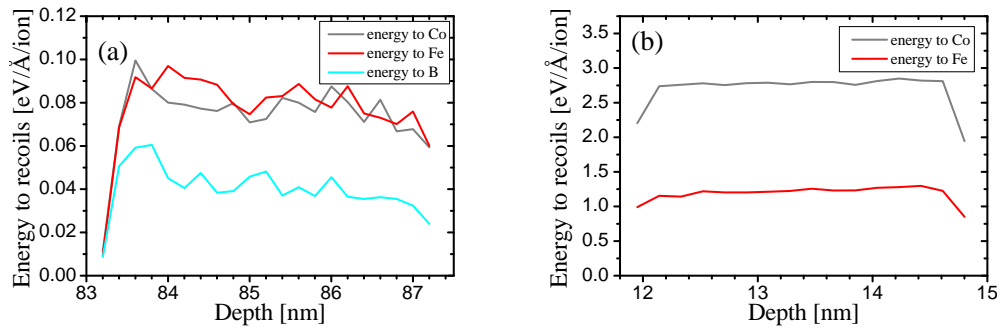


Figure 3.104: SRIM simulation of energy transferred per Å and ion to recoils in the pinned ferromagnetic layer (a) of stack  $MgO_{std}$  (averaged values: 0.076 eV/Å/ion to Co recoils, 0.080 eV/Å/ion to Fe recoils, 0.041 eV/Å/ion to B recoils, 0.2 eV/Å/ion to all Co & Fe & B ions, 7.9 eV/ion in total to CoFeB) and (b) of stack  $hMTJ$  (averaged values: 2.6 eV/Å/ion to Co recoils, 1.1 eV/Å/ion to Fe recoils, 3.7 eV/Å/ion to all Co & Fe recoils, 112 eV/ion in total to CoFe).

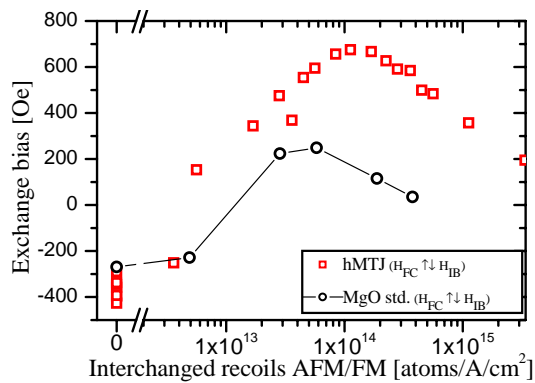


Figure 3.105: Exchange bias in dependence of the total number of atoms that are shifted from CoFeB to IrMn and vice versa for stack  $hMTJ$  and for stack  $MgO_{std}$ .



number of atoms that have crossed the AF / FM interface. Again, for both samples a similar behavior can be found at small ion doses and the EB of stack  $MgO_{\text{std}}$  decreases earlier. Therefore, the different position of the maxima in Fig. 3.99 can not be explained with the different depth of the AF / FM bilayer in the two stacks but might be attributed to the used ferromagnetic materials.

One possible explanation for this observation is that the CoFeB is amorphous when it is deposited and gets at least partly crystalline during the initial annealing step [193]. Maybe the reason for the earlier degradation of the EB in the CoFeB/IrMn bilayer of stack  $MgO_{\text{std}}$  can be found in the sensibility of a thin crystalline CoFeB layer against IB.

As an alternative to the simple method of replacing the ion dose by the energy transferred to ions in the IrMn layer, the equation resulting from the phenomenological model suggested by Engel *et al.* in Ref. [27] has been tested.

This model is based on the model suggested by Mougín *et al.* in Ref. [26]. Mougín *et al.* described a superposition of a linear increase of the EB for small ion doses with an exponential decrease at high ion doses [26]. Engel *et al.* replaced the linear increase by an exponential increase which converges against a certain value as with the linear increase the exchange bias could increase infinitely [27]. The following equation has been suggested for the exchange bias field  $H_{\text{EB}}$  normalized to the exchange bias field without IB ( $H_{\text{EB},0}$ ) in dependence of the number of impinging ions  $N$  for an enlargement of an existing EB:

$$\frac{H_{\text{EB}}}{H_{\text{EB},0}}(N) = [1 + C(1 - e^{-AN})] \cdot e^{-BN} \quad (3.11)$$

Here,  $C$  denotes a parameter which defines the EB field against which the EB field converges without the competing influence of the intermixing at the interface (max. EB =  $(H_{\text{EB},0} + C \cdot H_{\text{EB},0})$ ).<sup>56</sup>  $A$  describes how effectively the EB is increased by ion bombardment. Based on the model by Mougín *et al.* [26] which refers to the domain state model [47, 48, 49, 37],  $A$  is defined by Engel *et al.* as  $A = apt$  ( $a$ : efficiency of a volume defect to increase the exchange bias,  $p$ : probability of a displacement of atoms per ion and unit depth, and  $t$ : AF layer thickness). The efficiency of interface defects to decrease the exchange bias is denoted by  $B$ .

Engel *et al.* suggested different sets of parameters for antiparallel and parallel alignment of  $\mathbf{H}_{\text{IB}}$  and  $\mathbf{H}_{\text{FC}}$ . As the differences between the parameters they found in the parallel and the antiparallel case is rather small, here, the parameters except  $C$  are assumed to be independent of the relative orientation of  $\mathbf{H}_{\text{FC}}$  and  $\mathbf{H}_{\text{IB}}$  for this approximative calculations. Under the assumption that the maximum EB obtainable without the influence of the intermixing at the interface does not depend on the relative orientation of  $\mathbf{H}_{\text{FC}}$  and  $\mathbf{H}_{\text{IB}}$ , the constant  $C_{ap}$  with which  $C$  has to be replaced in the case of antiparallel  $\mathbf{H}_{\text{FC}}$  and  $\mathbf{H}_{\text{IB}}$  can be described by  $C_{ap} = -(2+C)$ .

<sup>56</sup>One has to keep in mind that under the assumption that the maximum EB obtainable with a certain sample by ion bombardment is fixed (e.g., all grains in the AF layer contribute optimally to the EB), the maximum enlargement relative to the initial EB value described in equation 3.11 depends on the value of the EB obtained by the initial field cooling. But this EB after field cooling depends on the field cooling parameters (compare, e.g., Fig. 2.6). Therefore, the parameter  $C$  depends not only on the stack but also on other parameters as the field cooling temperature.

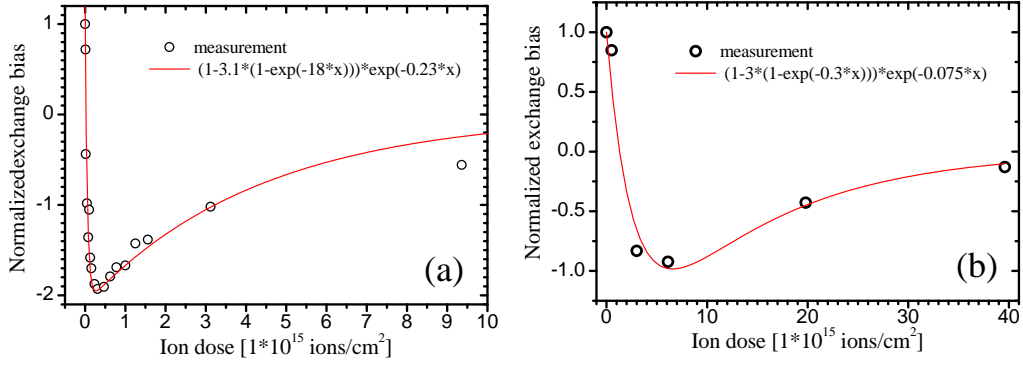


Figure 3.106: EB normalized to value without IB with the result of a fit of equation 3.11 from [27] for (a) stack  $hMTJ$  ( $A=18 \times 10^{-15} \text{cm}^2/\text{ion}$ ,  $B=0.23 \times 10^{-15} \text{cm}^2/\text{ion}$ ,  $C=3.1$ ) and (b) stack  $MgO_{std}$  ( $A=0.3 \times 10^{-15} \text{cm}^2/\text{ion}$ ,  $B=0.08 \times 10^{-15} \text{cm}^2/\text{ion}$ ,  $C=3.0$ ).

Equation 3.11 has been fitted to the measured values of the EB in dependence of the ion dose for stack  $hMTJ$  and  $MgO_{std}$  (Fig. 3.106). The obtained fit parameters are very different as it can be expected because of the different thickness of the layers above the AF / FM bilayer.

The measured EB after the bombardment of stack  $hMTJ$  with  $9 \times 10^{15}$  ions/cm $^2$  [Fig 3.106 (a)] is significantly larger than the calculated value at this dose. This might be connected to the fact that after bombardment with a high ion dose the probability that an additional ion crosses the AF / FM interface at a location where the EB interaction is already destroyed is higher compared to low ion doses. If this happens, the ion can not contribute to the decrease of the EB with increasing ion dose and, therefore, the strength of the EB decrease with increasing ion dose might be reduced at high ion doses. The fact that the fitted function and the measured value are very similar for stack  $MgO_{std}$  even after IB with  $4 \times 10^{16}$  ions/cm $^2$  [Fig. 3.106 (b)] does not rule out the existence of this effect, as the amount of intermixing which can be expected at this ion dose for stack  $MgO_{std}$  is smaller than the amount of intermixing expected for stack  $hMTJ$  after bombardment with  $9 \times 10^{15}$  ions/cm $^2$  (compare Fig. 3.105).

Engel *et al.* [27] observed a similar deviation between fit and measurement in Co/Cu 2.4 nm/Co/FeMn samples especially for an antiparallel alignment of  $\mathbf{H}_{FC}$  and  $\mathbf{H}_{IB}$ . But this was attributed to the increasing coupling between the FM layers and is not directly comparable to this experiment. Measurements of the EB in dependence of the ion dose with a corresponding fit analogue to equation 3.11 can be found for several combinations of FM and AF materials in Ref. [45]. Some but not all of these measurements also show a larger measured EB compared to the fit function at high ion doses. Therefore, other origins for the deviation in Fig. 3.106 can not be ruled out.

To test the possibility of predicting the EB versus ion dose dependence with this equation, further SRIM simulations have been carried out. It has been assumed that the probability of an ion to increase the EB and, therefore, the constant  $A$  in

equation 3.11 might be proportional to the average energy transferred per ion and Å depth to Ir and Mn recoiling atoms ( $E_{recoil}^{IrMn}$ ), to the average number of phonons produced per ion and Å in the IrMn layer ( $N_{phonon}^{IrMn}$ ), or to the average number of vacancies per ion and Å in the IrMn layer ( $N_{vac}^{IrMn}$ ). Furthermore, it has been assumed that the reduction of the EB due to intermixing depends on the number of atoms per ion which cross the AF / FM interface ( $N_{intermix}^{AF/FM}$ ) and that, therefore, the constant  $B$  in equation 3.11 is proportional to this quantity. When this is included into equation 3.11 one gets

$$\frac{H_{EB}}{H_{EB,0}}(N) = [1 + C (1 - e^{-\alpha \cdot A_{SRIM} \cdot N})] \cdot e^{-\beta \cdot N_{intermix}^{AF/FM} \cdot N} \quad (3.12)$$

with  $A_{SRIM} = E_{recoil}^{IrMn}$ ,  $A_{SRIM} = N_{phonon}^{IrMn}$ , or  $A_{SRIM} = N_{vac}^{IrMn}$ . To obtain these quantities, simulations have been carried out for stack  $hMTJ$  and stack  $Ru_{AF}^{zkOe,AP/P}$ . These stacks have been chosen because both contain a CoFe layer pinned on top of a 15 nm thick IrMn layer with a Cu seed layer with a similar thickness ( $Ru_{AF}^{zkOe,AP/P}$ : 25 nm,  $hMTJ$ : 30 nm).

The factors  $\alpha$  and  $\beta$  have been calculated for stack  $hMTJ$ :

- $A = 1.8 \times 10^{-14} \text{cm}^2/\text{ion}$  and  $E_{recoil}^{IrMn} = 3.8 \text{eV}/\text{ion}/\text{Å}$   
 $\Rightarrow \alpha_{recoil}^{hMTJ} = 4.8 \times 10^{-29} \text{m}^3/\text{eV}$
- $A = 1.8 \times 10^{-14} \text{cm}^2/\text{ion}$  and  $N_{phonon}^{IrMn} = 4.6 \text{phonons}/\text{ion}/\text{Å}$   
 $\Rightarrow \alpha_{phonon}^{hMTJ} = 3.9 \times 10^{-29} \text{m}^3/\text{phonon}$
- $A = 1.8 \times 10^{-14} \text{cm}^2/\text{ion}$  and  $N_{vac}^{IrMn} = 0.1 \text{vacancies}/\text{ion}/\text{Å}$   
 $\Rightarrow \alpha_{vac}^{hMTJ} = 1.8 \times 10^{-27} \text{m}^3/\text{vacancy}$
- $B = 2.3 \times 10^{-16} \text{cm}^2/\text{ion}$  and  $N_{intermix}^{AF/FM} = 0.36 \text{atoms}/\text{ion}$   
 $\Rightarrow \beta^{hMTJ} = 0.64 \times 10^{-19} \text{m}^2/\text{atom}$

These factors obtained with stack  $hMTJ$  have been used to calculate theoretical values of  $A = A_{SRIM} \cdot \alpha$  and  $B = N_{intermix}^{AF/FM} \cdot \beta$  for stack  $Ru_{AF}^{zkOe,AP/P}$  from the corresponding simulations also carried out for this stack:

- $E_{recoil}^{IrMn, Ru_{AF}} = 3.5 \text{eV}/\text{Å}/\text{ion} \Rightarrow A_{recoil}^{Ru_{AF}} = 1.70 \times 10^{-14} \text{cm}^2/\text{ion}$
- $N_{phonon}^{IrMn, Ru_{AF}} = 4.3 \text{phonons}/\text{ion}/\text{Å}$  in IrMn  $\Rightarrow A_{phonon}^{Ru_{AF}} = 1.71 \times 10^{-14} \text{cm}^2/\text{ion}$
- $N_{vac}^{IrMn, Ru_{AF}} = 0.1 \text{vacancies}/\text{ion}/\text{Å}$  in IrMn  $\Rightarrow A_{vac}^{Ru_{AF}} = 1.80 \times 10^{-14} \text{cm}^2/\text{ion}$
- $N_{intermix}^{AF/FM, Ru_{AF}} = 0.16 \text{atoms}/\text{ion} \Rightarrow B^{Ru_{AF}} = 1.9 \times 10^{-16} \text{cm}^2/\text{ion}$

Figure 3.107 shows the EB versus ion dose graph calculated for stack  $Ru_{AF}^{zkOe,AP/P}$  with equation 3.11 and these theoretically obtained values of  $A$  and  $B$ . The value  $C=3.1$  obtained with stack  $hMTJ$  has been used without changes for stack  $Ru_{AF}^{zkOe,AP/P}$ . As it can be expected from the very similar values for  $A_{recoil}^{Ru_{AF}}$ ,  $A_{phonon}^{Ru_{AF}}$ , and  $A_{vac}^{Ru_{AF}}$

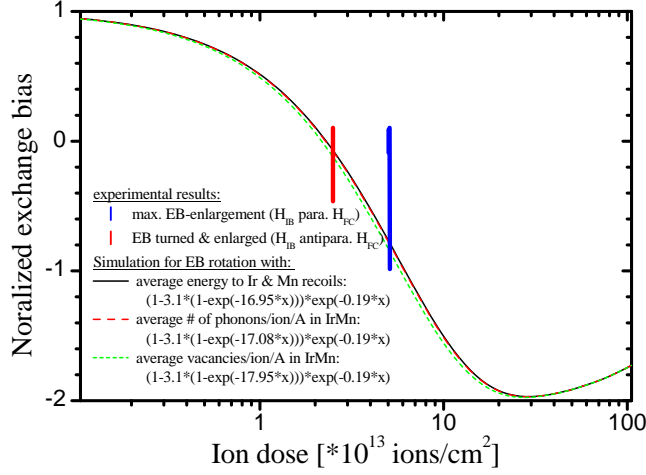


Figure 3.107: EB normalized to value without IB calculated for a rotation of the EB direction in stack  $Ru_{AF}^{zkOe,AP/P}$  with equation 3.11. The blue bar shows the ion dose at which the largest unidirectional anisotropy constant  $K_u$  has been observed experimentally after IB with  $\mathbf{H}_{IB} \uparrow \uparrow \mathbf{H}_{FC}$  (Fig. 3.38). The red bar shows the ion dose at which the EB direction has been turned by  $180^\circ$  and enlarged relative to the EB before IB with  $\mathbf{H}_{IB} \uparrow \downarrow \mathbf{H}_{FC}$  (Fig. 3.46).

the difference between the graphs obtained by simulating the number of phonons, the energy transferred to Ir and Mn atoms, and the number of vacancies in the IrMn layer is very small.

The calculation predicts that the EB direction is reversed after bombardment with about  $2.3 \times 10^{13}$  ions/cm<sup>2</sup> and has a maximum at about  $3 \times 10^{14}$  ions/cm<sup>2</sup>. During the experiments with this kind of sample (chapter 3.3) the strongest enlargement of the exchange bias coupling has been observed after IB in a magnetic field parallel to  $\mathbf{H}_{FC}$  with  $5 \times 10^{13}$  ions/cm<sup>2</sup> (Fig. 3.38). Furthermore, after IB with  $2.5 \times 10^{13}$  ions/cm<sup>2</sup> in a magnetic field antiparallel to  $\mathbf{H}_{FC}$ , the direction of the EB coupling has been rotated and the shift due to the EB was enlarged compared to the EB measured before IB (Fig. 3.46). This shows, that in the experiment the manipulation of the EB direction at sample  $Ru_{AF}^{zkOe,AP/P}$  is more efficient than it was predicted.

As an additional test of the calculated ion dose dependence of the normalized EB while turning the EB  $180^\circ$ , measurements carried out with magnetically patterned spin valves with the stack  $SV_{3.4nmCu}$ <sup>57</sup> are compared with the calculated EB in Fig. 3.108. The number of phonons produced per Å and ion in the IrMn layer has been used for this calculation.

The experimentally determined magnetization reversal process is shown in the small boxes on the top of Fig. 3.108 for one sample without IB and two samples bombarded with two different ion doses. As the sample has been magnetically structured and the MOKE signal is averaged over the diameter of the laser spot which is larger than the magnetic structures, in the graphs after IB the magnetic behavior of bombarded as well as not bombarded areas can be seen.

The measurement carried out at the sample which has been bombarded with  $1.9 \times 10^{13}$  ions/cm<sup>2</sup> shows that the reduction of the EB which is predicted by the calculation has not been found in the experiment. But the ion dose range in which the EB direc-

<sup>57</sup>Stack: wafer / Py 6 nm / Co 1.5 nm / Cu 3.4 nm / Co 5 nm / CoFe 1 nm / IrMn 10 nm / Ta 4 nm

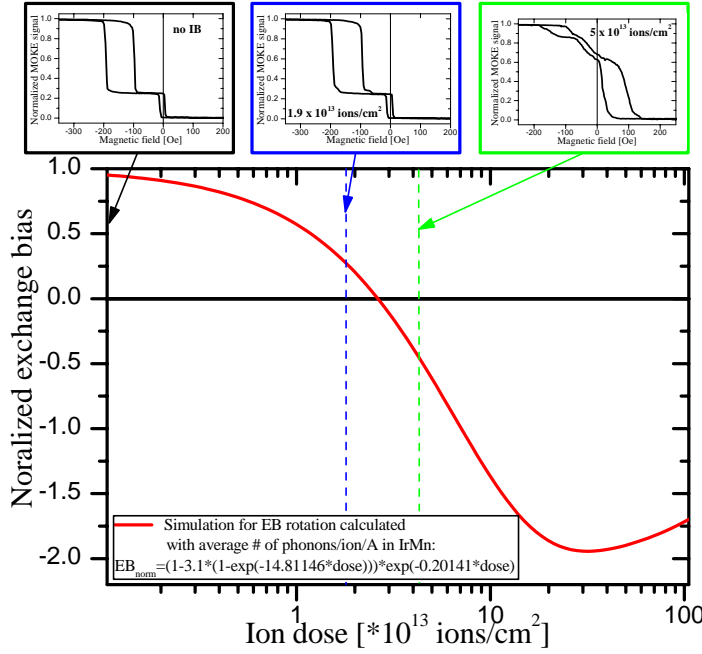


Figure 3.108: Main graph: Calculated ion dose dependence of the normalized EB for stack  $SV_{3.4nmCu}$ . The values of  $\alpha = 3.9 \times 10^{-29}$  m<sup>3</sup>/phonon and  $\beta = 0.64 \times 10^{-19}$  m<sup>2</sup>/atom have been obtained by a fit to the ion dose dependence of the EB measured at stack  $hMTJ$ . Small graphs: MOKE measurements without ion bombardment (left black box) and with  $1.9 \times 10^{13}$  ions/cm<sup>2</sup> (middle, blue box) and  $5 \times 10^{13}$  ions/cm<sup>2</sup> (right, green box).

tion is changed is correctly predicted as a comparison with the measurements carried out at the samples bombarded with  $1.9 \times 10^{13}$  ions/cm<sup>2</sup> and  $5 \times 10^{13}$  ions/cm<sup>2</sup> shows.

Therefore, only the basic behavior and not the details of the ion dose dependence of the EB can be calculated and this kind of simulations can be helpful to find the ion dose range which is worth investigating, but it can not replace an ion dose test. Similar calculations for the stack proposed in chapter 3.8.1 result in an optimum ion dose in the range around  $7 \times 10^{15}$  ions/cm<sup>2</sup>. This ion dose range will be used for the tests described in the following section.

### 3.8.3 Experimental test of the ion bombardment of an inverted magnetic tunnel junction with a pinned electrode located above the barrier

According to the considerations discussed above, a sample with the following stack ( $MTJ_{IB}^{MgOinv}$ ) has been deposited: Ta 5 nm / Ru 40 nm / Ta 5 nm / CoFeB 2.5 nm / MgO 2.1 nm / CoFeB 2.5 nm / Ru 0.88 nm / CoFe 6 nm / IrMn 9 nm / Ru 40 nm. It has been annealed to 375°C for one hour in an external magnetic field of 6.5 kOe to initialize the exchange bias coupling and induce a crystalline ordering process in the CoFeB/MgO/CoFeB region.

Several parts of the sample with stack  $MTJ_{IB}^{MgOinv}$  have been bombarded with 4.5 keV He ions with ion doses between  $2 \times 10^{14}$  ions/cm<sup>2</sup> and  $5 \times 10^{16}$  ions/cm<sup>2</sup> in a magnetic field  $\mathbf{H}_{IB}$  antiparallel to  $\mathbf{H}_{FC}$  as it has been suggested because of the SRIM

simulations in the last section. Major loops measured after this bombardment can be seen in Fig. 3.109.

For a detailed description of the magnetic switching processes compare the measurements carried out at the very similar sample with stack  $MTJ_{\text{Ru var.}}^{\text{MgOinv}}$  shown in Fig. 3.92 and the corresponding information given in the text.<sup>58</sup> The roman numbers in Fig. 3.92 (a) and Fig. 3.109 (a) can be used for an easy comparison of the measurements.

The ion bombardment with the lowest dose of  $2 \times 10^{14}$  ions/cm<sup>2</sup> does not change the TMR amplitude [Fig. 3.109 (a)]. But the switching in region **I** is shifted slightly to a larger negative magnetic field [Fig. 3.109 (b)]. This indicates an increased strength of the antiferromagnetic interlayer exchange coupling. A similar effect has been observed in chapter 3.3.

In the ion dose range of  $3 \times 10^{15}$  ions/cm<sup>2</sup> to  $5 \times 10^{15}$  ions/cm<sup>2</sup> the shift of the loop at region **I** and, therefore, the strength of the antiferromagnetic IEC is as large as it was prior to the IB. With further increasing ion dose the strength of the antiferromagnetic IEC is further decreasing but even after IB with the maximum ion dose of  $5 \times 10^{16}$  ions/cm<sup>2</sup> the antiferromagnetic interlayer exchange coupling is still present [Fig. 3.109 (b)].

Figure 3.109 (c) shows the same measurements normalized to the maximum TMR amplitude of each major loop. The  $5 \times 10^{16}$  ions/cm<sup>2</sup> measurement is again mirrored. This enables a comparison of the switching fields in region **IV**. Although it is more difficult to identify the shift of the switching field **IV**, an increase of the shift of the hysteresis loop for small ion doses and a decrease for high ion doses comparable to region **I** can be observed. The exchange bias indicated by the shift of the hysteresis loop in region **II** is decreasing for increasing ion doses up to  $1 \times 10^{16}$  ions/cm<sup>2</sup> [Fig. 3.109 (b)].

The IB with  $5 \times 10^{16}$  ions/cm<sup>2</sup> turns the EB direction by 180° [Fig. 3.109 (a)] according to the applied magnetic field  $\mathbf{H}_{\text{IB}}$  but the EB coupling after this ion dose is less strong than it was before IB. A comparison of the normalized mirrored major loop after  $5 \times 10^{16}$  ions/cm<sup>2</sup> with the other major loops shows that the reduction of the TMR amplitude is not due to a less good antiparallel alignment of the FM layer magnetizations adjacent to the barrier because the high resistance plateau is located between the switching of the free layer in region **III** which is not changed significantly by the IB and the switching of the not pinned layer in the AFi in region **IV**. And the position of this hysteresis loop is not determined by the EB but by the antiferromagnetic IEC.

Therefore, the reason for the reduced TMR has to be the changes in the electron transport properties in and around the barrier as it has been described for stack  $MgO_{\text{std}}$  above.

Figure 3.110 shows the size of the change of the TMR and the area resistance product in saturation ( $R_{\text{A}}^{\text{min}}$ ) in dependence of the ion dose measured at stack  $MTJ_{\text{IB}}^{\text{MgOinv}}$ .

It can be seen that the TMR amplitude is nearly constant up to an ion dose of

<sup>58</sup>This explanation is valid for all major loops except the one measured after IB with  $5 \times 10^{16}$  ions/cm<sup>2</sup> because at this ion dose the EB direction has turned. Therefore, the sign of the external magnetic field has been inverted in Fig. 3.109 (b) and (c) to get a comparable switching behavior.

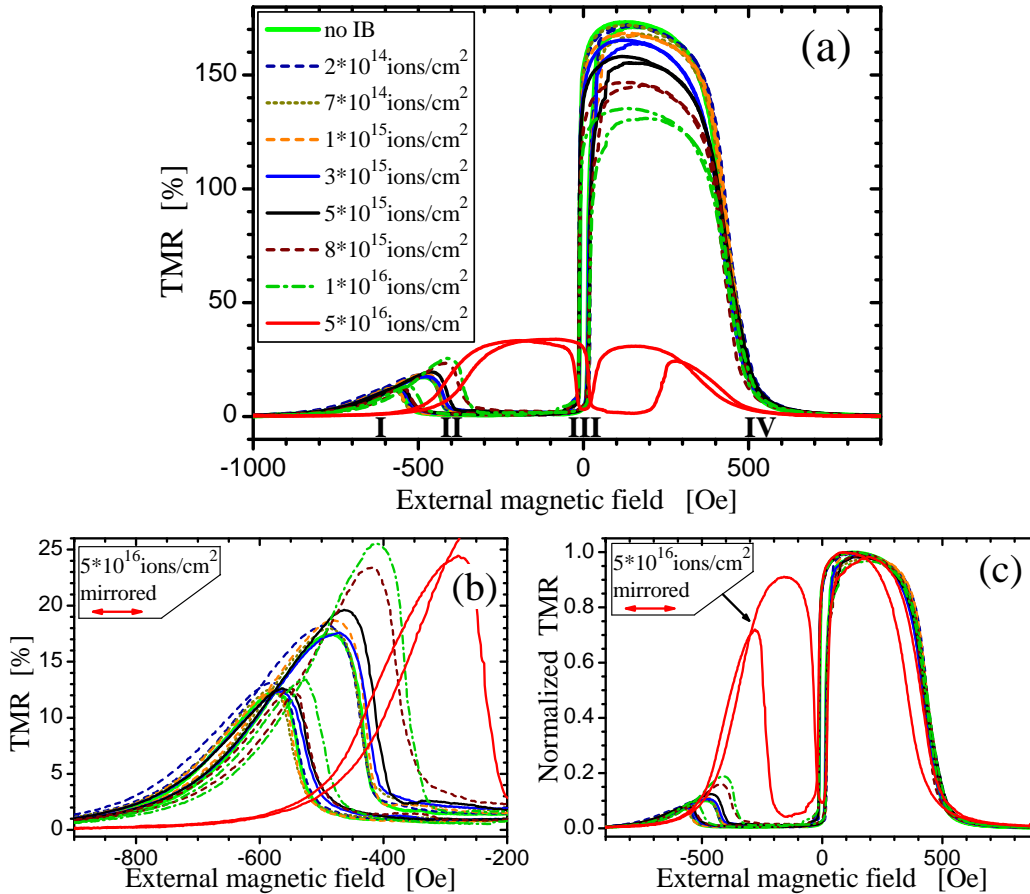


Figure 3.109: (a) Major loops measured at a sample with stack  $MTJ_{IB}^{MgOinv}$  without ion bombardment and after bombardment with several ion doses ( $E_{IB}=4.5$  keV,  $\mathbf{H}_{IB}\uparrow\downarrow\mathbf{H}_{FC}$ ). The roman numerals correspond to AGM measurement in Fig. 3.92. Part (b) shows a zoomed region of graph (a). Part (c) shows identical measurements as shown in (a) normalized to the maximum amplitude of each measurement. In (b) and (c) the major loop measured after IB with  $5 \times 10^{16}$  ions/cm<sup>2</sup> has been mirrored. The color code shown in (a) is valid for all graphs.

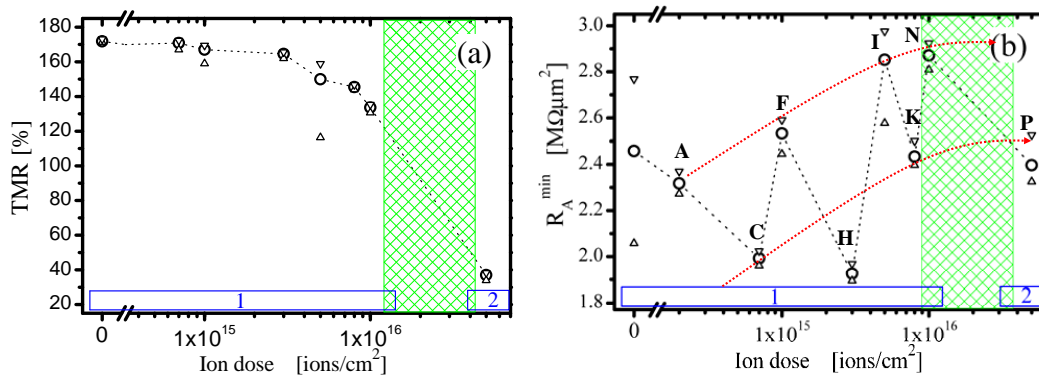
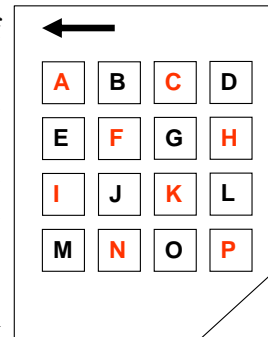


Figure 3.110: Average TMR amplitudes (a) and area resistance product in saturation ( $R_A^{\min}$ ) (b) in dependence of the ion dose measured at stack  $MTJ_{IB}^{MgO^{inv}}$ . Circles indicate the average value determined at five MTJs per ion dose (seven without IB) while triangles pointing up (down) symbolize the minimum (maximum) value measured at each dose. The green mesh indicates the ion dose range in which the EB direction is turned by  $180^\circ$  by the IB with  $\mathbf{H}_{IB} \uparrow \downarrow \mathbf{H}_{FC}$  ( $E_{IB}=4.5$  keV). The dotted lines are a guide to the eye. The letters in (b) indicate the location of each  $2\text{ mm} \times 2\text{ mm}$  sized bombarded area on the sample as shown in the sketch below (b). The arrow in the sketch points to the center of the sample holder during deposition. Red (black) letters in the sketch indicate bombarded (not bombarded) fields.



thicker  
layers

thinner  
layers



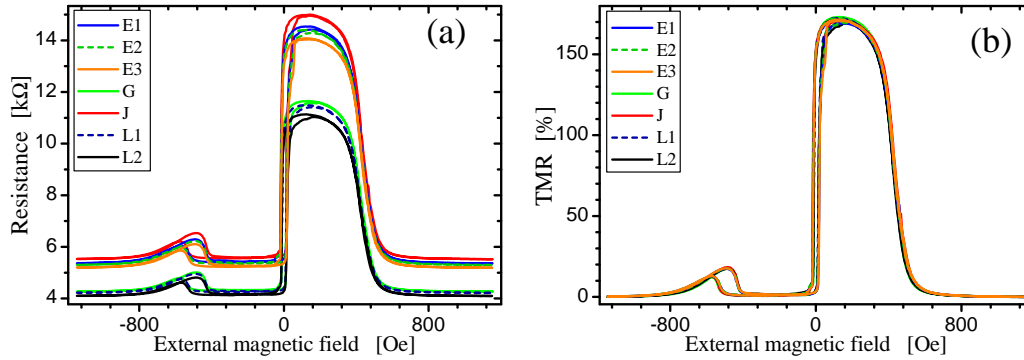


Figure 3.111: Major loops measured at not bombarded areas on different parts (denoted as E, G, J, and L) of the sample with stack  $MTJ_{IB}^{MgO^{inv}}$  which was used for the investigation of the effect of ion bombardment induced magnetic patterning on samples with this stack. For the same measurements (a) the resistance of the  $500\mu\text{m}^2$  sized MTJs and (b) the TMR in dependence of the external magnetic field are shown.

$3 \times 10^{15}$  ions/cm<sup>2</sup> and decreases slowly for higher ion doses up to  $1 \times 10^{16}$  ions/cm<sup>2</sup> [Fig. 3.110 (a)]. But after the IB with  $5 \times 10^{16}$  ions/cm<sup>2</sup> the TMR amplitude is reduced to about 37%.

Possible reasons for the decrease of the TMR amplitude have been described in chapters 3.4 and 3.7.

The resistance is oscillating with increasing ion dose. A comparison of the resistance with the position of the bombarded areas on the sample marked as A-P in Fig. 3.110 (b) and in the sketch of the sample shown below this graph, shows that for ion doses tested on areas closer to the left side in the sketch in Fig. 3.110 a higher resistance has been observed compared to regions located on the right side of the sample.

This coincides with results of investigations of the dependence of the resistance of not bombarded reference MTJs on their location on this sample [compare Fig 3.111 (a)]. Seven major loops measured on not bombarded areas on four different parts (denoted as E, G, J, and L, compare sketch in Fig. 3.110) across the sample are shown in Fig. 3.111. It can be seen that the resistance of the MTJs located at the fields G and L, which are located on the right side of the sample in Fig. 3.110 is smaller than that measured on the fields E and J on the left side of the sample [Fig. 3.111 (a)].

The arrow in the sketch in Fig. 3.110 points to the middle of the sample holder during the sputter deposition. The largest sputter rate can be found at the middle of the sample holder [123]. Because the about 15 mm wide sample as it is sketched in Fig. 3.110 represents an outer part of a larger sample which had a width of about 35 mm to 45 mm and was centered on the sample holder during deposition, a thicker MgO layer can be expected at the left side of the sample in the sketch in Fig. 3.110. Therefore, the oscillation of the resistance with increasing ion dose as well as the dependence of the resistance of the not bombarded reference MTJs on their location

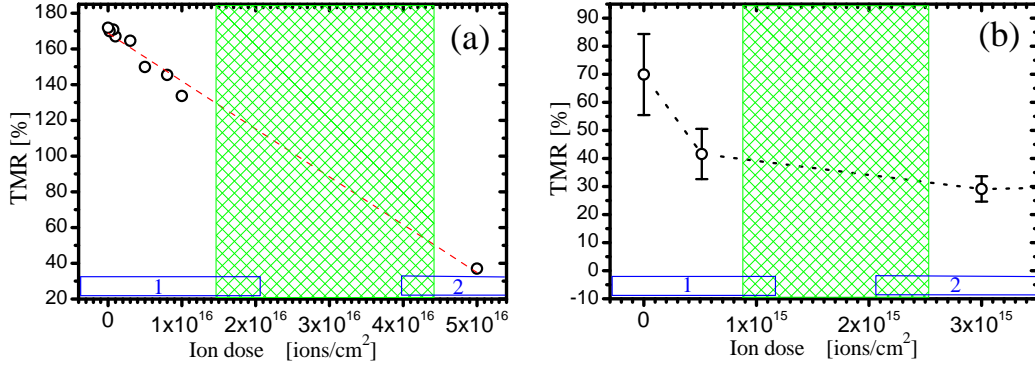


Figure 3.112: TMR amplitude in dependence of the ion dose measured (a) at stack  $MTJ_{IB}^{MgO^{inv}}$  and (b) at stack  $MgO_{std}$  (for full ion dose range investigated with stack  $MgO_{std}$  see Fig. 3.67). Circles indicate averaged values. Triangles in (a) indicate minimum / maximum values. Error bars in (b) indicate the standard deviation. The green mesh indicates the ion dose range at which the EB direction is turned by  $180^\circ$  by the IB with  $\mathbf{H}_{IB} \uparrow \downarrow \mathbf{H}_{FC}$ . (red dashed line in (a): linear fit, black dotted lines in (b): guide to the eye)

on the sample can be attributed to the MgO thickness gradient.

As the variation of the layer thickness is rather small, it can be detected only by the resistance and does not influence the TMR amplitude and the magnetic properties of the tested reference MTJs on the used sample area [Fig. 3.111 (b)]. Therefore, this effect does not prohibit an investigation of the ion bombardment induced effects on this kind of MgO based MTJs with this sample.

The dependence of the resistance on the position on the sample can be taken into account by considering the upper and the lower half of the sample separately. When this is done for the ion dose dependence of the resistance shown in Fig. 3.110 (b), a slightly increasing resistance can be found for increasing ion dose [compare red arrows in Fig. 3.110 (b)].

For an application of ion bombardment induced patterning, especially the combination of the change of the transport and the magnetic properties is of interest. Figure 3.112 (a) shows that the TMR decreases nearly linear with increasing ion dose up to the maximum investigated value of  $5 \times 10^{16}$  ions/cm<sup>2</sup> at which the EB direction has been turned. The dashed red line shows a linear fit to the measurements.

A similar plot of the TMR amplitude measured at the sample with stack  $MgO_{std}$  in the corresponding ion dose range up to the dose necessary to rotate the EB shows that the TMR of these MTJs has already been reduced to about 40% before the EB is turned. Therefore, although the exact ion dose at which the shift due to EB crosses zero is not known, it can be said that no linear relationship up to an ion dose at which the EB direction has been turned is present [Fig. 3.112 (b)].

The ion dose dependence of the TMR at a sample with MgO barrier might be described by a linear decrease at low ion doses (compare Fig. 3.112) a plateau at medium ion doses (compare Fig. 3.67) and a decrease at high ion doses (Fig. 3.67).

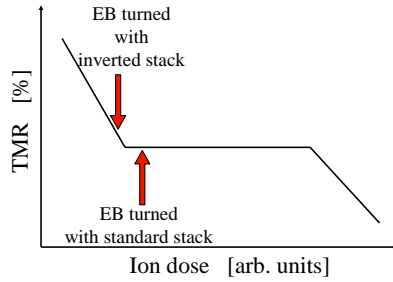


Figure 3.113: Sketch of the ion dose dependence of TMR for magnetic tunnel junctions with MgO barrier. The arrows indicate the position of the switching of the exchange bias direction in the case of sample  $MgO_{std}$  and  $MTJ_{IB}^{MgOinv}$ .

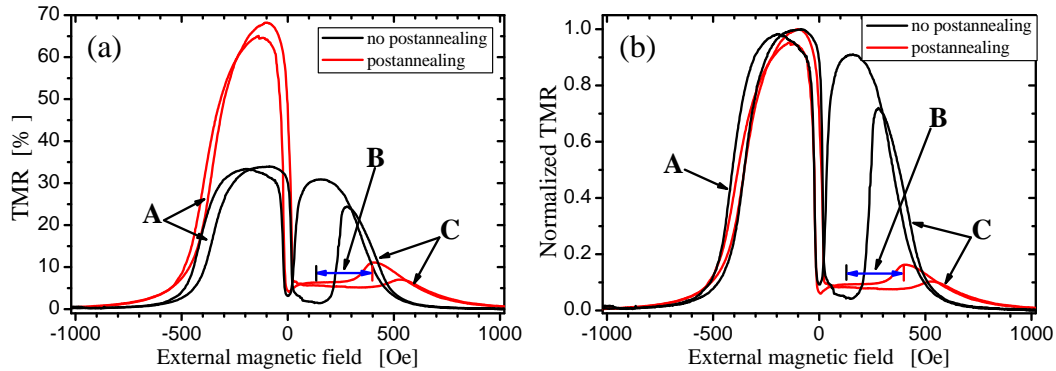


Figure 3.114: Major loops measured at two squared MTJs ( $500\mu\text{m}^2$ ) on a sample with stack  $MTJ_{IB}^{MgOinv}$  directly after ion bombardment with  $5 \times 10^{16}$  ions/ $\text{cm}^2$  (black) and after an additional postannealing without an external magnetic field for one hour at  $325^\circ\text{C}$  (red). (b) shows the same measurements as (a) normalized to the maximum TMR/resistance. (Resistance in saturation:  $R^{\min}(\text{postannealing})=2.5\text{ M}\Omega\mu\text{m}^2$ ,  $R^{\min}(\text{no postannealing})=2.5\text{ M}\Omega\mu\text{m}^2$ )

The change from a standard to an inverted stack and the adjustment of the ion energy have shifted the switching of the EB direction from the low dose part of the plateau (region 2) to the high dose part of region 1 (compare the sketch shown in Fig. 3.113). This is an improvement compared to the initial sample but is not enough for an application in, e.g., a magnetic logic.

Therefore, a more detailed optimization of the stack and the ion bombardment as, e.g., an experimental investigation of the influence of other types of ions in combination with a variation of the ion energy and ion dose would be helpful. The nearly constant TMR after IB with ion doses up to about  $3 \times 10^{15}$  ions/ $\text{cm}^2$  and the slow decrease in the range up to  $1 \times 10^{16}$  ions/ $\text{cm}^2$  shows that a magnetic patterning of full MTJs with MgO barrier might be possible. Furthermore, an additional postannealing step can increase the reduced TMR as it has been seen for sample  $MgO_{std}$ .

After a postannealing for one hour at  $325^\circ\text{C}$  without an external magnetic field a TMR amplitude of up to 68.3% has been found (Fig. 3.114). It is striking that the external magnetic field which is necessary to saturate the sample and, therefore, reach the minimum resistance (TMR=0) has not significantly decreased or is even slightly larger after the postannealing compared to the measurement done before the postannealing (A and C in Fig. 3.114). This shows that the antiferromagnetic

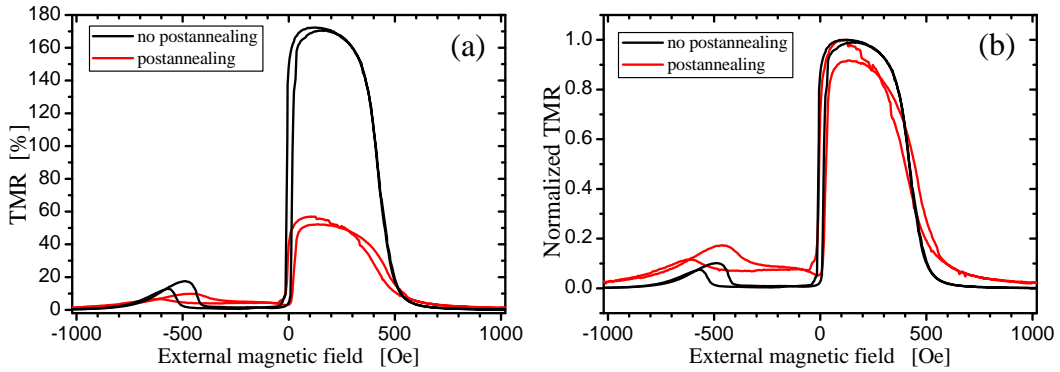


Figure 3.115: Major loops measured at two squared MTJs ( $500\mu\text{m}^2$ ) on a not bombarded part of a sample with stack  $MTJ_{\text{IB}}^{\text{MgO}^{\text{inv}}}$  without heating and after an additional postannealing for one hour at  $325^\circ\text{C}$ . (b) shows the same measurements as (a) normalized to the maximum TMR/resistance. (Resistance in saturation:  $R_{\text{A}}^{\text{min}}(\text{postannealing})=1.4\text{M}\Omega\mu\text{m}^2$ ,  $R^{\text{min}}(\text{no postannealing})=2.1\text{M}\Omega\mu\text{m}^2$ )

interlayer exchange coupling has not suffered during the postannealing.

Furthermore, the shift of the loop at small positive external magnetic fields (blue arrow  $B$  in Fig. 3.114) indicates that the exchange bias coupling has been enlarged by the postannealing without an external magnetic field. This can be explained by the fact that on the areas bombarded with  $5 \times 10^{16}$  ions/ $\text{cm}^2$  the remanence magnetization of the FM layer adjacent to the AF layer points in the same direction as during the ion bombardment. When the magnetization direction of the ferromagnetic layer adjacent to the antiferromagnetic layer is constant during the postannealing, the postannealing in remanence has for this MTJ the same effect as an annealing in a magnetic field parallel to the field during ion bombardment. Obviously this was the case for this MTJ although the temperature during the postannealing was significantly higher than the blocking temperature of the combination CoFe/IrMn. That it is possible that the magnetization direction of small structures is constant up to temperatures significantly above the blocking temperature has been shown during the PEEM measurements at elevated temperatures in chapter 3.2.5.

The disadvantage of postannealing with this high temperature is that it can be expected that on not structured regions of the sample the defined exchange bias coupling is lost and a domain pattern which results from the energy minimization without exchange bias is ‘frozen’ after cooling down to room temperature [compare, e.g., the domain structure in Fig. 3.23 (f)].

Furthermore, the not bombarded reference MTJs show a significantly decreased TMR amplitude after this thermal treatment (Fig. 3.115). An example of a major loop measured at a not bombarded MTJ after the postannealing (1 hour at  $325^\circ\text{C}$  without magnetic field) is shown in Fig. 3.115. To enable an easy comparison of the magnetic properties of not bombarded MTJs with and without postannealing, a major loop measured before the postannealing at another not bombarded MTJ located close to the MTJ used for the measurement after postannealing has been added to Fig. 3.115.

It can be seen that the magnetic properties of the MTJ are not significantly altered

by the postannealing. The exchange bias was initialized for one hour at a temperature of 375°C. Therefore, this heating to 325°C can not significantly enlarge the EB coupling.

As the magnetic properties of the sample can not be the reason for the reduced TMR amplitude, this effect has to be a result of changes in the barrier region or the creation of small shorts at the sides of the MTJ. The fact that besides the TMR amplitude also the resistance of this MTJ is reduced by the postannealing from about 2.1 MΩμm<sup>2</sup> to 1.4 MΩμm<sup>2</sup> also points in this direction.

Samples with a stack similar to  $MTJ_{IB}^{MgOinv}$  showed the highest TMR amplitude after an initial heating in a magnetic field to 400°C for one hour (field cooling for initialization of EB and at the same time crystallization of the MgO and CoFeB layers [204, 207, 205]). Therefore, it is unlikely that after the first heating of this sample to 375°C a large amount of material (e.g., Mn from the IrMn layer - compare [121, 205]) has diffused to the barrier. But the additional postannealing for one hour might continue diffusion processes which have been started during the initial annealing although the temperature of the postannealing was 50°C lower than the temperature of the initial annealing (compare postannealing of sample  $MgO_{std}$  in chapter 3.7.2).

It can be expected that the same mechanisms which are responsible for the TMR reduction in the not bombarded MTJ also reduce the TMR of the bombarded MTJ. Therefore, it is possible that after a postannealing with lower temperatures a higher TMR amplitude of the MTJs with rotated EB direction can be obtained. This is another hint that temperatures smaller than 325°C should be used for the postannealing of stack  $MTJ_{IB}^{MgOinv}$ .

Furthermore, a thicker Ru interlayer (higher antiparallel coupling maximum) in the artificial ferrimagnet might slow the Mn diffusion from the IrMn to the barrier down.

Because of the sensible MgO barrier, a local manipulation of the EB prior to the deposition of the FM/barrier/FM in a sample where the pinned FM layer is positioned underneath the barrier would be an interesting approach. This would prevent any damage to the barrier due to energy deposition by ions in this layer.

The largest challenge of this approach with the available machinery would be the fact that the sample is not in a vacuum during the lithography and the transfer to the IB setup and, therefore, the surface of the sample might be altered. But as, e.g., during the manufacturing of a computer CPU a high number of subsequent process steps including lithography are necessary, this should be no unsolvable problem in commercial facilities. If these procedures are not carried out in a vacuum it might be necessary to remove an oxide layer, e.g., by an etching step after the magnetic patterning.

If the simple stack AF/FM/barrier/FM<sup>59</sup> is used and the magnetic patterning is carried out after the AF/FM layers are deposited, this might result in an altered FM/barrier interface. It can be expected that the TMR amplitude would be decreased significantly by this procedure.

This might be avoided if, e.g., an AF/FM/non magnetic material(NM)/FM reference electrode (e.g., IrMn/CoFe/Ru/CoFeB) is used. During the experiments dealing with artificial ferrimagnets, frequently a ferromagnetic coupling between the FM

---

<sup>59</sup>The lower and upper conduction lines are omitted in the following discussion.

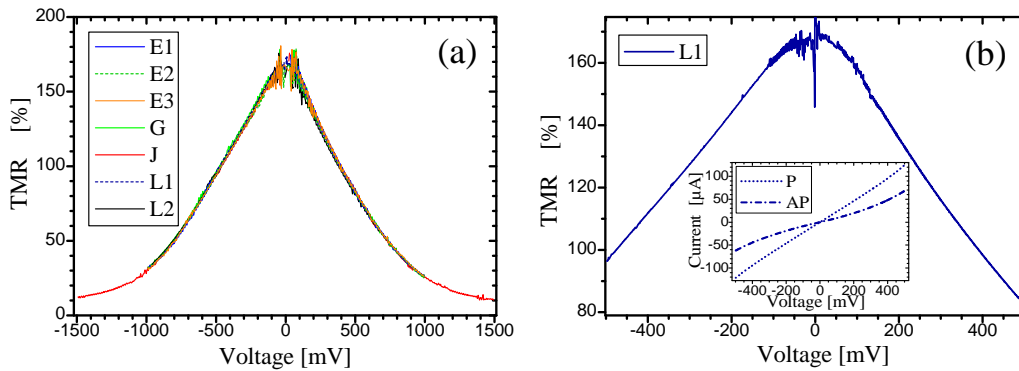


Figure 3.116: TMR in dependence of the bias voltage measured at room temperature on the sample with stack  $MTJ_{IB}^{MgO_{inv}}$  at several not bombarded MTJs distributed on the sample. In (a) some points have been removed in the range  $\pm 100$  mV for clarity. Inset in (b): current in dependence of the bias voltage measured at MTJ L1.

layers has been obtained when the FM/NM/FM trilayer was not perfect. A similar effect might occur when the IB is carried out after the deposition of the AF/FM or AF/FM/NM layers. But if the ferromagnetic coupling is strong enough the sample would behave magnetically like a sample with a AF/FM/barrier/FM stack and the TMR amplitude is not necessarily altered as both interfaces between the barrier and FM layers are prepared at the same time in high vacuum.

Alternatively, one might use two adjacent FM layers and do the magnetic patterning after the deposition of the AF and the first half of the FM bilayer. The second half of the FM layer can be deposited after the IB. This would prevent a strong alteration of the FM/barrier interface.

The application of one of the two last approaches might result in a high total magnetic moment of the reference layer (e.g., due to two ferromagnetically coupled FM layers or one thick FM layer composed of two parts deposited prior to and after IB). When the magnetic moment gets larger, the shift of the reference layer hysteresis loop is decreased for a constant coupling constant and the magnetic stray field coupling in a MTJ increases. To obtain a reasonable small magnetic moment, an artificial ferrimagnet (AFi) might be used (e.g., AF/half FM - ion bombardment - half FM/NM/FM/barrier/FM). This has the additional advantage that the Mn diffusion to the barrier is reduced when a Ru based AFi is used in combination with, e.g., IrMn.

To gain a better understanding of the processes which are responsible for the TMR decrease, the bias voltage dependence of the TMR amplitude at room temperature has been investigated. The voltage dependence of the TMR amplitude (compare page 142) without ion bombardment measured at several MTJs distributed over the sample with stack  $MTJ_{IB}^{MgO_{inv}}$  (compare Fig. 3.111 and 3.110) is shown in Fig. 3.116 (a).

For higher bias voltages (above about 100 mV) no difference can be seen between the measurements carried out at the different MTJs.

The strong noise at low voltages preventing a comparison of the bias voltage de-

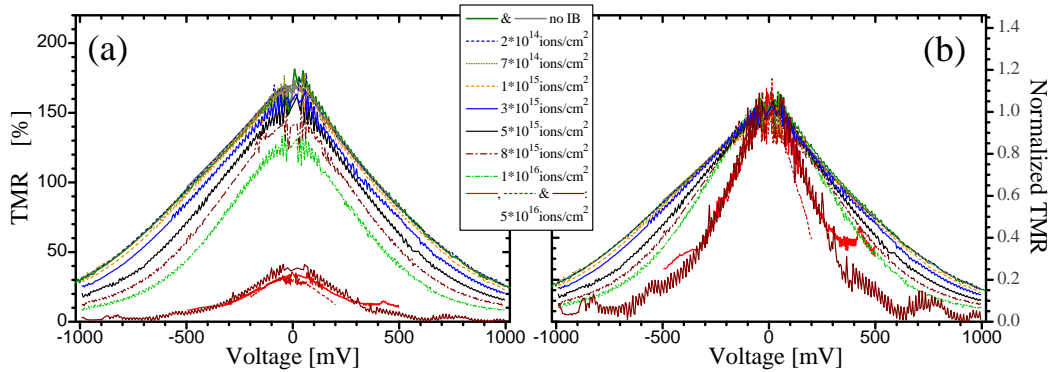


Figure 3.117: (a) TMR in dependence of the bias voltage and (b) normalized TMR in dependence of the bias voltage for several ion doses. Single points have been removed in the  $\pm 100$  mV region for clarity. (stack  $MTJ_{IB}^{MgO_{inv}}$ , measurement at room temperature)

pendence of the TMR in this voltage region in Fig. 3.116 (a) results from the fact that a small amplification has to be used for the whole measurements when high bias voltages are investigated. An example of a measurement up to 500 mV which allows a larger amplification in the measurement electronics is shown in Fig. 3.116 (b). In the inset the corresponding current-voltage measurements carried out with an antiparallel (+175 Oe) and a parallel (-175 Oe) alignment of the magnetizations can be seen.

This effect is no severe disadvantage because the thermal smearing of about 25 mV at room temperature would not allow to resolve fine structures anyway.

No change of the voltage dependence of the TMR has been found for IB with  $2 \times 10^{14}$  ions/cm<sup>2</sup> and  $7 \times 10^{14}$  ions/cm<sup>2</sup> (Fig. 3.117 (a)). Because after ion bombardment with these ion doses the maximum TMR amplitude as well as the change of the TMR amplitude due to an increasing bias voltage is not altered the measurements are nearly identical.

After an ion bombardment with  $1 \times 10^{15}$  ions/cm<sup>2</sup> and higher ion doses, significant differences between the measurements with and without IB can be seen. The maximum TMR amplitude as well as the slope of the measurement has been varied. To allow an easy comparison of the change of the TMR amplitude relative to the value at small bias voltages in dependence of the bias voltage, the same measurements are shown in Fig. 3.117 (b) again.<sup>60</sup> Here, all measurements are normalized to the approximated value around zero bias voltage. It can be seen that the voltage dependence increases with increasing ion dose for ion doses of  $1 \times 10^{15}$  ions/cm<sup>2</sup> and higher (Fig. 3.117 (b)).

<sup>60</sup>The stronger oscillation of the measurement up to 1000 mV after IB with  $5 \times 10^{16}$  ions/cm<sup>2</sup> is no general property of MTJs bombarded with this ion dose as one can see by comparing the three measurements of MTJs bombarded with this dose. Compared to the not bombarded MTJs, the resistance at high bias voltages is smaller (e.g., 179  $\Omega$  at -1 V compared to 2824  $\Omega$  at -1 V without IB). Therefore, less sensible measurement ranges have been used. Furthermore, in Fig. 3.117 (b) the noise is stronger compared to the other ion doses because the measurement is scaled by a significantly different factor due to the smaller absolute maximum TMR amplitude.

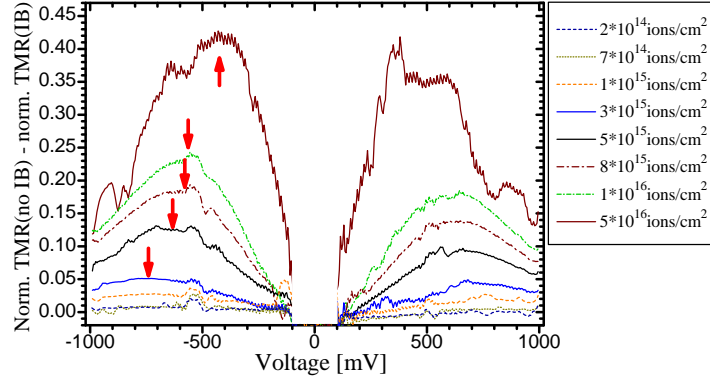


Figure 3.118: Normalized TMR measured at MTJs without IB minus normalized TMR measured at bombarded MTJs in dependence of the bias voltage for several ion doses. The measurements have been smoothed by averaging 5 adjacent points. The voltage region  $\pm 100$  mV is omitted due to strong noise. (stack  $MTJ_{IB}^{MgO_{inv}}$ )

To visualize the change of the bias voltage dependence of the TMR amplitude due to the IB, the normalized TMR measured at MTJs without IB minus the normalized TMR measured on bombarded MTJs in dependence of the bias voltage is shown in Fig. 3.118 for the same measurements as shown in Fig. 3.117.

Larger gradients in the normalized TMR versus voltage plots compared to the not bombarded MTJs at small voltages and smaller gradients at large voltages in Fig. 3.117 result in peaks in Fig. 3.118. The existence of the smaller gradient at high voltages can be connected to the fact that, when the TMR amplitude is already strongly decreased at low voltages, there is not much TMR left to be reduced at high voltages. Therefore, a TMR reduction of the not bombarded MTJ at high voltages results in a reduction of the ‘normalized TMR(no IB) – normalized TMR(IB)’ signal in Fig. 3.118. This can be most easily seen for  $5 \times 10^{16}$  ions/cm<sup>2</sup>.

It is striking that the peaks move to smaller voltages with increasing ion dose.

The peaks in Fig. 3.118 suggest that either paths via defect states allow more electrons to cross the barrier at this voltages or new states allow minority electrons to tunnel across the barrier. Furthermore, the spin polarization might be reduced by spin flip scattering. Jansen *et al.* [208] showed that electrons which have been scattered with a spin flip contribute inversely to the TMR. The fact that the peaks move towards lower voltages suggests that with increasing ion dose due to the generation of a higher number of defects in the barrier and the resulting reduction of the average distance between the defects a hopping over chains of defect states with a higher tunnel probability even at smaller voltages can occur. Furthermore, it is possible that with an increasing number of states which allow additional minority electrons to tunnel across the barrier also the number of this kind of states which have an energy closer to the Fermi level and which, therefore, allow tunneling with lower bias voltages, increases.

The fact that the maxima move to smaller bias voltages with increasing ion dose



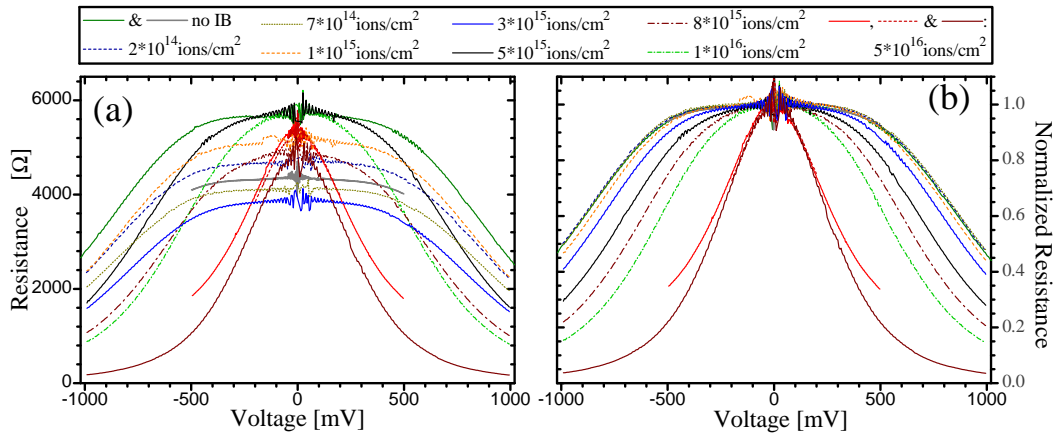


Figure 3.119: (a) Resistance in dependence of the bias voltage and (b) normalized resistance in dependence of the bias voltage for several ion doses. Single points have been removed in the  $\pm 100$  mV region for clarity. (stack  $MTJ_{IB}^{MgO_{inv}}$ )

coincides with the similar movement of the high voltage peak found in the IETS measurements at the sample with stack  $MgO_{std}$  for increasing ion dose (compare Fig. 3.77). It is likely that both effects are connected.

As a peak in the IETS measurement indicates that at this voltage an additional electron path gets available, the resistance versus bias voltage dependence has been investigated for this MTJs with stack  $MTJ_{IB}^{MgO_{inv}}$  (Fig. 3.119).<sup>61</sup>

As it has been observed for the TMR amplitude, the resistance of the bombarded MTJs shows a larger voltage dependence than the not bombarded MTJs.

The difference between the normalized resistance after IB and without IB is shown in Fig. 3.120. Again, peaks can be found which move for increasing ion dose towards smaller absolute values of the voltages. But a comparison with the corresponding graph calculated for the change of the normalized TMR due to IB in Fig. 3.118 shows that the peaks in the case of the resistance are located at higher voltages compared to the peaks of the IB induced change of the normalized TMR (e.g.,  $5 \times 10^{16}$  ions/cm<sup>2</sup>: peak TMR at about 430 mV and peak R at about 590 mV). This might be attributed to the fact that even if the TMR is reduced to zero there can still be a finite resistance because a vanishing TMR means only that the difference of the resistance with parallel and antiparallel alignment is zero. Therefore, the bias voltage where the resistance of the bombarded MTJs gets close to zero and the difference between the bombarded and the not bombarded MTJs gets smaller resulting in a decreasing ‘normalized resistance(no IB) – normalized resistance(IB)’ signal can be larger compared to the corresponding voltage in Fig. 3.118.

The main information one gets from the Figures 3.118 and 3.120 should not be the absolute position of the peaks but the behavior of the bias voltage dependence with increasing ion dose. Here, it can be seen that with increasing ion dose smaller volt-

<sup>61</sup>The resistance shown in Fig. 3.119 has been obtained by using the same current voltage measurements [compare, e.g., the inset in Fig. 3.116 (b)] as used for the calculation of the TMR over bias voltage graphs in the Figures 3.116 to 3.118 and dividing the applied bias voltage through the measured current.

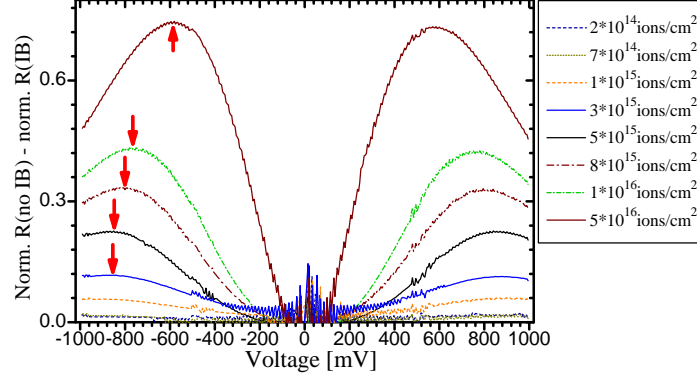


Figure 3.120: Normalized resistance measured at MTJ without IB minus normalized resistance measured on bombarded MTJs in dependence of the bias voltage for several ion doses. Single points have been removed in the  $\pm 100$  mV region for clarity. (stack  $MTJ_{IB}^{MgO_{inv}}$ , all measurements with parallel alignment)

ages are sufficient to transfer more electrons through the barrier. This fits to the generation of chains of defect states in the barrier with a higher tunnel probability because of the decreasing distance from defect to defect suggested as an explanation for the IETS high high voltage peaks observed at stack  $MgO_{std}$ .

### 3.8.4 Summary for ion bombardment of magnetic tunnel junction with pinned ferromagnetic layer on top of the MgO barrier

The MTJs with an inverted stack which have been developed for a better compatibility with the ion bombardment induced magnetic patterning show a TMR amplitude at room temperature of about 180%. This value is more than two times larger than the TMR amplitude of the MTJ with standard stack and suggests that a coherent tunneling is present in these samples.

The TMR amplitude which is left after turning the EB direction by  $180^\circ$  by IB in a magnetic field antiparallel to  $\mathbf{H}_{FC}$  is significantly reduced. Although the detailed ion dose dependence of the TMR suggests that the inverted sample in principle is less sensible to the side effects of the IB, the TMR amplitude left after turning the EB direction is in the same range as the value obtained after turning the EB direction at the sample with the standard stack.

The TMR amplitude of about 70% measured after turning the EB direction by  $180^\circ$  and applying a postannealing step at  $325^\circ\text{C}$  illustrates the advancement compared to the initial standard MgO based MTJ. The new inverted stack shows after the successful manipulation of the EB direction approximately the same TMR amplitude as the standard MgO based MTJ without any IB and is larger than the value obtained by MTJs with alumina barrier without IB. Furthermore, the small TMR amplitude found at not bombarded MTJs after this postannealing step suggests that the postannealing temperature was too high.

Therefore, it is likely that with a more detailed adjustment of the stack, the ion energy, and the postannealing parameters higher TMR amplitudes after manipulat-

ing the EB direction are possible even for MTJs with the extremely sensible MgO barrier.<sup>62</sup> The two main suggestions for future experiments are the application of a thinner capping layer on an inverted stack in combination with small ion energies and a smaller postannealing temperature.

This would make it possible to take advantage from the sharp peak of the deposited energy versus depth graph shown for small ion energies in the SRIM simulations (Fig. 3.93). When the strong decrease of the energy deposition with increasing depth obtained for small ion energies takes place in the range between the AF layer and the barrier, a much more advantageous ratio of the energy deposited in the AF layer and the energy deposited in the barrier can be obtained.

When the remaining defects in the barrier are healed by postannealing with smaller temperatures, the competing TMR reduction due to Mn diffusion can be expected to be smaller resulting in a larger TMR amplitude. This might be supported by the use of a higher AF maximum of the interlayer exchange coupling with a larger Ru thickness because this has been found to be more stable at higher temperatures (compare Fig. 3.91 and Ref. [207]).

---

<sup>62</sup>As it has been shown in chapter 3.4, the manipulation of the EB direction in MTJs with alumina barrier is no large problem although less tests have been carried out for MTJs with alumina barrier to optimize the stack and the ion bombardment parameters.

## Chapter 4

# Applications

After the demonstration of the possibilities of ion bombardment induced magnetic patterning (IBMP) and the discussion of the prerequisites of a technical application in the previous chapters, applications of this technology will be presented.

In the literature one can find, e.g., the application of IBMP in an angle sensor for magnetic fields [30]. This magnetic angle sensor consists of four NiFe/Co/Cu/Co/FeMn spin valves [Fig. 4.1 (a)] in a Wheatstone bridge configuration [Fig. 4.1 (b)]. The direction of the exchange bias (EB) pinning of the reference electrode has been rotated  $180^\circ$  at the place of two of the spin valves [Fig. 4.1 (c)]. This method to produce the opposite pinning of the reference layers of one half of the spin valves can be expected to be more effective than the alternatives as, e.g., the sputtering of the reference layers of one half of the spin valves in one magnetic field while the area of the others is covered by resist and a subsequent deposition of the two other reference layers in an oppositely oriented magnetic field after the first resist layer has been removed and a new one covering the area of the already deposited first spin valves has been produced.

Another application presented in the literature is the production of calibration samples which make it possible to obtain detailed information about the magnetic properties of a magnetic force microscopy (MFM) tip [45, 209, 78]. This is necessary for a quantitative analysis of the MFM measurements.

In the following two further applications of IBMP will be presented. The first one is the manipulation of magnetic nanoparticles by the strayfield of magnetically patterned ferromagnetic (FM) layers, e.g., on magnetic sensors (chapter 4.2). The second application is a novel type of reconfigurable magnetic logic which enables the use of all basic logic functions with only two magnetic tunnel junctions.

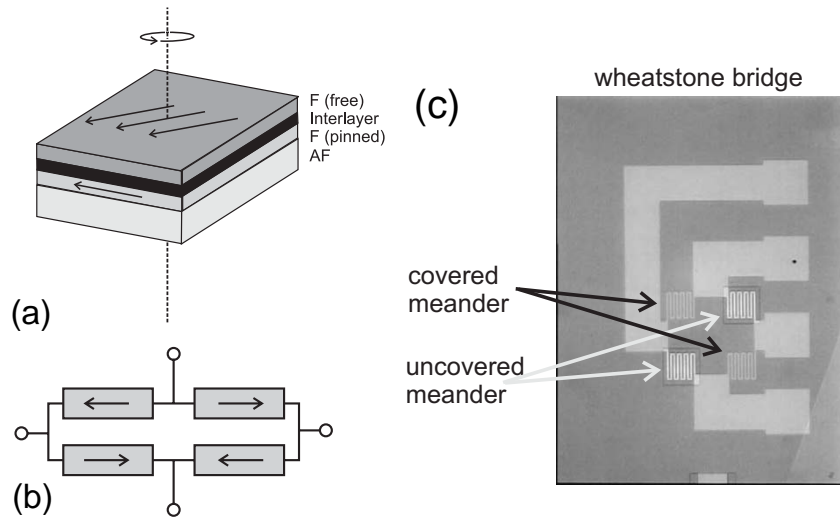


Figure 4.1: (a) Sketch of a spin valve consisting of two ferromagnetic layers separated by one non magnetic interlayer. The lower FM layer is pinned by the exchange bias coupling to the adjacent antiferromagnetic (AF) layer. (b) Wheatstone bridge configuration. The arrows indicate the pinning direction of the reference layer. (c) Experimental realization of a spin valve Wheatstone bridge. Two of the meander structured spin valves are bombarded with ions through two openings in the resist to turn the EB direction. The rest of the sample including the two other spin valves is protected against ion bombardment by the resist. (from [30])

## 4.1 Principle of magnetically patterned sensor for magnetic nanoparticles

Recent progress in the preparation and characterization of the unique properties of magnetic nanoparticles make them attractive for an increasing number of applications [210, 211, 212, 213]. One interesting application is, e.g., the *lab on a chip*. Here, the magnetic nanoparticles are linked to biomolecules. When this connection is established it is possible to detect the biomolecules by detecting the magnetic marker (see, e.g., [214, 215]). This can be done by measuring the magnetic strayfield of the nanoparticles, e.g., by giant magnetoresistance (GMR) or tunnel magnetoresistance (TMR) sensors. To detect small numbers of nanoparticles it is necessary to direct them on or close to the sensor. In the past, e.g., magnetic gradient fields resulting from currents in leads close to the sensor have been proposed for this task [215].

The approach described here, is to use the strayfield of the magnetic material of the sensor itself to guide the nanoparticles towards the sensor. In order to produce a significant strayfield on the area of the sensor and not only at the edges a magnetic patterning can be used. Figure 4.2 shows a sketch illustrating the principle of this approach.

The GMR sensor shown in Fig. 4.2 (a) consists of two ferromagnetic Co layers and a Cu interlayer. One of the FM layers is pinned to an antiferromagnetic (AF) IrMn layer (homogeneous initialization of the EB, e.g., by field cooling in a magnetic field

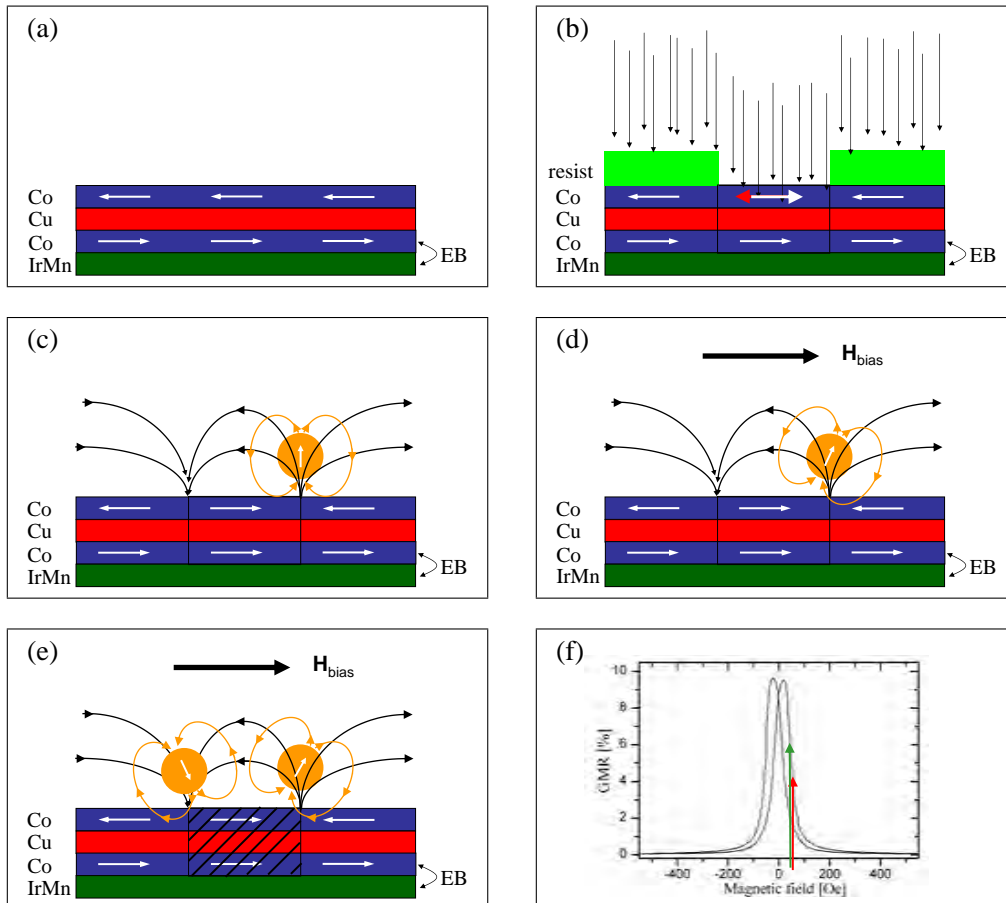


Figure 4.2: (a) Sketch of an exemplary pinned GMR sensor with an antiparallel alignment of the FM layers (b) Antiferromagnetic interlayer coupling locally transferred to ferromagnetic coupling by ion bombardment (only a part of the desirable periodic pattern of thin lines is shown) (c) Magnetic nanoparticles attracted by strayfield (d) External in plane bias field (e) Strayfield of both nanoparticles parallel to magnetization of upper FM layer in remanence (f) Arbitrary GMR measurement, red arrow: resistance for  $H_{\text{bias}}$ , green arrow: resistance for  $H_{\text{bias}}$  + strayfield of nanoparticle.

$H_{FC}$ ). But any other material combination showing a GMR effect with one FM layer which is significantly harder to switch by an external magnetic field could be used as well.

While most of the sensor is protected by a resist mask, small areas are bombarded with ions [Fig. 4.2 (b)]. One might use a high number of thin bombarded lines perpendicular to the direction of the unidirectional anisotropy divided by not bombarded areas. For a sufficiently high ion dose the antiferromagnetic coupling between the two FM layers gets ferromagnetic (compare chapters 2.4 and 3.3). Furthermore, the GMR amplitude on the bombarded lines is reduced or suppressed by very high ion doses and the measured signal originates mainly from the not bombarded areas. When no external magnetic field  $H_{IB}$  is applied during IB or a magnetic field is chosen which ensures that the magnetization of the FM layer adjacent to the AF layer is oriented parallel to the magnetic field during the initialization of the EB, the exchange bias coupling does not change its orientation.

When the resist is removed [Fig. 4.2 (c)] one gets a flat surface where the strayfield resulting from the opposite orientation of the magnetization of the upper FM layer can attract magnetic nanoparticles to the edges of the bombarded areas (experiments investigating this aspect will be shown in the next part).

When a small in plane magnetic field  $\mathbf{H}_{bias}$  parallel to the magnetization direction of the lower FM layer is applied, the orientation of the magnetization of the magnetic nanoparticle and the upper FM layer might be slightly turned [Fig. 4.2 (d)]. The applied magnetic field should be chosen small enough not to saturate the upper FM layer to make sure that the nanoparticle is still attracted by the strayfield of the FM layer.<sup>1</sup>

The magnetic strayfield of the nanoparticle in Fig. 4.2 (c) at the location of the not bombarded part of the upper FM layer is oriented antiparallel to  $\mathbf{H}_{bias}$ . Therefore, the effective magnetic field at this point is reduced when a magnetic nanoparticle is present.

The magnetic strayfield of nanoparticles reduces the effective magnetic field in the adjacent not bombarded area independent whether they are located on the right or left side of the bombarded line [hatched area in Fig. 4.2 (e)] or at the edges of the sensor. As only the not bombarded area contributes significantly to the magnetoresistance effect, all attracted nanoparticles have the same effect on the resistance of the sensor.

Figure 4.2 (f) shows a resistance measurement in dependence of the magnetic field for an arbitrary GMR sample similar to the one described above. When the red arrow indicates the resistance of the sample in a magnetic field  $H_{bias}$  than the green arrow shows that the effectively smaller magnetic field in the presence of magnetic nanoparticles would result in a higher resistance. Therefore, the answer to the question whether magnetic nanoparticles are present can directly be deduced from the resistance of the sensor.

For an application as a sensor further adjustments as, e.g., the implementation of crossed anisotropies and other FM materials should be carried out to reduce the large coercivity of the sample shown in Fig. 4.2 (f). But in principle one could even use samples with a high coercivity when the sample is saturated before each

---

<sup>1</sup>A high external magnetic field sufficient to saturate the sample can be used during the cleaning procedure to switch of the attracting magnetic strayfield of the sensor.

measurement to get a defined status of the system. Then the resistance can be connected with the number of particles on top of the sensor. Another possibility is to measure the difference of the resistance of two identical sensors where only one is in contact with the particle solution.

Furthermore, the fact that the magnetic moments of the nanoparticles are aligned by the strayfield of the sensor might suppress an antiparallel alignment of magnetic moments of nanoparticles relative to each other due to the dipole-dipole interaction between the nanoparticles themselves. This antiparallel alignment of the particle moments has been reported for ferromagnetic nanoparticles, e.g., in Ref. [137].<sup>2</sup> This coupling is unfavorable for the detection of the nanoparticles because of clustered nanoparticles only the net magnetic moment can be sensed.

---

<sup>2</sup> Once the particles are magnetized, the strayfield of the surrounding particles can be sufficient to keep the spins of a particle aligned. This particle now produces a magnetic strayfield itself which can align the spins of neighboring particles and so on.



## 4.2 Manipulation of magnetic nanoparticles by stray-fields of magnetically patterned ferromagnetic layers

### 4.2.1 Introduction

One requirement for, e.g., the successful implementation of the magnetically patterned sensor described in the last chapter is the possibility to attract magnetic nanoparticles with this kind of magnetically patterned FM layers.

But also other applications can profit from the possibility to manipulate the assembly of magnetic nanoparticles by the strayfield of magnetically patterned but nevertheless flat FM layers. For example for the investigation of nanoparticle properties as the electrical transport properties or the particle self-assembly process it might be helpful to have the possibility to place particles at defined locations.

Besides the local manipulation of the exchange bias other effects of the ion bombardment on the magnetic properties of thin films as, e.g., the reduction of the antiferromagnetic (AF) interlayer exchange coupling [28] or the variation of magnetic properties like, e.g., the coercivity [70] can be used to create magnetic strayfields. This enables a fine adjustment of the magnetic gradient field to the particular requirements of arbitrary applications without the sometimes unfavorable effects of topographic structures.

Therefore, on the following pages the influence of the magnetic strayfield produced by a pinned FM layer with a locally varying exchange bias coupling on the assembly of magnetic nanoparticles will be described.

### 4.2.2 Experiment

The preparation of the nanoparticles has been carried out by Carsten Waltenberg by the thermolysis of metal organic precursors ( $\text{Co}_2(\text{CO})_8$ ) with oleyl amine as surfactant for the stabilization of the particles, following the method of Puntès *et al.* [217].

As one can see in the transmission electron microscope (TEM) image in Fig. 4.3 the particles which are crystallized in the fcc-Co phase have a mean diameter of 12 nm with a standard deviation of  $\sigma = 1.34$  nm [218]. Therefore, these particles are expected to show a mainly superparamagnetic behavior at room temperature, as the superparamagnetic-ferromagnetic transition was found to occur for fcc-Co nanomagnets at a size of about 15.8 nm [219]. The particles are saturated in a magnetic field of about 3000 Oe [218].

The sample used to provide the magnetic strayfield is composed of the following layers: Cu 30 nm /  $\text{Mn}_{83}\text{Ir}_{17}$  15 nm /  $\text{Co}_{70}\text{Fe}_{30}$  3 nm / Al 1.4 nm +100 s electron cyclotron resonance plasma oxidation (stack *CoFe-Xray*). A homogeneous EB of the whole sample was initialized by field cooling (FC) in an external magnetic field of  $H_{FC} = 1500$  Oe. A resist mask with 1.6  $\mu\text{m}$  wide uncovered lines parallel to  $\mathbf{H}_{FC}$  and a periodicity of 5  $\mu\text{m}$  was patterned by electron beam lithography. The EB in the areas without a protecting resist capping has been turned by bombarding the sample through the resist mask with He ions with an energy of  $E_{IB} = 10$  keV and an

---

<sup>3</sup>Parts of the results have been published in [216].

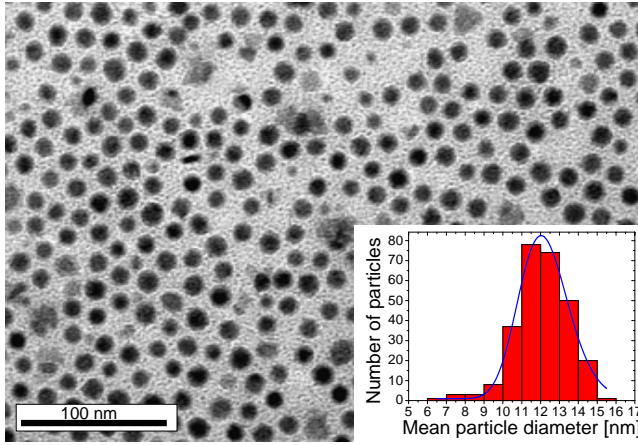


Figure 4.3: TEM bright-field image of the 12 nm sized Co particles, inset: corresponding particle size distribution [218].

ion dose of  $1 \times 10^{14}$  ions/cm<sup>2</sup>. The external magnetic field during ion bombardment  $\mathbf{H}_{IB}$  of 1000 Oe was oriented antiparallel to  $\mathbf{H}_{FC}$ . After the removal of the resist one can expect a magnetic grating with an approximately antiparallel orientation of the EB coupling at the bombarded lines and the area around them without a change of the topographical microstructure. This has been tested by atomic force microscopy (AFM) and MFM measurements.

The nanoparticles are transferred onto the sample by dropping 1  $\mu$ l of the colloidal solution on the sample, by dipping the sample into the solution and removing it slowly or by placing the sample in about 0.5 ml of the solution until the solvent is evaporated.

After the evaporation of the solvent the arrangement of the nanoparticles on the sample has been investigated for all three approaches by scanning electron microscopy (SEM) measurements with an electron energy of 5 keV.

### 4.2.3 Results and Discussion

To ensure that the particle assembly is not influenced by topographic structures AFM and MFM measurements have been carried out on the sample after the magnetic patterning (Fig. 4.4). An AFM measurement is shown in Fig. 4.4 (a). No topographic structure due to the horizontal bombarded lines approximately in the middle and at the top and bottom edges of the image can be seen. The corresponding MFM measurement of the same area can be found in Fig. 4.4 (b). The strayfield of the Néel walls at the sides of the magnetic line is clearly visible. Therefore, any change of the assembly of nanoparticles at this part of the sample can be attributed to magnetic strayfields. Line scans over the MFM signal measured at another sample with an identical stack and a similar magnetic patterning can be found in chapter 3.2 and Ref. [166]. These measurements show a larger MFM signal at the end of the line indicating a larger strayfield resulting from the head to head orientation of the magnetization compared to the sides.

Another test of the magnetic grating on the sample has been done by investigating the resonant scattering of soft x rays (chapter 3.1 and [160]). During these exper-

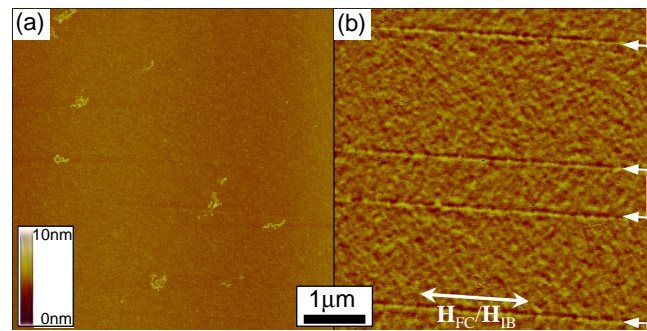


Figure 4.4: (a) AFM measurement on partly bombarded area with bombarded lines running from the left to the right side; (b) corresponding MFM measurement; The bombarded lines ( $H_{IB}\uparrow\downarrow H_{FC}$ ) are marked at the right side of the MFM image by red/white bars with arrows pointing in the direction of the continued edges of the bombarded lines.

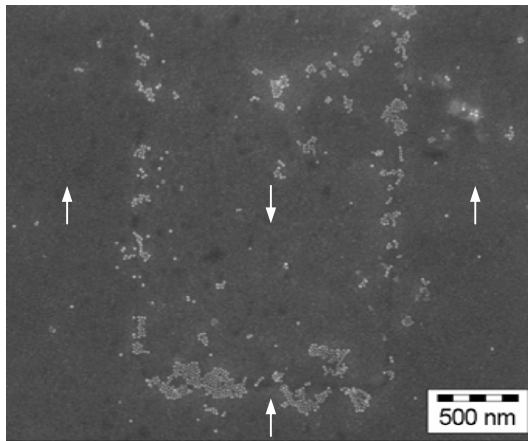


Figure 4.5: SEM image of magnetic nanoparticles on the sample after dipping the sample into the solution. The orientation of the remanence magnetization is indicated by the arrows. The boundaries of the bombarded line can be identified by the arrangement of nanoparticles.

iments the Bragg like scattering of the grating could clearly be attributed to the magnetic grating without any influence of a possible sample topography.

The result of dipping the sample into the Co-nanoparticle solution and removing it slowly can be seen in Fig. 4.5. The image depicts a part of the sample with one  $1.6\ \mu\text{m}$  wide bombarded line reaching into the image from the top and ending about 250 nm above the bottom of the image. Chains of clusters of nanoparticles can be seen at the edges of the bombarded area. This concentration of particles can be attributed to the strayfield of the Néel walls at the vertical sides of the magnetic line and the head to head orientation of the magnetic moments at the lower end of the line. The fact that some particles can be found, e.g., in the middle of the bombarded line can be explained by the short range of the strayfield. Particles which did not, e.g., due to Brownian motion get close to the edges of the bombarded line during the short time of the dipping can not be attracted by the strayfield (compare Fig. 4.9). Furthermore, clusters of particles might have been washed away from the edges during the dipping.

The experimental result is confirmed by numerical calculations carried out by

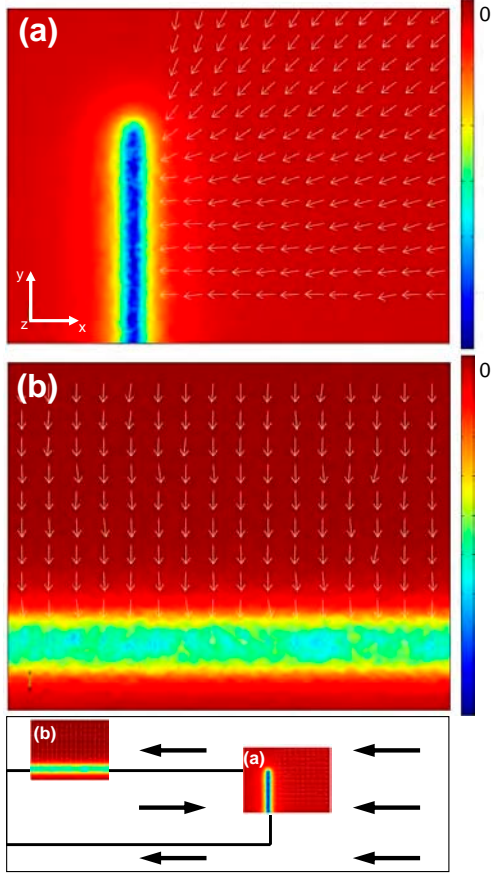


Figure 4.6: Simulation of the force acting on a point like magnetic nanoparticle in the strayfield of (a) the head to head magnetization configuration at the end of a bombarded line and (b) the Néel walls at the sides of the bombarded lines. The arrows in part (a) and (b) indicate the direction of the force parallel to the surface and the strength of the force in z direction perpendicular to the surface is illustrated by the color gradient. The scale is given in arbitrary units and is not comparable for both parts. Slight fluctuations can be attributed to numerical artifacts. The location of the simulated areas on the sample is shown in the sketch at the bottom. The black arrows in the sketch indicate the direction of the local remanence magnetization.

Alexander Weddemann using a finite element method employing the software Fem-Lab from Comsol AB.

Some results of this simulations of the force due to the strayfield given by

$$\vec{F} = \frac{\mu_0 m_s}{|\vec{H}|} (\vec{H} \vec{\nabla}) \vec{H} \quad (4.1)$$

and the resulting vector field described by

$$F_i \sim \frac{1}{|\vec{H}|} \left( \sum_j H_j \partial_j \right) H_i. \quad (4.2)$$

are shown in Fig. 4.6. The arrows in Fig. 4.6 (a) symbolize the local direction of the force in the x-y plane parallel to the surface are pointing towards the end of the bombarded line. The strength of the force in z-direction which is illustrated by the color gradient, is strongly growing with decreasing distance to the source of the strayfield. It is striking that a large field gradient can be observed only in a very small area. This limits the radius around the strayfield source from which the particles can be attracted.

An attracting vector field resulting in a smaller force is generated by the Néel walls at the sides of the bombarded line and can be seen in part (b). The color gradient used in part (b) is not directly comparable to the one used in part (a). A similar

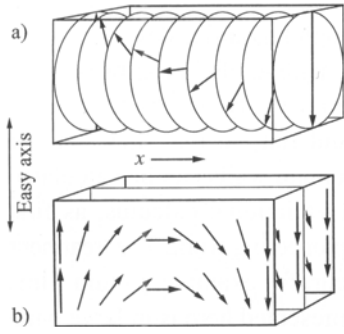


Figure 4.7: Change of the magnetization direction by  $180^\circ$  in (a) a Bloch wall and (b) a Néel wall. The easy axis and the arrow denoted as  $x$  span the plane of the FM layer. (from [174])

behavior has been found in simulations of Bloch walls. The differences of Bloch and Néel walls are illustrated in Fig. 4.7

In order to approximate a value for the force acting on a magnetic nanoparticle, simulations of a small area in the middle of the end of a bombarded line with the head to head orientation of the magnetization have been carried out. To calculate the force from this magnetic gradient field it is not possible to use an approximation of point like particles as one can not assume the force to be constant over the whole particle volume. Therefore, the force has been integrated over the particle volume for particles located directly on the surface with several distances between the center of the particle and the end of the bombarded line.

$$\vec{F} = \mu_0 M_S \int_{particle} \frac{\vec{H} \vec{\nabla}}{|\vec{H}|} \vec{H} dV \quad (4.3)$$

A detailed description of the calculations including, e.g., the boundary conditions can be found in Ref. [216].

The values of the force pulling the particles (diameter: 12.16 nm, saturation magnetization:  $m_s=1420$  kA/m) to the end of the line are in the range of  $10^{-11}$  N. The force resulting from the strayfield of a Néel wall and pulling a nanoparticle towards the Néel wall depends on the wall width and is roughly by a factor of 10 smaller than the forces calculated above. This result is in a good agreement with the experimental observation that less particles assemble at the sides of the lines than at the end in the not carbon capped areas.

A significant influence of topographic structures on the particle arrangement is unlikely, because in this case the number and size of particle clusters should be independent of whether the particles are located at the end or at the sides of the bombarded line.

Furthermore this influence can be ruled out by investigating the assembly of particles on top of a carbon layer across the magnetic grating which has been created during experiments with x rays. Figure 4.8 shows a partly carbon covered area of the magnetic grating. Again,  $1.6 \mu\text{m}$  wide bombarded lines reach into the image from the top. The end of the bombarded lines about  $7 \mu\text{m}$  from the bottom of the image is indicated by horizontal chains of clusters of nanoparticles. It is clearly visible that the nanoparticles are still preferentially located at the position of the stronger strayfield of the ends of the lines although eventually existing topographic structures

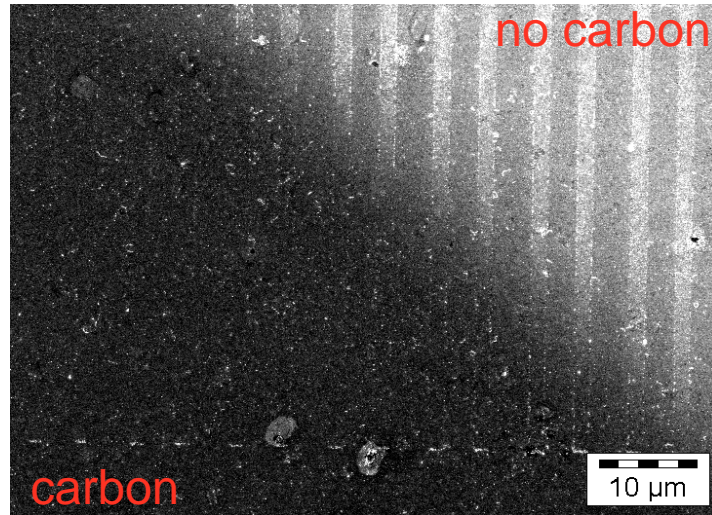


Figure 4.8: SEM image of magnetic nanoparticles after dipping the sample into the solution. The lower left part of the area shown here is covered with a carbon layer while the upper right part has no such capping. Small horizontal chains of nanoparticles about  $7\ \mu\text{m}$  from the bottom of the image indicate the lower boundaries of bombarded lines.

are covered by the carbon layer. A comparison of the particle density at the sides of the lines on top of the carbon (lower left area) and next to it (upper right area) shows that less particles assemble at the sides of the carbon covered lines. This can be explained by the fact that the nanoparticles on top of the carbon have a higher distance to the ferromagnetic layer and, therefore, sense a weaker strayfield.

In Fig. 4.9 the calculated force acting in plane and perpendicular to the plane on the 12 nm sized Co particles near the end of a bombarded line is shown in dependence of the distance between the center of the particle and the end of the bombarded line. The slight fluctuations in the slope are caused by the imperfect approximation of the spherical nanoparticles by finite elements. This graph shows that very small distances of a few nanometers are sufficient to reduce the force significantly. When

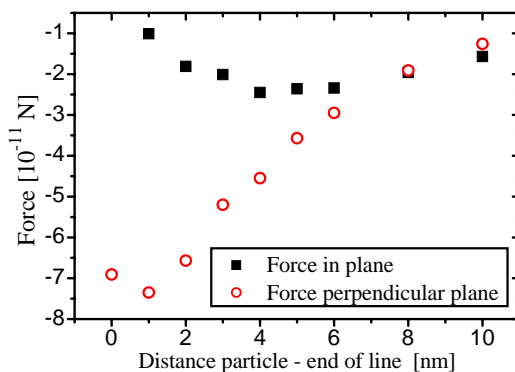


Figure 4.9: Force acting in plane and perpendicular to plane on a particle (diameter: 12.16 nm, saturation magnetization:  $m_s=1420\ \text{kA/m}$ ) in dependence of the distance between the center of the particle and the end of the bombarded line. The calculation has been carried out applying Eq. 4.3.

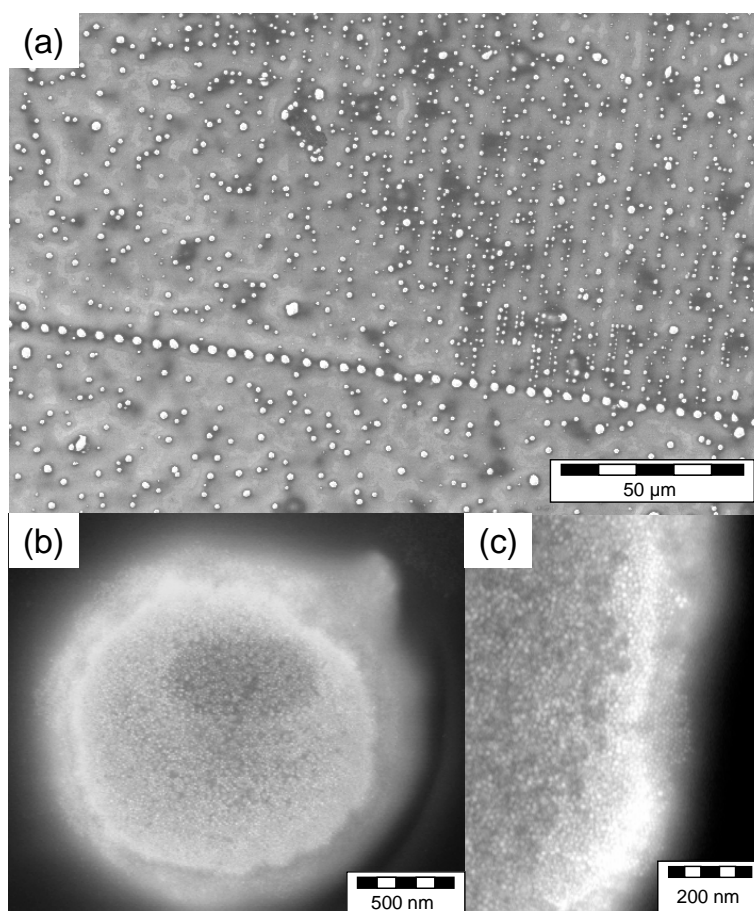


Figure 4.10: SEM images of Co nanocrystals after the slow evaporation of the solvent: (a) overview over the partly carbon covered part of the magnetic grating comparable to Fig. 4.8; (b) particle cluster build on the end of a bombarded line; (c) magnification of a particle cluster

the already by a factor 10 smaller force at the sides of the bombarded line is further reduced by the larger distance to the strayfield source on the carbon film it can be expected that less nanoparticles are attracted as it has been observed experimentally.

The results of another experiment where the particles got more time for the self-assembly is shown in Fig. 4.10. The sample has been placed inside about 0.5 ml of the solution until the solvent was evaporated. The part of the sample visible in Fig. 4.10 (a) is nearly the same as in Fig. 4.8. Hence, the lower left part of the area is covered with a carbon layer, again. The edges of the bombarded lines can be easily seen due to the big clusters of nanoparticles which appear as bright dots in the SEM image. The shape of the lines, which are not located below the carbon film, clearly can be seen due to a high number of smaller clusters of nanoparticles arranged in parallel lines starting at the large clusters at the end of the bombarded lines. These lines of clusters are missing in the carbon covered area, again showing that on this sample the strayfield of the Néel walls at the sides of the bombarded lines is not

strong enough to catch the particles when the minimum possible distance between particle and strayfield source is enlarged by an additional capping layer. The larger amount of particles assembled at the edges of the bombarded lines compared with the measurement on the sample after dipping can be explained by the longer time which allows more particles to order. The fact that the number of particles located at the end of the lines is much larger compared to the sides of the lines can be, again, attributed to the larger strayfields at this point. In Fig. 4.10 (b) and (c) a cluster located at the end of a line is shown in more detail.

This strong time dependence of the particle density on the sample opens opportunities to choose the number of particles on a special point of a sample like, e.g., a sensor by using a suitable solvent and ordering time, considering the particle density in the solution and the sample parameters like the strength of the strayfield.

#### 4.2.4 Summary

The assembly of Co nanocrystallites with a diameter of 12 nm and 1  $\mu\text{m}$  large particles under the influence of the strayfield produced by a magnetically patterned 3 nm thick CoFe layer without a topographic structure has been investigated. It has been shown that the strayfield at the magnetic structures with a head to head orientation of the local magnetization is sufficient to induce a controlled accumulation of magnetic nanoparticles at these places. The force due to the strayfield of Néel walls without head to head orientation of the magnetization has been calculated to be smaller by a factor of about 10 and has been just strong enough to attract some nanocrystals on the tested sample without additional capping layers.

The way of bringing the particle solution onto the magnetically patterned sample has turned out to be of great importance for a successful generation of a particle assembly according to the strayfields.

Consequently, the application of this technique, e.g., for particle attracting sensors or for a targeted manipulation of the self assembling process of magnetic nanoparticles seems possible.



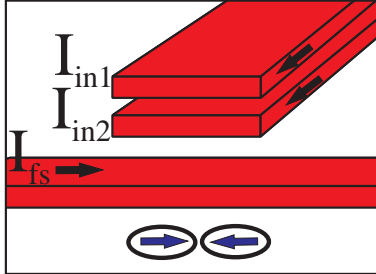


Figure 4.11: Setup for a reconfigurable magnetic logic consisting of two elliptical MTJs with opposite direction of EB (blue arrows indicate the direction of the magnetization of the pinned reference layers due to the unidirectional anisotropy).  $I_{in}$ : current resulting in magnetic field acting as logic input,  $I_{fs}$ : current resulting in magnetic field responsible for selection of logic function.

### 4.3 Reconfigurable Magnetic Logic

In the frequently used logic gates based on transistors different logic functions have to be simulated by the use of a high number of logic gates that are capable of performing only one fixed function. A promising approach to overcome this obstacle is a reconfigurable logic based on small arrays of magnetic tunnel junctions (MTJ). This has the additional advantage of a nonvolatile output as the technology is the same as in a magnetic random access memory (MRAM) [6]. One example of a TMR based configurable logic consisting of four MTJs per logic unit has been described in Ref. [221]. That design can be used for all basic logic functions except XOR. Here, an approach utilizing the ion bombardment induced patterning of the reference layer is proposed where the same logic unit consisting of only two magnetic tunnel junctions can be used for the AND, OR, NAND, NOR and XOR (XNOR) functions. On the following pages first the approach is described theoretically, followed by a presentation of a basic experimental proof of principle.

#### 4.3.1 Theoretical proposal

The proposed setup for a reconfigurable magnetic logic unit is shown in Fig. 4.11. The main part of this logic unit are two MTJs with an opposite orientation of the unidirectional anisotropy induced by the EB interaction. This results in an oppositely oriented magnetization of the two reference layers for the relatively small external magnetic fields which are used while measuring minor loops. To realize this approach, first the direction of the EB can be set homogeneously on the hole sample during the sputter deposition process by field growth (FG) or by an additional field cooling (FC) step after deposition. Then the direction of the exchange bias at the position of one of the MTJs can be rotated by  $180^\circ$  by IBMP. Now, one can get two elliptical MTJs with an opposite direction of the magnetization of the reference layer in remanence (indicated by arrows in Fig. 4.11) with the usual lithography and etching process. Orthogonal leads make it possible to apply magnetic fields parallel to the long as well as the short axis of the MTJ. The field strength should be identical at both MTJs. The logic input can be given by the sign of the current

<sup>4</sup>Parts of this chapter have been published in [220]. A patent application has been filed for the presented magnetic logic.

$I_{in1}$  and  $I_{in2}$  through the vertical leads in Fig. 4.11(a). Here positive (negative) currents represent the logic input 1 (0). The resulting magnetic field is oriented in the direction of the long axis of the MTJs. The superposition of the two magnetic fields results in a negative field for (0,0), zero field for (1,0) and (0,1) and a positive field for (1,1) (compare Fig. 4.12).

An additional possibility is to place pinned hard-magnetic FM lines on top of the  $I_{in}$ -leads. The thickness of the FM and the direction of the pinning should be chosen to get a strayfield with the same amplitude but the opposite direction of the magnetic field produced by  $I_{in}$  flowing through one input lead. This results in a magnetic field corresponding to (0,0) in Fig. 4.12 for no current through both leads, zero field for positive current through one lead ((1,0), (0,1)) and a positive field for positive currents through both leads (1,1). This has the advantage that no bipolar currents are needed at all. The third possibility for this kind of magnetic logic is the definition of  $H_{in}=0$ , small positive  $H_{in}$  and bigger positive  $H_{in}$  for (0,0), (0,1)/(1,0) and (1,1) as shown in Fig. 4.13. In this case no negative currents except for the initialization step and no additional magnetic layers are needed. The following explanations use the first approach, but they are valid for all three of them.

The output of the magnetic logic can be deduced from the resistivity of the two MTJs. One possibility is a parallel or serial connection of the two MTJs (high conductivity/low resistance: 1, low conductivity/high resistance: 0). This setup is used for the following explanations. Alternatively a measurement of the difference in the conductivity of the two MTJs (no resistance difference: 0, high resistance difference: 1) can be used to obtain the logical output. The *function select* current  $I_{fs}$  and the corresponding magnetic field  $H_{fs}$  perpendicular to the long axis of the MTJs is responsible for the selection of the logic function.

Figure 4.12 shows asteroids indicating the switching field of the soft magnetic layer measured in a minor loop for the two MTJs. The asteroids are shifted in opposite directions with respect to  $H_{in}=0$ . This shift can be realized by a magnetostatic interaction at the barrier (Neél- / orange peel coupling) in the case of large MTJs with several  $\mu\text{m}$  size and a significant correlated roughness of the two surfaces between the barrier and the two FM electrodes. In the case of smaller MTJs the shift will be dominated by the strayfield coupling between the two FM layers which produces an increasing shift for a decreasing size of the junction [222]. The size of the strayfield coupling can be tuned by adjusting the net magnetic moment of an artificial ferrimagnet (AFi) in the reference layer. The switching fields for the function select magnetic field  $H_{fs}$  indicated by the red horizontal line "1" in Fig. 4.12 (a) are marked with green dashed (blue dotted) lines for the case that the sample was initially saturated with a positive (negative)  $H_{in}$ . In the top area of Fig. 4.12 (a) the corresponding resistance of the single MTJs in dependence of  $H_{in}$  is symbolized by "+" and "-" for the high and low resistance state, respectively. When both MTJs have a low resistance the logic output of the whole setup is "low" while one or two MTJs with a high resistance represent the output "high resistance". A comparison of the effective fields  $H_{(i,j)}$  for the logic input (red solid vertical lines in Fig. 4.12 (a) with the total resistance shows that one gets a low resistance and high current corresponding to the output 1 for (1,0) and (0,1) and a high resistance or low current corresponding to the output 0 for (1,1) and (0,0). This corresponds to the XOR function.

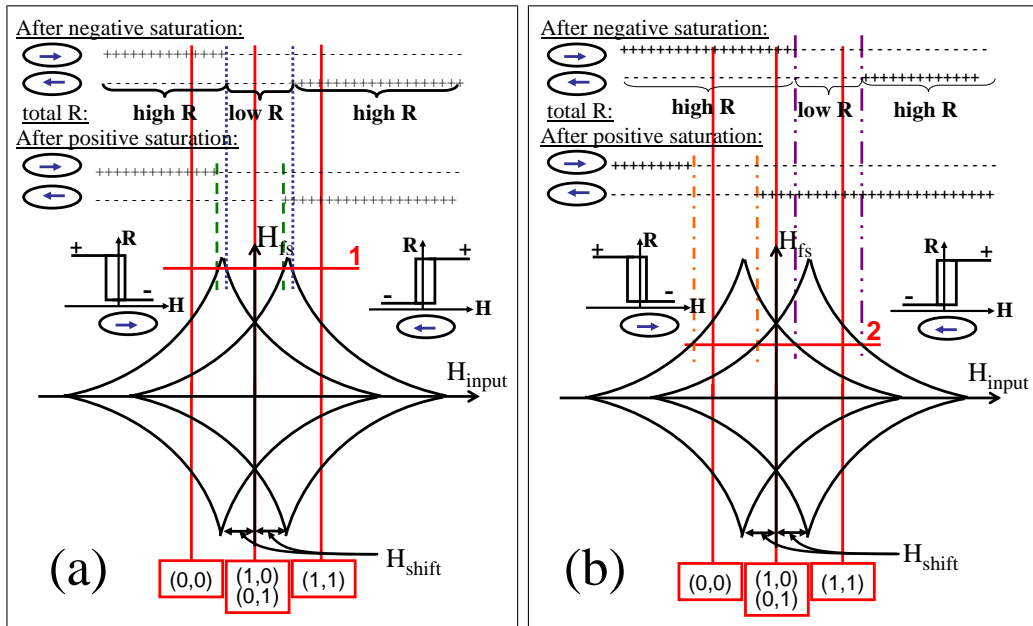


Figure 4.12: Lower part: Asteroids indicating switching fields of the soft magnetic layer measured in minor loops (see schematic sketches above the asteroids) for the two MTJs (blue arrows: magnetization direction of reference layer), solid vertical red lines: values of  $H_{in}$  corresponding to logic input (i,j); Upper part of (a): Resistance of single MTJs and total resistance for serial or parallel wiring of both MTJs in dependence of  $H_{in}$  for  $H_{fs}$  corresponding to horizontal red line "1". The vertical green dashed (blue dotted) lines indicate switching fields for initial positive (negative) saturation. + (-) indicates a high (low) resistance. Logic function: XOR; Upper part of (b): Resistance of single MTJs with function select magnetic field indicated by horizontal red line "2". Orange dash-dotted (purple dash-dot-dotted) line: switching fields for initial positive (negative) saturation. Logic functions: AND (neg. saturation) and NOR (pos. saturation)

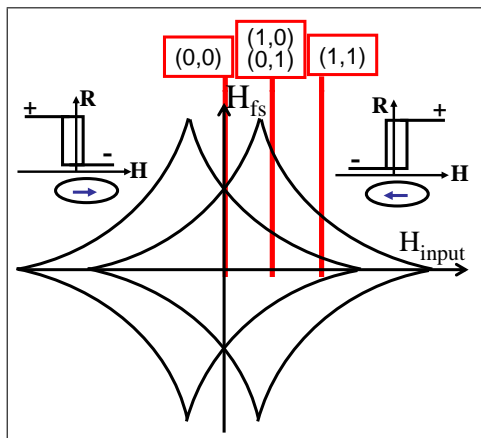


Figure 4.13: Asteroids indicating switching fields of the soft magnetic layer with definition of logic input with only positive values of  $H_{in}$ . This definition enables use of all basic logic functions without bipolar currents except for the initialization step and without additional ferromagnetic layers for strayfield generation.

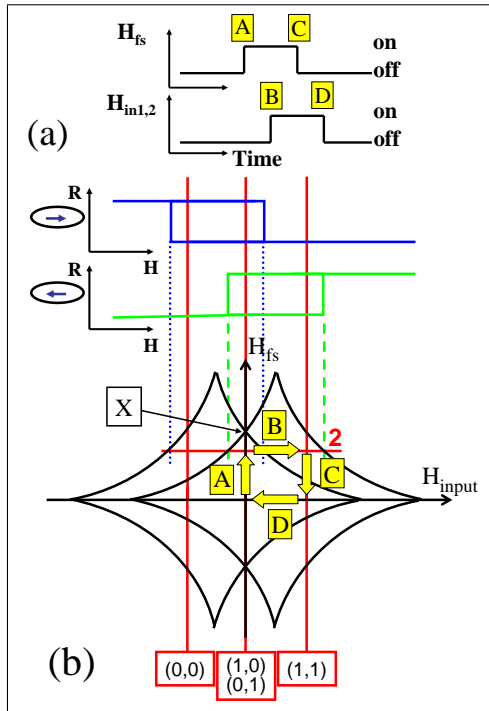


Figure 4.14: (a) Order of changes of magnetic fields  $H_{fs}$  and  $H_{in}$  which can be used for all values of  $H_{fs}$  to obtain a non volatile output.  $H_{in}$  = “on” symbolizes the magnetic field belonging to the actual logic input which can be positive, negative or zero. (b) Example of the magnetic fields switched in as described in (a) with  $H_{fs}$  indicated by the line “2” and logic input (1,1). (As for all sketches in this chapter arbitrary units have been used for all axis.)

In order to obtain a non volatile output the current pulses inducing the magnetic fields  $H_{fs}$  and  $H_{in}$  should be timed in a way that first  $H_{fs}$  is switched on, choosing the logic function (A in Fig. 4.14). Now, one has not to deal with a high number of possible minor loops characterized by the switching field asteroids any more. The two minor loops of the two MTJs belonging to the chosen value of  $H_{fs}$  which are relevant now, are shown on the top of Fig. 4.14 (b). Then the currents  $I_{in1}$  and  $I_{in2}$  through the two leads perpendicular to the long axis of the MTJs are switched on according to the logic input [e.g. (1,1) in Fig. 4.14, (B)]. During this step the magnetization of the free magnetic layers of the two MTJs switches to the configuration which determines the logic output. Therefore, this configuration has to be conserved. Then  $H_{fs}$  is switched off again (C) before finally  $H_{in}$  is switched off as well (D).

For values of  $H_{fs}$  below the point where the asteroids cross the  $H_{fs}$  axis [X in Fig. 4.14 (b)] as, e.g., the one used in Fig. 4.14 another order of the switching of the magnetic fields is possible, too. When high values of  $H_{fs}$  above X in Fig. 4.14 (b) are used, the switching order described above should be used because otherwise the magnetization of one MTJ might switch back and the output is volatile.

For the value “1” of  $H_{fs}$  as shown in Fig. 4.12 (a) the function is independent of the initial state. For other values of  $H_{fs}$  different logic functions can be observed in dependence of the initial state. The upper part of Fig. 4.12 (b), e.g., shows the resistances for  $H_{fs}$  = “2”. Here, a negative initial saturation results in the AND function while for a positive initial saturation one gets the NOR function. To use these values of  $H_{fs}$  an initialization step saturating the free layers of both MTJs in one direction is necessary before the logic function can be used to make sure to start with a defined state of the system. In the case of no pinned FM layer on the leads this can be done by, e.g., simultaneously setting the input to (0,0) and  $H_{fs}$  to the

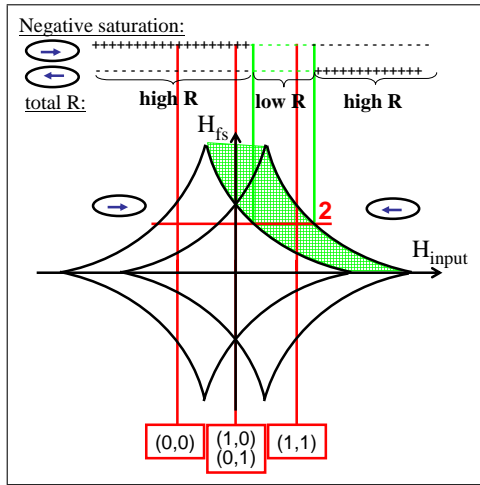


Figure 4.15: Shift of low total resistance region by variation of  $H_{fs}$  after saturation with a negative magnetic field.

value indicated by "1" in Fig. 4.12 or alternatively by using a larger current  $I_{in1}$  and  $I_{in2}$ . With a pinned FM layer on top of the lines in one direction only a pulse of  $H_{fs}$  is sufficient for the initialization.

By changing  $H_{fs}$  and, therefore, shifting the low total resistance region with respect to  $H_{in}$  (compare green region in Fig. 4.15), several other logic functions can be obtained. Table 4.1 gives a list of the possibilities. On the left side of Tab. 4.1 the total resistance is symbolized by high (low) circles for high (low) resistance equivalent to Fig. 4.12. Depending on the selected technique for measuring the output signal different logic functions result from this  $R_{total}(H_{in})$  distribution (right side of Table 4.1). The  $R_{total}$ -distribution on the last line is not obtainable with the same MTJs as the XOR/XNOR functions because a wide low resistance area is necessary, preventing that only (0,1)/(1,0) can be in a low resistance state. This corresponds to a higher shift of the asteroids and, therefore, a different layer stack.

During all explanations in the last paragraphs the described system was consisting of magnetic tunnel junctions with a manipulation of the EB pinning of the reference electrode by ion bombardment in a magnetic field. Furthermore the experimental proof of principle shown in chapter 4.3.2 will be demonstrated using this kind of setup. But in principle other realization of this kind of magnetic logic are possible, too. E.g., other magnetoresistance effects as, e.g., GMR or any other effect which results in a change of the resistance of the system when the relative orientation of two ferromagnetic layers is varied can be used instead of the tunnel magneto resistance (TMR) effect. But due to high effect amplitudes of up to 472% at room temperature [205] shown in the last time and the fact that the technically similar magnetic random access memory (MRAM) with magnetic tunnel junctions is already commercially available [10], at the moment the TMR effect seems to be the best candidate for a realization of a magnetic logic.

In principle it might even be possible to find other properties of the sample which are changed when the relative orientation of the magnetization is altered and use them to determine the logic output instead of the resistance.

Furthermore, other techniques to locally manipulate the direction of the EB as, e.g., local heating with a laser, a deposition of the two MTJs one after the other

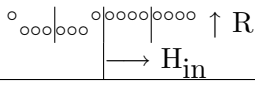
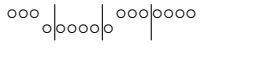
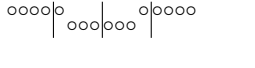
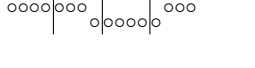
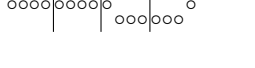

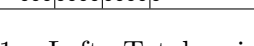
Total resistance	In	Parallel/serial		Diff. signal	
		Out	Logic	Out	Logic
	(0,0) (0,1)/(1,0) (1,1)	1 0 0	NOR	0 1 1	OR
	(0,0) (0,1)/(1,0) (1,1)	1 1 0	NAND	0 0 1	AND
	(0,0) (0,1)/(1,0) (1,1)	0 1 0	XOR	1 0 1	XNOR
	(0,0) (0,1)/(1,0) (1,1)	0 1 1	OR	1 0 0	NOR
	(0,0) (0,1)/(1,0) (1,1)	0 0 1	AND	1 1 0	NAND
		always 0		always 1	
		(always 1)		(always 0)	

Table 4.1: Left: Total resistance in dependence of  $H_{in}$  (increasing positive  $H_{in}$  to right) for varied  $H_{fs}$  (decreasing  $H_{fs}$  from top to bottom) and accordingly shifted area of low resistance (compare Fig. 4.15). High (low) circles represent high (low) total resistance due to a different (twice low) resistance of the single MTJs. The vertical lines represent the magnetic fields  $H_{in}$  corresponding to the logic input (from left to right: (0,0), (0,1)/(1,0) and (1,1)). Right: Logic functions resulting from the shift of the low resistance area shown on the left side for serial/parallel wiring and difference measurement. (Note the different width of low resistance area on last line.)

in oppositely oriented magnetic fields or any other technique capable of inducing a local variation of the unidirectional anisotropy of one ferromagnetic layer might be used instead of ion bombardment in a magnetic field. But at the moment IB seems to be the most suitable approach for a local manipulation on a whole wafer in the industrial production because, e.g., it is difficult to parallelize the EB manipulation by laser for large areas as it can be done by bombarding the whole wafer through a resist mask. The application of a separated field growth of the MTJs increases the number of necessary sputter and lithography steps and, therefore, does not appear very cost effective.

One can even think of replacing the EB interaction by something else that is capable of keeping the direction of the magnetization of the reference electrode fixed in the range of magnetic fields which can occur during the application in a magnetic logic and that can be manipulated in some way to obtain locally an opposite orientation of this magnetization. One possible example for this is the use of an additional ferromagnetic layer with a very strong uniaxial anisotropy and a very high coercive field where one can be sure that the magnetization will not be altered by all magnetic fields that it might be subjected to in the magnetic logic. When this magnetic layer is coupled to the reference layer of the, e.g., MTJ by the antiferromagnetic interlayer exchange coupling via, e.g., a Ruthenium interlayer, then the direction of the magnetization of the reference layer is fixed for all external magnetic fields that are not large enough to change the direction of the magnetization of the magnetically hard additional layer or to overcome the interlayer exchange coupling. The relative orientation of the magnetizations of the two FM layers due to the interlayer exchange coupling can be changed locally from antiparallel to parallel by ion bombardment (compare chapter 3.3). That means that the direction of the reference layer adjacent to the barrier is fixed regarding external magnetic fields but can be locally turned by  $180^\circ$ . Therefore, all requirements of the proposed kind of magnetic logic are fulfilled. In comparison with the application of the EB interaction this technique might be less favorable, anyway, because at least with the frequently used Ru interlayer a larger ion dose is necessary to change the antiferromagnetic interlayer exchange coupling to a ferromagnetic one than to change the direction of the EB (compare chapter 3.3). This higher ion dose can be a problem when the reference electrode in a MTJ with a for this purpose unfavorable design has to be manipulated after the deposition of the full stack. In this case a higher ion dose can result in a larger damage at the sensible barrier and might significantly disturb the correct functioning of the MTJ. Therefore, for this alternative approach it might be necessary to carry out the ion bombardment before the barrier is deposited. This might be an option for the manipulation of the EB interaction,<sup>5</sup> as well, but the effect of this approach on the growth of the following layers has not been investigated in detail until now.

The generation of magnetic fields responsible for the logic input as well as the selection of the logic function and the generation of a defined initial state will most likely be realized by currents through leads on the chip as this leads can be produced with the well established techniques used today for, e.g., the production of computer chips. But in principle the magnetic fields might as well be produced, e.g.,

---

<sup>5</sup>Compare discussion on page 181.

by the magnetic strayfield of a tip of a magnetic force microscope. Here, a parallel application of a large number of tips like it can be seen in the IBM Millipede project [223, 224] for data storage by an array of atomic force microscope like tips might be used. Alternatively, other new techniques developed in the field of micro electromechanical systems (MEMS) might be used to vary the effective magnetic field at the position of the logic elements.

To summarize, it can be said that two ferromagnetic layers, one of them fixed with a locally varying pinning direction and one free which can follow an external magnetic field are necessary. The relative orientation of this ferromagnetic layers has to be detected in some way as, e.g., by magnetoresistive effects. At the present state of the technology the manipulation of the exchange bias coupling by an ion bombardment in the presence of a magnetic field appears to be the best method to fulfill these requirements.

### 4.3.2 Experimental proof of principle

The aim of the following proof of principle is to show that the theoretically described concept of this novel magnetic logic can be transferred to the real world. It will be shown that it can be used even with existing samples which have been produced for other purposes and, therefore, are not optimized in any way for the requirements of this kind of logic or any magnetic logic in general. For an industrial application one would try to apply the knowledge about the details how to produce a good MTJ for, e.g., the technically similar MRAM technology like the choice of the shape of the MTJ, good buffer layers,... which has been gathered by many groups in the past and which finally led to the development of a commercially available product [10]. But this kind of optimization is not necessary for the purpose of this work.

For the proof of principle a sample described in Ref. [167] (Stack A) has been used. The layer stack is Cu 25 nm / Mn<sub>83</sub>Ir<sub>17</sub> 12 nm / Co<sub>70</sub>Fe<sub>30</sub> 3 nm / Al 1.3 nm + plasma oxidation / Ni<sub>80</sub>Fe<sub>20</sub> 4 nm / Ta 3 nm / Cu 47 nm / Au 26 nm. It has been annealed at 275°C for 1 hour in a magnetic field  $H_{FC}=1000$  Oe. A part of this sample has been bombarded with He ions ( $E_{IB}=10$  keV,  $3 \times 10^{15}$  ions/cm<sup>2</sup>) in a magnetic field  $\mathbf{H}_{IB}$  perpendicular to  $\mathbf{H}_{FC}$  and then annealed for 1 hour at 275°C without an external magnetic field. To obtain the antiparallel orientation of the magnetization of the reference layers a not bombarded part of the sample has been removed and turned 90°. On the not bombarded part new MTJs have been structured. Then the lower conduction lines have been connected. One bombarded and one not bombarded square MTJ (size: 100  $\mu\text{m} \times 100 \mu\text{m}$ ) have been contacted by Au wires (see Fig. 4.16). Figure 4.17 shows minor loops (10 mV bias voltage) measured at one only field cooled MTJ (TMR=48.5% ,  $R_A^{\min}=3.6 \text{ M}\Omega\mu\text{m}^2$ ), at one field cooled and additionally bombarded MTJ (TMR=35.6% ,  $R_A^{\min}=6.8 \text{ M}\Omega\mu\text{m}^2$ ) and at a serial wiring of this two MTJs ( $R_A^{\min}=10.5 \text{ M}\Omega\mu\text{m}^2$ ). It can be seen that the switching of the not bombarded MTJ (at positive values of  $H_{in}$ ) results in a 27 % smaller change of the resistance of the MTJ chain than the switching of the bombarded MTJ although its TMR value is 36% higher. This is a result of the higher resistance and, therefore, higher absolute change of resistance of the bombarded MTJ. By measuring minor loops of the two connected MTJs for several values of  $H_{fs}$  (Fig. 4.18) the switching



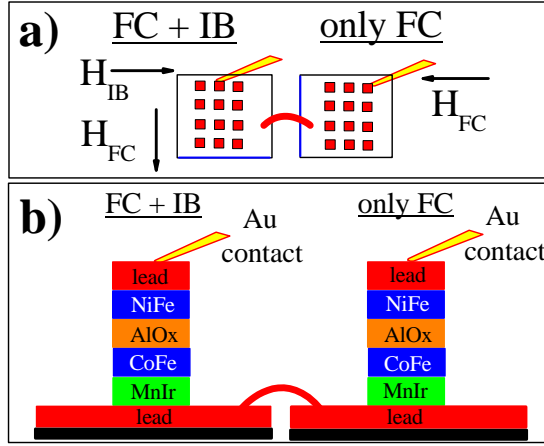


Figure 4.16: Sample setup [top view (a) and side view (b)]: sample divided into two parts [fractured edge indicated by blue line in (a)], one part rotated 90°, lower conduction lines connected, measurement of resistance of serial wiring of both MTJs.

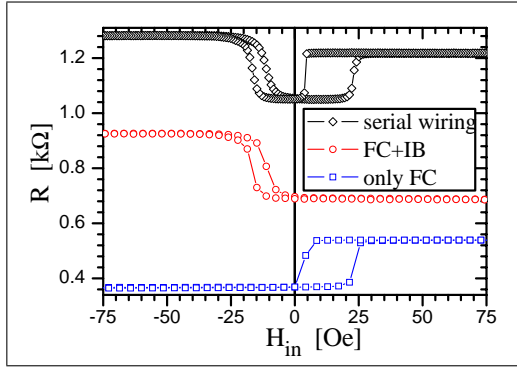


Figure 4.17: Minor loops measured at the single bombarded /not bombarded MTJs (both with  $100\mu\text{m} \times 100\mu\text{m}$  size) and at a MTJ chain of this MTJs as shown in Fig. 4.16 ( $H_{fs}=0$ ). The small coercivity and rounded shape of the hysteresis loop of the bombarded element is due to a slight tilt of the EB axis relative to the external field.

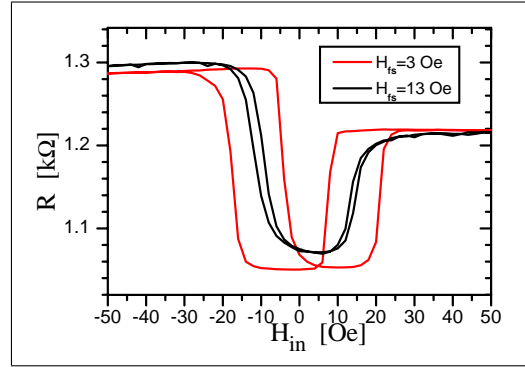


Figure 4.18: Minor loops of the same serial wired bombarded and not bombarded MTJs as used for the measurements shown in Fig. 4.17 with  $H_{fs}=3$  Oe and  $H_{fs}=13$  Oe.

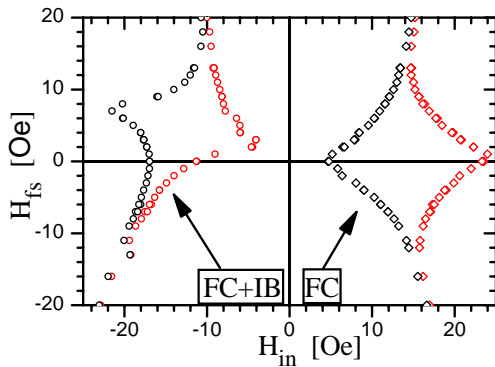


Figure 4.19: Switching field asteroids for bombarded (neg.  $H_{in}$ ,  $H_{in}$  was not perfectly aligned parallel to the EB direction during this measurements resulting in a tilt of asteroid) and not bombarded (pos.  $H_{in}$ ) MTJs deduced from double minor loops as shown in Fig. 4.18. Red (black) symbols represent a switching field with increasing (decreasing)  $H_{in}$ .

field asteroids of both MTJs can be obtained (Fig. 4.19). It is striking that the coercivity of the free layer is smaller than the shift of the asteroids. Therefore, it is not possible to use the NOR and AND function with this two MTJs (serial wiring). Furthermore the logic output is volatile because this MTJs have only one resistance state at remanence. Nevertheless the principle of this logic can be demonstrated (Fig. 4.20). Therefore,  $H_{in}$  and  $H_{fs}$  have been simulated by Helmholtz coils [(0,0): -13 Oe, (0,1)/(1,0): 0 Oe, (1,1): 17 Oe] while the resistance of the serial chain of MTJs is measured. Fig. 4.20 (a) shows measurements for  $H_{fs}=3$  Oe with initialization at positive  $H_{in}$ . First, after 5 s  $H_{fs}$  is set to 3 Oe. Then the sample is saturated at 60 Oe (15 s) before  $H_{in}$  is set to the value corresponding to the logic input (25-30 s). Now the logic output is visible. After 45 s  $H_{fs}$  is switched off and finally after 55 s  $H_{in}$  is switched off. This kind of measurement has been done for all three values of  $H_{in}$  corresponding to the logic inputs (0,0), (0,1)/1,0) and (1,1). The time dependence of the magnetic fields for the input (1,1) is sketched in the upper parts of all parts of Fig. 4.20. The time between the switching steps and the long and varying duration of the change of the magnetic fields and the corresponding change of the resistance are no intrinsic property of this kind of magnetic logic but result from the applied manual control mechanism of the current through the Helmholtz coils. The result of the measurements depicted in Fig 4.20 (a) is a high resistance (output 0) for (1,1) and low resistance (output 1) for (0,0)/(0,1) and (1,0). This represents the NAND function. In the same way the OR and XOR functions have been measured for  $H_{fs}=3$  Oe after initialization with a negative magnetic field [Fig. 4.20 (b)] and  $H_{fs}=13$  Oe after initialization with a positive magnetic field [Fig. 4.20 (c)]. A resistance above the legend indicates logic output 0 while a resistance below the legend is identical with a logic output 1. The different resistance of the measurement with logic input (1,1) in Fig. 4.20 (b) compared to the other measurements in this graph is due to a not perfect contact between the gold tips and the MTJs which makes this measurement sensible to mechanical influences of the environment. The fact that the output resistance (at about 35 s-45 s in the measurements) for the logic input (0,0) and (1,1) in Fig. 4.20 (c) is significantly different can be explained by the different TMR value / resistivity of the two utilized MTJs (compare Fig. 4.17 and 4.18). This clearly emphasizes the importance of an equal absolute change of the resistance for both MTJs in the case of a serial wiring. Additionally, the chosen values of  $H_{in}$  for the logic input do not perfectly fit to the chosen value of  $H_{fs}$  for this two MTJs. Nevertheless, the XOR function clearly can be identified.

To obtain all logic functions and a non volatile output small elliptic MTJs with a strayfield coupling tuned by the choice of the net moment of an AFi should be used (see, e.g., Ref. [222]) to get overlapping asteroids with two resistance states at remanence as shown in Fig. 4.12. Differences in TMR amplitude or resistance between bombarded and not bombarded MTJs can be compensated for serial wiring by an adjustment of the element size to obtain an equal change of resistance independent on the actually switching MTJ [compare Fig. 4.20 (c)]. A disadvantage of the resistance measurement of serial connected MTJs is the decreased relative change of the magnetoresistance of both MTJs compared with every single MTJ (see Fig. 4.17). In contrast to this, the full TMR values could be observed for the measurement of the resistance difference. But in this case the compensation of different resistances of bombarded and not bombarded MTJs by a variation of the element size is not

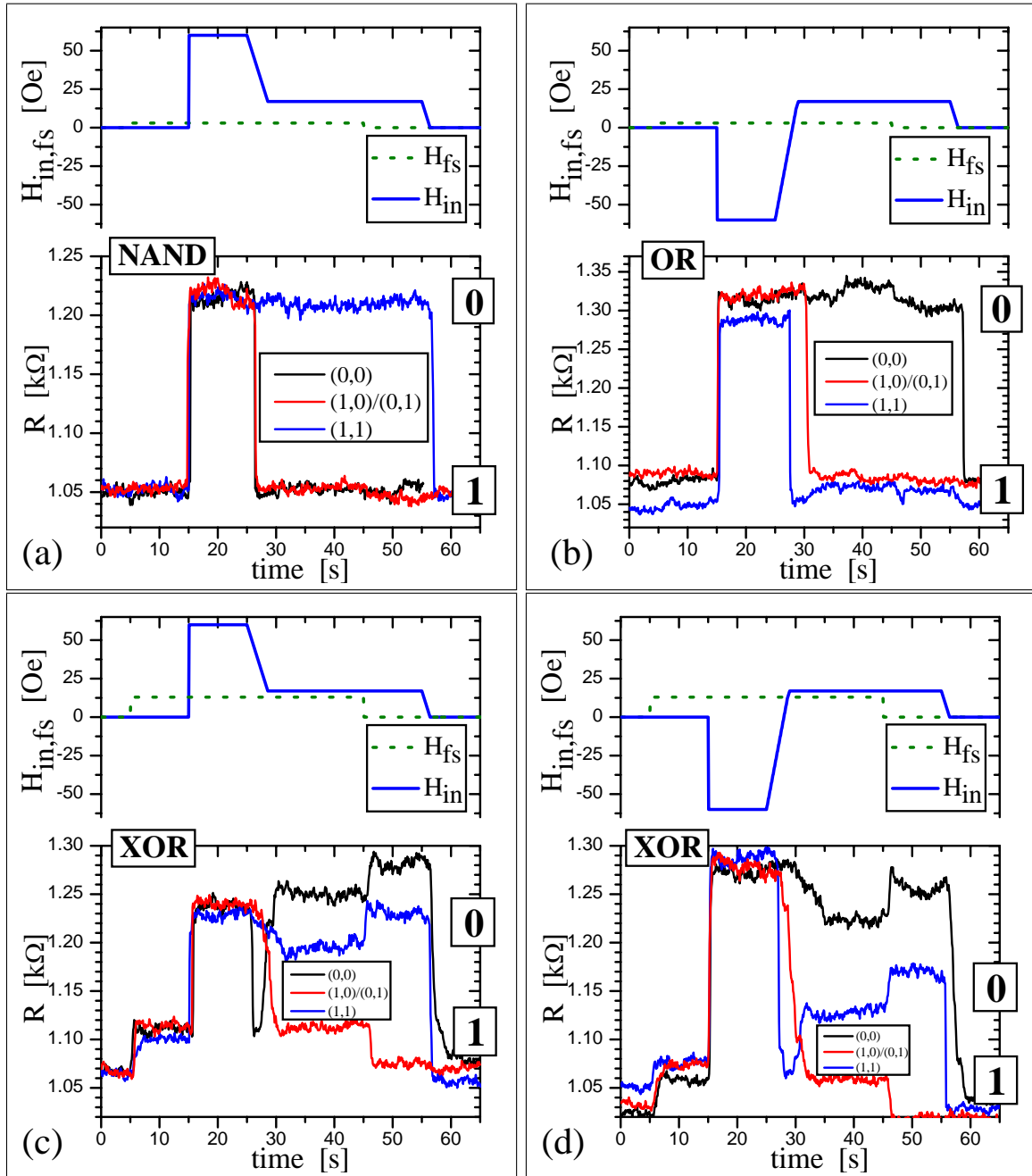


Figure 4.20: Experimental proof of principle for magnetic logic with (a)  $H_{fs}=3$  Oe, saturation with positive magnetic field, (b)  $H_{fs}=3$  Oe, saturation with negative magnetic field, (c)  $H_{fs}=13$  Oe, saturation with positive magnetic field, (d)  $H_{fs}=13$  Oe, saturation with negative magnetic field: upper part shows  $H_{fs}$  and exemplary  $H_{in}=17$  Oe in dependence of time, lower part shows resistance of one bombarded and one not bombarded MTJ with a serial wiring as shown in Fig. 4.16 for (0,0):  $H_{in}=-13$  Oe, (0,1)/(1,0):  $H_{in}=0$  Oe and (1,1):  $H_{in}=17$  Oe.  $H_{in}$  and  $H_{fs}$  have been applied by external Helmholtz coils.

possible. Therefore, the equality of all MTJs has to be guaranteed in this case by a good choice of ion dose and energy during IB, preferably the use of a stack with the pinned FM layer located above the barrier to minimize defect production at the barrier and a postannealing step to remove possible defects.

In summary, it has been shown in this chapter, that it is possible to utilize the IBMP to create a reconfigurable magnetic logic consisting of only two MTJs which is able to carry out all basic logic functions.

## Chapter 5

# Summary

In this thesis the applicability and applications of a patterning of the exchange bias coupling by ion bombardment in the presence of a magnetic field has been investigated. Special emphasis has been laid on the combination of this method with magnetic tunnel junctions.

The possibilities of the magnetic patterning have been demonstrated by a test of a magnetic grating for soft x-rays (chapter 3.1). It has been shown that it is possible to obtain an interference pattern which can be switched on and off by changing the external magnetic field as a kind of magnetic switch for x-rays.

The goal of the following test of the applicability of the ion bombardment induced magnetic patterning was to answer the question, whether the ion bombardment induced changes of the system might decrease the thermal stability and, therefore, prohibit applications where high temperatures can occur (chapter 3.2). Furthermore, a decreased temperature stability could be problematic for the production process. But the experiments did not show a hint for a reduction of the thermal stability by the ion bombardment. Furthermore, it was found that the magnetization of smaller elliptic topographic structures was stable up to temperatures far above their blocking temperature.

The next question which had to be answered resulted from observations reported in the literature that the ion bombardment can destroy an antiferromagnetic interlayer exchange coupling between two ferromagnetic layers. As this coupling is frequently used to enable a successful shrinking of magnetic tunnel junctions and its application is furthermore desired in a new type of magnetic logic developed in this thesis, it had to be tested whether this coupling survives the ion doses necessary to manipulate the exchange bias direction. For ferromagnetic layers separated by the frequently used ruthenium interlayer, it has been shown that the manipulation of an exchange bias coupling is possible without a destruction of the antiferromagnetic interlayer coupling. A system with a copper interlayer turned out to be more sensible to the side effects of the ion bombardment.

But the most important question one has to answer about the applicability of the ion bombardment induced patterning in magnetic tunnel junctions is the effect of the ion bombardment on the transport properties of the tunnel junctions. In my diploma thesis it has been shown that the patterning in magnetic tunnel junctions with alumina barrier is in principle possible [66], but the tunnel magnetoresistance

amplitude had suffered from the ion bombardment. A first test for the approach to repair this damage partly by an additional heating step without an external magnetic field has also been reported there. Starting from this point, the parameters of the additional heating step have been improved and it has been found that with a good choice of the ion dose and the annealing parameters, the reduction of the tunnel magnetoresistance amplitude can be totally reversed. Therefore, it is possible to turn the direction of the exchange bias coupling without decreasing the tunnel magnetoresistance amplitude.

These experiments have been carried out with magnetic tunnel junctions with an alumina barrier, which was the state of the art barrier material during the first half of this work. In the last time, reports about higher tunnel magnetoresistance amplitudes found at samples with an MgO barrier have been published. Therefore, also samples with this barrier material have been investigated.

Here, a larger decrease of the tunnel magnetoresistance amplitude has been observed, which could not totally be reversed by an additional heating step. Therefore, adjustments of the sample stack and the ion bombardment parameters have been investigated by simulations in order to find a system which reduces the side effects of the ion bombardment for this more sensible type of magnetic tunnel junctions. The main suggestions obtained from this are to place the pinned ferromagnetic layer on top of the barrier and use relatively low ion energies. These suggestions have also been tested experimentally.

Furthermore, in these samples other improvements have been implemented. One is a ruthenium based seed layer which significantly reduces the unfavorable shift of the hysteresis loop of the not pinned ferromagnetic layer. Additionally, an artificial ferrimagnet which allows to tune the magnetic moment of the electrode and, therefore, the strayfield coupling has been used. Another advantage of this artificial ferrimagnet is the reduced manganese diffusion which allows higher annealing temperatures. With this layer stack a tunnel magnetoresistance amplitude of up to 180% has been obtained. This is the highest amplitude obtained so far with the experimental tools available in our working group.

The ion bombardment of this kind of magnetic tunnel junctions with ion doses necessary to turn the exchange bias direction also results in a severe decrease of the tunnel magnetoresistance. A test of an additional annealing step resulted for magnetic tunnel junctions where the exchange bias direction has been turned by  $180^\circ$  in an increased tunnel magnetoresistance amplitude of about 70%. This value is much smaller than the value measured before the ion bombardment, but it is as large as the value obtained at the original MgO based magnetic tunnel junction without any ion bombardment and is larger than the magnetoresistance amplitude found for the alumina based tunnel junctions. A strong decrease of the magnetoresistance amplitude measured after the additional heating step at a not bombarded magnetic tunnel junction indicates that the used temperature of  $325^\circ\text{C}$  is too high. Therefore, the use of smaller temperatures for the additional annealing might further increase the tunnel magnetoresistance amplitude of the tunnel junctions with manipulated exchange bias directions.

Another possibility to decrease the side effects of the additional heating step might be the use of a thicker Ru interlayer in the artificial ferrimagnet which has allowed higher annealing temperatures without a negative effect on the magnetoresistance

amplitude in the literature [207]. Following the approach not to repair the damage done to the barrier, but to prevent the development of these side effects of ion bombardment from the beginning, one can try to use a thinner capping layer on top of the antiferromagnetic layer in combination with small ion energies below 5 keV in tunnel junctions with the pinned ferromagnetic layer located on top of the barrier. In this way one can take advantage of the strong depth dependence of the energy deposition of helium ions with small energies.

As the suitability of MgO based magnetic tunnel junctions for a magnetic patterning with ions has already been increased and further improvements seem possible, it can be summarized that the application of ion bombardment induced magnetic patterning is more difficult in the case of MgO barriers than for alumina barriers, but a successful application might be possible also for MgO based magnetic tunnel junctions.

Apart from the investigations regarding the applicability of the ion bombardment induced magnetic patterning, new applications of this method have been developed. One application has been suggested, which shows that a magnetic tunnel junction is not necessarily needed to apply this technique. The giant magnetoresistance based sensor suggested for the detection of small numbers of magnetic nanoparticles in fluids uses the strayfield obtained by magnetic patterning to attract the particles and align their magnetic moment in a favorable way.

It has been demonstrated that the approach to manipulate the assembly of magnetic nanoparticles by the strayfield of magnetically patterned ferromagnetic layers does work. Apart from the combination with a sensor, this method to manipulate the assembly of magnetic nanoparticles can as well be used for the investigation of, e.g., electron transport properties of the particles.

Finally, a novel type of reconfigurable magnetic logic has been presented. With this approach one logic unit consisting of only two magnetic tunnel junctions can be used for the AND, OR, NAND, NOR, and X(N)OR functions. Different possibilities to realize this kind of magnetic logic have been described. Furthermore, an experimental proof of principle has been shown.

The principle of this magnetic logic has been developed for and demonstrated by the use of an ion bombardment induced manipulation of the exchange bias coupling of the reference electrode, but it is not restricted to this. Any other method to obtain a fixed but locally definable magnetization direction of the reference electrode would be possible as well.

In summary, it has been shown that the application of ion bombardment induced magnetic patterning is possible and new applications of this technique have been developed.

## Chapter 6

# Acknowledgments

I would like to thank everybody who has contributed in one way or another to this thesis.

First, I would like to thank my advisors Jan Schmalhorst and Günter Reiss for the possibility to do my doctorate under their supervision and for the helpful suggestions and discussions during my time in the group.

Furthermore, I would like to thank many other current and former members of the group in Bielefeld: Marc D. Sacher for interesting long beam times at the BESSY and at the ALS, for providing a nice box of samples, and for proofreading parts of this thesis, Dirk Meyners for his valuable judgment whether the magnetic logic is reasonable and for very good ideas on this topic, Inga Ennen not only for the good cooperation regarding nanoparticles in a strayfield and for proofreading parts of this thesis, Alexander Weddemann for simulations of the nanoparticles in a strayfield, Volker Drewello and Andy Thomas for the joint assembling of the IETS setup and furthermore Andy for providing the amoeba code, Karsten Rott for sharing his large knowledge about nearly everything in our lab and what one can do with it, Oliver Schebaum for the introduction to and assistance with the He cryostat, Daniel Ebke for the 24/7 Leybold emergency service, Xinli Kou for providing the sample with stack  $MgO_{std}$  and corresponding measurements, Markus Meinert for the measurement of several sputter rate calibration samples and providing the density of our sputtered materials for the SRIM simulations, Michael Schilling for the rescue of our Linux server and his help to create a video from PEEM images, Markus Schäfers for the highly motivated takeover of the laser lithography tool which was very helpful during writing, Felix Keseberg for the search of untraceable magnetic structures with the MFM, Astrit Shoshi for MOKE measurements on several bilayers, Marlene Hahn, Anette Panhorst, Karin Wisotzky, and Aggi Windmann for the help with the unavoidable bureaucracy, Gerd Ahlers for keeping all the valuable measurement data save and accessible, everybody in the mechanical workshop for building precise things based on rough sketches, everybody in the electronic workshop for the fast repair of our TMR measurement device, Jörg Schotter, Dirk Brinkmann, Jan Bornemeier, and Maik Justus for introducing lab equipment to me when I started with my work and especially everybody who is missing in this list although he or she should be mentioned. I want to thank these and all other members of our group for the good atmosphere and helpful discussions.



For the good cooperation and for carrying out all ion bombardment work for this thesis, I would like to thank Arno Ehresmann, Dieter Engel, Dörte Junk, Tanja Weis, Dirk Backes and Daniel Lengemann from the Kaiserslautern University of Technology and Kassel University.

Furthermore, I want to thank Andreas Scholl and Andrew Doran for the helpful assistance during the measurements at the ALS in Berkeley.

For the possibility to use the ALICE experimental setup and the valuable assistance during the measurements at the BESSY, I want to thank Hartmut Zabel, Alexei Nefedov, and Arndt Remhof from the Ruhr-Universität Bochum. Furthermore, I would like to thank Franz Schäfers and Andreas Gaupp for the helpful assistance with the BESSY polarimeter and the beamlines in Berlin.

For the support and the good cooperation concerning the patent application I would like to thank Uwe Schneider (patent attorney), Rolf Klingelberger (PROvendis GmbH), Ulrike Garus, Axel Wohlgemuth, and Ines Meyer (Bielefeld University). I have learned many new things from them during this procedure.

Furthermore, I want to thank James F. Ziegler for providing SRIM free of charge and everybody who contributed to the development of the many helpful free programs as, e.g., L<sup>A</sup>T<sub>E</sub>X, Linux or ghostview which have been used during this work.

Furthermore, I gratefully acknowledge financial support from the European Union (Project “Exploring the Frontiers of Magnetic Logic” (MAGLOG<sup>1</sup>)), Wilhelm and Else Heraeus support program of the DPG (travel expenses conferences), BMBF (travel expenses BESSY), and DFG (travel expenses ALS).

And finally, I want to thank my family and Inga for their support during my studies and the work for this thesis.

---

<sup>1</sup>The views expressed are solely those of the authors, and the other Contractors and/or the European Community cannot be held liable for any use that may be made of the information contained herein.

## Appendix A

# Layer stacks

The following tables state the stack of the most important types of samples. Furthermore, some details about the annealing and ion bombardment carried out with these samples are given.

Samples which have been used, e.g., to find the best parameters for following experiments are omitted to keep the list readable. The only exception are optimization experiments which are described in detail in the text (e.g., in chapter 3.8.1).

In some cases the information is given for a series of samples with one or two varying parameters as, e.g., the annealing temperature or the thickness of a certain layer. The varying parameter usually is replaced by an  $x$ . In these and many other cases more information about the treatment of the samples can be found in the chapters listed in the last column.

The stated composition is always the composition of the sputter target. When nothing else is stated the following compositions have been used:  $\text{Ir}_{17}\text{Mn}_{83}$ ,  $\text{Co}_{70}\text{Fe}_{30}$  (single samples have been deposited with  $\text{Co}_{50}\text{Fe}_{50}$ ),  $\text{Ni}_{80}\text{Fe}_{20}$  (Py), and  $\text{Co}_{40}\text{Fe}_{40}\text{B}_{20}$ .

Sample name, EB manipulation by IB	Sputter deposition: Stack (layer thickness in nm)	Field cooling			Ion bombardment		Chap- ter
		Temp. [°C]	Time [min]	H <sub>FC</sub> [kOe]	Orientation H <sub>IB</sub>	H <sub>IB</sub> [kOe]	
$Ru_{AF}^{1\text{kOe,AP}}$ , EB enlarged	Cu 25/IrMn 15/CoFe 2/Ru 0.95/CoFe 3/Al 1.4 + ox.	275	30	6.5	H <sub>IB</sub> ↑↓ H <sub>FC</sub>	1	3.3
$Ru_{AF}^{5.4\text{kOe,AP}}$ , EB turned	Cu 25/IrMn 15/CoFe 2/Ru 0.95/CoFe 3/Al 1.4 + ox.	275	30	6.5	H <sub>IB</sub> ↑↓ H <sub>FC</sub>	5.4	3.3
$Ru_{AF}^{5.4\text{kOe,P}}$ , EB enlarged	Cu 25/IrMn 15/CoFe 2/Ru 0.95/CoFe 3/Al 1.4 + ox.	275	30	6.5	H <sub>IB</sub> ↑↑ H <sub>FC</sub>	5.4	3.3
$Ru_{AF}^{\text{no IrMn}}$ , no IB	Cu 25/CoFe 2/Ru 0.9/CoFe 3/Al 1.4 + ox.	no FC			no IB		3.3
$Cu_{AF}$ , EB turned	Cu 25/IrMn 10/NiFe 2/Co 2/Cu 1.05/Co 2/Al 1.4	field growth			H <sub>IB</sub> ↑↓ H <sub>grow</sub>	1	3.3
$hMTJ$ , EB initialized	Cu 30/IrMn 15/CoFe 3/Al 1.4 + ox./NiFe 4/Ta 6	no FC			H <sub>IB</sub>	1	2.2, 3.3, 3.8.2
$hMTJ$ , EB enlarged	Cu 30/IrMn 15/CoFe 3/Al 1.4 + ox./NiFe 4/Ta 6	250	5	1.5	H <sub>IB</sub> ↑↑ H <sub>FC</sub>	1	2.2, 3.3, 3.8.2
$hMTJ$ , EB turned	Cu 30/IrMn 15/CoFe 3/Al 1.4 + ox./NiFe 4/Ta 6	250	5	1.5	H <sub>IB</sub> ↑↓ H <sub>FC</sub>	1	2.2, 3.3, 3.8.2
$FM-A_{\text{pinned}}^{x\text{IrMn}/y\text{FM}}$ , no IB	Cu 30/IrMn $x$ /FM $y$ /AlOx 1.8 (FM=CoFe/Py)	275	60	1.5	no IB		3.3
$FM-B_{\text{pinned}}^{x\text{CoFe}/10\text{IrMn}}$ , no IB	Ta 5/CoFe $x$ /IrMn 10	275	30	1.5	no IB		3.3
$FM-C_{\text{pinned}}^{x\text{Co}/10\text{IrMn}}$ , no IB	Cu 5/ Co $x$ /IrMn 10	275	30	1.5	no IB		3.3
$FM-C_{\text{pinned}}^{x\text{Py}/10\text{IrMn}}$ , no IB	Cu 5/ Py $x$ /IrMn 10	275	30	1.5	no IB		3.3
$CoFe\text{-Xray}$ , EB turned	Cu 30/ Mn <sub>83</sub> Ir <sub>17</sub> 15/Co <sub>70</sub> Fe <sub>30</sub> 3/Al 1.4 +ox.	275	60	1.5	H <sub>IB</sub> ↑↓ H <sub>FC</sub>	1	3.1, 4.2
$Co_{\text{TS}}^{\text{PEEM}}$ , EB init.	Cu 30 / Ni <sub>80</sub> Fe <sub>20</sub> 1.9 /Mn <sub>83</sub> Ir <sub>17</sub> 25 / Co 3 / Al 1.4 +ox.	no FC			H <sub>IB</sub>	1	3.2.2, 3.2.3, 3.7.2, 3.8.2
$Co_{\text{TS}}^{\text{PEEM}}$ , FC + IB (EB enlarged)	Cu 30 / Ni <sub>80</sub> Fe <sub>20</sub> 1.9 /Mn <sub>83</sub> Ir <sub>17</sub> 25 / Co 3 / Al 1.4 +ox.	200	60	1.5	H <sub>IB</sub> ↑↑ H <sub>FC</sub>	1	3.7.2, 3.8.2
$Co_{\text{TS}}^{\text{PEEM}}$ , no IB	Cu 30 / Ni <sub>80</sub> Fe <sub>20</sub> 1.9 /Mn <sub>83</sub> Ir <sub>17</sub> 25 / Co 3 / Al 1.4 +ox.	275	60	1.5	no IB		3.2.2
$CoFe_{\text{TS}}^{\text{PEEM}3\text{nm}}$ , no IB	Cu 30 / Mn <sub>83</sub> Ir <sub>17</sub> 15 / Co <sub>70</sub> Fe <sub>30</sub> 3 / Al 1.4 +ox.	275	60	1.5	no IB		2.1, 3.2.2
$CoFe_{\text{TS}}^{\text{PEEM}3\text{nm}}$ , EB turned	Cu 30 / Mn <sub>83</sub> Ir <sub>17</sub> 15 / Co <sub>70</sub> Fe <sub>30</sub> 3 / Al 1.4 +ox.	275	60	1.5	H <sub>IB</sub> ↑↓ H <sub>FC</sub>	1	3.2.2, 3.2.3, 3.2.5
$CoFe_{\text{TS}}^{\text{PEEM}5\text{nm}}$ , EB turned	Cu 30 / Mn <sub>83</sub> Ir <sub>17</sub> 15 / Co <sub>70</sub> Fe <sub>30</sub> 5 / Al 1.4 +ox.	275	60	1.5	H <sub>IB</sub> ↑↓ H <sub>FC</sub>	1	3.2.4

Table A.1: Stack of selected samples with layer thickness in nm and parameters of field cooling (max. temperature, heating duration and magnetic field H<sub>FC</sub> applied during field cooling) and ion bombardment (orientation of magnetic field during IB (H<sub>IB</sub>) relative to the field during field cooling (H<sub>FC</sub>) or field during field growth (H<sub>grow</sub>) and strength of H<sub>IB</sub>).

Sample name, EB manipulation by IB	Sputter deposition: Stack (layer thickness in nm)	Field cooling			Ion bombardment		Chapter
		Temp. [°C]	Time [min]	H <sub>FC</sub> [kOe]	Orientation H <sub>IB</sub>	H <sub>IB</sub> [kOe]	
$MTJ_{\text{AlOx}}^{\text{inv}}$ , EB rot. 90°	Cu 30 / Ta 5 / Ni <sub>80</sub> Fe <sub>20</sub> 5 / Co <sub>70</sub> Fe <sub>30</sub> 2 / Al 1.4 + ox. / Co <sub>70</sub> Fe <sub>30</sub> 4 / Ir <sub>17</sub> Mn <sub>83</sub> 12 / Ta 5 / Cu 35 / Ta 5 / Au 20	275	60	1.5	H <sub>IB</sub> ⊥H <sub>FC</sub>	1	3.4
$MTJ_{\text{AlOx}}^{\text{std}}$ , EB rot. 90°	Cu 25 / Ir <sub>17</sub> Mn <sub>83</sub> 12 / Co <sub>70</sub> Fe <sub>30</sub> 3.1 / Al 1.3 + ox. / Ni <sub>80</sub> Fe <sub>20</sub> 3.6 / Ta 3.1 / Cu 47 / Au 26	275	60	1.5	H <sub>IB</sub> ⊥H <sub>FC</sub>	1	3.4, 3.5
$MTJ_{\text{AlOx}}^{\text{std+}}$ , EB rot. 90°	Cu 25 / Ir <sub>17</sub> Mn <sub>83</sub> 12 / Co <sub>70</sub> Fe <sub>30</sub> 3.1 / Al 1.3 + ox. / Ni <sub>80</sub> Fe <sub>20</sub> 3.6 / Ta 6 / Cu 47 / Ta 6 / Au 26	275	60	1.5	H <sub>IB</sub> ↑↑H <sub>FC</sub>	1	3.5
$MgO_{\text{std}}$ , EB turned	Ta 5 / Cu 30 / Ta 5 / Cu 5 / IrMn 12 / CoFeB4 / Mg 0.75 / MgO 1.5 / CoFeB 6 / Ta 5 / Cu 40 / Au 30	325	60	1.5	H <sub>IB</sub> ↑↓H <sub>FC</sub>	1	3.7, 3.8.1, 3.8.2
$MgO_{\text{Ru}}^{\text{thin FM pinned}}$ , no IB	Ta 5 / Ru 40 / Ta 5 / CoFeB 2.5 / MgO 2.1 / CoFeB 4 / Ru 0.9 / CoFe 2 / IrMn 9 / Ru 40	325	60	6.5	no IB		3.8.1
$MTJ_{\text{Ru}}^{\text{MgOinv}}$ , no IB var.	Ta 5 / Ru 40 / Ta 5 / CoFeB 2.5 / MgO 2.1 / CoFeB 2.5 / Ru $x$ / CoFe 6 / IrMn 9 / Ru 40	$x$	60	6.5	no IB		3.8.1
$MTJ_{\text{IB}}^{\text{MgOinv}}$ , EB turned	Ta 5 / Ru 40 / Ta 5 / CoFeB 2.5 / MgO 2.1 / CoFeB 2.5 / Ru 0.88 / CoFe 6 / IrMn 9 / Ru 40	375	60	6.5	H <sub>IB</sub> ↑↓H <sub>FC</sub>	1	3.7, 3.8.1, 3.8.3
$SV_{3.4\text{nmCu}}$ , turned	Py 6 / Co 1.5 / Cu 3.4 / Co 5 /CoFe 1 IrMn 10 / Ta 4	240	5	1.5	H <sub>IB</sub> ↑↓H <sub>FC</sub>	1	2.7.1, 3.8.2

Table A.2: Stack of selected samples with layer thickness in nm and parameters of field cooling (max. temperature, heating duration and magnetic field H<sub>FC</sub> applied during field cooling) and ion bombardment (orientation of magnetic field during IB (H<sub>IB</sub>) relative to the field during field cooling (H<sub>FC</sub>) or field during field growth (H<sub>grow</sub>) and strength of H<sub>IB</sub>).

## Appendix B

# Thermal stability of the manipulated exchange bias coupling in elliptical structures

Four elliptical structures with a long (short) axis of  $5.7 \mu\text{m}$  ( $2.6 \mu\text{m}$ ) as described in chapter 3.2.5 have been investigated by x-ray photoemission electron microscopy (PEEM) measurements at several elevated temperatures (Fig. B.1 and B.2). The magnetization direction in the bombarded areas before the heating results in a dark contrast in these measurements (bombarded structures: A and D).

It is striking that the first change of the magnetic structure at  $200^\circ\text{C}$  can be found at the elliptical structure B which has not been bombarded [Fig. B.1 (d)]. Therefore, for this elliptic structures, again, no hint for a reduction of the magnetic stability due to the ion bombardment can be observed.

On this part of the sample the same rotation of the preferred magnetization direction on the not bombarded elliptical structures at  $360^\circ\text{C}$  can be found as described in chapter 3.2.5.

For a more detailed description of this experiments and the results obtained for triangular and smaller elliptic structures see chapter 3.2.5.

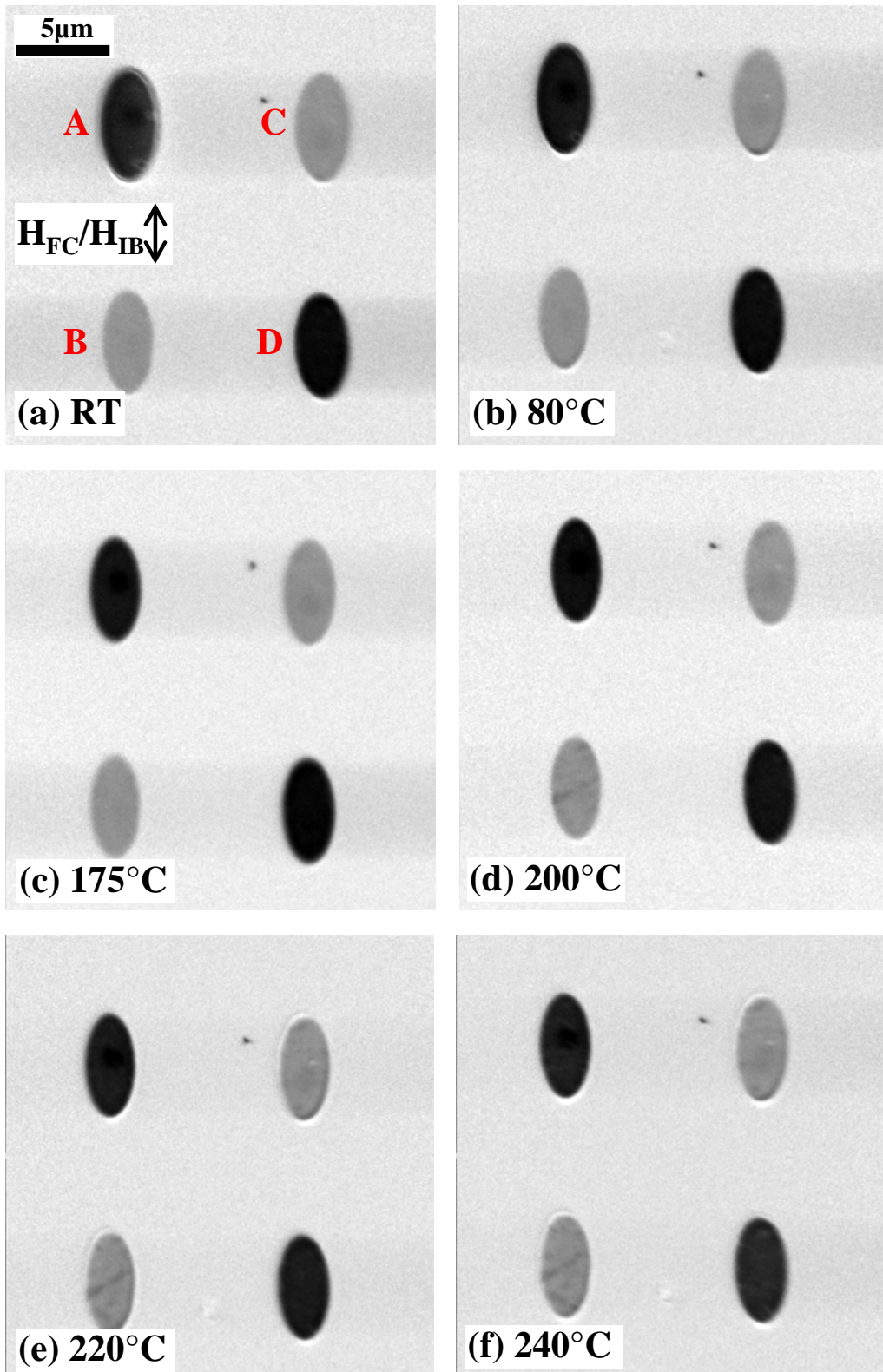


Figure B.1: PEEM images of elliptic etched structures with an alternating EB direction on a sample with stack  $CoFe_{TS}^{PEEM3nm}$  before (a) and during (b)-(f) the heating.

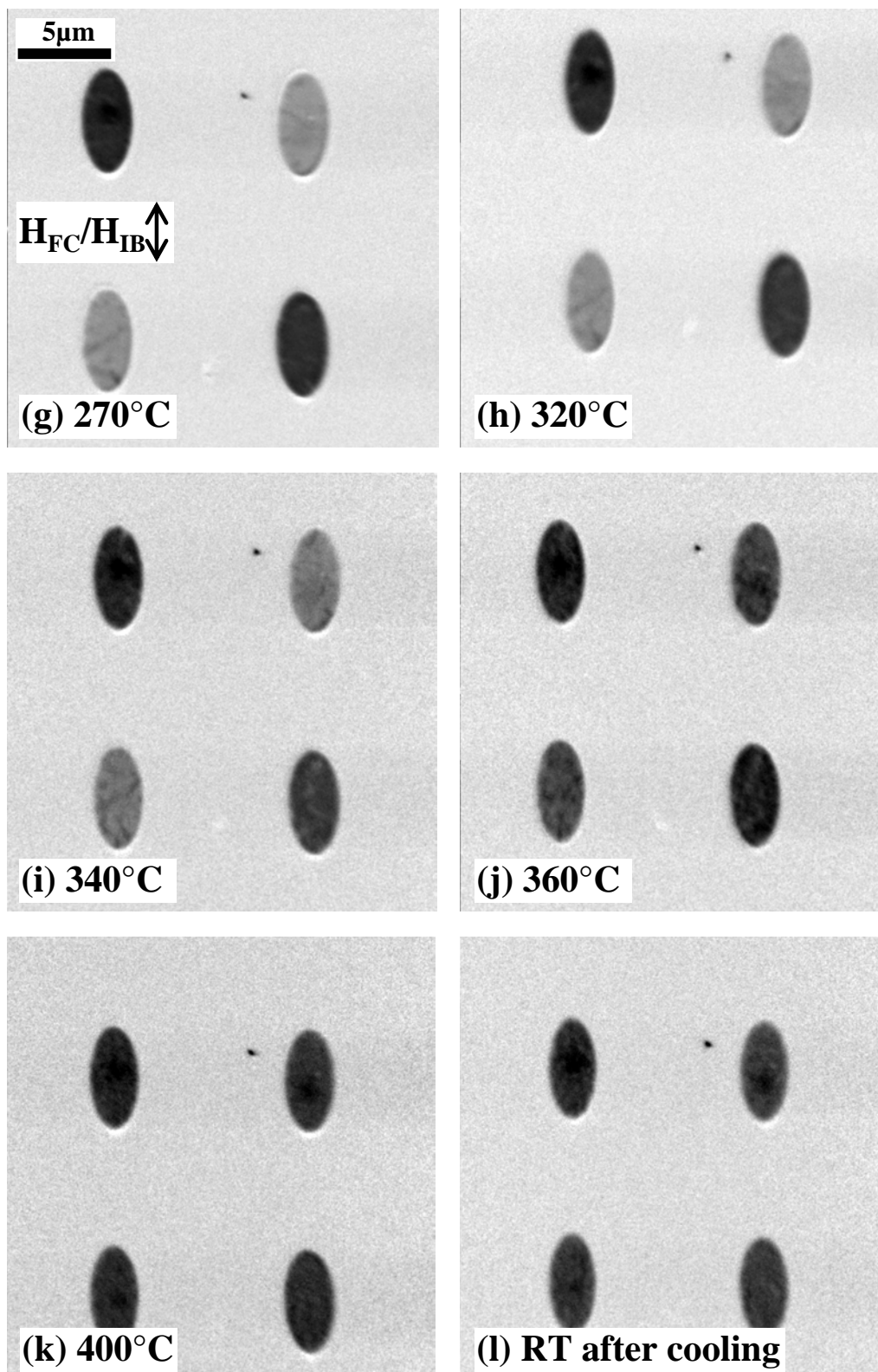


Figure B.2: PEEM images of elliptic and triangular etched structures with an alternating EB direction on a sample with stack  $CoFe_{TS}^{PEEM3nm}$  during (g)-(k) the heating and after cooling the sample down to RT (l).

## Appendix C

# Ru based artificial ferrimagnet - calculated magnetization reversal processes for stack

$Ru_{AF}^{5.4kOe,P}$

In chapter 3.3 the bilinear and biquadratic interlayer exchange coupling constants and the unidirectional anisotropy constant of samples with stack  $Ru_{AF}^{5.4kOe,P}$  are discussed in dependence of the ion dose (Fig. 3.38). Here, the underlying calculated magnetization reversal processes are shown for samples with stack  $Ru_{AF}^{5.4kOe,P}$  after bombardment with several ion doses which have been omitted in chapter 3.3.



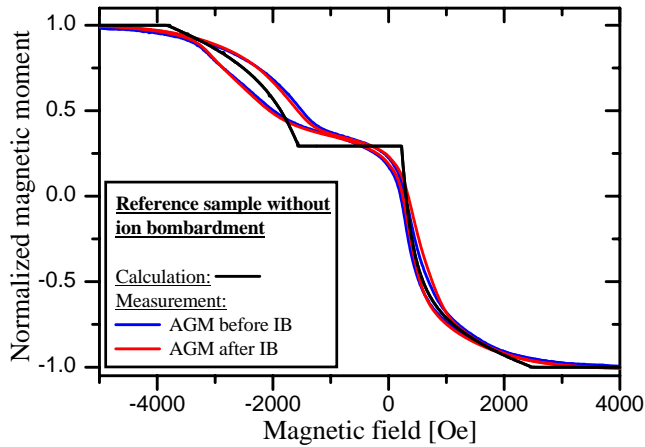


Figure C.1: AGM measurements of not bombarded part of sample  $Ru_{AF}^{5.4kOe,P}$  carried out together with the measurements shown in Fig. C.2 to C.8 before and after the other samples have been bombarded. The calculated magnetization reversal has been obtained with  $J_L = -2.7 \times 10^{-4} \text{ J/m}^2$ ,  $J_Q = -7.2 \times 10^{-5} \text{ J/m}^2$  and  $K_u = 2.2 \times 10^{-4} \text{ J/m}^2$ .

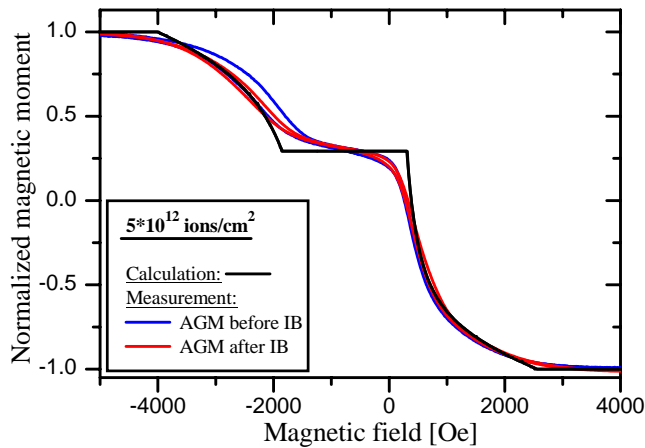


Figure C.2: AGM measurements carried out before and after IB with  $5 \times 10^{12} \text{ ions/cm}^2$  and  $H_{IB} = 5.4 \text{ kOe}$ . The best agreement of the calculated magnetization reversal with the measurement after IB has been obtained with  $J_L = -3.1 \times 10^{-4} \text{ J/m}^2$ ,  $J_Q = -6.0 \times 10^{-5} \text{ J/m}^2$  and  $K_u = 2.35 \times 10^{-4} \text{ J/m}^2$ .

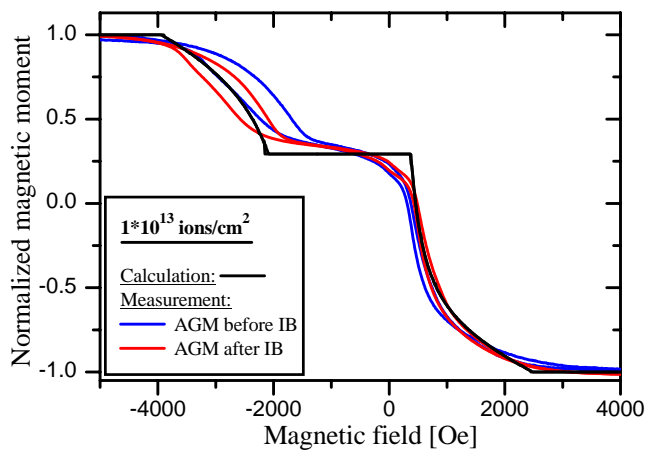


Figure C.3: AGM measurements carried out before and after IB with  $1 \times 10^{13} \text{ ions/cm}^2$  and  $H_{IB} = 5.4 \text{ kOe}$ . The best agreement of the calculated magnetization reversal with the measurement after IB has been obtained with  $J_L = -3.4 \times 10^{-4} \text{ J/m}^2$ ,  $J_Q = -4.0 \times 10^{-5} \text{ J/m}^2$  and  $K_u = 2.38 \times 10^{-4} \text{ J/m}^2$ .

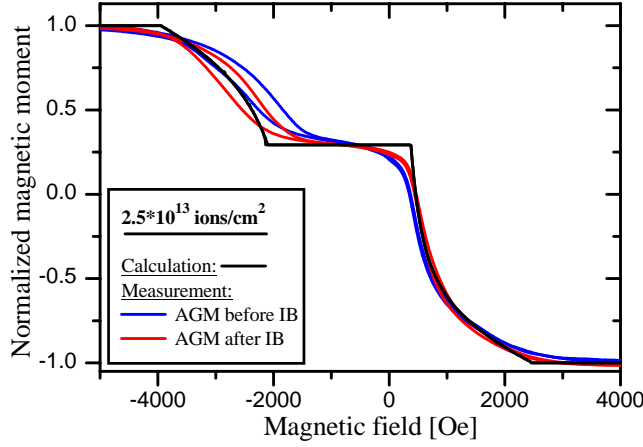


Figure C.4: AGM measurements carried out before and after IB with  $2.5 \times 10^{13}$  ions/cm<sup>2</sup> and  $H_{IB} = 5.4$  kOe. The best agreement of the calculated magnetization reversal with the measurement after IB has been obtained with  $J_L = -3.4 \times 10^{-4}$  J/m<sup>2</sup>,  $J_Q = -4.0 \times 10^{-5}$  J/m<sup>2</sup> and  $K_u = 2.4 \times 10^{-4}$  J/m<sup>2</sup>.

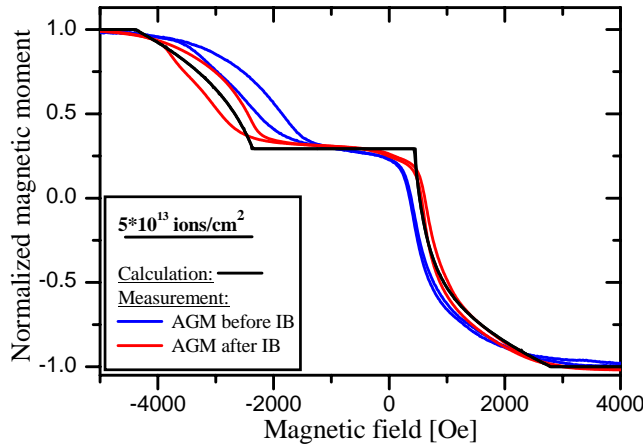


Figure C.5: AGM measurements carried out before and after IB with  $5 \times 10^{13}$  ions/cm<sup>2</sup> and  $H_{IB} = 5.4$  kOe. The best agreement of the calculated magnetization reversal with the measurement after IB has been obtained with  $J_L = -3.9 \times 10^{-4}$  J/m<sup>2</sup>,  $J_Q = -4.0 \times 10^{-5}$  J/m<sup>2</sup> and  $K_u = 2.6 \times 10^{-4}$  J/m<sup>2</sup>.

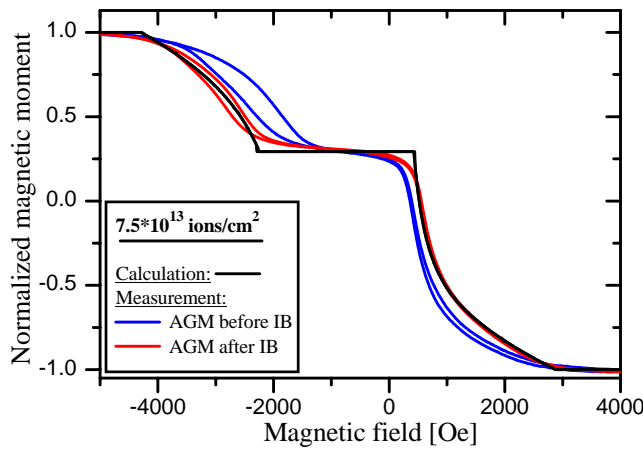


Figure C.6: AGM measurements carried out before and after IB with  $7.5 \times 10^{13}$  ions/cm<sup>2</sup> and  $H_{IB} = 5.4$  kOe. The best agreement of the calculated magnetization reversal with the measurement after IB has been obtained with  $J_L = -4.0 \times 10^{-4}$  J/m<sup>2</sup>,  $J_Q = -3.6 \times 10^{-5}$  J/m<sup>2</sup> and  $K_u = 2.3 \times 10^{-4}$  J/m<sup>2</sup>.

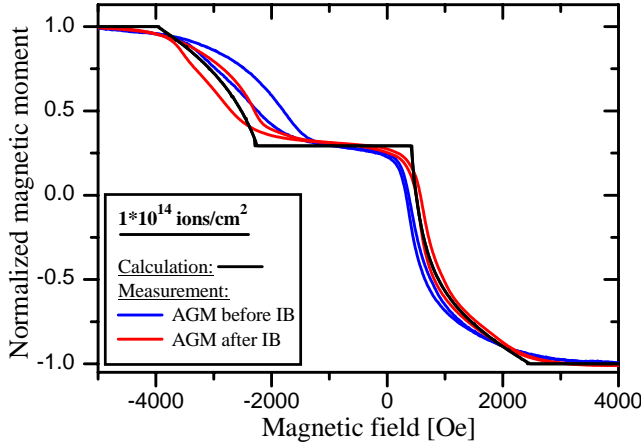


Figure C.7: AGM measurements carried out before and after IB with  $1 \times 10^{14}$  ions/cm<sup>2</sup> and  $H_{IB} = 5.4$  kOe. The best agreement of the calculated magnetization reversal with the measurement after IB has been obtained with  $J_L = -3.6 \times 10^{-4}$  J/m<sup>2</sup>,  $J_Q = -3.0 \times 10^{-5}$  J/m<sup>2</sup> and  $K_u = 2.45 \times 10^{-4}$  J/m<sup>2</sup>.

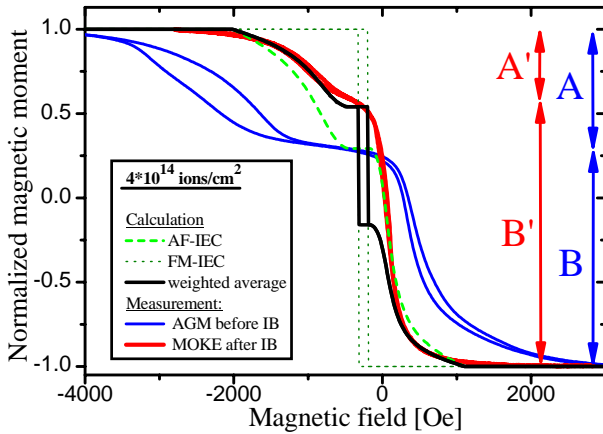


Figure C.8: AGM measurements carried out before and MOKE measurements carried out after IB with  $4 \times 10^{14}$  ions/cm<sup>2</sup> and  $H_{IB} = 5.4$  kOe. The calculated magnetization reversals have been obtained for *antiferromagnetic inter-layer exchange coupling (IEC)* (dashed bright green line) with:  $J_L = -8.0 \times 10^{-5}$  J/m<sup>2</sup>,  $J_Q = -6.0 \times 10^{-5}$  J/m<sup>2</sup> and  $K_u = 1.5 \times 10^{-4}$  J/m<sup>2</sup>, and for

*ferromagnetic IEC* (dotted dark green line) with:  $J_L = +4.0 \times 10^{-3}$  J/m<sup>2</sup>,  $J_Q = 0$  J/m<sup>2</sup> and  $K_u = 1.5 \times 10^{-4}$  J/m<sup>2</sup> and weighted superposition (black solid line) of both calculations with 65% antiferromagnetic IEC and 35% ferromagnetic IEC. A and B (A' and B') indicate the change of the normalized magnetic moment in the positive and negative magnetic field range, respectively.

## Appendix D

# Ru based artificial ferrimagnet without pinning - calculation including uniaxial anisotropy

In chapter 3.3 calculated magnetization reversal processes are shown for samples with stack  $Ru_{AF}^{5.4kOe,P}$ ,  $Ru_{AF}^{1kOe,AP}$ ,  $Ru_{AF}^{no\ IrMn}$ , and  $Cu_{AF}$ . In these calculations the uniaxial anisotropy constants  $K_1$  and  $K_2$  are set to zero, because the FM layers in the investigated samples have a polycrystalline structure and, therefore, the easy axes of the grains are not necessarily aligned. This results in a hysteresis free calculated magnetization reversal. Here, one calculation for stack  $Ru_{AF}^{no\ IrMn}$  corresponding to the calculation shown in Fig. 3.32 is shown (Fig. D.1). The anisotropy terms are used here as an approximative measure for several mechanisms inducing a hysteresis. The unidirectional anisotropy constant  $K_u$  has been set to zero as due to the lack of an antiferromagnetic layer no exchange bias is present. The bilinear and bi-quadratic interlayer exchange interaction constants resulting in the best fit between calculation and measurement for sample  $Ru_{AF}^{no\ IrMn}$  are  $J_L = -5.4 \times 10^{-4} \text{ J/m}^2$  and  $J_Q = -9 \times 10^{-9} \text{ J/m}^2$  as observed during the calculation without  $K_i$  (compare Fig. 3.32).

The uniaxial anisotropy constants have been chosen to be  $K_1=K_2=0.3 \times 10^4 \text{ J/m}^3$  in order to obtain the correct width of the hysteresis loop around zero magnetic field. The direction of the assumed effective uniaxial anisotropy deviates about  $\Theta_{easy} = \pi/4$  from the axis of the external magnetic field to match the rounded shape of the measurement, e.g., in the range 100 Oe - 700 Oe.

The jump in the angle of layer 1 from one side of the axis "2 $\pi$ " to the other denoted by  $i$  in Fig. 3.32 (b) and the corresponding jump  $ii$  of layer 2 is physically not reasonable. This kind of jumps in the calculated angle has been observed only with a nonzero uniaxial anisotropy constant.

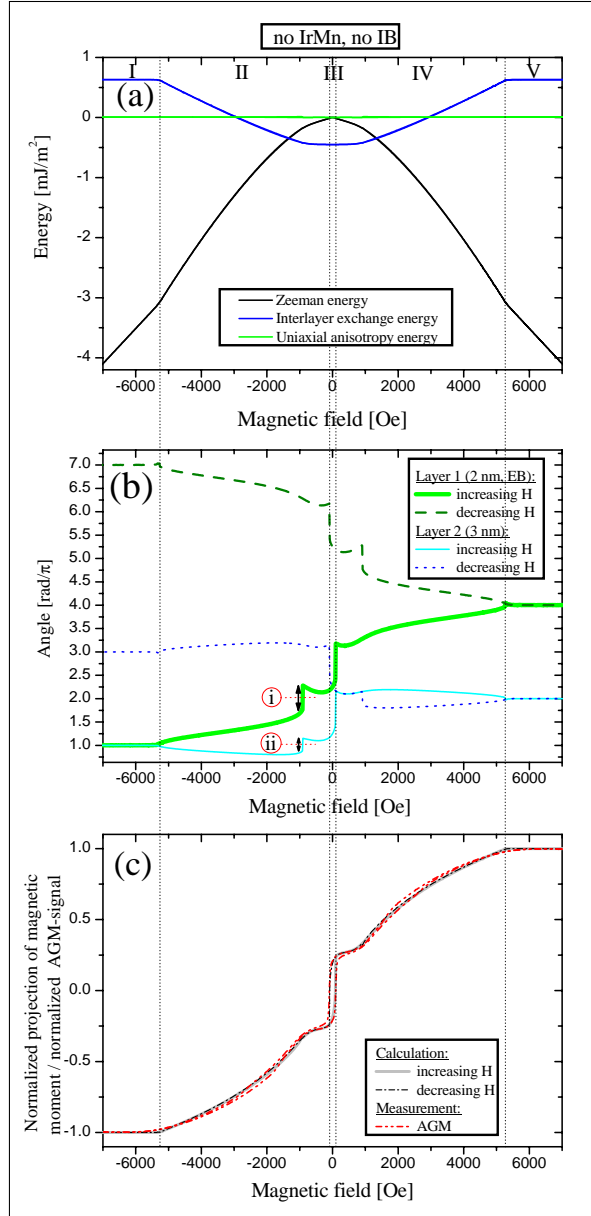


Figure D.1: (a) Energy of Zeeman interaction, interlayer exchange interaction and effective uniaxial anisotropy calculated for the angles of the magnetization of the two FM layers ( $\mathbf{M}_i$ ) which result in the minimum sum of this energies at each value of the external magnetic field. (b) Direction of  $\mathbf{M}_i$  described by the angle relative to the axis of the external magnetic field. (even (odd) multiples of  $\pi$  correspond to positive (negative) external magnetic field) (c) Calculated magnetization reversal and normalized AGM measurement for sample  $Ru_{AF}^{no IrMn}$ .

## Appendix E

# Cu based artificial ferrimagnet - measurement and calculation

In this chapter the results of the measurements and calculations concerning the influence of the ion bombardment on the magnetization reversal of sample  $Cu_{AF}$  are shown in detail. The description of the experiments and the method used for the calculations can be found in chapter 3.3.

Experiments and calculations for several ion doses between zero and  $3 \times 10^{14}$  ions/cm<sup>2</sup> are presented. The ion dose used in each experiment is written at the top of each graph. Part (a) of all graphs in this chapter shows the Zeeman energy and the energy due to exchange bias and interlayer exchange interaction in dependence of the external magnetic field. The variation of the angle of the magnetization of the upper and the lower FM layer relative to the direction of the external magnetic field by a varying external magnetic field strength is shown in part (b). Even (odd) multiples of  $\pi$  represent an alignment parallel to positive (negative) external fields. The comparison between the calculated magnetization reversal process and its experimental counterpart can be seen in part (c). The AGM measurements have been normalized to make them comparable to the normalized projection of the total magnetization on the direction of the external magnetic field obtained by the calculation. The roman numbers and dotted vertical lines correspond to the marks used in Fig. 3.32. **The details of the calculations can be found in table 3.3.**

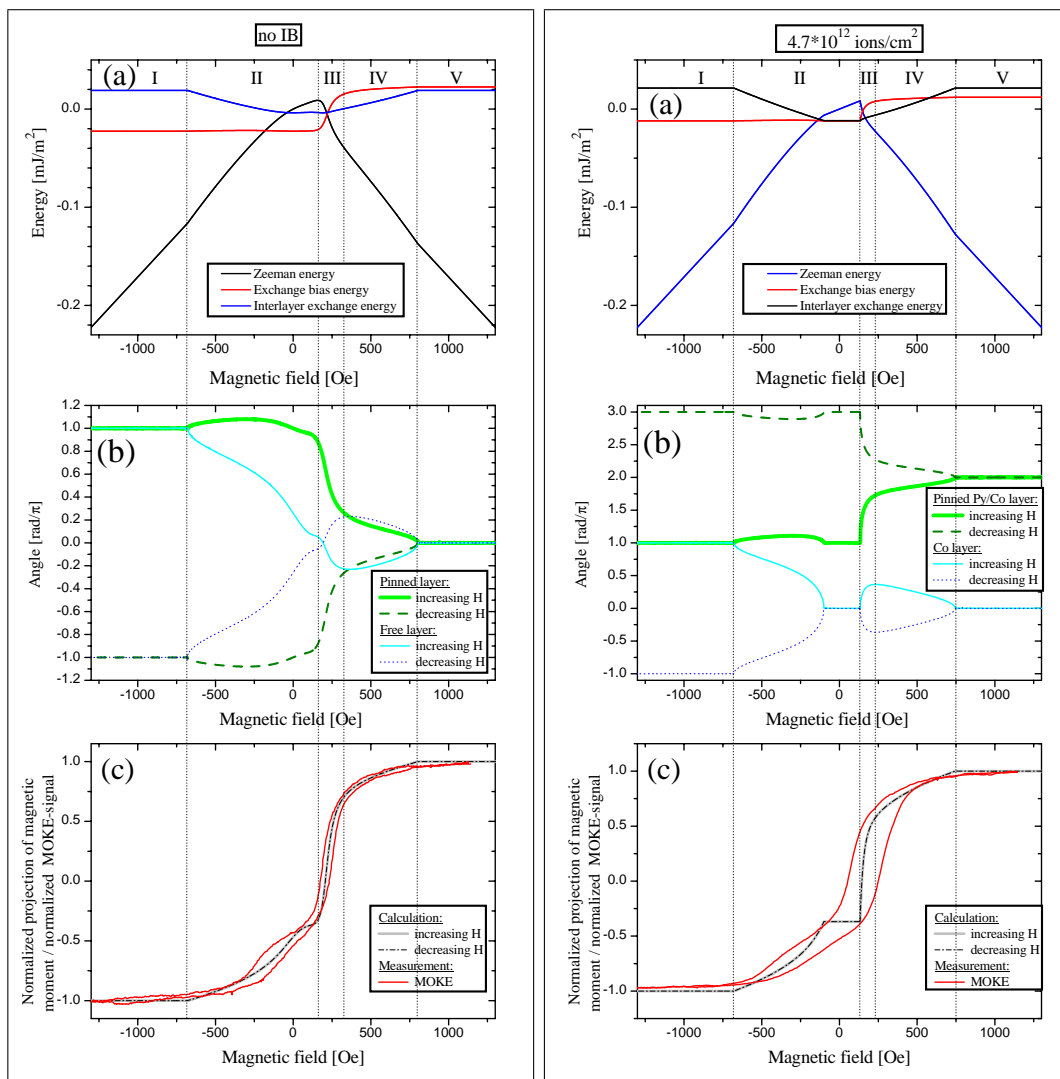


Figure E.1:

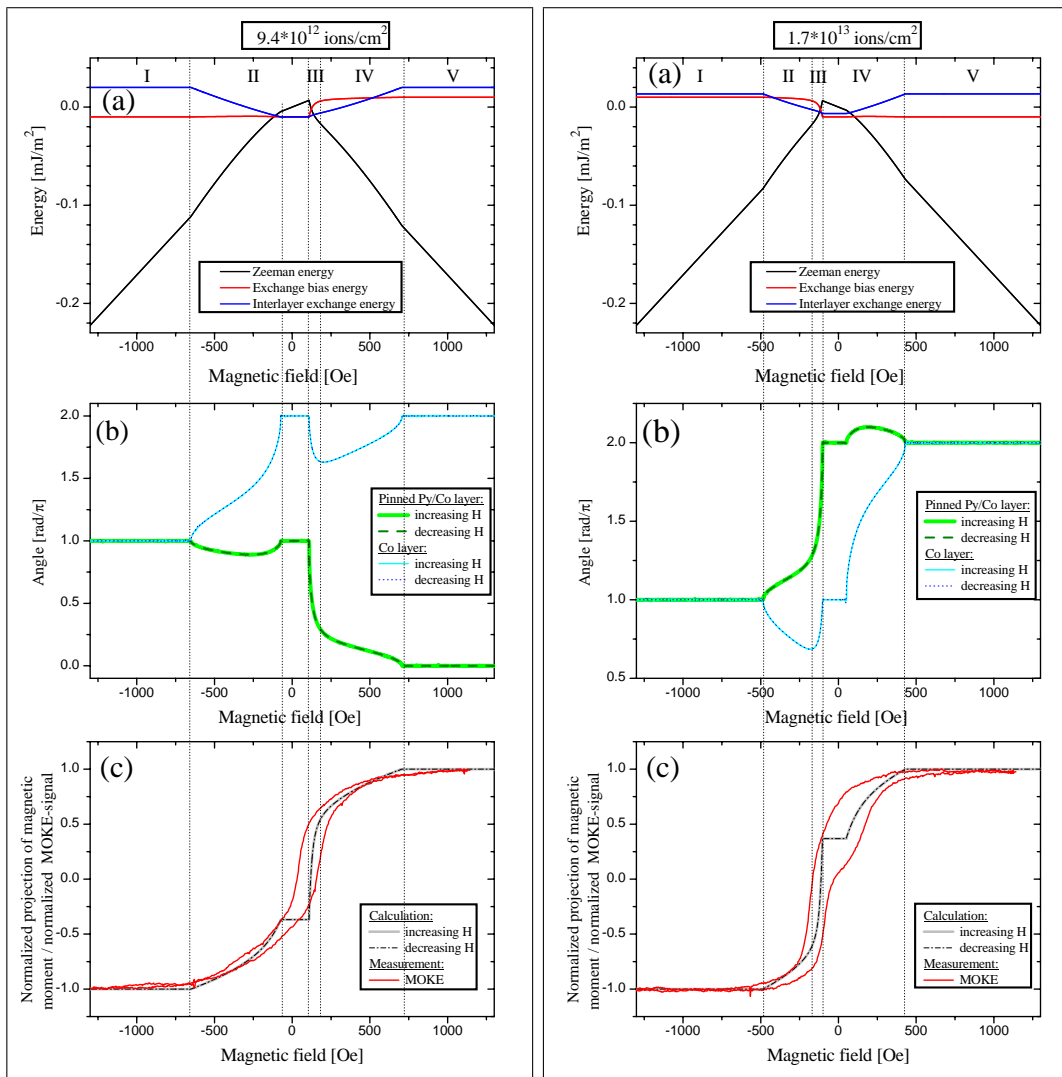


Figure E.2:



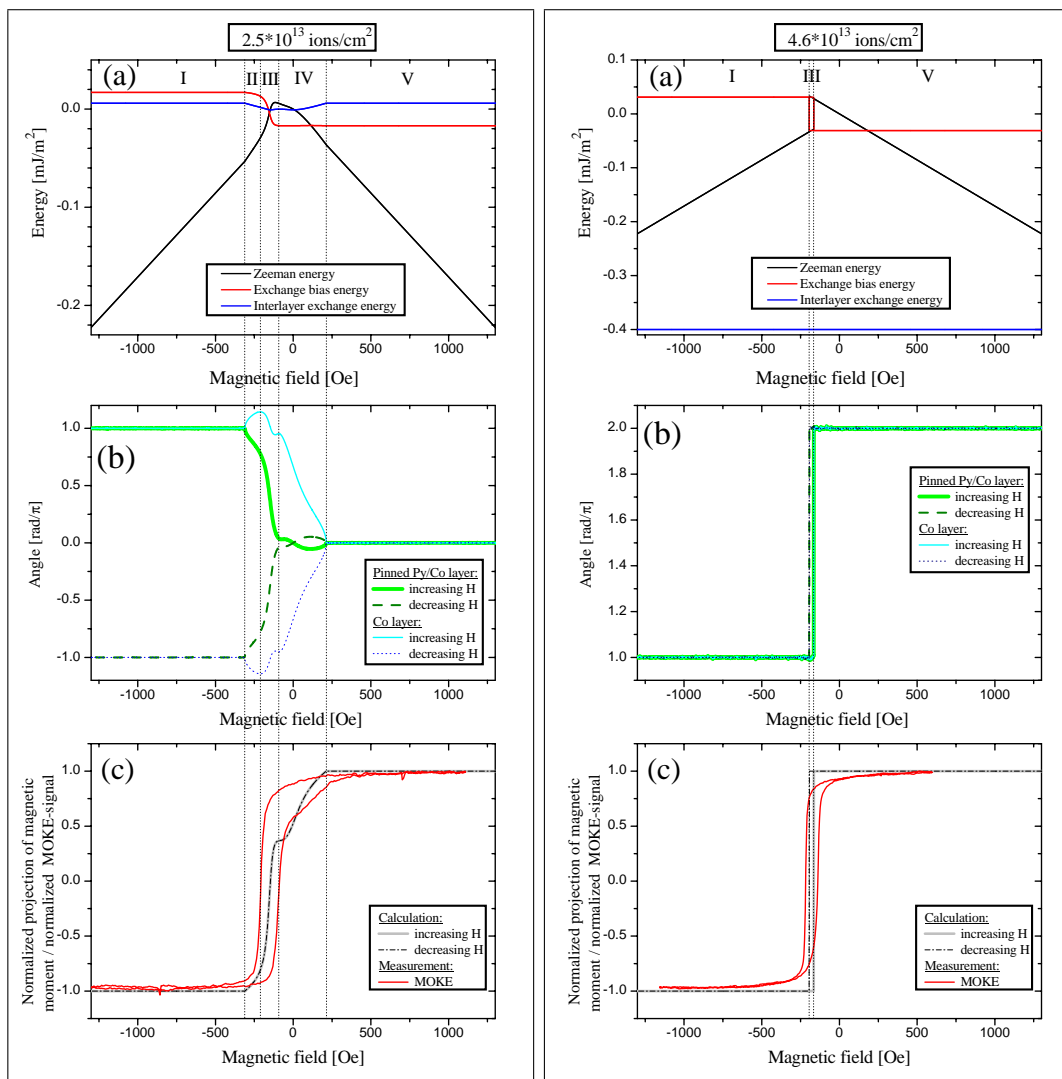


Figure E.3:

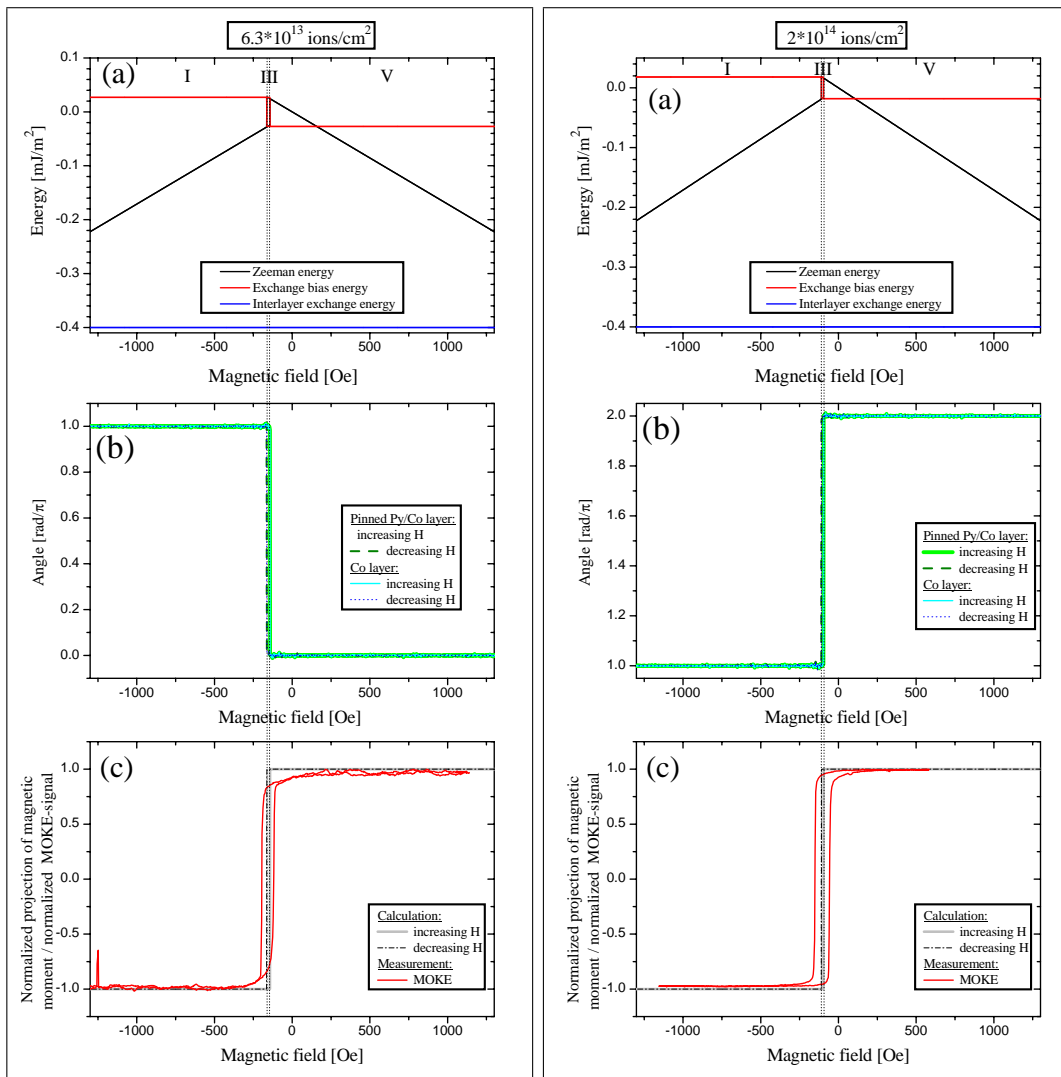


Figure E.4:

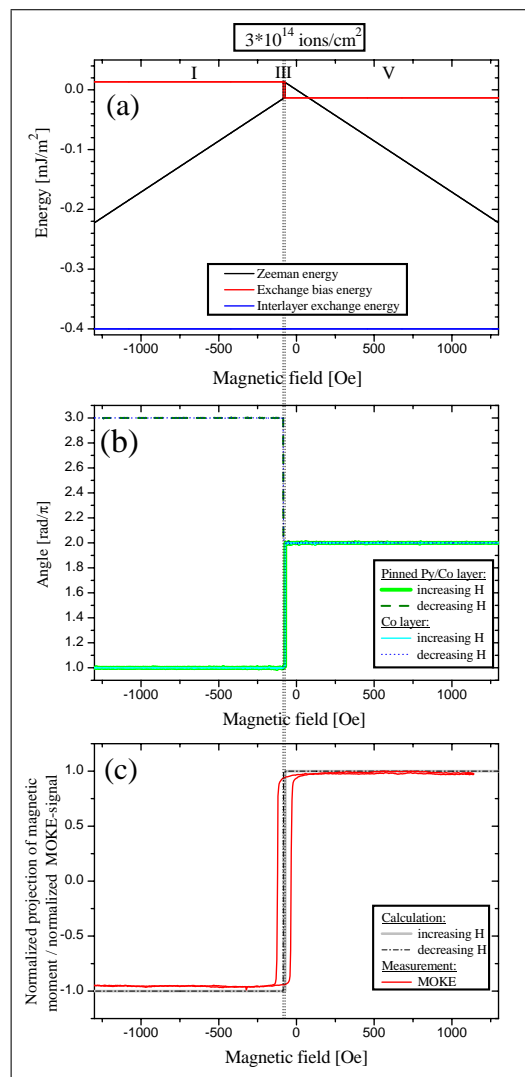


Figure E.5:

# Bibliography

- [1] S. Wolf, D. Awschalom, R. Buhrmann, J. Daughton, S. von Molnar, M. Roukes, A. Chtchelkanova and D. Treger, *Spinelectronics: A Spin-Based Electronics Vision for the Future*, Science **294**, 1488 (2001). 10, 23
- [2] P. P. Freitas, R. Ferreira, S. Cardoso and F. Cardoso, *Magnetoresistive sensors*, Journal of Physics: Condensed Matter **19**, 165221 (2007). 10, 23
- [3] J. R. Childress and R. E. Fontana Jr., *Magnetic recording read head sensor technology*, Comptes Rendus Physique **6**, 997 (2005). 10, 23
- [4] Western Digital Technologies, Inc, *Press Release: WD Demonstrates highest hard drive density*, [www.wdc.com/en/company/releases/PressRelease.asp?release={05F7E0B4-B357-4D6A-8993-73172269E411}](http://www.wdc.com/en/company/releases/PressRelease.asp?release={05F7E0B4-B357-4D6A-8993-73172269E411}) (2007). 10
- [5] S. N. Piramanayagam, *Perpendicular recording media for hard disk drives*, Journal of Applied Physics **102**, 011301 (2007). 10
- [6] W. J. Gallagher and S. S. P. Parkin, *Development of the magnetic tunnel junction, MRAM at IBM: From first junctions to a 16-Mb MRAM demonstrator chip*, IBM Journal of Research and Development **50**, 5 (2006). 10, 23, 24, 77, 201
- [7] J. M. Slaughter, R. W. Dave, M. DeHerrera, M. Durlam, B. N. Engel, J. Janesky, N. D. Rizzo and S. Tehrani, *Fundamentals of MRAM Technology*, Journal of Superconductivity: Incorporating Novel Magnetism **15**, 19 (2002). 10, 23
- [8] R. C. Sousa and I. L. Prejbeanu, *Non-volatile magnetic random access memories (MRAM)*, Comptes Rendus Physique **6**, 1013 (2005). 10, 23
- [9] Freescale Semiconductor Inc., *White paper: "Magnetoresistive Random Access Memory"*, MRAMWP.pdf available at [www.freescale.com](http://www.freescale.com) (revised June 23, 2006). 10, 23
- [10] Freescale Semiconductor, *Data Sheet 256K x 16-Bit 3.3-V Asynchronous Magnetoresistive RAM, MR2A16A*, 2006, Document Number: MR2A16A, Rev. 3, 6/2006, published at [www.freescale.com](http://www.freescale.com). 10, 23, 205, 208
- [11] A. Ney, C. Pampuch, R. Koch and K. H. Ploog, *Programmable computing with a single magnetoresistive element*, Nature **425**, 485 (2003). 10, 23

- [12] R. Richter, *Logic gates realized with spin dependent tunneling elements*, Doctoral thesis, Universität Bielefeld, 2002. 10, 23
- [13] J. S. Moodera and P. Leclair, *SPIN ELECTRONICS - A quantum leap*, nature materials **2**, 707 (2003). 10, 23
- [14] J. William C. Black and B. Das, *Programmable logic using giant-magnetoresistance and spin-dependent tunneling devices*, Journal of Applied Physics **87**, 6674 (2000). 10, 23
- [15] D. Meyners, *Herstellung und Charakterisierung von Logikarrays mit ultrakleinen magnetischen Tunnelementen*, Doctoral thesis, Universität Bielefeld, 2006. 10, 23, 31, 34
- [16] J. Dressen, *Magnetoelektronik in Technologieführer - Grundlagen - Anwendungen - Trends* (Springer, 2007). 10
- [17] G. A. Prinz, *Magnetolectronics applications*, Journal of Magnetism and Magnetic Materials **200**, 57 (1999). 10
- [18] J. Schotter, *Development of a magnetoresistive biosensor for the detection of biomolecules*, Doctoral thesis, Universität Bielefeld, 2004. 10, 23, 31
- [19] H. Brückl, M. Brzeska, D. Brinkmann, J. Schotter, G. Reiss, W. Schepper, P.-B. Kamp and A. Becker, *Magnetoresistive logic and biochip*, Journal of Magnetism and Magnetic Materials **282**, 219 (2004). 10, 23
- [20] M. Ben Schrag, *Applications - Semiconductor Fault Isolation and Failure Analysis*, micromagnetics.com/app\_semiconductor.html (2007). 10
- [21] C. H. Smith, R. W. Schneider and A. V. Pohm, *High-resolution giant magnetoresistance on-chip arrays for magnetic imaging*, Journal of Applied Physics **93**, 6864 (2003). 10
- [22] C. H. Smith and R. W. Schneider, *Low-Field Magnetic Sensing with GMR Sensors*, www.nve.com/Downloads/lowfield.pdf . 10
- [23] M. Ben Schrag, *Applications - Detection of Magnetic Media and Inks*, micromagnetics.com/app\_currencymedia.html (2007). 10
- [24] TROY Group, Inc., *MICR - Magnetic Ink Character Recognition*, www.whatismicr.com (2007). 10
- [25] Y. M. Lee, J. Hayakawa, S. Ikeda, F. Matsukura and H. Ohno, *Effect of electrode composition on the tunnel magnetoresistance of pseudo-spin-valve magnetic tunnel junction with a MgO tunnel barrier*, Applied Physics Letters **90**, 212507 (2007). 11, 12, 24, 125, 147, 148
- [26] A. Mougin, T. Mewes, M. Jung, D. Engel, A. Ehresmann, H. Schmoranzler, J. Fassbender and B. Hillebrands, *Local manipulation and reversal of the exchange bias field by ion irradiation in FeNi/FeMn double layers*, Physical Review B **63**, 060409 (2001). 11, 19, 21, 169

- [27] D. Engel, I. Krug, H. Schmoranzer, A. Ehresmann, A. Paetzold, K. Röhl, B. Ocker and W. Maass, *Alteration of exchange anisotropy and magnetoresistance in Co/Cu/Co/FeMn spin valves by ion bombardment*, Journal of Applied Physics **94**, 5925 (2003). 11, 77, 106, 169, 170
- [28] J. Fassbender, D. Ravelosona and Y. Samson, *Tailoring magnetism by light-ion irradiation*, Journal of Physics D: Applied Physics **37**, R179 (2004). 11, 22, 23, 77, 98, 164, 193
- [29] A. Ehresmann, *He-ion bombardment induced exchange bias modifications: Fundamentals and applications*, Recent Research Developments in Applied Physics **7 part 2**, 401 (2004). 11, 18, 23, 77, 92, 101, 164
- [30] J. Fassbender, S. Poppe, T. Mewes, J. Juraszek, B. Hillebrands, K.-U. Barholz, R. Mattheis, D. Engel, M. Jung, H. Schmoranzer and A. Ehresmann, *Ion irradiation of exchange bias systems for magnetic sensor applications*, Applied Physics A **77**, 51 (2003). 11, 19, 20, 22, 54, 188, 189
- [31] D. Wang, C. Nordman, J. M. Daughton, Z. Qian and J. Fink, *70% TMR at Room Temperature for SDT Sandwich Junctions With CoFeB as Free and Reference Layers*, IEEE Transactions on magnetics **40**, 2269 (2004). 12, 24
- [32] W. H. Meiklejohn and C. P. Bean, *New Magnetic Anisotropy*, Phys. Rev. **102**, 1413 (1956). 13, 14
- [33] W. H. Meiklejohn and C. P. Bean, *New Magnetic Anisotropy*, Phys. Rev. **105**, 904 (1957). 13, 14
- [34] J. Noguès, J. Sort, V. Langlais, S. Doppiu, B. Dieny, J. S. Muñoz, S. Suriñach, M. Barò, S. Stoyanov and Y. Zhang, *Exchange bias in ferromagnetic nanoparticles embedded in an antiferromagnetic matrix*, International Journal of Nanotechnology **2**, 23 (2005). 13
- [35] J. Noguès, J. Sort, V. Langlais, V. Skumryev, S. Suriñach, J. Muñoz and M. Barò, *Exchange bias in nanostructures*, Physics Reports **422**, 65 (2005). 13, 16, 18, 80
- [36] P. J. van der Zaag, Y. Ijiri, J. A. Borchers, L. F. Feiner, R. M. Wolf, J. M. Gaines, R. Erwin and M. A. Verheijen, *Difference between Blocking and Néel Temperatures in the Exchange Biased Fe<sub>3</sub>O<sub>4</sub> / CoO System*, Physical Review Letters **84**, 6102 (2000). 14
- [37] 15, 18, 21, 169  
B. Beschoten, A. Tillmanns, J. Keller, G. Güntherodt, U. Nowak and K. D. Usadel, *Domain State Model for Exchange Bias: Influence of Structural Defects on Exchange Bias in Co/CoO* in Advances in Solid State Physics Vol. 42 (Springer, 2002).
- [38] J. Noguès and I. K. Schuller, *Exchange Bias*, Journal of Magnetism and Magnetic Materials **192**, 203 (1999). 14, 15, 18, 54, 59, 60, 92

- [39] F. Radu and H. Zabel, *Exchange bias effect of ferro-/antiferromagnetic heterostructures*, arXiv.org - Condensed Matter - Materials Science: arXiv:0705.2055v1[cond-mat.mtrl-sci] (2007). 16, 18
- [40] D. Mauri, H. C. Siegmann, P. S. Bagus and E. Kay, *Simple model for thin ferromagnetic films exchange coupled to an antiferromagnetic substrate*, Journal of Applied Physics **62**, 3047 (1987). 16
- [41] A. P. Malozemoff, *Random-field model of exchange anisotropy at rough ferromagnetic-antiferromagnetic interfaces*, Physical Review B **35**, 3679 (1987). 16
- [42] A. P. Malozemoff, *Heisenberg-to-Ising crossover in a random-field model with uniaxial anisotropy*, Physical Review B **37**, 7673 (1988). 16
- [43] A. P. Malozemoff, *Mechanisms of exchange anisotropy (invited)*, Journal of Applied Physics **63**, 3874 (1988). 16
- [44] E. Fulcomer and S. H. Charap, *Thermal fluctuation aftereffect model for some systems with ferromagnetic-antiferromagnetic coupling*, Journal of Applied Physics **43**, 4190 (1972). 16, 17, 58
- [45] W. D. Engel, *Modifikation der magnetischen Eigenschaften von polykristallinen Mehrschichtsystemen mit Austauschverschiebung durch He-Ionenbeschuss*, Doctoral thesis, Technische Universität Kaiserslautern, 2004. 17, 18, 21, 23, 41, 106, 107, 170, 188
- [46] M. D. Stiles and R. D. McMichael, *Model for exchange bias in polycrystalline ferromagnet-antiferromagnet bilayers*, Physical Review B **59**, 3722 (1999). 18
- [47] P. Miltényi, M. Gierlings, J. Keller, B. Beschoten, G. Güntherodt, U. Nowak and K. D. Usadel, *Diluted Antiferromagnets in Exchange Bias: Proof of the Domain State Model*, Physical Review Letters **84**, 4224 (2000). 18, 21, 169
- [48] U. Nowak, K. Usadel, J. Keller, P. Miltényi, B. Beschoten and G. Güntherodt, *Domain state model for exchange bias. 1 Theory*, Physical Review B **66**, 014430 (2002). 18, 169
- [49] J. Keller, P. Miltényi, B. Beschoten, G. Güntherodt, U. Nowak and K. Usadel, *Domain state model for exchange bias. 2 Experiments*, Physical Review B **66**, 014431 (2002). 18, 169
- [50] A. Ehresmann, D. Junk, D. Engel, A. Paetzold and K. Röhl, *On the origin of ion bombardment induced exchange bias modifications in polycrystalline layers*, Journal of Physics D: Applied Physics **38**, 801 (2005). 18, 21, 58, 77, 101
- [51] A. E. Berkowitz and K. Takano, *Exchange anisotropy - a review*, Journal of Magnetism and Magnetic Materials **200**, 552 (1999). 18
- [52] R. L. Stamps, *Mechanisms for exchange bias*, J. Phys. D: Appl. Phys. **33**, R247 (2000). 18

- [53] M. Kiwi, *Exchange bias theory*, Journal of Magnetism and Magnetic Materials **234**, 584 (2001). 18
- [54] H. Xi, *Study of exchange bias for magnetoelectronic sensors*, Doctoral thesis, Carnegie Mellon University, 2001. 18
- [55] A. Thomas, *Preparation and characterization of magnetic single and double barrier junctions*, Doctoral thesis, Universität Bielefeld, 2003. 18, 19, 25, 31, 34, 113, 116
- [56] T. Mewes, R. Lopusnik, J. Fassbender, B. Hillebrands, M. Jung, D. Engel, A. Ehresmann and H. Schmoranzer, *Suppression of exchange bias by ion irradiation*, Applied Physics Letters **76**, 1057 (2000). 19, 21, 41, 164
- [57] A. Mougini, T. Mewes, R. Lopusnik, M. Jung, D. Engel, A. Ehresmann, H. Schmoranzer, J. Fassbender and B. Hillebrands, *Modification of the Exchange Bias Effect by He Ion Irradiation*, IEEE Trans. Magn. **36**, 2647 (2000). 19, 21
- [58] K. Potzger, L. Bischoff, M. O. Liedke, B. H. M. Rickart, P. P. Freitas, J. McCord and J. Fassbender, *Domain Structure of Magnetically Micro-Patterned PtMn/NiFe Exchange Bias Bilayers*, IEEE TRANSACTIONS ON MAGNETICS **41**, 3610 (2005). 19, 22
- [59] J. Fassbender, S. Poppe, T. Mewes, A. Mougini, B. Hillebrands, D. Engel, M. Jung, A. Ehresmann, H. Schmoranzer, G. Faini, K. J. Kirk and J. D. Chapman, *Magnetization Reversal of Exchange Bias Double Layers Magnetically Patterned by Ion Irradiation*, Physical Status Solidi (a) **189**, 439 (2002). 19, 22
- [60] A. Ehresmann, D. Engel, T. Weis, A. Schindler, D. Junk, J. Schmalhorst, V. Höink, M. D. Sacher and G. Reiss, *Fundamentals for magnetic patterning by ion bombardment of exchange bias layer systems*, Phys. Stat. Sol. **243**, 29 (2006). 19, 21, 48, 77, 164
- [61] J. Juraszek, J. Fassbender, S. Poppe, T. Mewes, B. Hillebrands, D. Engel, A. Kronenberger, A. Ehresmann and H. Schmoranzer, *Tuning exchange bias and coercive fields in ferromagnet/antiferromagnet bilayers with ion irradiation*, Journal of Applied Physics **91**, 6896 (2002). 19
- [62] D. Engel, A. Kronenberger, M. Jung, H. Schmoranzer, A. Ehresmann, A. Paetzold and K. Röhl, *Exchange anisotropy modification in NiO/NiFe bilayers by ion bombardment*, JMMM **263**, 275 (2003). 19, 20, 92
- [63] C. H. Yang, C.-H. Lai and S. Mao, *Reversing exchange fields in CoFe/PtMn and CoFe/IrMn bilayers by carbon field irradiation*, Journal of Applied Physics **93**, 6596 (2003). 19, 20
- [64] D. McGrouther, W. A. P. Nicholson, J. N. Chapman and S. McVitie, *Focused ion beam irradiation of ferromagnetic thin films in the presence of an applied field*, Journal of Physics D: Applied Physics **38**, 3348 (2005). 19



- [65] C.-H. Lai, C. Yang, R. Huang, C. Chen, F. Chen, J. Kai and H. Niu, *Effects of structure and ion irradiation on the exchange field of NiFe/NiMn*, Journal of Magnetism and Magnetic Materials **239**, 390 (2002). 21
- [66] V. Höink, *Exchange Bias und Ionenbestrahlung in magnetischen Tunnelementen*, Diploma thesis, Universität Bielefeld, 2003. 21, 31, 34, 108, 213
- [67] D. Engel, A. Ehresmann, J. Schmalhorst, M. Sacher, V. Höink and G. Reiss, *Initialization of unidirectional anisotropy in a ferromagnet/antiferromagnet bilayer by keV-He ion bombardment*, Journal of Magnetism and Magnetic Materials **293**, 849 (2005). 21, 48
- [68] D. McGrouther, J. N. Chapman and F. W. M. Vanhelmont, *Effect of Ga ion irradiation on the structural and magnetic properties of CoFe/IrMn exchange biased bilayers*, Journal of Applied Physics **95**, 7772 (2004). 21, 22
- [69] S. Poppe, J. Fassbender and B. Hillebrands, *On the mechanism of irradiation-enhanced exchange bias*, Europhysics Letters **66**, 430 (2004). 21, 22, 164
- [70] C. Chappert, H. Bernas, J. Ferré, V. Kottler, J.-P. Jamet, Y. Chen, E. Cambril, T. Devolder, F. Rousseaux, V. Mathet and H. Launois, *Planar Patterned Magnetic Media obtained by Ion Irradiation*, Science **280**, 1919 (1998). 22, 193
- [71] T. Devolder, C. Vieu, H. Bernas, J. Ferré, C. Chappert, J. Gierak, J.-P. Jamet, T. Aign, P. Meyer, Y. Chen, F. Rousseaux, V. Mathet and H. Launois, *Ion beam-induced magnetic patterning at the sub-0.1  $\mu\text{m}$  level*, C. R. Acad. Sci Paris, Série II b **327**, 915 (1999). 22
- [72] G. S. Chang, A. Moewes, S. H. Kim, J. Lee, K. Jeong, C. N. Whang, D. H. Kim and S. C. Shin, *Uniaxial in-plane magnetic anisotropy of a CoPt thin film induced by ion irradiation*, APPLIED PHYSICS LETTERS **88**, 092504 (2006). 22
- [73] C. Vieu, J. Gierak, H. Launois, T. Aign, P. Meyer, J. Jamet, J. Ferré, C. Chappert, V. Mathet and H. Bernas, *High resolution magnetic patterning using focused ion beam irradiation*, Microelectronic Engineering **53**, 191 (2000). 22
- [74] A. Mougin, S. Poppe, J. Fassbender, B. Hillebrands, G. Faini, U. Ebels, M. Jung, D. Engel, A. Ehresmann and H. Schmoranzler, *Magnetic micropatterning of FeNi/FeMn exchange bias bilayers by ion irradiation*, Journal of Applied Physics **89** (2001). 22
- [75] T. Devolder, C. Chappert and H. Bernas, *Theoretical study of magnetic pattern replication by He<sup>+</sup> ion irradiation through stencil masks*, Journal of Magnetism and Magnetic Materials **249**, 452 (2002). 22
- [76] *SRIM 2006 online help*, (2006). 22
- [77] D. Junk, *Aufbau einer Ionenstrahlanlage und Untersuchung von ionenbeschussinduzierten magnetischen Modifikationen in polykristallinen*

- Zweischichtsystemen und Tunnelementen*, Diploma thesis, Technische Universität Kaiserslautern, 2003. 23, 41
- [78] D. Backes, *Herstellung und rasterkraftmikroskopische Untersuchung von topografisch strukturierten, magnetischen Schichtsystemen*, Diploma thesis, Technische Universität Kaiserslautern, 2004. 23, 41, 188
- [79] T. Weis, *Einfluss des Ferromagneten und der Ioneneindringtiefe bei Modifikationen der Austauschverschiebung von polykristallinen Antiferromagnet/Ferromagnet-Zweilagenschichtsystemen*, Diploma thesis, Technische Universität Kaiserslautern, 2004. 23, 41
- [80] W. Clemens, *30. Ferienkurs des IFF 1999, Magnetische Schichtsysteme* (Forschungszentrum Jülich GmbH, 1999), chapter D5, GMR Sensoren in der industriellen Anwendung. 23
- [81] I. Giaever, *Energy Gap in Superconductors Measured by Electron Tunneling*, Physical Review Letters **5**, 147 (1960). 23
- [82] P. Tedrow and R. Meservey, *Spin-Dependent Tunneling into Ferromagnetic Nickel*, Phys. Rev. Lett. **26**, 192 (1971). 23
- [83] M. Julliere, *Tunneling between ferromagnetic films*, Physics Letters **54A**, 225 (1975). 24
- [84] J. S. Moodera, L. R. Kinder, T. M. Wong and R. Meservey, *Large Magnetoresistance at Room Temperature in Ferromagnetic Thin Film Tunnel Junctions*, Physical Review Letters **74**, 3273 (1995). 24
- [85] T. Miyazaki and N. Tezuka, *Giant magnetic tunneling effect in Fe/Al<sub>2</sub>O<sub>3</sub>/Fe junction*, Journal of Magnetism and Magnetic Materials **139**, L231 (1995). 24
- [86] P. R. LeClair, *Fundamental Aspects of Spin Polarized Tunneling*, Doctoral thesis, Technische Universität Eindhoven, 2002. 25
- [87] E. Y. Tsybal, O. N. Mryasov and P. R. LeClair, *Spin-dependent tunnelling in magnetic tunnel junctions*, J. Phys.: Condens. Matter **15**, R109 (2003). 25
- [88] J.-G. J. Zhu and C. Park, *Magnetic tunnel junctions*, materials today **9**, 36 (2006). 25, 77
- [89] C. Heiliger, P. Zahn and I. Mertig, *Microscopic origin of magnetoresistance*, materials today **9**, 46 (2006). 25
- [90] C. L. Dennis, R. P. Borges, L. D. Buda, U. Ebels, J. F. Gregg, M. Hehn, E. Jouguelet, K. Ounadjela, I. Petej, I. L. Prejbeanu and M. J. Thornton, *The defining length scales of mesomagnetism: a review*, Journal of Physics: Condensed Matter **14**, R1175 (2002). 25, 26
- [91] J. Schelten, *30. Ferienkurs des IFF 1999, Magnetische Schichtsysteme* (Forschungszentrum Jülich GmbH, 1999), chapter D7, Tunnelmagnetowiderstand. 25

- [92] G. Binasch, P. Grünberg, F. Saurenbach and W. Zinn, *Enhanced magnetoresistance in layered magnetic structures with antiferromagnetic interlayer exchange*, Physical Review B **39**, 4828 (1989). 25
- [93] M. N. Baibich, J. M. Broto, A. Fert, F. N. V. Dau, F. Petroff, P. Eitenne, G. Creuzet, A. Friederich and J. Chazelas, *Giant Magnetoresistance of (001)Fe/(001)Cr Magnetic Superlattices*, Physical Review Letters **61**, 2472 (1988). 25
- [94] N. Mott, Proc. Roy. Soc. **156**, 368 (1936). 25
- [95] R. Coehoorn, *Giant Magnetoresistance in Exchange-Biased Spin-Valve Layered Structures and its Applications in Read Heads in Magnetic Multilayers and giant magneto resistance: fundamentals and industrial applications*, Springer series in surface science Vol. 37, U. Hartmann (Ed.) (Springer, Berlin, 2000), chapter 4. 25, 97
- [96] E. Y. Tsybal and D. G. Pettifor, *Perspectives of Giant Magnetoresistance*, Solid State Physics Vol. 56 (Academic Press, 2001), page 113. 25, 26
- [97] D. M. Edwards, J. Mathon and R. B. Muniz, *A Resistor Network Theory of the Giant Magnetoresistance in Magnetic Superlattices*, IEEE Transactions on magnetics **21**, 3548 (1991). 25
- [98] J. MATHON, *Exchange interactions and giant magnetoresistance in magnetic multilayers*, Contemporary Physics **32**, 143 (1991). 25
- [99] U. Hartmann, editor, *Magnetic multilayers and giant magneto resistance: fundamentals and industrial applications* (Springer-Verlag, 2000). 26, 27, 28, 29, 81, 98
- [100] S. Heitmann, *Cobalt / Copper Multilayers: Interplay of Microstructure and GMR and Recrystallization as the Key Towards Temperature Stability*, Doctoral thesis, Universität Bielefeld, 2004. 26
- [101] I. Mertig, *30. Ferienkurs des IFF 1999, Magnetische Schichtsysteme* (Forschungszentrum Jülich GmbH, 1999), chapter D2, Theorie des Magnetowiderstandes. 26
- [102] G. Reiss, H. Brückl and A. Hütten, *30. Ferienkurs des IFF 1999, Magnetische Schichtsysteme* (Forschungszentrum Jülich GmbH, 1999), chapter D3, GMR Experimente. 26
- [103] P. Grünberg, R. Schreiber, Y. Pang, M. B. Brodsky and H. Sowers, *Layered Magnetic Structures: Evidence for Antiferromagnetic Coupling of Fe Layers across Cr Interlayers*, Physical Review Letters **57**, 2442 (1986). 26
- [104] S. S. P. Parkin, N. More and K. P. Roche, *Oscillations in Exchange Coupling and Magnetoresistance in Metallic Superlattice Structures: Co/Ru, Co/Cr, and Fe/Cr*, Physical Review Letters **64**, 2304 (1990). 26

- [105] J. Unguris, R. J. Celotta and D. T. Pierce, *Observation of Two Different Oscillation Periods in the Exchange Coupling of Fe/Cr/Fe(110)*, Physical Review Letters **67**, 140 (1991). 26, 27
- [106] B. Hillebrands, *Spin-wave calculations for multilayered structures*, Physical Review B **41**, 530 (1990). 27
- [107] J. Barnaś and P. Grünberg, *Spin waves in exchange-coupled epitaxial double-layers*, Journal of Magnetism and Magnetic Materials **82**, 186 (1989). 27
- [108] J. Fassbender, F. Nötemann, R. L. Stamps, R. E. Camley, B. Hillebrands, G. Güntherodt and S. S. P. Parkin, *Oscillatory interlayer exchange coupling of Co/Ru multilayers investigated by Brillouin light scattering*, Physical Review B **46**, 5810 (1992). 27
- [109] P. Bruno, *Theory of interlayer exchange interactions in magnetic multilayers*, Journal of Physics: Condensed Matter **11**, 9403 (1999). 27, 28, 29, 98
- [110] M. D. Stiles, *Interlayer Exchange Coupling* Ultrathin Magnetic Structures III - Fundamentals of Nanomagnetism (Springer, Berlin, 2005), chapter 4. 27, 28, 29, 97, 98, 99
- [111] J. Slonczewski, *Overview of interlayer exchange theory*, Journal of Magnetism and Magnetic Materials **150**, 13 (1995). 28, 29, 98
- [112] S. O. Demokritov, *Biquadratic interlayer coupling in layered magnetic systems*, Journal of Physics D: Applied Physics **31**, 925 (1998). 28, 29, 98, 99
- [113] B. Heinrich, Z. Celinski, J. F. Cochran, A. S. Arrott, K. Myrtle and S. T. Purcell, *Bilinear and biquadratic exchange coupling in bcc Fe/Cu/Fe trilayers: Ferromagnetic-resonance and surface magneto-optical Kerr-effect studies.*, Physical Review B **47**, 5077 (1993). 29
- [114] U. Rucker, S. Demokritov, E. Tsymbal, P. Grünberg and W. Zinn, *Biquadratic coupling in Fe/Au/Fe trilayers: Experimental evidence for the magnetic-dipole mechanism*, Journal of Applied Physics **78**, 387 (1995). 29
- [115] M. Schäfer, S. Demokritov, S. Müller-Pfeiffer, R. Schäfer, M. Schneider, P. Grünberg and W. Zinn, *Investigation of 90° coupling in Fe/Ag/Fe structures: Loose spins and fluctuation mechanism*, J. Appl. Phys. **77**, 6432 (1995). 29, 98
- [116] M. Stiles, *Interlayer exchange coupling*, Journal of Magnetism and Magnetic Materials **200**, 322 (1999). 29
- [117] P. Bruno, *30. Ferienkurs des IFF 1999, Magnetische Schichtsysteme* (Forschungszentrum Jülich GmbH, 1999), chapter B8, Theory of interlayer exchange coupling. 29
- [118] S. Tegen, I. Mönch, J. Schumann, H. Vinzelberg and C. M. Schneider, *Effect of Néel coupling on magnetic tunnel junctions*, Journal of Applied Physics **89** (2001). 30

- [119] L. Neel, *Comptes Rendus Acad. Sci.* **255**, 1545 and 1676 (1962). 30
- [120] J. C. S. Kools and W. Kula, *Effect of finite magnetic film thickness on Neel coupling in spin valves*, *Journal of Applied Physics* **85**, 4466 (1999). 30
- [121] M. D. Sacher, *Charakterisierung der Barrieren-Grenzflächen magnetischer Tunnelemente mit halbmetallischen Elektroden*, Doctoral thesis, Universität Bielefeld, 2007. 31, 34, 38, 39, 46, 166, 181
- [122] S. Kämmerer, *The Heusler alloy  $\text{Co}_2\text{MnSi}$  in thin films*, Doctoral thesis, Universität Bielefeld, 2004. 31
- [123] M. Sacher, *Präparation und Charakterisierung von Mehrfachbarrieren für magnetische Tunnelemente*, Diploma thesis, Universität Bielefeld, 2002. 31, 34, 41, 177
- [124] W. Schweika, *30. Ferienkurs des IFF 1999, Magnetische Schichtsysteme* (Forschungszentrum Jülich GmbH, 1999), chapter A5, Schichtpräparation und Sputterverfahren. 31
- [125] V. Drewello, *Untersuchung der Spinpolarisation von 3d-Ferromagneten in MgO Tunnelsystemen*, Diploma thesis, Universität Bielefeld, 2006. 31, 34, 36
- [126] K. Rott, personal communication. 32
- [127] S. K. Khanna and J. Lambe, *Inelastic Electron Tunneling Spectroscopy*, *Science* **220**, 1345 (1983). 35, 36
- [128] C. J. Adkins and W. A. Philips, *Inelastic electron tunneling spectroscopy*, *Journal of Physics C: Solid State Physics* **18**, 1313 (1985). 36, 133, 134
- [129] E. L. Wolf, *Principles of electron tunneling spectroscopy* (Oxford University Press, 1989). 36
- [130] V. Drewello, J. Schmalhorst, A. Thomas and G. Reiss, *submitted*, (2007). 36, 134
- [131] D. E. Fowler, *Magneto-optic Kerr rotation* in *Encyclopedia of materials characterization*, (Butterwoth-Heinemann, Stoneham and Manning Publications Co., Greenwich, 1992), chapter 12.3. 37
- [132] K. Shinagawa, *Faraday and Kerr effects in ferromagnets* in *Magneto-Optics*, S. Sugano and N. Kojima (Ed.) (Springer Berlin Heidelberg, 2000), chapter 5. 37
- [133] N. Wiese, *Coupling phenomena and scalability of CoFeB/Ru/CoFeB sandwiches*, Doctoral thesis, Bielefeld University, 2006. 37, 83
- [134] D. Sudfeld, *Aufbau eines Meßplatzes für magnetfeldabhängige Messungen der Magnetisierung und des Magnetowiderstands dünner Schichten*, (Staatsexamensarbeit, Universität Bielefeld, 2000). 37

- [135] R. Vollmer, *30. Ferienkurs des IFF 1999, Magnetische Schichtsysteme* (Forschungszentrum Jülich GmbH, 1999), chapter C7, Lineare und nichtlineare Magnetooptik an ultradünnen ferromagnetischen Schichten und Vielfachschichten. 37
- [136] P. S. Bechthold, *30. Ferienkurs des IFF 1999, Magnetische Schichtsysteme* (Forschungszentrum Jülich GmbH, 1999), chapter C8, Magnetooptische Effekte: Phänomenologische Beschreibung und Anwendungen. 37
- [137] I. Ennen, *Charakterisierung von Cobalt-Nanopartikeln und Untersuchungen zur Herstellung granularer Strukturen*, Diploma thesis, Universität Bielefeld, 2003. 37, 192
- [138] Princeton Measurements Corporation, *Micro MagTM2900 Instruction Manual*, 2002. 37
- [139] S. Anders, H. A. Padmore, R. M. Duarte, T. Renner, T. Stammer, A. Scholl, M. Scheinfein, J. Stöhr, L. Stéve and B. Sinkovic, *Photoemission electron microscope for the study of magnetic materials*, Review of Scientific Instruments **70**, 3973 (1999). 38, 39, 61
- [140] S. W. Lovesey and S. P. Collins, *X-Ray Scattering and Absorption by Magnetic Materials* (Clarendon Press, Oxford, 1996). 38, 39
- [141] D. Lott, *Magnetic X-ray Reflectivity*, Doctoral thesis, Ludwig-Maximilians-Universität München, 2001. 38, 39
- [142] R. Nakajima, *X-ray magnetic circular dichroism spectroscopy in transition metal thin films*, Doctoral thesis, Stanford University, 1998. 38, 39
- [143] H. Ohldag, *Exchange coupling of Co and Fe on Antiferromagnetic NiO Investigated by Dichroism X-Ray Absorption Spectroscopy*, Doctoral thesis, Heinrich-Heine-Universität Düsseldorf, 2006. 38, 39
- [144] J. Stöhr, *X-ray magnetic circular dichroism spectroscopy of transition metal thin films*, Journal of Electron Spectroscopy and Related Phenomena **75**, 253 (1995). 38, 39, 61
- [145] T. Funk, A. Deb, S. J. George, H. Wang and S. P. Cramer, *X-ray magnetic circular dichroism - a high energy probe of magnetic properties*, Coordination Chemistry Reviews **249**, 253 (2005). 38, 39
- [146] Homepage of the photoemission electron microscopy division of the experimental systems group at the Advanced Light Source, Lawrence Berkeley National Laboratory, Berkeley, CA , [xraysweb.lbl.gov/peem2/webpage/Home.shtml](http://xraysweb.lbl.gov/peem2/webpage/Home.shtml). 39
- [147] U. Hartmann, *Magnetic force microscopy*, Annual Review of Materials Science **29**, 53 (1999). 40
- [148] R. S. Howland and M. D. Kirk, *Scanning tunneling microscopy and scanning force microscopy* in Encyclopedia of materials characterization, (Butterworth-Heinemann, Stoneham and Manning Publications Co., Greenwich, 1992), chapter 2.3. 40

- [149] U. Hartmann, *30. Ferienkurs des IFF 1999, Magnetische Schichtsysteme* (Forschungszentrum Jülich GmbH, 1999), chapter B7, Magnetisch abbildende Rastersondenverfahren. 40
- [150] J. Schmalhorst, *Magnetische, thermische und dielektrische Stabilität von magnetischen Tunnelementen*, Doctoral thesis, Universität Bielefeld, 2001. 40, 41
- [151] Y. E. Strausser, *Auger electron spectroscopy* in Encyclopedia of materials characterization, (Butterworth-Heinemann, Stoneham and Manning Publications Co., Greenwich, 1992), chapter 5.3. 40, 41
- [152] R. H. Geiss, *Energy dispersive x-ray spectroscopy* in Encyclopedia of materials characterization, (Butterworth-Heinemann, Stoneham and Manning Publications Co., Greenwich, 1992), chapter 3.1. 40, 41
- [153] J. B. Bindell, *Scanning electron microscopy* in Encyclopedia of materials characterization, (Butterworth-Heinemann, Stoneham and Manning Publications Co., Greenwich, 1992), chapter 2.2. 41
- [154] K. Kopitzki, *Einführung in die Festkörperphysik* (B.G. Teubner, Stuttgart, 1986). 42
- [155] J. Ziegler, *S R I M Instruction Manual, Version 96.xx* ([www.srim.org](http://www.srim.org), 1998/2003). 42, 43
- [156] J. F. Ziegler, J. Biersack and U. Littmark, *The Stopping and Range of Ions in Solids* (Pergamon Press, 1995). 43
- [157] J. A. Nelder and R. Mead, *Computer Journal* **7**, 308 (1965). 43
- [158] W. H. Press, S. A. Teukolsky, W. T. Vetterling and B. P. Flannery, *Numerical Recipes in Fortran*, second Auflage (Cambridge University Press, 1992). 44
- [159] W. H. Press, B. Flannery, S. Teukolsky and W. Vetterling, *Numerical Recipes in C* (Cambridge University Press, 1988). 44, 81
- [160] V. Höink, M. D. Sacher, J. Schmalhorst, G. Reiss, D. Engel, T. Weis and A. Ehresmann, *Switchable resonant x-ray Bragg scattering on a magnetic grating patterned by ion bombardment*, *Journal of Applied Physics* **100**, 063903 (2006). 46, 194
- [161] J. Grabis, A. Nefedov and H. Zabel, *Diffractionmeter for soft x-ray resonant magnetic scattering*, *Review of Scientific Instruments* **74**, 4048 (2003). 46
- [162] M. R. Weiss, R. Follath, K. J. S. Sawhney, F. Senf, J. Bahrtdt, W. Frentrup, A. Gaupp, S. Sasaki, M. Scheer, H. C. Mertins, D. Abramsohn, F. Schäfers, W. Kuch and W. Mahler, *The elliptically polarized undulator beamlines at BESSY II*, *Nuclear Instruments and Methods in Physics Research A* **467** **468**, 449 (2001). 46

- [163] K. Sawhney, F. Senf, M. Scheer, F. Schäfers, J. Bahrtdt, A. Gaupp and W. Gudat, *A novel undulator-based PGM beamline for circularly polarised synchrotron radiation at BESSY II*, Nuclear Instruments and Methods in Physics Research A **390**, 395 (1997). 46
- [164] *X-Ray Data Booklet, second edition* (Center for X-Ray Optics , Advanced Light Source, Berkeley, 2001). 50
- [165] M. Bode, M. Dreyer, M. Getzlaff, M. Kleiber, A. Wadas and R. Wiesendanger, *Recent progress in high-resolution magnetic imaging using scanning probe techniques*, J. Phys.: Condens. Matter **11**, 9387 (1999). 52
- [166] V. Höink, M. D. Sacher, J. Schmalhorst, G. Reiss, D. Engel, T. Weis and A. Ehresmann, *Thermal stability of magnetic nanostructures in ion-bombardment-modified exchange-bias systems*, Physical Review B **73**, 224428 (2006). 54, 194
- [167] V. Höink, M. D. Sacher, J. Schmalhorst, G. Reiss, D. Engel, D. Junk and A. Ehresmann, *Postannealing of magnetic tunnel junctions with ion-bombardment-modified exchange bias*, Applied Physics Letters **86**, 152102 (2005). 54, 77, 113, 208
- [168] A. Thomas, H. Brückl, M. Sacher, J. Schmalhorst and G. Reiss, *Aluminium oxidation by a remote electron cyclotron resonance plasma in magnetic tunnel junctions*, J. Vac. Sci. Tech. B **21**, 2120 (2003). 54, 113
- [169] J. Schmalhorst, V. Höink, G. Reiss, D. Engel, D. Junk, A. Schindler, A. Ehresmann and H. Schmoranzner, *Influence of ion bombardement on transport properties and exchange bias in magnetic tunnel junctions*, Journal of Applied Physics **94**, 5556 (2003). 54, 63, 108
- [170] A. Paetzold and K. Roöll, *Thermally activated self-alignment of exchange coupling in NiO/NiFe bilayers*, Journal of Applied Physics **91**, 7748 (2002). 58
- [171] J. Schmalhorst, M. Sacher, V. Höink, G. Reiss, D. Engel and A. Ehresmann, *X-ray absorption and magnetic circular dichroism studies of ion-bombarded ferromagnet-antiferromagnet bilayers*, Physical Review B **70**, 184403 (2004). 63, 164, 165, 166
- [172] M. Mulazzi, K. Chesnel, A. Marty, G. Asti, M. Ghidini, M. Solzi, M. Belakhovsky, N. Jaouen, J. Tonnerre and F. Sirotti, *Stripe domains nucleation observed by X-ray magnetic scattering: temperature variation of exchange and anisotropy*, Journal of Magnetism and Magnetic Materials **272276**, e895 (2004). 65
- [173] A. P. Malozemoff and J. C. Slonczewski, *Magnetic domain walls in bubble materials* (Academic Press, 1979). 65
- [174] A. Hubert and R. Schäfer, *Magnetic Domains* (Springer-Verlag, 1998). 65, 80, 81, 197



- [175] V. Höink, J. Schmalhorst, G. Reiss, D. Lengemann, D. Engel and A. Ehresmann, *Influence of ion bombardment induced patterning of exchange bias in pinned artificial ferrimagnets on the interlayer exchange coupling*, submitted (2007). 77
- [176] J. Schmalhorst, V. Höink, G. Reiss, D. Engel, D. Junk, A. Schindler, A. Ehresmann and H. Schmoranzer, *Influence of ion bombardment on transport properties and exchange bias in magnetic tunnel junctions*, *Journal of Applied Physics* **94**, 5556 (2003). 77, 78
- [177] J. Fassbender, L. Bischoff, R. Mattheis and P. Fischer, *Magnetic domains and magnetization reversal of ion-induced magnetically patterned Ruderman-Kittel-Kasuya-Yoshida-coupled Ni<sub>81</sub>Fe<sub>19</sub>/Ru/Co<sub>90</sub>Fe<sub>10</sub> films*, *Journal of Applied Physics* **99**, 08G301 (2006). 77, 85, 97
- [178] S. Demokritov, C. Bayer, S. Poppe, M. Rickart, J. Fassbender, B. Hillebrands, D. I. Kholin, N. Kreines and O. Liedke, *Control of Interlayer Exchange Coupling in Fe/Cr/Fe Trilayers by Ion Beam Irradiation*, *Physical Review Letters* **90**, 097201 (2003). 77, 93, 97, 100, 106, 107
- [179] V. E. Demidov, D. I. Kholin, S. O. Demokritov, B. Hillebrands, F. Wegelin and J. Marien, *Magnetic patterning of exchange-coupled multilayers*, *Applied Physics Letters* **84**, 2853 (2004). 77, 97
- [180] S. Blomeier, B. Hillebrands, V. E. Demidov, S. O. Demokritov, B. Reuscher, A. Brodyanski and M. Kopnarski, *Magnetic patterning of Fe/Cr/Fe (001) trilayers by Ga<sup>+</sup> ion irradiation*, *Journal of Applied Physics* **98**, 093503 (2005). 77, 97
- [181] D. Engel, H. Schmoranzer, A. Ehresmann, H. Mertins, D. Abramsohn and W. Gudat, *Soft X-ray resonant magnetic reflection investigations of FeMn/Co/Cu/Co spin valves modified by He-ion bombardment*, *Physica B* **345**, 185 (2004). 77, 99
- [182] Y. Saito, H. Sugiyama, T. Inokuchi and K. Inomata, *Interlayer exchange coupling dependence of thermal stability parameters in synthetic antiferromagnetic free layers*, *Journal of Applied Physics* **99**, 08K702 (2006). 83
- [183] N. Wiese, T. Dimopoulos, M. Rührig, J. Wecker, H. Brückl and G. Reiss, *Antiferromagnetically coupled CoFeB/Ru/CoFeB trilayers*, *Applied Physics Letters* **85**, 2020 (2004). 83
- [184] J. Schmalhorst, H. Brückl, G. Reiss, G. Gieres and J. Wecker, *Thermally induced changes of magnetic coupling in a pinned artificial antiferromagnet used in magnetic tunnel junctions*, *Journal of Applied Physics* **94**, 3268 (2003). 97, 98
- [185] H. A. M. van den Berg, *Physics of and Methods for Studying Metallic Multilayers with Interlayer Exchange Coupling and GMR Response in Magnetic multilayers and giant magneto resistance: fundamentals and industrial applications*,

- Springer series in surface science Vol. 37, U. Hartmann (Ed.) (Springer, Berlin, 2000), chapter 6. 97, 98
- [186] V. Höink, D. Meyners, J. Schmalhorst, G. Reiss, D. Junk, D. Engel and A. Ehresmann, *Reconfigurable magnetic logic for all basic logic functions produced by ion bombardment induced magnetic patterning*, Applied Physics Letters **91**, 162505 (2007). 102
- [187] J. Schmalhorst, H. Brückl, G. Reiss, G. Gieres and J. Wecker, *Magnetotransport and microstructure of annealed magnetic tunnel junctions*, Journal of Applied Physics **91**, 6617 (2002). 113, 114, 147, 155
- [188] J. Schmalhorst, M. Sacher, A. Thomas, H. Brückl, G. Reiss and K. Starke, *X-ray absorption and magnetic circular dichroism studies of annealed magnetic tunnel junctions*, Journal of Applied Physics **97**, 123711 (2005). 113, 115, 116, 147, 166
- [189] X. Kou, personal communication. 125, 147, 159
- [190] J. Schmalhorst, A. Thomas, G. Reiss, X. Kou and E. Arenholz, *Influence of chemical and magnetic interface properties of Co-Fe-B/MgO/Co-Fe-B tunnel junctions on the annealing temperature dependence of the magnetoresistance*, Journal of Applied Physics **102**, 053907 (2007). 128, 146, 147
- [191] Y. Jang, C. Nam, K.-S. Lee, B. K. Cho, Y. J. Cho, K.-S. Kim and K. W. Kim, *Variation in the properties of the interface in a CoFeB/MgO/CoFeB tunnel junction during thermal annealing*, Applied Physics Letters **91**, 102104 (2007). 128, 129, 130, 132
- [192] G.-X. Miao, K. B. Chetry, A. Gupta, W. H. Butler, K. Tsunekawa, D. Djayaprawira and G. Xiao, *Inelastic tunneling spectroscopy of magnetic tunnel junctions based on CoFeB/MgO/CoFeB with Mg insertion layer*, Journal of Applied Physics **99**, 08T305 (2006). 130, 134
- [193] R. Matsumoto, Y. Hamada, M. Mizuguchi, M. Shiraishi, H. Maehara, K. Tsunekawa, D. D. Djayaprawira, N. Watanabe, Y. Kurosaki, T. Nagahama, A. Fukushima, H. Kubota, S. Yuasa and Y. Suzuki, *Tunneling spectra of sputter-deposited CoFeB/MgO/CoFeB magnetic tunnel junctions showing giant tunneling magnetoresistance effect*, Solid State Communications **136**, 611 (2005). 133, 134, 146, 169
- [194] O. Schebaum, personal communication. 133
- [195] J. S. Moodera, J. Nowak and R. J. M. van de Veerdonk, *Interface Magnetism and Spin Wave Scattering in Ferromagnet-Insulator-Ferromagnet Tunnel Junctions*, Physical Review Letters **80**, 2941 (1998). 133
- [196] K. Ono, T. Daibou, S.-J. Ahn, Y. Sakuraba, T. Miyakoshi, T. Morita, Y. Kikuchi, M. Oogane, Y. Ando and T. Miyazaki, *Tunneling spectroscopy in CoFeB/MgO/CoFeB magnetic tunnel junctions*, Journal of Applied Physics **99**, 08A905 (2006). 134, 135, 143

- [197] P. A. Thiry, M. Liehr, J. J. Pireaux and R. Caudano, *Infrared optical constants of insulators determined by high-resolution electron-energy-loss spectroscopy*, Physical Review B **29**, 4824 (1984). 134
- [198] M. Mizuguchi, Y. Hamada, R. Matsumoto, S. Nishioka, H. Maehara, K. Tsunekawa, D. D. Djayaprawira, N. Watanabe, T. Nagahama, A. Fukushima, H. Kubota, S. Yuasa, M. Shiraishi and Y. Suzuki, *Tunneling spectroscopy of magnetic tunnel junctions: Comparison between CoFeB/MgO/CoFeB and CoFeB/AlO/CoFeB*, Journal of applied Physics **99**, 08T309 (2006). 134
- [199] Y. Ando, T. Miyakoshi, M. Oogane, T. Miyazaki, H. Kubota, K. Ando and S. Yuasa, *Spin-dependent tunneling spectroscopy in single-crystal Fe/MgO/Fe tunnel junctions*, Applied Physics Letters **87**, 142502 (2005). 134, 135, 143
- [200] Y. Xu, D. Ephron and M.R.Beasley, *Directed inelastic hopping of electrons through metal-insulator-metal tunnel junctions*, Physical Review B **52**, 2843 (1995). 139
- [201] J. Hayakawa, S. Ikeda, F. Matsukura, H. Takahashi and H. Ohno, *Dependence of giant tunnel magnetoresistance of sputtered CoFeB/MgO/CoFeB magnetic tunnel junctions on MgO barrier thickness and annealing temperature*, Japanese Journal of Applied Physics **44**, L587 (2005). 143
- [202] S. Yuasa, A. Fukushima, T. Nagahama, K. Ando and Y. Suzuki, *High tunnel magnetoresistance at room temperature in fully epitaxial Fe/MgO/Fe tunnel junctions due to coherent spin-polarized tunneling*, Japanese Journal of Applied Physics **43**, 588 (2004). 143
- [203] S. S. P. Parkin, C. Kaiser, A. Panchula, P. M. Rice, B. Hughes, M. Samant and S. Yang, *Giant tunneling magnetoresistance at room temperature with MgO (100) tunnel barriers*, Nature Materials **3**, 862 (2004). 143
- [204] D. D. Djayaprawira, K. Tsunekawa, M. Nagai, H. Maehara, S. Yamagata, N. Watanabe, S. Yuasa, Y. Suzuki and K. Ando, *230% room-temperature magnetoresistance in CoFeB/MgO/CoFeB magnetic tunnel junctions*, Applied Physics Letters **86**, 092502 (2005). 143, 181
- [205] J. Hayakawa, S. Ikeda, Y. M. Lee, F. Matsukura and H. Ohno, *Effect of high annealing temperature on giant tunnel magnetoresistance ratio of CoFeB/MgO/CoFeB magnetic tunnel junctions*, Applied Physics Letters **89**, 232510 (2006). 147, 154, 181, 205
- [206] T. Dimopoulos, G. Gieres, J. Wecker, N. Wiese, Y. Luo and K. Samwer, *Large tunnel magnetoresistance with plasma oxidized MgO barrier*, Journal of Applied Physics **98**, 073705 (2005). 148
- [207] Y. M. Lee, J. Hayakawa, S. Ikeda, F. Matsukura and H. Ohno, *Giant tunnel magnetoresistance and high annealing stability in CoFeB/MgO/CoFeB magnetic tunnel junctions with synthetic pinned layer*, Applied Physics Letters **89**, 042506 (2006). 156, 159, 181, 187, 215

- [208] R. Jansen and J. S. Moodera, *Magnetoresistance in doped magnetic tunnel junctions: Effect of spin scattering and impurity-assisted transport*, Physical Review B **61**, 9047 (2000). 184
- [209] I. Krug, *Charakterisierung von ionenstrahlinduzierten lateralen magnetischen Strukturen in austauschverschobenen Zweifachschichten durch Magnetkraftmikroskopie*, Diploma thesis, Universität Kaiserslautern, 2002. 188
- [210] S. Sun, C. B. Murray, D. Weller, L. Folks and A. Moser, *Monodisperse FePt Nanoparticles and Ferromagnetic FePt Nanocrystal Superlattices*, Science **287**, 1989 (2000). 189
- [211] Q. A. Pankhurst, J. Connolly, S. Jones and J. Dobson, *Applications of magnetic nanoparticles in biomedicine*, Journal of Physics D: Applied Physics **36**, R167 (2003). 189
- [212] U. Häfeli, W. Schütt and J. Teller, *Scientific and Clinical Applications of Magnetic Carriers* (Plenum, 1997). 189
- [213] G. Reiss and A. Hütten, *Magnetic nanoparticles - Applications beyond data storage*, Nature materials **4**, 725 (2005). 189
- [214] M. Panhorst, P. B. Kamp, G. Reiss and H. Brückl, *Sensitive bondforce measurements of ligand-receptor pairs with magnetic beads.*, Biosensors and Bioelectronics **20**, 1685 (2005). 189
- [215] G. Reiss, H. Brückl, A. Hütten, J. Schotter, M. Brzeska, D. Sudfeld, A. Becker, P. B. Kamp, A. Pühler, K. Wojczykowski and P. Jutzi, *Magnetoresistive Sensors and Magnetic Nanoparticles for Biotechnology*, Journal of Material Research **20**, 3294 (2005). 189
- [216] I. Ennen, V. Höink, A. Weddemann, A. Hütten, J. Schmalhorst, G. Reiss, C. Waltenberg, P. Jutzi, T. Weis, D. Engel and A. Ehresmann, *Manipulation of magnetic nanoparticles by the strayfield of magnetically patterned ferromagnetic layers*, Journal of Applied Physics **102**, 013910 (2007). 193, 197
- [217] V. F. Puentes, K. M. Krishnan and A. P. Alivisatos, *Colloidal Nanocrystal Shape and Size Control: The Case of Cobalt*, Science **291**, 2115 (2001). 193
- [218] I. Ennen, personal communication. 193, 194
- [219] A. Hütten, D. Sudfeld, I. Ennen, G. Reiss, W. Hachmann, U. Heinzmann, K. Wojczykowski, P. Jutzi, W. Saikaly and G. Thomas, *New magnetic nanoparticles for biotechnology*, Journal of Biotechnology **112**, 47 (2004). 193
- [220] V. Höink, D. Meyners, J. Schmalhorst, G. Reiss, D. Junk, D. Engel and A. Ehresmann, *Reconfigurable magnetic logic for all basic logic functions produced by ion bombardment induced magnetic patterning*, Applied Physics Letters **91**, 162505 (2007). 201

- [221] R. Richter, L. Bär, J. Wecker and G. Reiss, *Nonvolatile field programmable spin-logic for reconfigurable computing*, Applied Physics Letters **80**, 1291 (2002). 201
- [222] D. Meyners, K. Rott, H. Brückl, G. Reiss and J. Wecker, *Submicron-sized magnetic tunnel junctions in field programmable logic gate arrays*, Journal of Applied Physics **99**, 023907 (2006). 202, 210
- [223] IBM Corporation, *IBM's 'Millipede' Project Demonstrates Trillion-Bit Data Storage Density*, [domino.research.ibm.com/comm/pr.nsf/pages/news.20020611\\_millipede.html](http://domino.research.ibm.com/comm/pr.nsf/pages/news.20020611_millipede.html) (2002). 208
- [224] E. Eleftheriou, T. Antonakopoulos, G. Binnig, G. C. adn M. Despont, A. Dhoulakia, U. Duerig, M. Lantz, H. Pozidis, H. Rothuizen and P. Vettiger, *Millipede - A MEMS-based scanning-probe data-storage system*, IEEE Transactions on Magnetics **39**, 938 (2003). 208